PhD-FSTC-2018-40
The Faculty of Sciences, Technology and Communication

DISSERTATION

Defence held on 07/06/2018 in Luxembourg

to obtain the degree of

DOCTEUR DE L'UNIVERSITÉ DU LUXEMBOURG

EN PHYSIQUE

by

Conrad Spindler
Born on 21 March 1986 in Halle (Saale), Germany

OPTICAL DETECTION OF DEEP DEFECTS IN $Cu(In,Ga)Se_2$

Dissertation defence committee

Dr. Susanne Siebentritt, Dissertation supervisor
Professor, University of Luxembourg

Dr. Roland Scheer
Professor, Martin-Luther-University of Halle-Wittenberg

Dr. Alex Redinger, Chairman
Associate Professor, University of Luxembourg

Dr. Jürgen Christen
Professor, Otto-von-Guericke-University of Magdeburg

Dr. Ludger Wirtz, Vice Chairman
Professor, University of Luxembourg

Optical detection of deep defects in $Cu(In,Ga)Se_2$

Conrad Spindler
Laboratory for Photovoltaics
University of Luxembourg

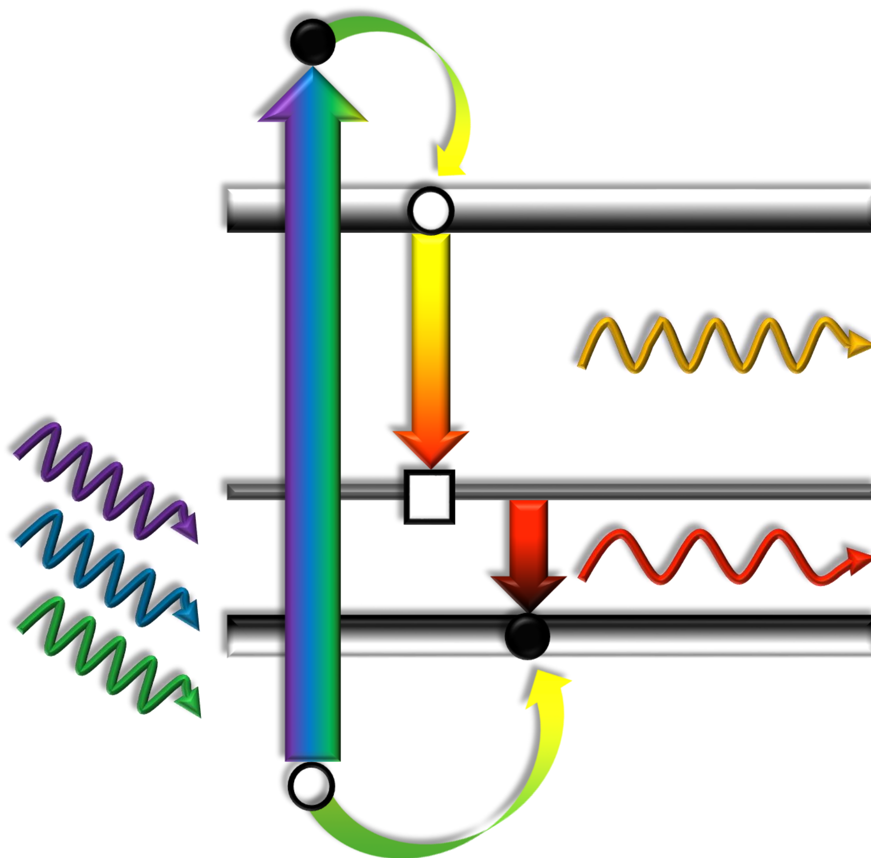

Contents

Acronyms and Symbols **9**

Abstract **13**

Introduction **15**

1 Fundamentals of Chalcopyrites **19**
1.1 Crystal structure . . . 19
1.1.1 Chalcopyrite lattice . . . 19
1.1.2 Phase diagram and copper content . . . 21
1.1.3 Electronic properties . . . 22
1.2 Absorber for solar cells . . . 24
1.2.1 Solar cell structure and efficiency losses . . . 24
1.2.2 Defect recombination in the absorber . . . 25
1.3 Point Defects . . . 27

2 Heteroepitaxial Growth **31**
2.1 Metalorganic vapour phase epitaxy . . . 31
2.1.1 Basic growth principles . . . 31
2.1.2 Substrate lattice mismatch . . . 33
2.2 Growth process at LPV . . . 35
2.2.1 DTBSe compared to DIPSe precursor . . . 36
2.2.2 General recipes for Cu(In,Ga)Se_2 . . . 38

3 Defect spectroscopy by Photoluminescence **41**
3.1 Photoluminesence transitions . . . 41
3.1.1 Band-to-band . . . 43
3.1.2 Exciton . . . 44
3.1.3 Free-to-bound . . . 45
3.1.4 Donor-acceptor pair . . . 46
3.2 Phonon interaction . . . 47
3.3 Photoluminescence setup . . . 53
3.3.1 Basic measurement setup . . . 53
3.3.2 Extension with InAs-detector . . . 58

4 Model for Excitation-dependent Photoluminescence **61**
4.1 Theoretical excitation dependence . . . 62
4.1.1 Rate equations and charge balance . . . 62
4.1.2 Defect-free case . . . 65
4.1.3 One shallow acceptor (donor) . . . 65
4.1.4 Donor and acceptor: compensated . . . 66
4.1.5 Donor and acceptor with deep level: compensated . . . 68
4.1.6 Bound excitons . . . 69
4.2 Fitting curved log-log plots . . . 70
4.3 Testing of the model . . . 73

5 Defect Band at 1.1 eV **79**
5.1 Defect spectroscopy on $CuGaSe_2$ . . . 79
5.1.1 Crystal quality of Cu-rich $CuGaSe_2$ . . . 80
5.1.2 $CuGaSe_2$ reference sample . . . 83
5.1.3 Excitation-dependent photoluminescence energy . . . 87
5.1.4 Excitation-dependent photoluminescence intensity . . . 90
5.1.5 Temperature dependent measurements . . . 94
5.2 Defect spectroscopy on $Cu(In,Ga)Se_2$ . . . 97
5.2.1 Addition of Indium to $CuGaSe_2$ . . . 97
5.2.2 Zero-phonon line of the deep defect band . . . 101
5.2.3 Defect position with varying band gap . . . 107
5.2.4 Simulations for solar cell devices . . . 111

6 Defect Band at 0.7/0.8 eV **117**
6.1 Photoluminescence at low temperatures . . . 117
6.1.1 Measurements on $CuGaSe_2$ and high-Ga $Cu(In,Ga)Se_2$ . . . 118
6.1.2 Measurements on $CuInSe_2$ . . . 120
6.2 Photoluminescence at room temperature . . . 120
6.2.1 Measurements on low band gap samples . . . 120
6.2.2 Influence of the copper content . . . 123
6.3 Comparison with substrate luminescence . . . 124

7 Defect Model and Summary **127**
7.1 Theoretical predictions from literature . . . 127
7.1.1 Point defects in $CuInSe_2$ . . . 129
7.1.2 Point defects in $CuGaSe_2$ . . . 134
7.1.3 Defect complexes . . . 136
7.2 Summary of experiment and theory . . . 137
7.2.1 Shallow defects . . . 137
7.2.2 Deep Cu_{In} and Cu_{Ga} doubly charged defects . . . 139
7.2.3 Shallow In_{Cu} and shallow/deep Ga_{Cu} defects . . . 141
7.3 Defect model conclusion . . . 143

Outlook **145**

Appendix **147**
A Optical density filters . . . 147
B Spectrosil-B transmission . . . 147
C SCAPS simulations . . . 148

Publications and Presentations **149**

Acknowledgments **151**

Bibliography **164**

Acronyms and Symbols

List of acronyms

BB	band-to-band transition
BX	bound exciton transition
CISe	copper-indium-diselenide
CIGSe	copper-indium-gallium-diselenide
CGSe	copper-gallium-diselenide
CGI	Cu/(Ga+In) ratio
Cu-rich	Cu/(Ga+In) ratio above 1
Cu-poor	Cu/(Ga+In) ratio below 1
DA	donor-acceptor pair transition
DIPSe	di-isopropyl-selenide
DTBSe	di-tertiary-butyl-selenide
EDX	energy dispersive x-ray spectroscopy
FB	free-to-bound transition
FWHM	full width at half maximum
FX	free exciton transition
GGI	Ga/(Ga+In) ratio
LO	longitudinal optical phonon
MOVPE	metal organic chemical vapor phase epitaxy
ODC	ordered defect compound
PL	photoluminescence
PVD	physical vapor deposition
SA	deep donor-acceptor pair transition

SCAPS	solar cell capacitance simulator software
SEM	scanning electron microscopy
SRH	Shockley-Read-Hall
XRD	x-ray diffraction
QFLS	quasi Fermi level splitting
ZPL	zero-phonon line

List of symbols

d_{FC}	Franck-Condon shift
d_{S}	Stokes shift
E_{A}	ionization energy of acceptor defects
E_{D}	ionization energy of donor defects
E_{d}	general energy of defects with respect to valence band
E_{C}	energy of conduction band minimum
E_{F}	Fermi level energy
E_{S}	energy level of deep defects with respect to valence band
E_{V}	energy of valence band maximum
$\hbar\omega_{\mathrm{max}}$	energy at maximum photoluminescence peak intensity
E_0	energy of zero-phonon line
G	Gaussian distribution
$\hbar\omega$	photoluminescence energy
$\hbar\Omega$	phonon energy of dominant phonon mode
I	photoluminescence intensity
I_0	photoluminescence intensity peak maximum
k	power law exponent
k_{B}	Boltzmann constant
L	photoluminescence lineshape
λ	wavelength

n	electron concentration
n_0	equilibrium electron concentration
δn	excess electron concentration
N_i	defect density
N_i^0	defects occupied with electrons (donor) or holes (acceptor)
p	hole concentration
p_0	equilibrium hole concentration
δp	excess hole concentration
P	Poisson distribution
S	Huang-Rhys factor
T	temperature
V_{oc}	open circuit voltage
ΔV_{oc}	open circuit voltage deficit $E_{\mathrm{g}} - V_{\mathrm{oc}}$
w	full width at half maximum of phonon mode
W	full width at half maximum of photoluminescence peak
W_0	full width at half maximum of photoluminescence peak at $T = 0\,\mathrm{K}$

Symbols for defects

$\mathrm{Cu_i}$	interstitial defects – e.g. copper interstitial
$\mathrm{V_{Cu}}$	vacancy defects – e.g. copper vacancy
$\mathrm{Ga_{Cu}}$	antisite defects – e.g. gallium on copper antisite
$\mathrm{Ga_{Cu}}$-$\mathrm{V_{Cu}}$	defect complexes – e.g. gallium on copper antisite and copper vacancy
$\mathrm{Cu_{III}}$	atom is group-III element – e.g. copper on indium or gallium antisite

Abstract

The aim of this thesis is to shed light on the deep defect structure in Cu(In,Ga)Se_2 by photoluminescence measurements and to propose a possible conclusive defect model by attributing experimental findings to a literature review of defect calculations from first principles.

Epitaxial films are grown on GaAs by metal organic vapor phase epitaxy and characterized by photoluminescence at room or low temperature. In $CuGaSe_2$, deep defect bands at ca. 1.1 eV and 1.23 eV are resolved. A model for the power law behavior in excitation dependent measurements of the peak intensities is derived, which leads to the experimental finding of two deep donor-like defects as a result.

In Cu(In,Ga)Se_2, the deeper band at around 1.1 eV remains constant in energy when more and more gallium is replaced by indium in the solid solution. For decreasing Ga-contents, the band gap is mainly lowered by a decrease of the conduction band energy. From fitting models for electron-phonon coupling, the dominating deep donor-like defect is determined at 1.3 eV above the valence band maximum. This level is proposed to be crucial for high Ga-contents when it is deep inside the band gap and most likely acts as a recombination center. At low Ga-contents it is resonant with the conduction band. The larger open circuit voltage deficits for high Ga-contents are proposed to stem at least partly from this defect which is qualitatively supported by simulations.

Additionally another defect band at around 0.7 eV is observed for high Ga-contents at low temperatures and at 0.8 eV for low Ga-contents. The intensity of the 0.8 eV band seems to disappear in a sample with Cu-deficiency. In general, deep luminescence is always observed with similar energies in all Cu-rich compositions, independent of the Ga-content. The deep defect involved could explain inferior efficiencies of Cu-rich devices which show increased non-radiative recombination in general. It is further discussed that the same deep defect could be the origin of a level at 0.8 eV which is observed in several photo-capacitance measurements in literature.

Based on the literature review for intrinsic defect calculations by hybrid-functionals, a possible defect model for shallow and deep defects is derived with a focus on those results, where different authors using different methods agree. By comparing the experimental results in the scope of this thesis, the deep defect found at 1.3 eV above the valence band is attributed to the Ga_{Cu} antisites. The single (0/-1) charge transition of Cu_{In} and Cu_{Ga} is proposed to be the main shallow acceptor in the near-band-edge luminescence of Cu-rich compositions at $60-100$ meV, whereas the second (-1/-2) charge transition is attributed to the deep 0.8 eV defect band.

The present findings could be useful for the improvement of Cu(In,Ga)Se_2 solar cells with stochiometric absorber compositions (Cu-rich growth) or with high band gaps (high Ga-content). Furthermore, the results show a very good agreement of experiment and recent theoretical calculations of defects, which can be seen as a promising relation between photoluminescence spectroscopy and predictions from theory for other complex materials.

Introduction

In the field of renewable energy production by photovoltaics, light absorbers made of $Cu(In,Ga)Se_2$ chalcopyrite crystals yield the highest conversion efficiencies of thin film solar cells with a recored efficiency of 22.9 % [1]. Nevertheless, after more than 30 years of research, still some fundamental questions of the electronic properties arise. The band gap of the solid solution $Cu(In,Ga)Se_2$ can be tuned between 1.0 and 1.68 eV by replacing indium with gallium. The highest efficiencies are achieved for band gaps around 1.1 eV and large improvements are still possible, since the Shockley-Queisser limit is at ca. 32 % [2, 3]. Especially the electrical losses from undesirable recombination paths are about 15 – 25 % below the possible maximum of single junction solar cells, whereas e.g. GaAs devices have nearly reached this limitation [4]. Furthermore, high band gap compositions of $Cu(In,Ga)Se_2$ can be used e.g. for the top cell in tandem solar cell configurations [5] or for water splitting in hydrogen production [6], but they suffer from much higher open circuit voltage deficits (difference of the open circuit voltage to the band gap) compared to the low band gap compositions. When compared to the Shockley-Queisser limit, the losses for $CuGaSe_2$ record cells are approx. 400 meV and much higher than approx. 200 meV for $CuInSe_2$. In addition to this, the thin films grown under Cu-excess yield much higher carrier mobilities [7] and less total intrinsic defect concentrations [8], but again much higher open circuit voltage losses compared to the Cu-deficient compositions occur. The quasi Fermi level as an upper limit for the open circuit voltage is about 140 meV lower in Cu-rich compositions compared to Cu-poor ones [9].

In order to understand the physical reasons behind these observations, the properties of the generally very high concentrations of intrinsic defects inside this complex material have to be known. In $Cu(In,Ga)Se_2$, intrinsic defects are mainly responsibly for the doping by shallow defects, but also for detrimental carrier recombination via deep defects. Whereas the main shallow defect energies are well known in literature by photoluminescence measurements [10], much less is known about the deep ones [11, 12].

Optical measurements like photoluminescence spectroscopy have the advantage to measure bare thin films without the influence of other layers in a solar cell stack and to directly observe the joint density of states from defect transitions at low temperatures. From these measurements it is shown in $CuInSe_2$ and $CuGaSe_2$ that at least one shallow donor exists at approx. 10 – 12 meV below the conduction band minimum and at least two shallow acceptors exist at 40 and 60 meV in $CuInSe_2$ and at 60 and 100 meV in $CuGaSe_2$ above the valence band maximum [13]. Also a third acceptor at 135 meV is found in $CuGaSe_2$ [14] and under debate in $CuInSe_2$.

In the case of deep defects from photoluminescence, which are further away from the band edges, Meeder et. al. reported a donor level at 200 meV and an acceptor level at 240 meV [15, 12] in $CuGaSe_2$ and Krustok et. al. reported a defect band at 1.0 – 1.2 eV in $CuGaSe_2$ [11] and at approx. 400 – 500 meV below the conduction band minimum in several $Cu(In,Ga)Se_2$ compositions [16]. The fact that most of the observed

photoluminescence transitions are donor-acceptor pair transitions makes it challenging to seperate the individual donor and acceptor levels. Furthermore, deep defects which are highly localized can lead to strong electron-phonon coupling [17] which hinders the direct determination of the zero-phonon line and therefore the involved defect levels in general [17]. In this case the so-called Franck-Condon shift between the photoluminescence maximum and the zero-phonon line has to be determined experimentally.

It is essential to study observed deep defect bands by a combination of several methods from photoluminescence which includes excitation dependent measurements over several orders of magnitude, temperature dependent measurements or fittings of the peak shape. By applying these methods, the present thesis aims to shed new light on the deep defect structure in $Cu(In,Ga)Se_2$ from photoluminescence measurements.

The already known near-band-edge luminescence is first confirmed on epitaxial samples of $CuGaSe_2$ and $CuInSe_2$ and the results are further used for the characterization of deep levels which are observed in the form of deep donor to shallow acceptor pair transitions. The current defect picture from optical measurements on $Cu(In,Ga)Se_2$ [13] will be extended by a deep donor-like defect at approx. 1.3 eV, as well as a deep level at 0.7 − 0.8 eV and both nearly constant above the valence band maximum for different Ga/(Ga+In) compositions. The defect at 1.3 eV is proposed to be a detrimental recombination center for high gallium contents in $Cu(In,Ga)Se_2$ where the defect energy is far away from the conduction band minimum. And it is further shown that this defect can be a possible reason for the large open circuit voltage losses found in literature for wide-gap compositions.

Additionally, all measured shallow and deep transitions will be attributed to point defects from a detailed literature review of theoretical calculations by hybrid functionals. As a result, it is proposed that the deep level at 1.3 eV stems from Ga_{Cu} antisites and the deep level at 0.7 − 0.8 eV is proposed to stem from the double charge transition of the $(In,Ga)_{Cu}$ antisites. Predictions from theory are in good agreement with the experimental results of shallow and deep defects and the proposed defect picture could be helpful for future improvements of the crystal quality.

Structure of the thesis

In the first Chapter 1 an overview of the fundamental properties of Cu(In,Ga)Se_2 is given, including the crystal structure, occuring phases and its characteristics of the tunable band gap. Because Cu(In,Ga)Se_2 is mainly used as an absorber layer in thin films solar cells, possible loss mechanisms of generated carriers including the recombination over deep defects in the bulk are briefly discussed.

In the second Chapter 2, the expitaxial growth of the samples is explained. The used growth conditions at LPV are given and the properties of the formerly used selenium precursor DTBSe are compared to the new precursor DIPSe, which had to be used to replace DTBSe after the first year of the project.

A new mirror-based setup as well as an extended setup for measuring wavelengths up to 3100 nm was built up for the photoluminescence spectroscopy in the scope of this thesis. A brief description of the two systems is part of the third Chapter 3. But before, the general properties of photoluminescence transitions are explained together with a focus on the influence of strong electron-phonon coupling.

In Chapter 4, a model for photoluminescence intensity measurements with large variations of the excitation intensity is derived in order to understand unusual experimental observations in the following chapters of results. Already known models for the excitation dependence of the near-band-edge luminescence are extended by the contribution of deep defects, which is later used for the discrimination of deep donor-like levels in very broad defect bands from donor-acceptor pair transitions.

Chapter 5 and Chapter 6 contain the experimental defect spectroscopy by photoluminescence. Starting with a reference sample of $CuGaSe_2$ and a full characterization of two observed deep defect bands at 1.1 eV and 1.24 eV by excitation and temperature dependent measurements, Cu(In,Ga)Se_2 solid solutions are studied in a next step. Deep defect bands are measured for decreasing Ga/(Ga+In) ratio and characterized by models for electron-phonon coupling to determine the zero-phonon energy and therefore a dominant deep defect level at 1.3 eV.

Another defect band which is observed at 0.7 eV in high gallium compositions and at 0.8 eV in low gallium compositions will be shown and discussed in Chapter 6. The measurements are partly done with the extended setup down to 0.5 eV and give first insights into the possible defect structure, considerably extending the very limited literature results of optical measurements in that range.

The last Chapter 7 gives an overview of literature data for intrinsic point defects from hybrid-functional calculations. Together with the experimental findings in this thesis, a consistent defect picture between theory and experiment is proposed and discussed. At the end of this chapter, the main results of this thesis are summarized in an overview.

Chapter 1

Fundamentals of Chalcopyrites

In the following chapter, the characteristic properties of the chalcopyrite Cu(In,Ga)Se_2 semiconductor crystals are given. Fundamental basics like the lattice structure, the phase diagram and major electronic properties like the tunable band gap are described in the first Section 1.1.

The usage of Cu(In,Ga)Se_2 as an absorber for photovoltaic applications is briefly discussed in the second Section 1.2 together with possible electrical losses of a solar cell in general. This further motivates the description of recombination losses in the bulk absorber from e.g. deep defects. A short introduction to Shockley-Read-Hall statistics is given to derive the dependence of the defect concentration and the defect energy position inside the forbidden band on the recombination rate.

Deliberate doping by shallow defects and unintended recombination centers from deep defects in the crystal play an important role e.g. for the performance of a completed solar cell device, in particular for its open circuit voltage and its efficiency as a consequence. The last Section 1.3 of this chapter contains a brief overview of possible intrinsic point defects. Already known defect transitions from photoluminescence results in literature are also highlighted in this last part. A detailed literature review and discussion of likely and unlikely occurrences of the point defects is given at the end of this thesis in Chapter 7.

1.1 Crystal structure

1.1.1 Chalcopyrite lattice

Semiconductors of group-IV elements like silicon and germanium crystallize in the diamond structure with tetrahedral bonds and 4 valence electrons. According to the Grimm-Sommerfeld rule [18], different combinations of compounds with the same tetrahedral bonds are possible if the average amount of valence electrons remains at 4. As shown in Fig. 1.1, the zincblende structure can be derived from the diamond structure by replacing the group-IV element by either one group-III and group-V element or by one group-II and group-VI element. As an example, ZnSe crystallizes in the zincblende structure (the name stems from the mineral ZnS) which is shown in Fig. 1.2 on the left hand side. If the group-II element is further replaced by half a group-I and half a group-III element, the chalcopyrite structure of e.g. $CuInSe_2$ and $CuGaSe_2$ with selenium as the group-IV element is formed. In this chalcopyrite structures (the name stems from the mineral $CuFeS_2$ [19]) each Cu- and In-/Ga-atom is tetrahedrally bound to four Se-atoms.

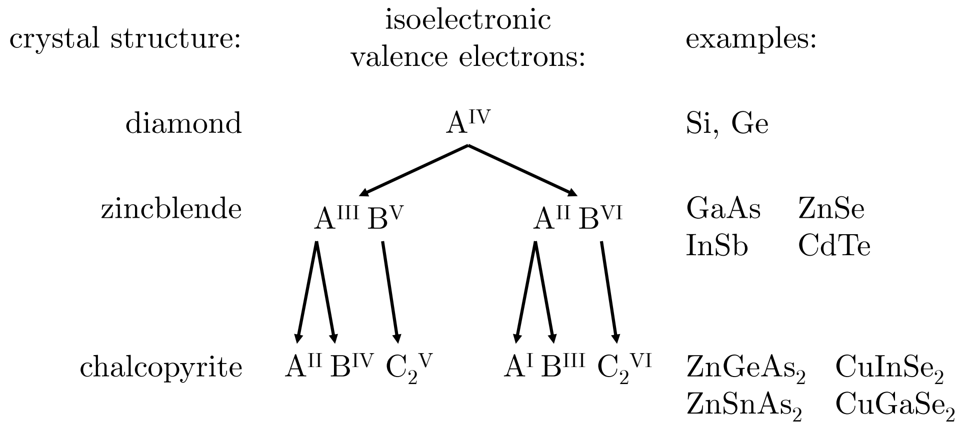

Figure 1.1: Relation between the diamond and the chalcopyrite crystal structure by maintaining an average of four valence electrons together with examples.

In Fig. 1.2 the tratragonal unit cell of the solid solution $Cu(In,Ga)Se_2$ is depicted on the right side, which is a superlattice of the cubic zincblende structure and the lattice constant c is approximately two times the lattice constant a. Since the bond length of Cu-Se and In/Ga-Se are slightly different, the ratio for the lattice constants of the ternaries is $c/a \approx 2.01$ in $CuInSe_2$, $c/a \approx 1.96$ in $CuGaSe_2$ [19] and somewhere in between for the solid solution. In the $Cu(In,Ga)Se_2$, indium and gallium atoms are randomly distributed on their positions. The macroscopic ratio of Ga/(Ga+In) determines the electronic properties. In this thesis, a high or low gallium content will be referred to a high or low ratio of Ga/(Ga+In), rather than using this expression for the ratio of the gallium over copper content. In order to express high or low copper contents, the ratio Cu/(Ga+In) is used. A stable chalcopyrite structure also exists with copper contents below the stoichiometry with $Cu/(Ga+In) < 1$, which is shown in the following part.

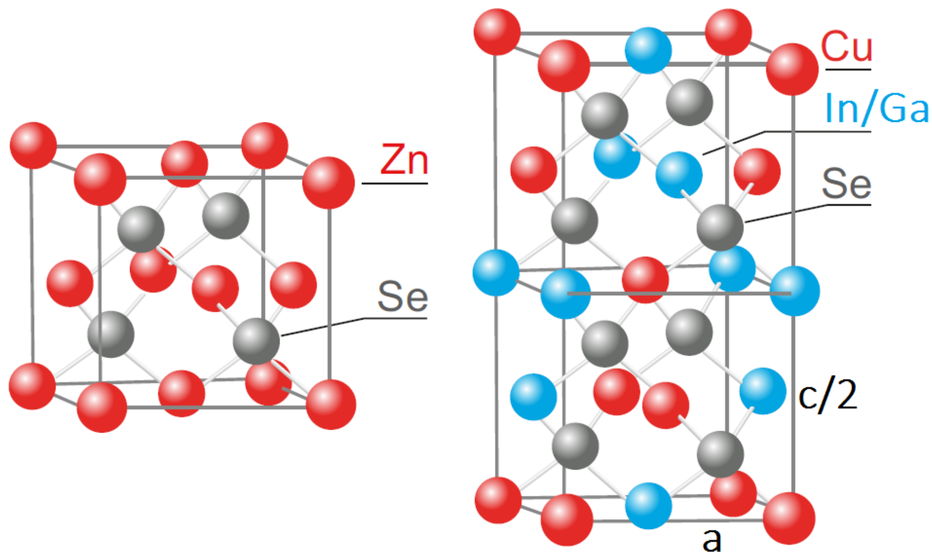

Figure 1.2: Cubic unit cell of ZnSe in comparison to the stacked superlattice of the tetragonal chalcopyrite $Cu(In,Ga)Se_2$ (reprinted with permission from Ref. [20]).

1.1.2 Phase diagram and copper content

Depending on the growth conditions, especially the growth temperature and the availablity of copper, different phases can occur in addition to the chalcopyrite α-phase. In Fig. 1.3, the pseudo-binary phase diagram is shown for $CuInSe_2$. The phase diagram for $CuGaSe_2$ has similar main properties as described in the following and can be found e.g. in Ref. [21]. On the abscissa, the atomic percentage of the copper content varying between the binaries In_2Se_3 and Cu_2Se is given. In this depiction, 25 % of copper corresponds to the stoichiometric composition in $CuInSe_2$. But the chalcopyrite α-phase is also stable below this value. For growth temperatures in the range of $470° - 570°$, typically used in PVD or MOVPE processes at LPV, the copper content can be as low as 22 % (corresponding to a Cu/In ratio of approx. 0.8) without the occurrence of additional phases like $CuIn_3Se_5$ (β-phase) or the high temperature δ-phase with zincblende structure and complete disorder of copper and indium. These considerations are only valid at thermal equilibrium. If the crystal is cooling down to room temperature, the existence region for the pure α-phase narrows, but remains still stable for Cu-contents below stoichiometry at around 24 % or above. This high tolerance to off-stoichiometry is often assumed to be possible by forming clusters of In_{Cu}–$2V_{Cu}$ defect complexes [22]. But this observations remain under debate since recent defect calculations question these high amounts of defect complexes due to very low binding energies calculated [23].

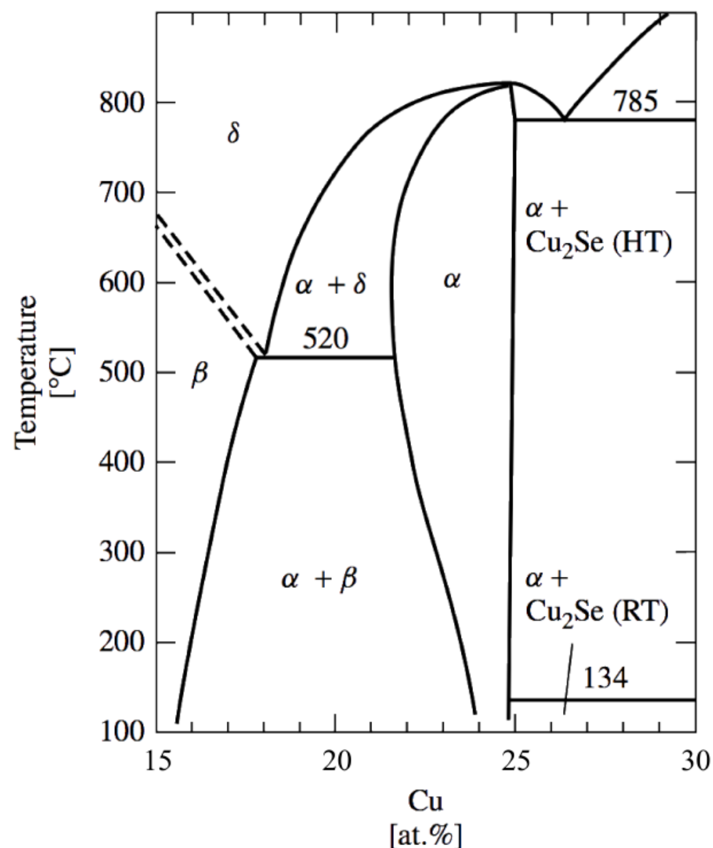

Figure 1.3: Pseudo-binary phase diagram for the copper content between In_2Se_3 and Cu_2Se and varying growth temperature [24]. The α-phase corresponds to the chalcopyrite $CuInSe_2$. Above 25% copper content, the Cu-rich region consists of the stoichiometric $CuInSe_2$ α-phase and the Cu_2Se secondary phase. (sketch on the basis of Ref. [18])

On the other hand, if the copper content is increased above 25 %, the $CuInSe_2$ α-phase is stoichiometric and the excess copper segregates in an additional $Cu_{2\text{-}x}Se$ phase. This secondary phase usually occurs in form of islands at the surface of the thin film and can be removed by etching with potassium cyanide (KCN) [25]. After cooldown to room temperature, the $Cu_{2\text{-}x}Se$ phase can be present also for Cu-contents slightly below 25 %. But even for Cu-rich samples, etching with KCN solution resulted in no spectral change of the room or low temperature photoluminescence in various tests. Therefore signals from this secondary phase can be excluded. Nevertheless, etching is desirable before measuring the sample. It usually results in higher overall photoluminescence signals because the degradation of the sample surface in air is recovered [26]. Afterwards, the same luminescence efficiency can be reached as it is present directly after growth or when the film is covered with a cadmium sulfide (CdS) layer for protection from degradation. But covering with CdS can potentially lead to a change of defect compensation due to possible in- or out-diffusion of e.g. cadmium or copper [27].

The compositions in this thesis are measured by EDX and always refer to the unetched thin films, which includes the contribution of the excess copper in the $Cu_{2\text{-}x}Se$ phases. Otherwise, after etching, always stoichiometric compositions would be measured for Cu-rich samples without any information on the Cu-excess during growth. As initially mentioned, all phase characteristics of $CuInSe_2$ remain nearly the same in $CuGaSe_2$, whereas e.g. $CuGa_3Se_5$ can occur as the β-phase in Cu-poor compositions below the stoichiometric point, Cu-rich growth results in a stoichiometric crystal and $Cu_{2\text{-}x}Se$ phases mainly at the surface. But the principle electronic properties like the band gap energy of the two ternaries are very different and can be tuned in the solid solution $Cu(In,Ga)Se_2$, which is discussed in the next part.

1.1.3 Electronic properties

One of the main advantage of the solid solution $Cu(In,Ga)Se_2$ is its tunable band gap between 1.0 eV for $CuInSe_2$ and 1.68 eV for $CuGaSe_2$, spanning the optimum band gap range for solar cells according to the Shockley-Queisser limit with maximum efficiencies above 30 % [2]. Ternary alloys usually don't shown a linear dependence of the band gap with the composition in the solid solution. Empirically a quadratic dependence is found with a so-called bowing parameter b. In $Cu(In,Ga)Se_2$ only a small bowing parameter of $b = 0.167\,\text{eV}$ [28] is measured. The band gap dependence is depicted in Fig. 1.4 with the following equation for the quadratic dependence:

$$E_{\text{g}}^{\text{CIGSe}} = xE_{\text{g}}^{\text{CISe}} + (1-x)E_{\text{g}}^{\text{CGSe}} - x(1-x)b. \qquad (1.1)$$

In this figure, the same bowing parameter is assumed at low temperature (10 K) and room temperature (300 K) and the composition x corresponds to the Ga/(Ga+In) ratio. For the band gaps of the ternaries, the values for Cu-rich samples grown by MOVPE on GaAs are taken from Ref. [29] and from the measurements in this thesis with $E_{\text{g}}^{\text{CISe}}[10\,\text{K}/300\,\text{K}] = [1.04\,\text{eV}/1.02\,\text{eV}]$ and $E_{\text{g}}^{\text{CGSe}}[10\,\text{K}/300\,\text{K}] = [1.72\,\text{eV}/1.68\,\text{eV}]$. It is worth mentioning that chalcopyrites generally consist of 3 non-degenerate valence bands, leading to three band gap energies, due to tetragonal distortion and spin-orbit coupling. In $CuInSe_2$, the tetragonal distortion of the crystal is very small (see Section 1.1.1) and the second band gap E_{b} is difficult to distinguish from the one shown in Fig. 1.4 (fundamental band gap E_a). However, in $CuGaSe_2$ with a larger and negative tetragonal lattice distortion, the value of E_{b} is 80 –90 meV above the lowest band gap of

1.68 eV [30] and can be seen in room temperature photoluminescence measurements (see Section 5.1.2). An overview of the band structure can be found in Ref. [19].

Furthermore in Fig. 1.4, also the LO-phonon energy, which is the energetically highest phonon mode E1 in Ref. [31] is shown for 5 different compositions. For the solid solution, the energy values of the same mode belonging to either $CuInSe_2$ or $CuGaSe_2$ is weighted with the composition and drawn with an interpolated line as a guide for the eye. For the ternaries, this optical phonon mode is also measured in the literature and in the results of this thesis from weak electron-phonon coupling of a shallow donor-acceptor pair transition (see Section 3.2 for explanations of electron-phonon coupling). The phonon energies $\hbar\Omega_{\text{CISe}} = 28.4\,\text{meV}$ and $\hbar\Omega_{\text{CGSe}} = 34.4\,\text{meV}$ in Fig. 1.4 are close to the ones found by photoluminescence measurements in Section 6.1.2 ($\hbar\Omega_{\text{CISe}} = 28\,\text{meV}$) and 5.2.1 ($\hbar\Omega_{\text{CGSe}} = 33\,\text{meV}$). It is reasonable to assume that these phonons are also involved in the broad photoluminescence bands, which result from strong electron-phonon coupling, given in Chapter 5 and 6. The knowledge of these phonon energies is needed for the determination of the zero-phonon line of the deep defect transitions observed and therefore for the evaluation of the defect energies in the band diagram.

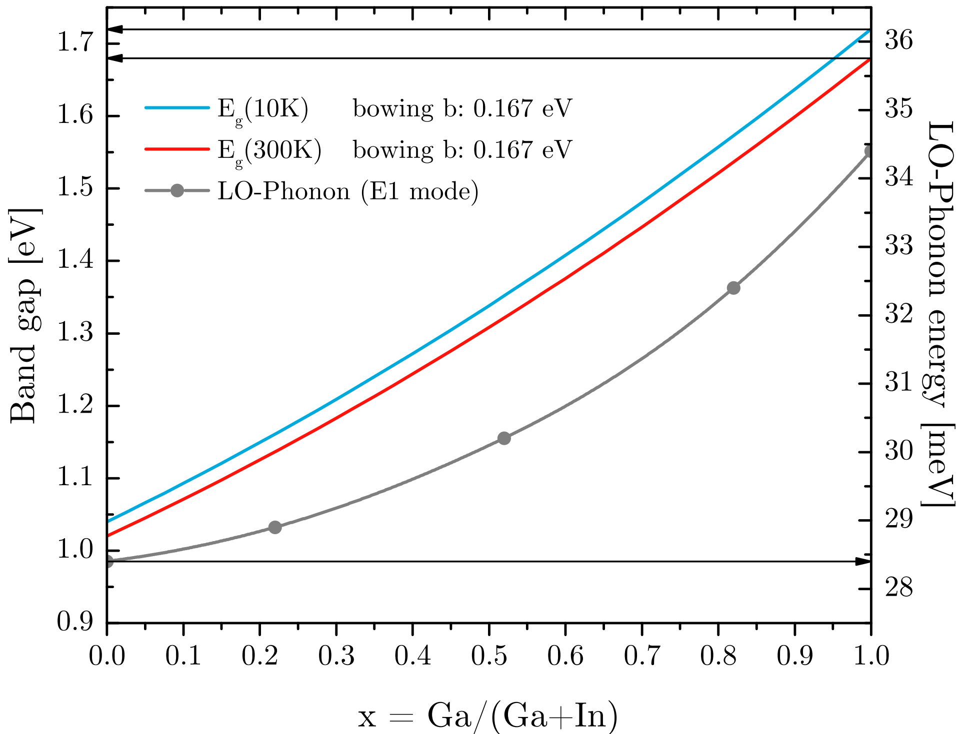

Figure 1.4: Band gap and LO-phonon energy of $Cu(In,Ga)Se_2$ in dependence of the Ga/(Ga+In) ratio. The band gaps of the ternaries are taken from Ref. [29] for epitaxial thin films on GaAs. The dependence is calculated with Eq. (1.1) and an empirical bowing parameter $b = 0.167\,\text{eV}$ [28]. Values for the LO-phonon energy are taken from Ref. [31]. For the solid solution, values of the E1 mode from CISe and CGSe are weighted with respect to the Ga/(Ga+In) ratio

The optimum band gap range for absorbers in solar cells and extensive research on $Cu(In,Ga)Se_2$ lead to the highest photovoltaic conversion efficiencies of thin film technologies [32]. For this reason, in the next section a brief overview of the structure and the recombination mechanisms in a solar cell are given as a motivation for the present study on deep defects.

1.2 Absorber for solar cells

Solar cells with $Cu(In,Ga)Se_2$ absorber yield the highest conversion efficiencies for thin film technologies of 22.9 % [1]. In order to motivate the study of deep defects, the basic structure of a CIGSe solar cell is given in the first part together with possible electrical losses which can lower the open circuit voltage V_{oc}. Based on this, a brief exemplary calculation for Shockley-Read-Hall recombination is given in the second part for highlighting the dependence of the defect energy and its concentration on the recombination rate and therefore on V_{oc} and the solar cell efficiency.

1.2.1 Solar cell structure and efficiency losses

In the following Fig. 1.5, the schematic band diagram of a typical $Cu(In,Ga)Se_2$ solar cell structure is given. The back-contact usually consists of a molybdenum layer which is deposited on a glass, steel or polymer substrate and the front contact is usually made from nickel/aluminum grids. On the top of the p-type $Cu(In,Ga)Se_2$ absorber, a highly n-doped transparent conductive oxide (TCO) is used to form the pn-junction. This TCO is e.g. Al-doped ZnO in the record cells. It was found that a buffer layer of CdS yields the highest efficiencies [33]. There are several possible reasons for this observation, whereas the protection of the absorber surface during the sputtering process of the TCO or the passivation of defects at the absorber surface are just two of them. But the main advantage is a favorable band alignment between the absorber, buffer and window layer.

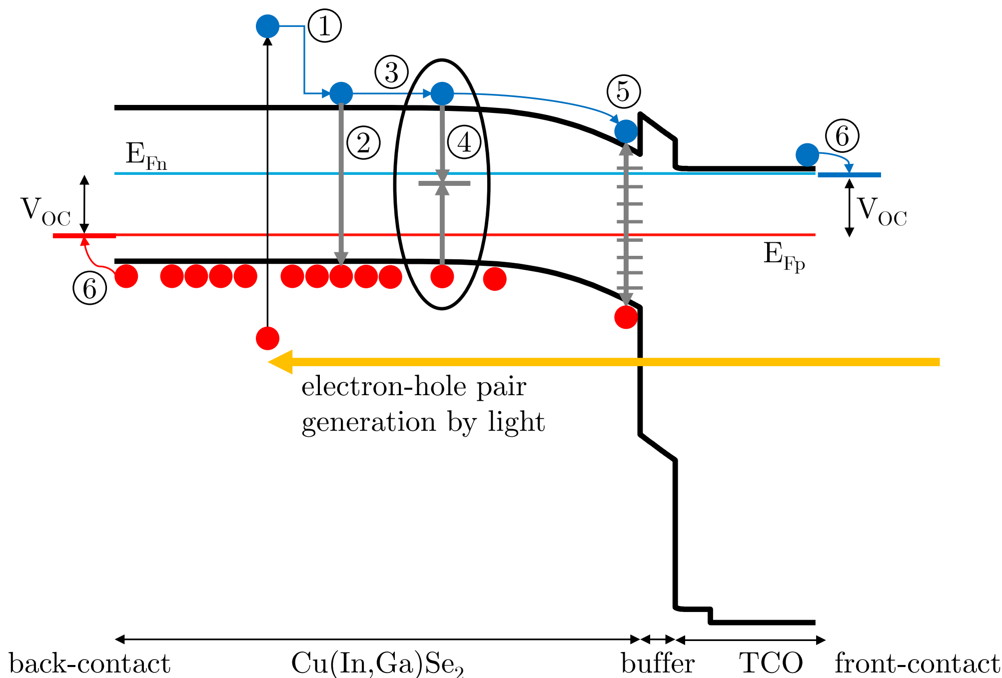

Figure 1.5: Schematic overview of efficiency losses in solar cells, depicted in a $Cu(In,Ga)Se_2$ band diagram. Possible losses are labeled with (1) thermalization losses, (2) radiative recombination losses (not avoidable), (4) bulk defect recombination losses (highlighted), (5) interface recombination losses, (6) contact recombination and thermalization losses. Process (3) depicts current losses due to low diffusion length which can indirectly lower the open circuit voltage.

After the creation of electron-hole pairs inside the absorber by incident photons, the free excess carriers thermalize to the band edges by emitting the excess energy to the lattice in form of phonons. This is the first loss mechanism (No. 1) which can just be avoided by e.g. the theoretical principle of hot-carrier solar cells [34]. After thermalization, which is a process in the order of picoseconds [35], the free carriers can be lost by radiative recombination (No. 2 and unavoidable), defect recombination (No. 4 and not desired) or if the diffusion length is too small, so that not every carrier is collected before recombining (No. 3, depends on the defects, carrier mobilities and absorber thickness). Furthermore losses can occur by non-radiative recombination at the interface (No. 5, with interface defects states distributed over the whole band gap) or at the contacts (No. 6 with unavoidable thermal losses or contact interface recombination).

In state-of-the-art absorbers, temperature-dependent measurements of the open circuit voltage yield activation energies close to the band gap. This is also the case e.g. in Cu-rich absorber with applied In-Se treatments which form a Cu-poor surface [36] or in record devices with $CuGaSe_2$ absorber [37]. If the activation energy of V_{oc} is equal or close to the band gap E_g, the dominant recombination path is assumed to occur in the bulk rather than the interface. In these examples, mechanism No. 5 can be neglected over mechanism No. 4.

It is reasonable to assume that at least in devices with very high open circuit voltage deficits compared to the band gap, the defect recombination in the bulk (No. 4) is one of the main reasons if dominant interface recombination is ruled out before. The deficit is $\approx 700\,\mathrm{meV}$ in $CuGaSe_2$ [37] and $\geq 500\,\mathrm{meV}$ in Cu-rich $Cu(In,Ga)Se_2$ [9], compared to $\approx 300\,\mathrm{meV}$ in the best solar cells with GaAs [4]. Dominant bulk defect recombination is furthermore supported by the measured effective lifetimes for minority carriers in the range of 0.2–250 ns [38]. For often observed doping densities in the order of $N_\mathrm{A} = 10^{16}\,\mathrm{cm}^{-3}$, the radiative lifetime is at $1 - 2\,\mu$s and much higher than the usual measured lifetimes. This indicates that the recombination is likely to be limited by recombination over deep defects, which can be described by Shockley-Read-Hall statistics. A brief overview for this unwanted recombination path in dependence of the defect density and the defect energy position inside the band gap is given in the following.

1.2.2 Defect recombination in the absorber

If recombination over deep defects occurs, the so-called Shockley-Read-Hall recombination rate can be calculated from [39]:

$$R_\mathrm{SRH}^\mathrm{bulk} = \frac{np - n_\mathrm{i}^2}{\tau_0^\mathrm{e}(n + n^*) + \tau_0^\mathrm{h}(p + p^*)}, \tag{1.2}$$

with the auxiliary carrier densities n^* and p^*, which would be present in the bands if the Fermi-level was exactly at the defect position E_d (valence band energy $E_\mathrm{V} = 0$). Their value depends further on the effective density of states in the bands $N_{C/V}$ and the band gap E_g, at a given temperature T:

$$n^* = N_\mathrm{C} \exp\left(-\frac{E_\mathrm{g} - E_\mathrm{d}}{k_\mathrm{B}T}\right) \qquad p^* = N_\mathrm{V} \exp\left(-\frac{E_\mathrm{d}}{k_\mathrm{B}T}\right). \tag{1.3}$$

The minimum lifetime of electrons τ_0^e and holes τ_0^h is defined by:

$$\tau_0^\mathrm{e,h} = \frac{1}{v_\mathrm{e,h}\sigma_\mathrm{e,h}N_\mathrm{d}}, \tag{1.4}$$

with the capture cross section σ, the thermal velocity v_{th} and the defect density N_{d}. Assuming the same capture cross sections and thermal velocities for electrons and holes, Eq. (1.2) can be simplified for a p-type semiconductor under low-injection conditions ($n \ll p = N_{\mathrm{A}}$) to:

$$\frac{1}{\tau_{\mathrm{SRH}}} = \frac{R_{\mathrm{SRH}}}{n} = \frac{v_{\mathrm{th}}\sigma N_{\mathrm{d}} N_{\mathrm{A}}}{N_{\mathrm{A}} + 2n_{\mathrm{i}} \cosh\left(\frac{E_{\mathrm{d}} - E_{\mathrm{g}}/2}{k_{\mathrm{B}}T}\right)}, \tag{1.5}$$

with the doping density N_{A} and the intrinsic carrier concentration n_{i}. The recombination rate is plotted in Fig. 1.6 for $CuInSe_2$ in dependence of the defect energy E_{d} above the valence band maximum. Inserted values for the calculation are a thermal velocity of $v_{\mathrm{th}} = 10^7$ cm/s, a capture cross section of $\sigma = 10^{-13}$ cm^2 and varying defect concentrations N_{d}. It is evident that the recombination rate reaches the highest and constant value for defect levels in the middle of the band gap at 0.5 eV and far away from the band edges. Only close to the conduction or valence band, the recombination rate drops exponentially, due to the higher probability of carrier re-emission of holes into the valence band or electrons into the conduction band.

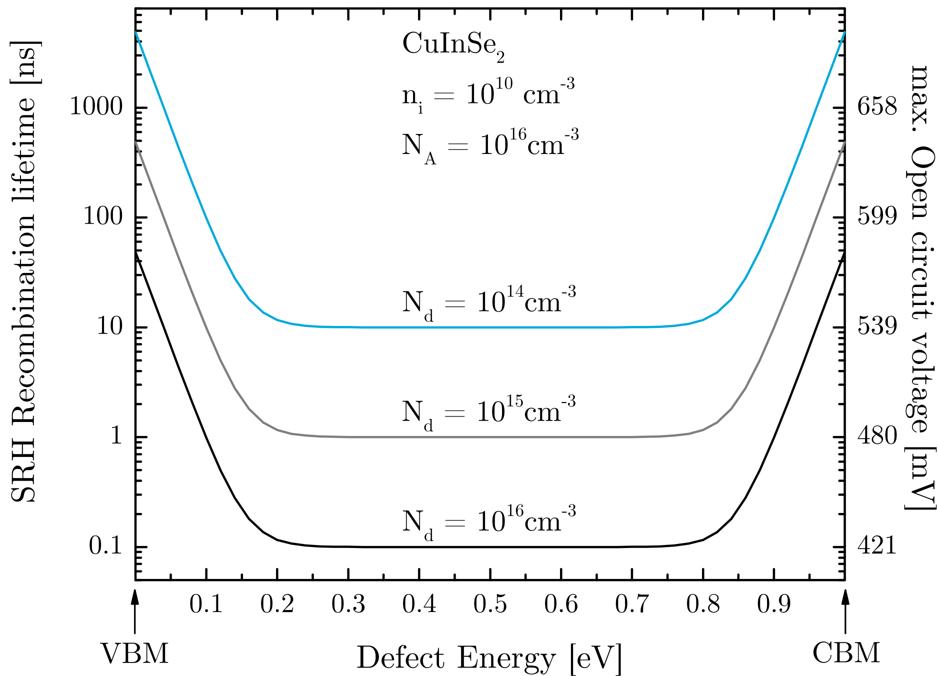

Figure 1.6: Shockley-Read-Hall recombination rate for a defect energy varying from the valence band maximum (VBM) to the conduction band minimum (CBM) in an exemplary $CuInSe_2$ semiconductor with a fixed doping density N_A and different defect densities N_d.

The open circuit voltage for a solar cell can be estimated from the bulk SRH recombination rate if this is the main limitation for the carrier lifetime. In the examples in Fig. 1.6, the minimum minority carrier lifetime of the electrons is 0.1 ns, 1 ns and 10 ns for $N_{\mathrm{d}} = 10^{16}, 10^{15}, 10^{14}$ cm^{-3}, respectively. In the ideal case, the open circuit voltage of a solar cell is equal to the quasi Fermi level splitting in the bare absorber. For a given minority carrier lifetime τ, the quasi Fermi level splitting (or the maximum V_{oc} respectively) can be calculated from the excess carrier density Δn in low-injection conditions from:

$$V_{\mathrm{oc}}^{\max} = \Delta\mu = k_{\mathrm{B}}T \ln\left(\frac{np}{n_{\mathrm{i}}^2}\right) = k_{\mathrm{B}}T \ln\left(\frac{\Delta n N_{\mathrm{A}}}{n_{\mathrm{i}}^2}\right) = k_{\mathrm{B}}T \ln\left(\frac{\phi_{\mathrm{s}} d^{-1} \tau N_{\mathrm{A}}}{n_{\mathrm{i}}^2}\right), \tag{1.6}$$

with the photon flux density of the sun for energies higher than the band gap $\phi \approx 2.7 \times 10^{17}\,\mathrm{cm}^{-2}s^{-1}$ and the assumption of flat Fermi levels with a homogeneous excess carrier distribution over an absorber thickness $d = 2\,\mu$m. This simple relation estimates the maximum open circuit voltage for the three defect densities in Fig. 1.6 when the lifetime is dominated by SRH recombination over the defect E_d. The aim of this example is to highlight the detrimental influences of defects on the open circuit voltage of a solar cell and therefore the proportional conversion efficiency as a result. For this reason, a careful knowledge of deep defects in $Cu(In,Ga)Se_2$ is needed and possible occurring point defects, especially intrinsic ones, are given in the following section.

1.3 Point Defects

In this last section, an overview of point defects in $Cu(In,Ga)Se_2$ is given. In $Cu(In,Ga)Se_2$ high concentrations of intrinsic defects determine the doping as well as the recombination in the material. Thus, it is important to understand the defect picture in order to develop new process recipes with desirable amounts for the doping concentrations and lowest deep defect concentrations. An overview of possible intrinsic point defects is given together with well known results from photoluminescence spectroscopy in literature. A detailed study of the defect levels and their abundance from theoretical calculations in literature as well as from following experimental results is discussed at the end of this thesis in Chapter 7.

Intrinsic defects and their detection by photoluminescence are the main topic of this thesis. In Ref. [40], epitaxial $CuGaSe_2$ samples prepared by MOVPE yield donor and acceptor concentrations in the range of $10^{16} - 10^{19}\mathrm{cm}^{-3}$ with high degrees of compensation around $N_\mathrm{D}/N_\mathrm{A} \approx 0.9$. Controlling these high amounts of defects which are of an intrinsic origin and also found in single crystals, requires the knowledge of the full defect structure. This can be done by e.g. identifying the defect levels for different preparation conditions and attributing them to certain intrinsic defects from theoretical calculations.

Table 1.1: Possible intrinsic point defects in $Cu(In,Ga)Se_2$

	Copper related	Indium related	Gallium related	Selen related
Vacancies	V_{Cu}	V_{In}	V_{Ga}	V_{Se}
Interstitials	Cu_i	In_i	Ga_i	Se_i
Antisites	Cu_{In} Cu_{Ga}	In_{Cu} In_{DX}	Ga_{Cu} Ga_{DX}	- -
Complexes	Cu_i-V_{Cu} Cu_i-V_{In} Cu_i-Cu_{In}	In_{Cu}-V_{Cu} In_{Cu}-2V_{Cu}	Ga_{Cu}-V_{Cu} Ga_{Cu}-2V_{Cu}	V_{Se}-V_{Cu} V_{Se}-2V_{Cu}

The main difficulty in $Cu(In,Ga)Se_2$ arises from the numerous possibilities of intrinsic defects with often no straightforward attribution from theory. Already in the ternaries, 3 vacancies, 3 interstitials, 6 antisites and various complexes need to be considered as possible sources for intrinsic defects. In Table 1.1 an overview of the possibities in the $Cu(In,Ga)Se_2$ solid solution is given. All combinations of vacancies, interstitials and antisites are shown, but selenium-related antisites are omitted since cation-anion antisites

have generally much too high formation enthalpies, which is estimated e.g. by the Van Vechten model [41].

Also several complexes, as discussed in literature, are given in Table 1.1 for a complete overview. The subscript DX for the In_{Cu} and Ga_{Cu} antisites labels the proposed metastable state if these defects capture two electrons $III_{Cu}^{2+} + 2e^- \rightarrow III_{DX}^0 = V_{Cu} + III_i$ [42]. The most prominent and most discussed intrinsic defects in literature are the vacancies, the antisites and the copper interstitial, which are schematically shown in Fig. 1.7.

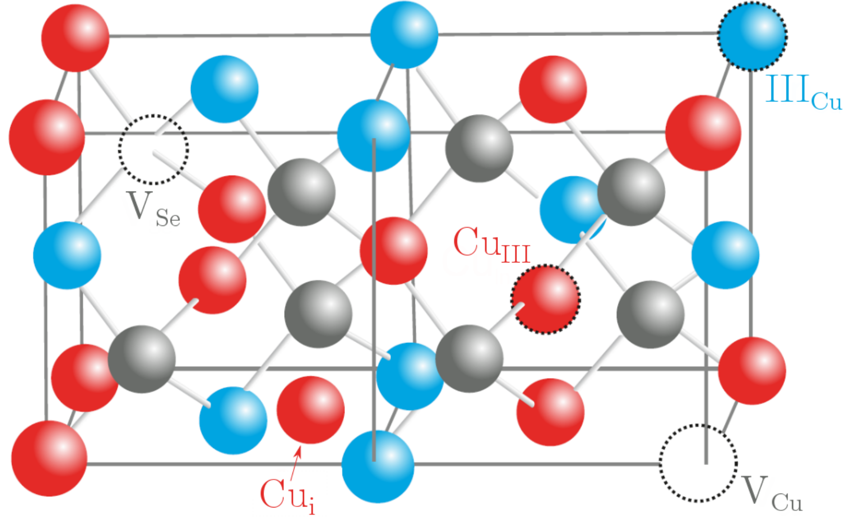

Figure 1.7: Exemplary tetragonal unit cell of $CuInSe_2$ with the most discussed intrinsic point defects (adapted with permission from Ref. [20]).

From optical measurements in literature, several shallow intrinsic defects are already found in $CuInSe_2$ and $CuGaSe_2$. In Fig. 1.8 the well known near-band edge luminescence for the ternaries is given in dependence of the Cu-content [10, 43, 13]. Both ternaries, $CuInSe_2$ and $CuGaSe_2$, appear to have the same fundamental structure of shallow defects. The blue curve is corresponding to a nearly stoichiometric compositions. In this case, the shallowest donor-acceptor pair DA1 transition is dominant which involves an acceptor at around 40 meV in CISe and 60 meV in CGSe. This shallow acceptor, closest to the valence band, is often attributed to the copper vacancy V_{Cu}.

If the copper-content is further lowered below stoichiometry, very high degrees of compensating large donor and acceptor quantities lead to potential fluctuations. They broaden the transition energies and shift them to lower energies due to occurring recombination from potential wells. In this case, the photoluminescence characterization is more or less limited to evalouations of the degree of compensation or the potential fluctuation amplitude rather than discrete defect level energies [44].

For Cu-contents above stoichiometry a second donor-acceptor pair transition becomes more pronounced and dominates the near-band-edge luminescence for Cu-contents above approx. 1.1 (see black curve in Fig. 1.8). This second donor-acceptor pair transition DA2 involves a shallow acceptor at around 60 meV in CISe and 100 meV in CGSe. A third acceptor with much lower intensity is found in $CuGaSe_2$ at an energy of around 135 meV [14].

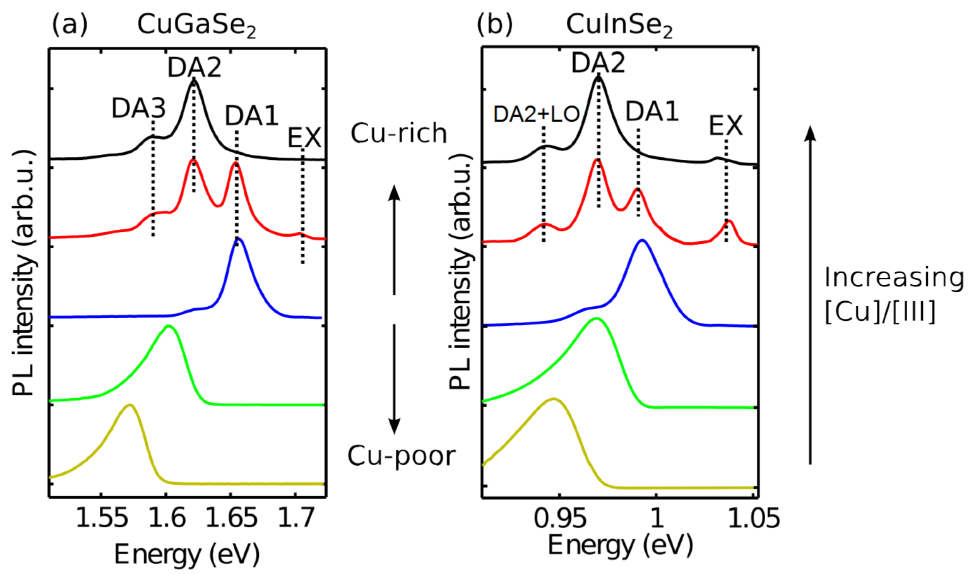

Figure 1.8: Typically observed near-band-edge photoluminescence at 10 K of (a) $CuGaSe_2$ and (b) $CuInSe_2$ in dependence of the Cu-content (reprinted from Ref. [45]). The blue spectrum corresponds to a nearly stoichiometric composition whereas the upper and lower spectra are Cu-rich and Cu-poor respectively.

Chapter 2

Heteroepitaxial Growth

In the second chapter, the epitaxial growth of the samples for defect spectroscopy by metal organic vapor phase epitaxy (MOVPE) is described. In the first section 2.1, the basic processes which occur during growth inside the reactor chamber are explained. Furthermore, the choice for GaAs-substrates is motivated from the relatively low lattice mismatch of Cu(In,Ga)Se_2 crystals compared to other commercially available single crystals.

A schematic overview of the MOVPE machine at LPV is given in the second section 2.2 together with the growth properties like the temperatures and partial pressures of the precursors which are used in the recipes. General differences of the older, formerly used selenium precursor Di-tertbutyl-selenide (DTBSe) compared to the new precursor Di-isopropyl-selenide (DIPSe) are shown in the last part. After more than 20 years of research on CVD-grown Cu(In,Ga)Se_2, the conventionally used selenium precursor was no longer available on the market and a new one needed to be found during the project of this thesis. The main difference is its decomposition temperatures which strongly influences the range of possible substrate temperatures for transport-limited growth.

2.1 Metalorganic vapour phase epitaxy

Sample preparation by MOVPE can be used to grow single crystals with a high purity and well defined interfaces. If the grown single crystal is different to the epitaxial substrate it is called heteroepitaxial growth. The basic processes which occur during growth are schematically explained in the first part and the lattice mismatch of Cu(In,Ga)Se_2 to the used GaAs substrates is discussed briefly in the second one.

2.1.1 Basic growth principles

In general, the MOVPE system consists of a reactor chamber where a constant gas flow is present, consisting of the carrier gas (here hydrogen) and all metal organic precursors with different partial pressures. A high quality single crystal is used as a substrate (here GaAs) and heated with infrared light sources to achieve the decomposition of the precursors and the growth of the metals. An overview of occurring processes inside the reactor chamber during growth is given in Fig. 2.1.

If the temperature inside the reactor and close to the substrate is below the decomposition temperatures of a precursor, the growth rate will have strong temperature dependence since the incorporation of atoms into the crystal will depend on the availability of decomposed reactants, transported to the surface (kinetically limited growth). In this

regime, the decomposition and therefore the growth rate increases exponentially with the temperature and a characteristic activation energy.

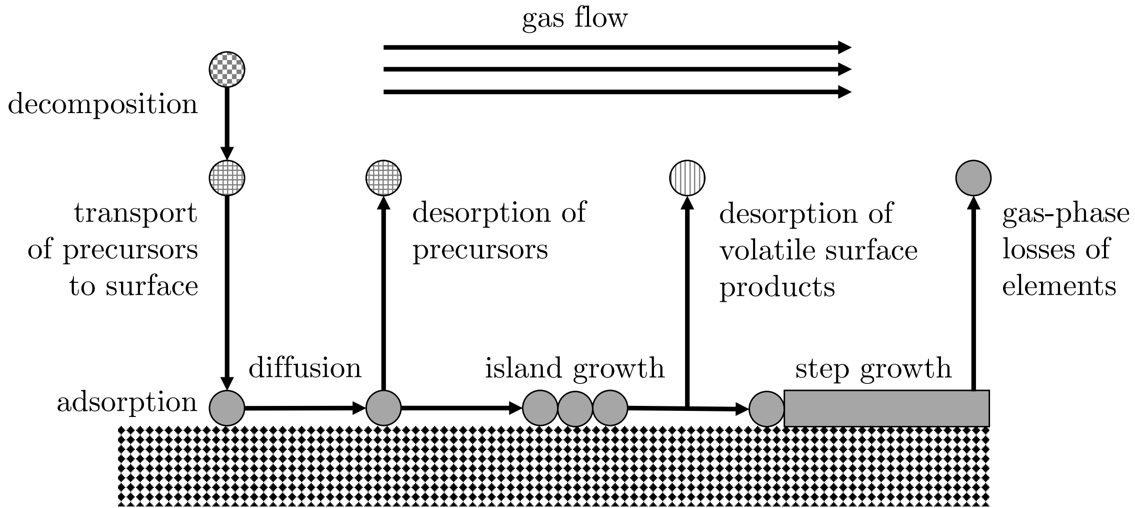

Figure 2.1: Processes which occur during growth by metal organic vapor phase epitaxy (depiction adapted from Ref. [46])

For high enough temperatures the precursor material can be completely decomposed and diffuses vertically to the surface where it can get adsorbed (see Fig. 2.1). If the temperature is above the decomposition temperatures of the precursors, the growth process will be mostly limited by the supply of the raw material (partial pressure) and the diffusion of the same (diffusion limited growth). But since the gas phase diffusion has only a weak temperature dependence, the growth rate remains almost constant in the diffusion limited regime [47]. While lateral diffusion of the adsorbed material takes place at the surface of the epitaxial crystal, the precursor material can get again desorbed or preferably only the remaining organic compounds get decomposed, leaving behind the e.g. metal atom.

For too high temperatures, already adsorbed material gets desorbed significantly. This results in an exponential decrease of the growth rate with temperature (desorption limited growth). Furthermore at too high temperatures, high amounts of precursor material can already be deposited on the reactor walls before reaching the substrate, reducing the growth rate even further.

Due to the above reasons, diffusion limited growth is favored for the process. In this case, fine adjustments of the partial pressures of each precursor allow precise control of the final composition of the crystal. But even after island or step growth took place, atoms which are already incorporated into the crystal can be lost back into the gas-phase. This is especially the case for the chalcogens in chalcopyrites [48, 49] (here selenium), where much higher partial pressures compared to the metals are needed for minimizing these losses. The partial pressure of each precursor in MOVPE is defined by the following equation [50]:

$$P_{\mathrm{MO}} = P_{\mathrm{MO}}^{\mathrm{eq}}(T_{\mathrm{B}}) \frac{Q_{\mathrm{B}}}{Q_{\mathrm{R}}} \frac{P_{\mathrm{R}}}{P_{\mathrm{B}}}, \tag{2.1}$$

with the equilibrium vapor pressure of the metal precursor for a given bubbler temperature $P_{\mathrm{MO}}^{\mathrm{eq}}(T_{\mathrm{B}})$, the flux through the bubbler (Source flux) Q_{B}, the total flux inside the reactor

Q_R, the set pressure inside the bubbler P_B and the set total pressure inside the reactor P_R. The so-called bubblers are the steel container for the metal organic precursor which are stored in a temperature controlled water bath or an oven. The pressure inside the bubbler and inside the reactor can be controlled independently and remains constant for all process variations discussed here. The bubbler temperature is always regulated to the same value, achieving a constant equilibrium vapor pressure $P_{MO}^{eq}(T_B)$. Also the total flux inside the reactor Q_R, which is the sum of all partial pressures, will remain constant for different recipes. In this case, the partial pressure of each precursor and therefore the availability of the actual raw material only depends on the chosen flux of the hydrogen carrier gas through the bubbler Q_B. Apart from the growth temperature and if not stated otherwise, in all recipes for the sample growth in this thesis, only the fluxes through each bubbler are adjusted. More details can be found in the following Section 2.2.

2.1.2 Substrate lattice mismatch

The choice of the epitaxial substrate plays a crucial role for minimizing the lattice mismatch to the grown crystal structure and therefore reducing strain, dislocations or cracks inside the thin film. In general, the lattice mismatch f between the lattice constant of the substrate a_S and the grown layer a_L is given by [50]:

$$f = \frac{a_S - a_L}{a_L} \tag{2.2}$$

In Fig. 2.2 an overview of the lattice constants a of several commercially available semiconductors with cubic structure is given in comparison to the lattice constants a and $c/2$ of $CuInSe_2$ and $CuGaSe_2$. From this figure, it can be seen that AlAs, GaAs and Ge yield the best average lattice match if the same substrate is considered for all $Cu(In,Ga)Se_2$ compositions.

Considering these three suitable crystals as a substrate, GaAs is generally chosen due to the lowest costs, highest commercial availability and long experiences from literature with the epitaxial growth of chalcopyrites [30]. In Fig. 2.2 also the lattice constants and band gaps from the alloys of the binaries GaP and GaAs, as well as GaAs and InAs are shown. It is in principle possible that with compositions of $GaAs_{1-x}P_x$ and $In_{1-x}Ga_xAs$ the full range of lattice constants for $Cu(In,Ga)Se_2$ can be covered in order to achieve the best lattice matching.

In this thesis, undoped semi-insulating GaAs substrates with (100)−orientation are used for all samples. The wafers are epi-ready, meaning that the surface for growth is polished, etched and the wafers are packed in a sealed atmosphere with an inert gas. Inserting the values from Fig. 2.2 into Eq. (2.2), the mismatch of the lattice constant a with GaAs is only $f^{CISe} = -0.023$ for $CuInSe_2$ and $f^{CGSe} = 0.008$ for $CuGaSe_2$. From the sign it can be concluded that tensile strain (positive sign) occurs in $CuInSe_2$ and low-Ga content $Cu(In,Ga)Se_2$ and compressive strain (negative sign) occurs in $CuGaSe_2$ and high Ga-content $Cu(In,Ga)Se_2$. Nevertheless, after a certain critical thickness d_c, pseudomorphic growth is no longer present and the layer is relaxed, approaching the lattice parameters of a single crystal. This critical thickness depends on the lattice constant of the $Cu(In,Ga)Se_2$ compositions and is in the order of $d_c = 30 \ldots 200$ nm for the lattice constant a and $d_c = 30 \ldots 400$ nm for the lattice constant $c/2$ [52].

In the past, measurements at LPV have shown that layer thicknesses equal or above approx. 500 nm yield a relaxed $CuInSe_2$ crystal and for $CuGaSe_2$ only thermal strain is

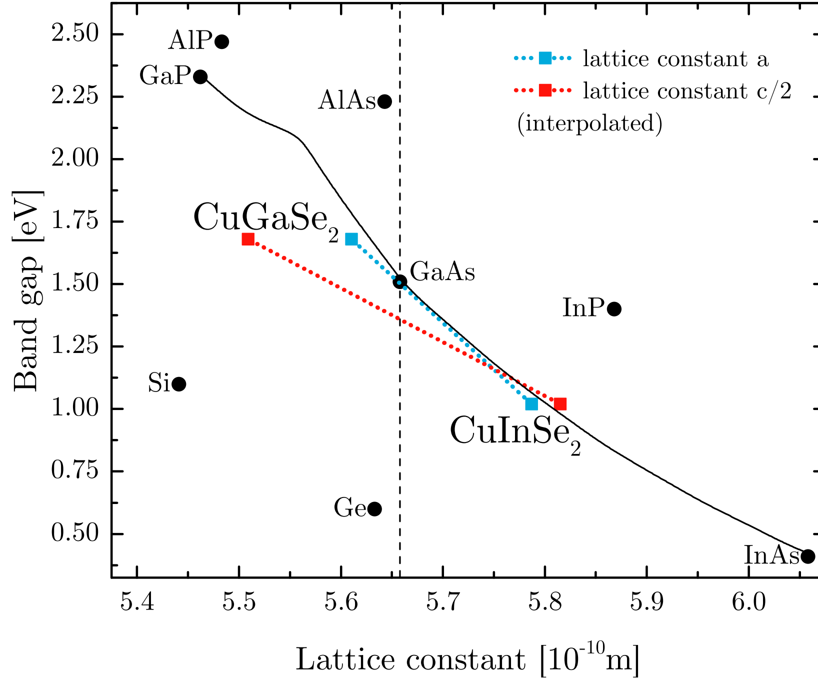

Figure 2.2: Lattice constants and band gaps of several commercially used semiconductors (values taken from Ref. [51]) together with the linearly extrapolated lattice constants a and $c/2$ for $Cu(In,Ga)Se_2$ (values taken from Ref. [52]).

induced [43]. For this reason and if not stated otherwise, all samples in this thesis are grown with a minimum thickness of 500 nm, which is guaranteed by a minimum growth duration of 4 h and usually measured growth rates of 120 − 130 nm/h.

Furthermore, from Fig. 2.2 it can be seen that the lattice constant a of both ternary chalcopyrites is closer to the lattice constant of GaAs a_{GaAs} than it is the case for the half value of the c-axis $c/2$. From this characteristic it is known that the c-axis of the ternaries grows parallel to the surface normal of a (100)-GaAs wafer. On the other hand for $Cu(In,Ga)Se_2$ compositions with Ga/III ratios between approx. 0.2 and 0.7, it is more favorable that the growth occurs with the c-axis perpendicular to the surface normal [52]. In the special case of Ga/III ≈ 0.5, the value of $c/2$ is equal to a_{GaAS} and no strain due to a lattice mismatch occurs.

2.2 Growth process at LPV

In this section the recipes and the settings for the MOVPE growth process at LPV are described together with the properties of the newly used selenium precursor DIPSe compared to the old one DTBSe. The MOVPE system AIX200 from Aixtron is used at LPV and for the sample preparation in this thesis. In Fig. 2.5 an overview of the machine is given. In standby, all lines and the reactor are constantly purged with nitrogen to avoid any contamination with oxygen. During the process, the hydrogen carrier gas H_2 is guided trough the metal organic precursors (Source) and parallel to each of it (Push). This configuration is needed in order to maintain the same total fluxes for all recipes. The total flux of each bubbler is the sum of the fluxes at the Source and at the Push line. A bypass can be used if the precursor is not needed. The hydrogen carrier gas flowing through the Source line collects the precursor material depending on the Source flux and on the vapor pressure of the precursor.

The precursors are stored in stainless steel containers (bubbler) which are temperature controlled in a water bath. The set bubbler temperatures are given in Fig. 2.5 and determine the equilibrium vapor pressure. Higher amounts of the precursor material in the reactor are adjusted by increasing the Source flux and decreasing the Push flux proportionally without changing the vapor pressure inside the bubblers. Only the copper precursor (CpCuTep) is stored in an oven since a higher bubbler temperature of 65° is needed. For the same reason, the lines from the copper precursor to the reactor are heated to 70° to avoid condensation at the walls. Since all precursor are kept liquid, a constant evaporation rate is guaranteed by a constant surface area, independent of the filling of the container.

All lines merge into the glass reactor chamber with a rotating graphite disc for the wafer substrate and an infrared heating source of 8 lamps. The GaAs substrates can be transferred to the reactor from a purged gloove box with oxygen concentrations below the detection limit of 0.1 ppm.

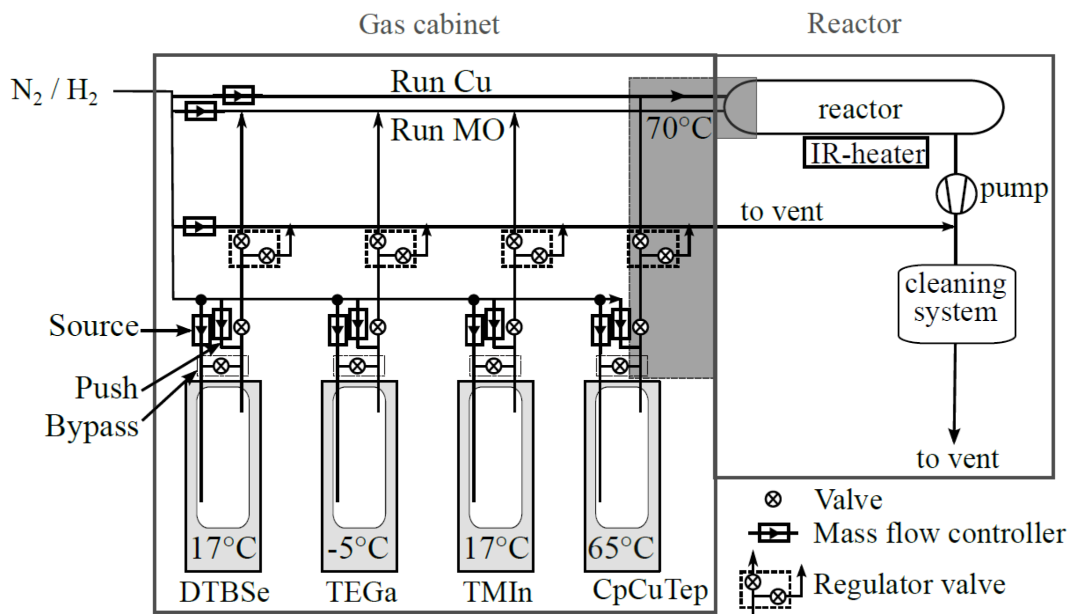

Figure 2.3: Schematic overview of the MOVPE growth system at LPV (reprinted with permission from Ref. [52]).

2.2.1 DTBSe compared to DIPSe precursor

As mentioned in the previous section, the decomposition temperature of a precursor material (for a given reactor pressure) determines the usable reactor temperatures for the diffusion limit growth regime. In the past 20 to 30 years, Di-tertbutyl-selenide (DTBSe) precursor were used as the selenium source. Unfortunately during the project of this thesis, the former supplier decided to not produce the material anymore and the supply of DTBSe at LPV went empty. Furthermore, no other supplier for DTBSe was available and an alternative selenium source needed to be chosen.

From extensive research on MOVPE grown samples of ZnSe, three mainly used selenium precursor exist on the market: Di-isopropyl-selenide (DIPSe), Di-ethyl-selenide (DESe) and Di-methyl-selenide (DMSe). In Ref. [53] an overview of the transition temperatures for diffusion-controlled growth is given for the three selenium sources and the growth of ZnSe at 400 mbar. As a result, DIPSe yields the lowest transition temperature of $T_{\mathrm{r}}^{\mathrm{DIPSe}} = 450°\mathrm{C}$, compared to $T_{\mathrm{r}}^{\mathrm{DMSe}} = 480°\mathrm{C}$ and $T_{\mathrm{r}}^{\mathrm{DESe}} = 500°\mathrm{C}$ for the given growth conditions. These differences might not be large, but the formerly used precursor DTBSe had exclusively low decomposition temperatures of e.g. 300° at atmospheric pressure [54] and 315° for diffusion-controlled growth of ZnSe at 20 mbar [55]. Chemically, DIPSe and the old precursor only differ by two hydrocarbons (see Fig. 2.4).

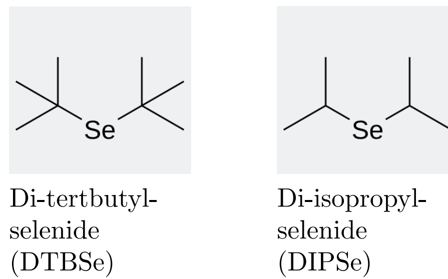

Figure 2.4: Skeletal formula of the old (DTBSe) and new (DIPSe) selenium precursor.

The decomposition temperatures of the copper precursor (≈ 120° [56]), indium precursor (≈ 350° [57]) and gallium precursor (≈ 330° [58]) are of no concern since they are all well below the typically used growth temperatures of 470 – 520° at LPV [43, 52]. The problem arises from the fact that even for DIPSE, which is the selenium precursor with the lowest decomposition temperatures currently available, much higher temperatures are needed as compared to DTBSe used before. In order to proof the actual transition temperature for diffusion-controlled growth, several thin films of $\mathrm{CuInSe_2}$ where grown with the standard total reactor pressure of 50 mbar and varying growth temperatures.

In Fig. 2.6 the growth rate, which is calculated from the growth duration and the thin film thickness by SEM measurements, is depicted over the growth temperature in an Arrhenius plot. It can be clearly seen that above approx. 530° the growth rate remains constant and therefore the diffusion-limited growth regime is reached. This result is in very good agreement of the findings in Ref. [53], where the same onset of a constant growth rate was found for ZnSe, using the same limiting precursor DTBSe and the same reactor pressure (value interpolated at 50 mbar in Ref. [53]). It can be concluded that with formerly used recipes and reactor pressures of 50 mbar, the diffusion-limited growth occurs only at growth temperatures of 530° or above. With the MOVPE system at LPV, $\mathrm{CuInSe_2}$ samples were usually grown at 470° to reduce the in-diffusion of gallium from the substrate [43]). Samples of $\mathrm{CuGaSe_2}$ are usually grown at 520°, yielding best crystal

qualities and highest growth rates [43]. Growth temperatures for the solid solutions $Cu(In,Ga)Se_2$ were interpolated between these two values from the ternaries [52]. With the new precursor DIPSe, obviously all used growth temperatures are below the transition temperature of 530°.

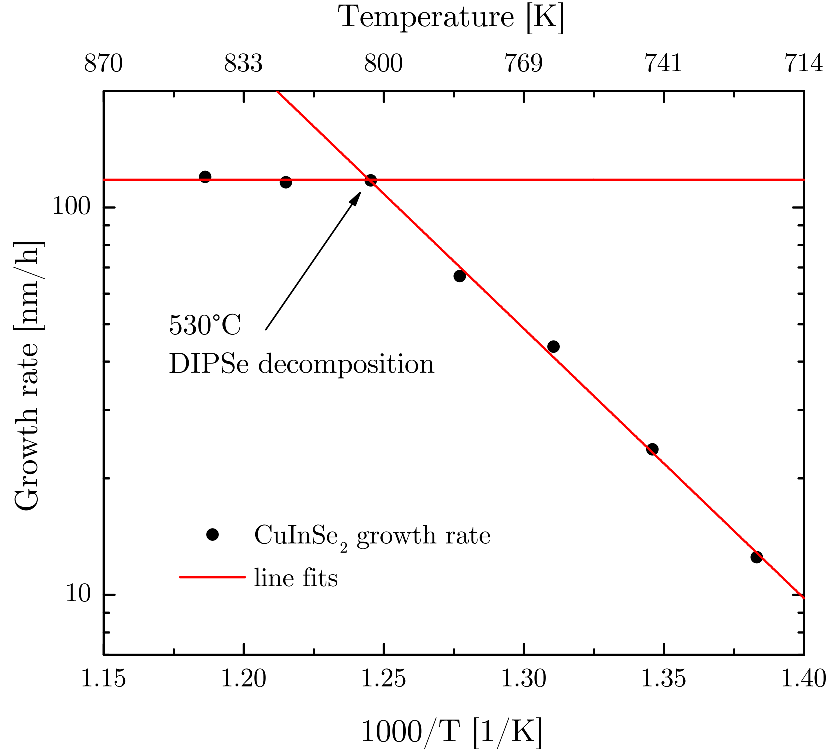

Figure 2.5: Growth rate of epitaxial $CuInSe_2$ thin films in dependence of the growth temperature for the new DIPSe precursor.

One possibility to lower the transition temperature is to increase the total reactor pressure during growth. From Ref. [53] it is known that the transition temperature of processes for ZnSe growth and a limiting DIPSe decomposition can be lowered from 530° to e.g. 450° for reactor pressures of 300 mbar instead of 50 mbar. But by using the same high 300 mbar pressure for several processes, no thin films could be grown. In this case the problem arises from the copper precursor. The copper precursor CpCuTep has a very low decomposition temperature of around 80°. In this case, some copper is already deposited on the reactor walls before reaching the substrate. Since the copper precursor is very sensitive to any changes in the partial pressures of the source and push lines, only selenium, gallium and indium are changed for compositional variations of different samples. Using the higher reactor pressure of 300 mbar increases the deposition of copper inside the reactor significantly and nearly no copper is reaching the substrate anymore.

In a second attempt, several samples were grown at a reactor pressure of 100 mbar instead of 50 mbar. In this case the expected transition temperature is at 470° [53] which is sufficient for formerly used recipes. But again the higher reactor pressure leads to a strong loss of copper. At least, with 100 mbar it was possible to grow thin films with different compositions of $Cu(In,Ga)Se_2$, but lower expected film thicknesses (the growth rate gets approximately halved) and much lower expected copper contents in the crystal. Targeted values for a copper content of $Cu/III = 1.1 - 1.2$ resulted in Cu-poor films with $Cu/III = 0.5 - 0.7$. The samples will be used for supporting the findings of a deep defect

at 1.3 eV in Chapter 5 rather than for direct conclusions. Future studies are needed to optimize the growth with 100 mbar or to improve the reaction-limited growth with low temperatures at 50 mbar by e.g. photo-assisted MOVPE [59]. If not stated otherwise, the reactor pressure is always set to 50 mbar in the scope of this thesis. Other process parameters for the used recipes are given in the following and last part.

2.2.2 General recipes for Cu(In,Ga)Se_2

Based on the results of the different selenium precursor, the conventionally used recipes with the old precursor DTBSe and the new recipes with DIPSe will be given in the following. All processes have in common that the partial pressure of the copper source is always maintained constant. Usually the copper source limits the growth rate due to the 50 times lower vapor pressure of CpCuTEP compared to the other metal organics. This could be different with the new selenium precursor. The set bubbler temperatures for the precursors are shown before in Fig. 2.3. In the following Fig. 2.6, the equilibrium vapor pressure for gallium, indium and selenium is depicted in dependence of the bubbler temperature. The setting of the gallium source at -5° and the indium source at 17° yields nearly the same equilibrium vapor pressure between 1 and 2 mbar. The vapor pressure of selenium is higher with around 9 mbar and a set temperature of 17° which is favorable for the processes. From Fig. 2.6 it can be further seen that the vapor pressure of the old (DTBSe) and new (DIPSe) selenium precursor is nearly the same, while the new one is slightly, but negligibly lower.

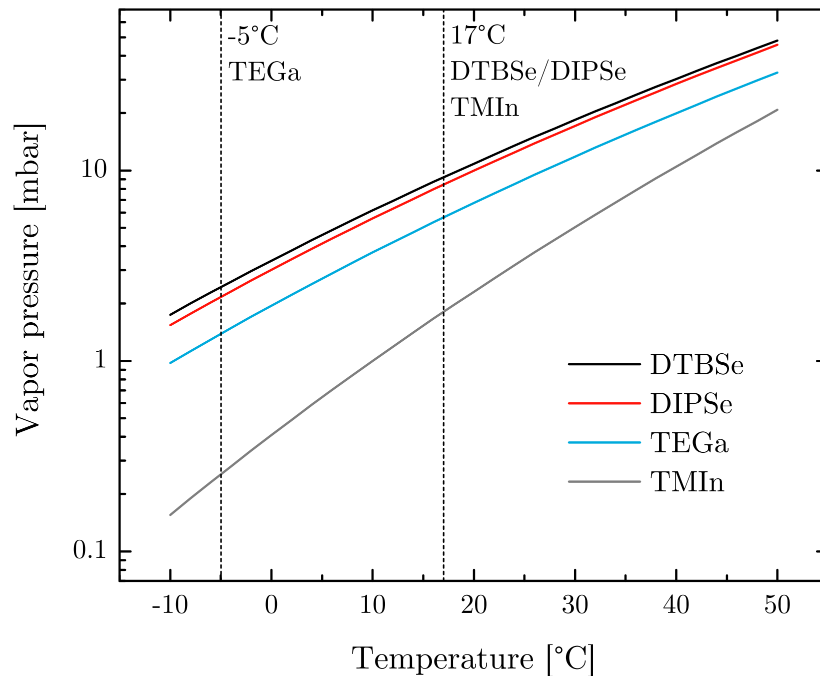

Figure 2.6: Vapor pressure of the metal organic precursors inside the bubbler in dependence of the temperature (given by the manufacturer).

Variations of the Ga/III or Cu/III ratio are realized by only changing the partial pressures of indium, gallium and selenium. In order to vary the Ga/III ratio, the total fluxes (Source and Push) for indium and gallium are always kept constant, but the ratio of the Source (through the bubbler) and Push (bypassing the bubbler) line is varied. The

partial pressures for the Source line of indium and for the Source line of gallium determine the targeted Ga/III ratio. The same holds true for changing the Cu/III ratio, where the copper fluxes are not varied, but the fluxes of gallium or indium are reduced or increased respectively.

For selenium, a high overpressure is needed for best crystal qualities since selenium is very volatile and can decompose from the film during growth or during cool down. The standard setting for the partial pressures of the selenium over metal ratio Se/(Cu+In+Ga) was optimized at LPV in the past to Se/metal ≈ 26 for $CuInSe_2$ and Se/metal ≈ 11 for the growth of $CuGaSe_2$ [43, 52]. The ratios for the solid solution $Cu(In,Ga)Se_2$ are linearly interpolated between these two values, proportional to the Ga/III ratio.

The optimum temperature for $CuGaSe_2$ was found at 520° in the past. $CuInSe_2$ films were grown at only 470° to reduce gallium in-diffusion from the GaAs substrate. Again for $Cu(In,Ga)Se_2$ the temperature values of the ternaries are linearly interpolated depending on the Ga/III ratio. This growth conditions are the standard recipes used at LPV, but due to the higher decomposition temperature for the DIPSe precursor, some thin films were also grown at 530° which will be noted for the respective samples in the text.

Chapter 3

Defect spectroscopy by Photoluminescence

In the following chapter, the fundamental basics of photoluminescence in semiconductors and the properties of the measurement setup are given. The first section contains an overview of possible photoluminescence transitions in experiments. The characteristics of the band-to-band, exciton, free-to-bound and donor-acceptor pair transitions are explained to discriminate them in experiments. The excess carrier generation and recombination in general is briefly discussed in the beginning. More detailed descriptions of the theory can be found in Ref. [60, 61, 62, 63, 64].

Because the free-to-bound and donor-acceptor pair transition can involve strong coupling of electrons and phonons, a model for the phonon interaction in the so-called one-dimensional configuration coordinate is described in the second section 3.2. The model is used to obtain the zero-phonon line of the measured broad photoluminescence bands in the experimental result chapters of this thesis. The general overview of phonon coupling is based on the tutorial in Ref. [17] and the model from Reshchikov et. al. [65].

The used photoluminescence setup is described in the third and last section of this chapter. Starting with the properties of the basic setup for wavelengths up to 1600 nm, the spectral correction for each measurement and the calculation of the excitation photon flux density are explained. In a second part, the extension of the basic setup with an lock-in amplified InAs-detector for wavelengths up to 3100 nm is described.

3.1 Photoluminesence transitions

In a photoluminescence experiment, electron-hole pairs are generated by absorbing photons from the incident light source e.g. from a laser source with a photon energy above the band gap. For steady-state illumination, the photon flux density ϕ inside a semiconductor is given by the Beert-Lambert law in one dimension:

$$\phi(x) = \phi_0(1 - R)e^{-\alpha x} \tag{3.1}$$

with the sample surface at $x = 0$, the photon flux incident at the surface ϕ_0, the energy dependent reflection at the surface $R(\hbar\omega)$ and the energy dependent absorption coefficient $\alpha(\hbar\omega)$. The generation rate follows from:

$$G(x) = -\frac{\partial\phi(x)}{\partial x} = \phi_0(1 - R)\alpha e^{-\alpha x} \tag{3.2}$$

It is assumed that every not reflected photon is absorbed and therefore creates an electron hole pair. Furthermore, the thickness of the layer d is large enough so that transmission of the excitation light with an energy $\hbar\omega_E$ is negligible with $\alpha(\hbar\omega_\mathrm{L}) \gg 1/d$. For a given photon energy of laser excitation, the photoluminescence light mainly stems from a volume corresponding to $1/\alpha$ in depth (initial excitation intensity drops to 1/e). Typical values of $1/\alpha$ for the used laser wavelengths of $\lambda_1 = 514\,\mathrm{nm}$ ($\alpha^{\mathrm{CISe}}_{\lambda 1} = 7.5 \times 10^4 \mathrm{cm}^{-1}$ [66]) and $\lambda_2 = 663\,\mathrm{nm}$ ($\alpha^{\mathrm{CISe}}_{\lambda 2} = 6 \times 10^4 \mathrm{cm}^{-1}$ [66]) are 130 nm and 170 nm respectively.

In a short timescale in the range of picoseconds [35] the generated carriers relax to the band edges by the emission of the excess energy to the lattice in the form of phonons. This process is much faster than the recombination lifetimes in the order of nanoseconds. After thermalization, all free electrons and holes are in a quasi-equilibrium with the lattice temperature, following a Fermi distribution inside the bands before recombination takes place. At very low temperatures, the Fermi distribution can be neglected and the carrier distribution only depends on the density of states.

After the creation of electron-hole pairs and their thermalization, different recombination processes can take place and the carrier recombination balances the carrier generation in steady-state conditions. The most common transitions which can be observed in a semiconductor are depicted in Fig. 3.1. It is worth mentioning that in the following only semiconductors with discrete defect levels and without high amounts of tail states or potential fluctuations are considered. If not stated otherwise this is true for all samples in this thesis, which is a characteristic of the stoichiometric compositions in the bulk.

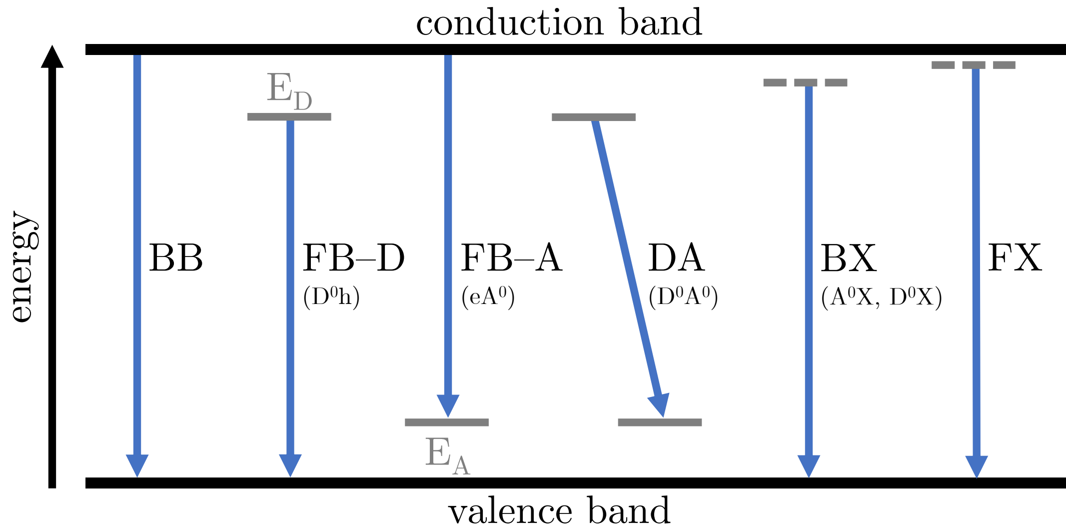

Figure 3.1: Typically observed radiative transitions in a photoluminescence experiment with band-to-band (BB), free-to-bound (FB-D, donor involved), free-to-bound (FB-A, acceptor involved), donor-acceptor pair transition (DA), bound exciton (BX) and free exciton (FX) transition.

At high temperatures where most of the defects are ionized, the band-to-band transition (BB) dominates. If the temperature gets lowered, free-to-bound transitions (FB) from the recombination of an electron on a donor site (neutral defect D^0) with a free hole in the valence band (h) or the recombination of a free electron in the conduction band (e)

with a hole on an acceptor site (A^0) can be observed. The observation of donor-acceptor pair transitions (DA) gets more likely than the free-to-bound transition when the temperature is further decreased and the free carrier concentrations become even lower. If the thermal energy is below the Coulomb attraction of an electron-hole pair, transitions from free excitons (FX) or excitons bound to defects (BX) can occur.

In most photoluminescence measurements, just spontaneous emission of one of the processes in Fig. 3.1 is observed and stimulated emission which occurs at very high carrier densities is not considered here. In this case, the rate of spontaneous emission R_{sp} is equal to the radiative recombination rate R_{rad}. Based on Fermi's golden rule the spontaneous emission rate is proportional to the carrier density in the initial state n_1 and the density of empty states in the final state n_2 [64] and it is:

$$R_{\mathrm{sp}} \propto W_{12} n_1 n_2, \tag{3.3}$$

with the transition probability W_{12} that one carrier in a given volume recombines with one hole in a given volume. In the following, some characteristics of each recombination process are given which can be used to discriminate unknown transition peaks in a photoluminescence spectrum. This includes e.g. the excitation dependence of the transition energy, the temperature dependence of the intensity as well as the peak shape. Detailed descriptions of the excitation dependent peak intensities can be found in Chapter 4.

3.1.1 Band-to-band

Generally at room temperature, shallow defects are emptied by thermal ionization and radiative recombination of excess carriers occurs mainly by band-to-band transitions. The radiative band-to-band transition is an unavoidable process in direct band gap semiconductors and it's ratio over the total recombination rate inside the crystal is an important material property, which is often referred to the internal radiative quantum efficiency. The total recombination rate in a semiconductor is equal to the sum of radiative and non-radiative recombination rates:

$$R = R_{\mathrm{rad}} + R_{\mathrm{nrad}} \tag{3.4}$$

The radiative recombination rate of the band-to-band transition is according to Eq. (3.3) proportional to the free electron concentration n and the free hole concentration p with:

$$R_{\mathrm{rad}} = Bnp, \tag{3.5}$$

and the radiative recombination coefficient B (e.g. for $\mathrm{CuInSe_2}$ $B = 6 \times 10^{-11}\mathrm{cm^{-3}s^{-1}}$ [67]). In the dark, most of the free carriers are generated from the thermal activation of shallow defects (n_0, p_0) and the recombination rate in equilibrium is proportional to the square of the intrinsic carrier density n_{i} with:

$$R^0_{\mathrm{rad}} = Bn_0p_0 = Bn_{\mathrm{i}}^2. \tag{3.6}$$

In a photoluminescence experiment with excess carrier generation by laser light, usually the deviation from the thermal equilibrium is measured and the net recombination rate is given by:

$$R^{\mathrm{net}}_{\mathrm{rad}} = B(np - n_0p_0). \tag{3.7}$$

The non-equilibrium carrier concentrations n and p can be described with a separate Fermi level for electrons E_{Fn} and holes E_{Fp} and it is:

$$n = N_{\mathrm{C}} \exp\left(-\frac{E_{\mathrm{C}} - E_{\mathrm{Fn}}}{k_{\mathrm{B}}T}\right) \qquad p = N_{\mathrm{V}} \exp\left(-\frac{E_{\mathrm{Fp}} - E_{\mathrm{V}}}{k_{\mathrm{B}}T}\right), \tag{3.8}$$

As a result, the net recombination rate can be linked to the so-called quasi Fermi level splitting $\Delta\mu = E_{\mathrm{Fn}} - E_{\mathrm{Fp}}$ with:

$$R_{\mathrm{rad}}^{\mathrm{net}} = B(np - n_0 p_0) = B n_{\mathrm{i}}^2 \left(\frac{np}{n_{\mathrm{i}}^2} - 1\right) = B n_{\mathrm{i}}^2 \left(\exp\left(\frac{\Delta\mu}{k_{\mathrm{B}}T}\right) - 1\right). \tag{3.9}$$

From Eq. (3.9) it can be seen that the intensity of the band-to-band transition scales exponentially with the quasi Fermi level splitting, which is usually much larger than $k_{\mathrm{B}}T$ and the exponential term is much higher than 1. This splitting value $\Delta\mu$ is an upper limit for the open circuit voltage in a solar cell. The intensity of the band-to-band transition is an important parameter for the crystal quality (radiative quantum efficiency η_{RQE}) and the solar cell parameters (maximum open circuit voltage V_{OC}) at the same time.

Peak shape

The peak shape of the band-to-band transition in the ideal case with no tail states is given by the square-root density of states and their Boltzmann distributed occupation:

$$I_{\mathrm{BB}}(\hbar\omega) \propto (\hbar\omega - E_{\mathrm{g}})^{\frac{1}{2}} \exp\left(-\frac{\hbar\omega - E_{\mathrm{g}}}{k_{\mathrm{B}}T}\right), \tag{3.10}$$

with $\hbar\omega > E_{\mathrm{g}}$. From the derivative of Eq. (3.10) it directly follows that the peak maximum is at $E_{\mathrm{G}} + k_{\mathrm{B}}T/2$. The full width at half maximum in the ideal case equals $1.8\, k_{\mathrm{B}}T$ which is about 46 meV at room temperature. From this, the band gap can be determined from the peak maximum, but distributions of tail states can shift the peak to lower energies [68].

3.1.2 Exciton

Excitons are electron-hole pairs which are bound to each other by their Coulomb attraction. The formation of excitons can occur at low temperatures where the binding energy exceeds the thermal energy. If a free exciton recombines, the energy equals the band gap energy at the set temperature minus the exciton binding energy: $\hbar\omega_{\mathrm{FX}} = E_{\mathrm{g}} - E_x$. Like in Fig. 3.1, this value is often sketched as a virtual, but not existing state close to the conduction band in order to depict the released photon energy. The Coulomb attraction between the electron and the hole can be calculated in the hydrogen model, taking into account the dielectric constant and the reduced electron-hole mass of the material and it follows for the first excited state:

$$\hbar\omega_{\mathrm{FX}} = E_{\mathrm{g}} - E_{\mathrm{x}} = E_{\mathrm{g}} - \frac{m_{\mathrm{r}}^* e^4}{2(4\pi\varepsilon_0\varepsilon_{\mathrm{r}}\hbar)^2} \frac{1}{n^2} \overset{n=1}{=} E_{\mathrm{g}} - \frac{R_{\mathrm{y}}}{\varepsilon_{\mathrm{r}}^2} \frac{m_{\mathrm{r}}^*}{m_0}, \tag{3.11}$$

with the Rydberg energy $R_{\mathrm{y}} = 13.6\,\mathrm{eV}$ and the reduced electron-hole mass:

$$1/m_{\mathrm{r}}^* = 1/m_{\mathrm{e}}^* + 1/m_{\mathrm{h}}^*. \tag{3.12}$$

Inserting values of the effective masses and dielectric constants for $CuInSe_2$ and $CuGaSe_2$ yields an exciton binding energy of $E_{\mathrm{x}}^{\mathrm{CISe}} = 6\,\mathrm{meV}$ ($m_{\mathrm{e}}^*/m_0 = 0.09$, $m_{\mathrm{h}}^*/m_0 = 0.71$,

$\varepsilon_r = 13.6$) and $E_x^{CGSe} = 13\,\text{meV}$ ($m_e^*/m_0 = 0.14$, $m_h^*/m_0 = 0.64$, $\varepsilon_r = 11.0$). The values are taken from a literature overview in the appendix of Ref. [10] and the calculation of the hole mass in $CuGaSe_2$ from excitonic shifts [69]. Experimentally observed binding energies are $E_x^{CISe} = 8\,\text{meV}$ [70] and $E_x^{CGSe} = 13\,\text{meV}$ [71]. If these values are known, the low temperature band gap can be determined from the free exciton transition. Or vice versa, if the band gap is known, exciton binding energies can be determinded and used for the characterization of e.g. the effective mass.

Apart from free excitons, the electron-hole pairs can also be bound to a defect site and the recombination energy is usually further reduced, which depends on the so-called Hayne's rule [72]. For the recombination of excitons which are bound to charged defects, their transition energy is equal to the band gap energy reduced by a factor of the defect ionization energy $E_{D/A}$ of the donor or acceptor respectively: $\hbar\omega_{BX}^q = E_g - c_q E_{D/A}$. If the excitons are bound to neutral defects, the binding energy of the free exciton has to be substracted additionally: $\hbar\omega_{BX}^0 = E_g - E_x - c_0 E_{D/A}$. The constants c_i depend on the ratio of the effective masses and if they are known, defect energies can be determined from bound exciton transitions [15].

Exciton transition show no energy shift with increasing excitation, but it should be considered that very high laser intensities could lead to a redshift from unintentional heating of the sample.

3.1.3 Free-to-bound

If free electrons in the conduction band recombine with holes on a shallow acceptor defect (eA^0) or if free holes in the valence band recombine with electrons on a shallow donor defect (D^0h), this process is called free-to-bound transition. Without strong potential fluctuations of the bands, which could lead to an intensity dependent amplitude of the fluctuating band edges [73], the free-to-bound transition shows no peak shift in energy with increasing excitation. In the low temperature limit where the thermal energy is negligible, the free-to-bound transition energy follows directly from the band gap, together with the ionization energy of the involved donor or acceptor defect with $\hbar\omega_{FB} = E_g - E_{D/A}$.

Apart from the temperature dependence of the band gap, this transition energy has an additional temperature dependence in the order of $k_B T$ which results from the Fermi distribution of the free carriers inside the involved conduction or valence band [74]:

$$\hbar\omega_{FB}(T) = E_g(T) - E_{D/A} + \frac{k_B T}{2} \tag{3.13}$$

The temperature dependent band gap energy leads to a redshift of the free-to-bound transition with increasing temperature, whereas the term $k_B T/2$ leads to a blueshift. But in most cases the free-to-bound transition is thermally quenched before a significant blueshift can be observed.

3.1.4 Donor-acceptor pair

Donor-acceptor pair transitions are likely to occur at low temperatures in materials with sufficient amounts of donors and acceptors present. In the most simple case of singly charged defects, the recombination process takes places from a neutral donor into a neutral acceptor, leaving a singly positive charged donor and singly negative charged acceptor. A photon is emitted with the energy difference of the two final states. Therefore, the photon energy not only depends on the involved defect energies. Also the Coulomb interaction of the donor-acceptor pair in the final state (attractive potential) need to be added and it follows:

$$\hbar\omega_{\mathrm{DA}}(r_{\mathrm{DA}}) = E_{\mathrm{g}} - (E_{\mathrm{D}} + E_{\mathrm{A}}) + \frac{e^2}{4\pi\epsilon_{\mathrm{r}}\epsilon_0 r_{\mathrm{DA}}} = E_\infty + E_{\mathrm{Coul.}}(r_{\mathrm{DA}}). \tag{3.14}$$

If the excitation intensity is increased, more donors and acceptors are neutralized by excess carriers. The average spatial distance for recombination decreases, the effective Coulomb attraction increases and the transition energy increases as a result. The photon energy without any additional Coulomb energy E_∞ is indexed with an infinity sign, since it is referred to donor-acceptor pairs infinitely separated ($r_{\mathrm{DA}} \to \infty$). Furthermore, for very small distances another term accounting for the Van-der-Waals interaction can be added, but its contribution is usually very small in conventional experiments and will be neglected here. In the hydrogen model, the shallower impurity involved in the donor-acceptor pair has a larger Bohr-radius than the deeper one. If the Bohr-radius of the deeper impurity is neglected over the shallower one, in Ref. [75] the dependence of the used laser excitation ϕ on the transition energy $\hbar\omega_{\mathrm{DA}}$ is given by:

$$\phi(\hbar\omega_{\mathrm{DA}}) \propto \frac{(\hbar\omega_{\mathrm{DA}} - E_\infty)^3}{E_{\mathrm{B}} + 2E_\infty - 2\hbar\omega_{\mathrm{DA}}} \exp\left(-\frac{2E_{\mathrm{B}}}{\hbar\omega_{\mathrm{DA}} - E_\infty}\right). \tag{3.15}$$

If the laser intensity in an experiment is varied over several orders of magnitude and the transition energy is plotted over the laser intensity ϕ in a logarithmic scale, a typical s-shape can be observed. At lowest excitation, the transition energy $\hbar\omega_{\mathrm{DA}}$ approaches E_∞ and at highest excitation it approaches $E_\infty + \frac{1}{2}E_{\mathrm{B}}$. By fitting the curvature, the energy E_{B}, which corresponds to the Coulomb energy with the Bohr-radius R_{B} can be extracted as a free parameter. In this model, E_{B} is the defect level of the shallower impurity e.g. E_{d} in general. The maximum Coulomb energy in the donor-acceptor pair transition is given by:

$$E^{\max}_{\mathrm{Coul.}} = \frac{1}{2}E_{\mathrm{B}} = \frac{e^2}{4\pi\epsilon_0\epsilon_{\mathrm{r}}}\frac{1}{2R_{\mathrm{B}}} = \frac{R_{\mathrm{y}}}{\epsilon_{\mathrm{r}}^2}\frac{m^*}{m_0} = E_{\mathrm{d}}, \tag{3.16}$$

If one of the involved donor or acceptor defect energies is known, the other one can be calculated from the knowledge of the fitting parameter E_∞ in Eq. (3.15) and the band gap in Eq. (3.14). The peak width of a donor-acceptor pair transition can be extremely small (lifetime limited), much lower than the thermal energy, since moderate defect concentrations which do not form a defect band have discrete energy values without thermally distributed carriers. On the other hand, highly localized (deep) defects can lead to electron-phonon coupling and very broad photoluminescence peaks which will be explained in the next section.

Temperature dependence

The temperature dependent intensity of a donor-acceptor pair transition is given in the most simple case by two different slopes for the activation energies in an Arrhenius plot:

$$I_{\mathrm{DA}}(T) = \frac{I_{\mathrm{DA}}(0)}{1 + c_1 T^{3/2} \exp\left(-\frac{E_{\mathrm{D}}}{k_{\mathrm{B}}T}\right) + c_2 T^{3/2} \exp\left(-\frac{E_{\mathrm{A}}}{k_{\mathrm{B}}T}\right)} \tag{3.17}$$

One activation energy corresponds to the ionization energy of the donor $\mathrm{E_D}$ and the other one to the ionization energy of the acceptor $\mathrm{E_A}$. The temperature dependent prefactors result from the temperature dependent density of states in the conduction band (for $\mathrm{E_D}$) and the valence band (for $\mathrm{E_A}$). This dependence of $T^{3/2}$ can also lead to spuriously small activation energies in the range of a few $k_{\mathrm{B}}T$ [76] and if so, another term of $c_0 T^{3/2}$ can be added to the denominator. On the other hand, if deep defects are present with high capture cross section for electrons and holes, abrupt thermal quenching could be observed which yields unreasonable high activation energies [77]. In the simple model of only shallow donors and acceptors, the sum of both activation energies and the peak position should be equal to the band gap (see Eg. 3.14). In the case of a free-to-bound transition, one term for the activation energy can be simply omitted.

3.2 Phonon interaction

If defects are involved in the photoluminescence transition (free-to-bound or a donor to acceptor pair transition), strong electron-phonon coupling can influence the observed peak position which can lead to misinterpretations of the defect level. Usually shallow defects have a weak interaction with phonons, since the wavefunction is delocalized and therefore the electron density at the defect site is low enough so that the spatial positions of neighboring atoms are not influenced. But if a defect is highly localized (usually a deep defect in the band gap), atoms can get displaced when the charge of the defect changes by e.g. capture or emission of electrons. Atoms of the surrounding rearrange locally which can shift the potentials of the electrons spatially, away from the equilibrium position.

This behavior can be described in the most simple case by the so-called 1-dimensional configuration coordinate diagram. The following argumentation is based on a review in Ref. [17]. Atomic displacements by charging or neutralizing defects are approximated by a configuration coordinate which is proportional to the bond length of the atoms. All bonds of the surrounding atoms are treated as harmonic springs. An example is given in Fig. 3.2. For simplicity reasons the same parabolic potentials are used for all different states. Also assuming the same zero-point energy at 0 K for all potentials, leads to the same energetic differences of parabola minima or the differences between the corresponding zero-point energies ($+\frac{1}{2}\hbar\Omega$). An excited state which corresponds to a shallow donor is sketched in light blue, following the potential of the conduction band and no displacement of the parabola. In this case the thermal activation energy of an electron into the conduction band would be equal to the energetic difference of the two minima. If an electron in the excited state at the shallow donor site is recombining with e.g. a hole in the valence band (ground state) it can release the energetic difference of the two parabola minima under the emission of photons and without the emission of phonons.

The situation is different for the deep defect in grey, where e.g. the potential minimum of the excited state of an electron (now captured by the deep defect) is displaced compared to the ground state (valence band). As an example, one can assume a p-type

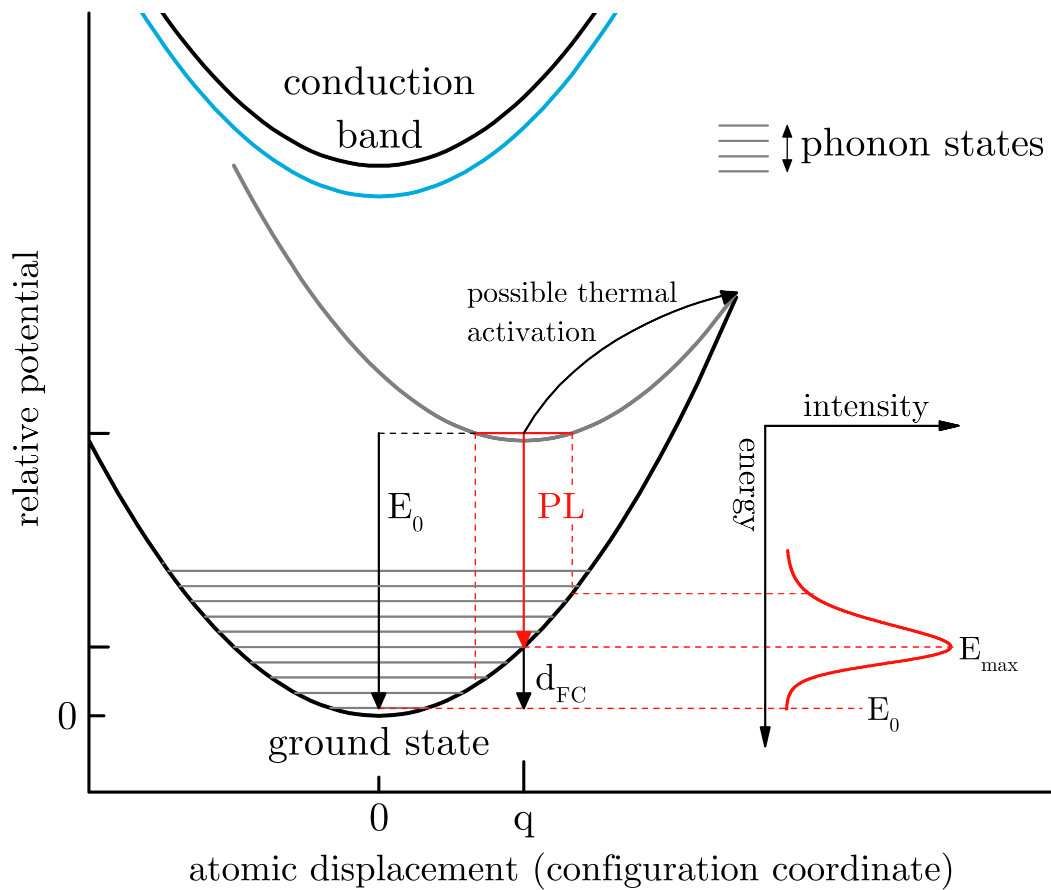

Figure 3.2: Example of the one-dimensional configuration coordinate for different energetic states with the same parabolic potential. The ground state corresponds to the valence band and the highest excited state to the conduction band. The blue curve is exemplary for the excited state of a shallow defect with no displacement. The grey curve is exemplary for the excited state of a deep defect with an atomic displacement q from the ground state (the schematic of the configuration coordinate diagram is based on Ref. [78]).

semiconductor. In the dark, the Fermi level is close to the valence band and the ground state of a deep donor defect is singly positive charged and no atomic displacement in the equilibrium position (like for the shallow defect) occurs. If an electron is excited into the conduction by e.g. laser light, it can be captured by this deep donor. The defect becomes neutralized which leads to changing bond length to the neighboring atoms, since before a highly localized charge density was present. A new quasi-equilibrium position for the potential minimum occurs at q. The defect has gained energy equal to the Franck-Condon shift d_{FC}. When the electron is released from the deep defect by e.g. recombination with a hole in the valence band it can return to the ground state and a photon as well as several phonons are emitted. The optical transition is a very fast process and the relaxation of the system to the ground state is much slower (under emission of phonons). The actual energetic distance of the defect to the ground state is called the zero-phonon line E_0. This is the total energy and the sum of the emitted photon energy and the Franck-Condon shift. Therefore the measured maximum photoluminescence energy is not equal to the zero-phonon line like it is the case for the shallow defect. But it is equal to the zero-phonon line, reduced by the Franck-Condon shift.

The defect level cannot be extracted from just measuring the photoluminescence maximum at low temperatures. In some cases the zero-phonon line may be visible as a much sharper line and taken as the conventionally treated transition energy. But if not, the zero-phonon line has to be determined from the knowledge of the Franck-Condon shift by a careful analysis and fitting of the peak shape. In Fig. 3.2 it is also sketched that the appearing broad photoluminescence peak usually arises from the sum of different phonon lines ($E_0 - 1\hbar\Omega, E_0 - 2\hbar\Omega, \dots$) and an asymmetric peak shape is observed (sometimes just visible in log-scale [65]). In $Cu(In,Ga)Se_2$ it can be shown from optical measurements of the near band edge luminescence that the longitudinal optical phonon is involved in the recombination (for the LO-energies see Section 1.1.3), corresponding to the E1 mode with the highest energy of the lattice vibrations in the crystal [31]. But in other materials it is also possible that the spectral density of phonon coupling follows an energy distribution rather than one dominating phonon energy [17]. If not visible in the spectrum, the determination of the zero-phonon line is explained in the following.

Zero-phonon line

The zero-phonon line can be extracted from the photoluminescence peak maximum and the Franck-Condon shift by:

$$E_0 = \hbar\omega_{\mathrm{max}} + d_{\mathrm{FC}} \tag{3.18}$$

The Franck-Condon shift is defined by the average amount of phonons S which are involved in the recombination process and the single phonon energy $\hbar\Omega$ involved:

$$d_{\mathrm{FC}} = S\hbar\Omega \tag{3.19}$$

For spectral distributions of phonon coupling, the average phonon energy has to be inserted. The factor S is called Huang-Rhys factor. If not known, the phonon energy can be determined from temperature dependent measurements of the peak width [17]. Due to their much higher energies, usually just optical phonons are involved in the process. In the case for $CuInSe_2$ and $CuGaSe_2$, the phonon energy of the coupling LO-phonon mode is shown in Fig. 1.4 in Section 1.1.3.

From literature it is well known that at low temperatures, the amplitudes of the zero-phonon line and the corresponding phonon replicas follow a Poisson distribution P [79].

The intensity of the n-th phonon line is given by:

$$I_{\mathrm{n}} \propto P_{\mathrm{n}}(S) \propto \exp(-S)\frac{S^{\mathrm{n}}}{n!} \tag{3.20}$$

From this equation it can be already concluded that for $S < 1$ (weak coupling) the zero phonon line (ZPL) is the strongest and nearly no peak shift will occur. For $S = 1$, the ZPL and the first phonon replica have the same amplitude and the average peak maximum is shifting by $\frac{1}{2}\hbar\Omega$, since e.g. the summation of two broad Gaussian peaks will yield a maximum in between (see Fig. 3.3). This factor of $\frac{1}{2}\hbar\Omega$ has to be included if the actual photoluminescence maximum from overlapping phonon lines is considered rather than the "center of mass" of all lines. The Franck-Condon shift from Eq. (3.19) can be slightly modified for broad unresolved phonon lines and higher Huang-Rhys factors ($S \geq 1$), so that it still accounts for the distance of the measured photoluminescence maximum and the ZPL:

$$d^{*}_{\mathrm{FC}} = (S - \frac{1}{2})\hbar\Omega \tag{3.21}$$

Furthermore, for an intermediate coupling strength ($S > 1$), the phonon replicas will have higher intensities than the ZPL and the peak maximum shifts further away. The peak shape approaches a Gaussian intensity distribution for increasing phonon coupling and especially for Huang-Rhys factors above e.g. 10.

Model with Gauss-modes

In the easiest assumption, every phonon line is replaced by a Gaussian peak function with a full-width-at-half-maxmimum ω. The separation of every phonon line is given by the phonon energy $\hbar\Omega$ and one obtains the following functions for the photoluminescence shape:

$$\begin{aligned} L(\hbar\omega) &\propto \sum_n P_n(S) G_\sigma(E_0 - n\hbar\Omega - \hbar\omega) \\ L(\hbar\omega) &\propto \sum_n \exp(-S)\frac{S^n}{n!}\frac{1}{\sigma\sqrt{2\pi}} \exp\left(-\frac{1}{2}\left(\frac{E_0 - n\hbar\Omega - \hbar\omega}{\sigma}\right)^2\right) \\ L(\hbar\omega) &\propto \sum_n \exp(-S)\frac{S^n}{n!} \exp\left(-\frac{1}{2}\left(\frac{E_0 - n\hbar\Omega - \hbar\omega}{w/\sqrt{8\ln 2}}\right)^2\right) \end{aligned} \tag{3.22}$$

The lineshape is described by the summation of all Gaussian phonon lines G_σ, which are amplitude-weighted with the formerly shown Poisson distribution P_{n}. For $n = 0$ the zero phonon line is at E_0. The width of each phonon line is given by the standard deviation σ or the full-width-at-half-maximum w. This value not only depends on the temperature of the crystal. It can be broadened e.g. due to alloy fluctuations in $Cu(In,Ga)Se_2$ solid solutions, compositional fluctuations of different grains in polycrystalline samples or due to strain from the lattice mismatch in epitaxial samples. In order to scale the lineshape to the intensity maximum of the measured photoluminescence, the maximum is determined numerically with a script and Eq. (3.23) is used for fitting of the experimental data:

$$I_{\mathrm{PL}}(\hbar\omega) = I^{\mathrm{max}}_{\mathrm{PL}}\frac{L(\hbar\omega)}{max[L(\hbar\omega)]} \tag{3.23}$$

Several examples for the intensity of this Gaussian phonon model are given in Fig. 3.3. The phonon energy is fixed at $\hbar\Omega = 30\,\text{meV}$. From the left to the right, the full-width-at-half-maximum of each phonon line is set to 2 meV, 20 meV and 50 meV. From the top to the bottom, the Huang-Rhys factor S is varied between 0 and 10 and the upper curve corresponds to the zero-phonon line of a hypothetical defect recombination at 1.0 eV. All spectral maxima are normalized for comparison.

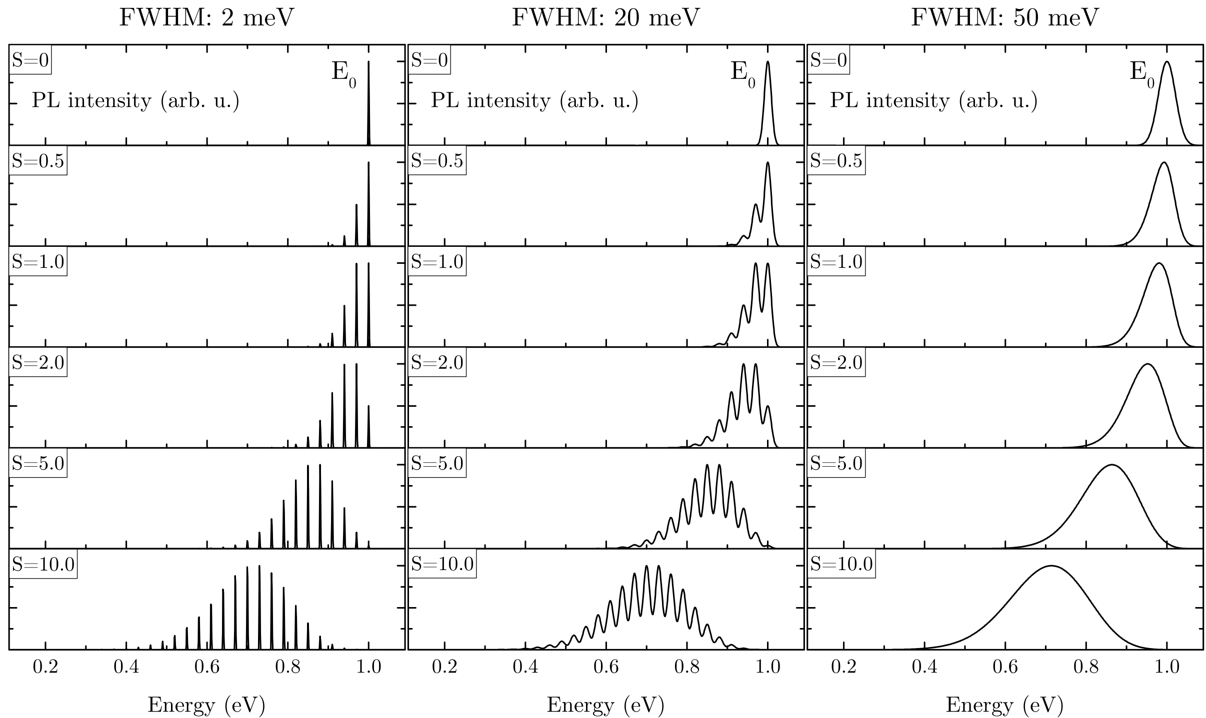

Figure 3.3: Exemplary photoluminescence spectra calculated from Eq. (3.22) with a zero-phonon line at $E_0 = 1.0\,\text{eV}$ and varying values of w and S. The phonon energy is chosen at $\hbar\Omega = 30\,\text{meV}$.

As it can be seen in Fig. 3.3, high values of S lead to very broad peaks and the intensity of the zero-phonon line becomes vanishing small. The photoluminescence maximum shifts to lower energies by max. $S\hbar\Omega$. Broad peaks due to phonon coupling have to be separated from broad defect distributions which are possible for forming defect bands or high potential fluctuations involved. In Fig. 3.3 it is also visible that depending on the line width and the phonon energy, the summation over all phonon modes not necessarily merges into one unresolved band. Examples for resolved phonon lines can be found e.g. in Ref. [80] for strong coupling or in Section 5.2.1 for weak coupling.

Model from Reshchikov

Another fitting function for photoluminescence peaks with exclusively strong phonon coupling were only a broad single band can be observed was derived by Reshchikov et. al. [65] and is given in Eq. (3.24).

$$I_{\mathrm{PL}}(\hbar\omega) = I_{\mathrm{PL}}^{\max} \exp\left(-2S\left(\sqrt{\frac{E_0 + \frac{1}{2}\hbar\Omega - \hbar\omega}{E_0 - \hbar\omega_{\max}}} - 1\right)^2\right) \tag{3.24}$$

In this case, the energy of the peak maximum $\hbar\omega_{\max}$ is another fitting parameter, whereas the width of the phonon lines is not needed. This model seems to be better suited, since $\hbar\omega_{\max}$ is directly known from the measured spectrum, whereas the width w is unknown in the Gauss-model. But this fitting function is unsuited if the zero-phonon line is broadened due to e.g. strain or alloy fluctuations. A brief comparison of the two models with experimental data will be given in Section 5.2.2 in Chapter 5.

3.3 Photoluminescence setup

In this section, the setup which is used for all photoluminescence measurements is described in detail. In the scope of this thesis a new setup, based on mirrors rather than lenses for light collection, was planned and built. In the first part, the basic system for wavelength measurements up to 1600 nm is sketched and explained together with the spectral correction of the data. Also a brief overview for the calculation of the excitation density is given which is crucial for the comparison with results from other laboratories and publications. In the second part, the extension of the basic setup with a lock-in amplified InAs-detector is explained in order to measure photoluminescence spectra up to 2500 nm with spectral correction and 3100 nm without correction.

3.3.1 Basic measurement setup

A schematic overview of the used photoluminescence setup is shown in Fig. 3.4. The setup was built on the basis of luminescence light collection by parabolic mirrors. The advantage of using mirrors instead of lenses is given by the absence of chromatic aberration and the application over a broad wavelength range (250 nm – 20 μm), without adjusting the focus of light collection. For example, placing an unknown sample into the focus can be done precisely by finding the maximum signal of scattered laser light, while the focus for the emitted unknown long-wavelength light from the sample remains unchanged.

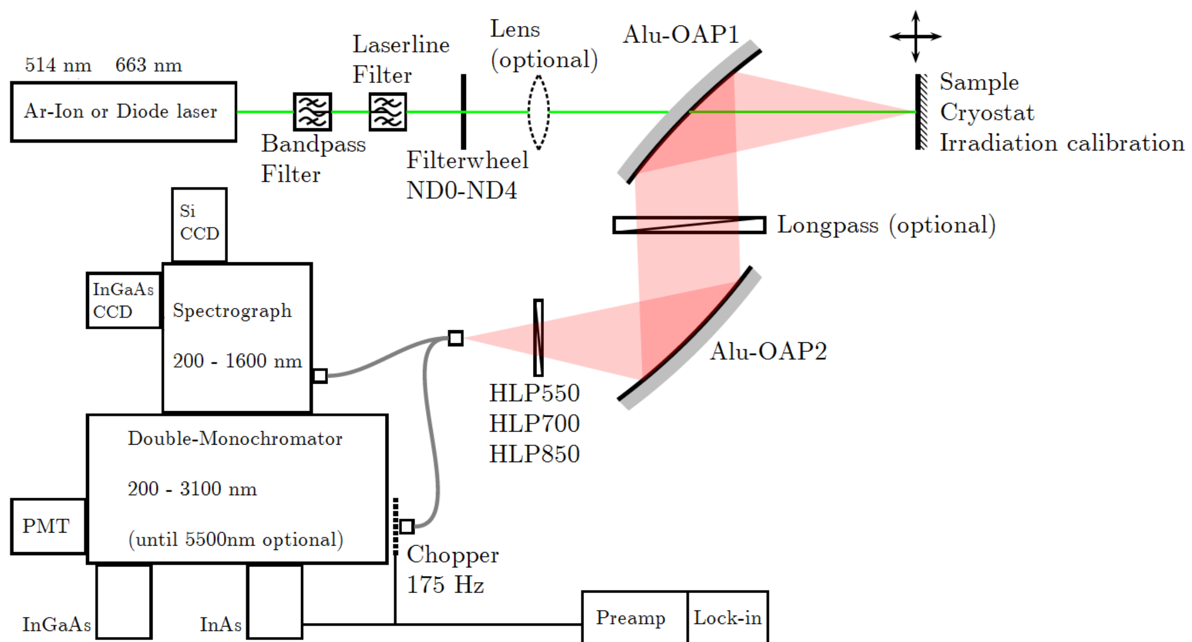

Figure 3.4: Home-build photoluminescence setup used for the experiments.

Furthermore, in the new constructed setup, the excitation and collection paths can be tuned and aligned independently. The laser light from an argon-ion laser ($\lambda = 514$ nm) or from a laser diode ($\lambda = 663$ nm) is guided to the sample surface through an aperture in the middle of the first mirror (Alu-OAP1). Unwanted wavelengths inside the laser beams are suppressed by several bandpass and laserline filters in front of the laser outputs and the laser light can be attenuated by a filter wheel with neutral density filters (ND) and optical densities from OD1 to OD4. For precise excitation intensity dependent measurements,

the exact transmission values for each neutral density filter need to be known for the green and the red laser which can be found in Appendix A.

To increase the photon density by decreasing the spot size on the sample, an optional convex lens with a focus length of $f_{L1} = 150\,\mathrm{mm}$ can be used. If not stated otherwise all measurements in the results of this thesis are done by using the focusing lens, which results in a spot size of approx. $80\,\mu\mathrm{m}$. This value is far above typical diffusion length in Cu(In,Ga)Se_2 of a few microns [81]. For this reason, signal reduction from lateral diffusion is negligible. The sample is mounted on an xyz-translation stage and illuminated parallel to its surface normal. For angle-resolved photoluminescence measurements a special sample holder can be used where the sample can be rotated, while its axis of rotation is at the sample surface. This enables e.g. the correction of spectra disturbed by interferences [82]. For low temperature measurements a liquid helium continuous flow cryostat mounted on a second xyz-translation stage is used.

The aluminum off-axis parabolic mirror Alu-OAP1 is fixed, so that the collected light from its focal point on the sample surface is reflected into a collimated beam by an angle of 90°. A second identical mirror Alu-OAP2 is fixed in turned direction to the first one for re-focusing of the collimated light onto a multimode optical fiber. Unwanted collected laser light is filtered out by high quality long pass filters with an edge wavelength at e.g. 550 nm for the 514.5 nm argon-ion laser (HLP550) or 700 nm for the 660 nm diode laser (HLP700). For measurements with the InGaAs-array detector a high quality longpass filter with an edge wavelength at 850 nm (HLP850) is used for the suppression of light in the second order.

The spectrograph for light dispersion is equipped with an Si-CCD (200 – 1100 nm) and an InGaAs-array detector (800 – 1600 nm). The resolution depends on the chosen fiber and grating density. In all experiments in this thesis, the light is dispersed with a grating density of 100 lines/mm which results in a wavelength resolution e.g. in the visible range of approx. $\Delta\lambda = 6\,\mathrm{nm}$ for a used fiber core diameter of $200\,\mu\mathrm{m}$ and approx. $\Delta\lambda = 16\,\mathrm{nm}$ for the fiber core diameter of $550\,\mu\mathrm{m}$. For each measurement a center wavelength is chosen and a spectral range of nearly $\pm 200\,\mathrm{nm}$ is recorded at the same time. For larger measurement ranges, several spectra with different center wavelengths are stitched together by averaging intensities at the same overlapping wavelengths.

Off-axis parabolic mirrors

Both parabolic mirrors have a diameter of $D = 50.8\,\mathrm{mm}$ (2"). The first collecting mirror Alu-OAP1 which faces the sample, has a focus length of $f_{M1} = 101.6\,\mathrm{mm}$ (4"). The focus length should be as small as possible in order to reach a high angular aperture for highest collection efficiency of the photoluminescence light. The angular aperture can be expressed in a simplified way by the f-number $N = f/D$. The collecting mirror has a f-number of $N_{M1} = 2$. For higher collection efficiency (smaller f-number), the focus length cannot be chosen arbitrarily small due to the fact that the mirror-mounting and the sample chamber of the cryostat set a lower limit for the needed space between the mirror and the sample surface. The value of $f_{M1} = 101.6\,\mathrm{mm}$ is a good trade-off.

The second mirror Alu-OAP2 for the re-focusing of the collected light onto the fiber has a larger focus length of $f_{M2} = 152.4\,\mathrm{nm}$ (6"). The used multimode fibers have always a numerical aperture of $\mathrm{NA} = \sin\theta_{\mathrm{fib}} = 0.22$, which corresponds to an aperture half-angle θ_{fib} of 12.7°. Therefore, the half-angle of the focussing mirror should be smaller to not lose light from inappropriate total reflection inside the fiber. The half-angle of the mirrors is given by $\theta = \arctan\frac{D}{2f}$, which is $\theta_{M1} = 14°$ for the collecting mirror. This value

would be too high for the fiber coupling and for this reason, the next higher commercially available focus length was chosen for the focussing mirror. The half-angle is $\theta_{\mathrm{M2}} = 9.5°$ and inside the acceptance cone of the fibers. It is worth mentioning that the different focus length of the two mirrors leads to a magnification of the illuminated sample spot at the fiber input. This magnification is given by $m = f_{\mathrm{M2}}/f_{\mathrm{M1}} = 1.5$, assuming no spherical abberation. The typical focused laser spot size on the sample surface of $80\,\mu$m is magnified to $120\,\mu$m at the fiber input and the fiber core diameter should be chosen larger for highest throughput. In the experiments of this thesis only a $200\,\mu$m or $550\,\mu$m core diameter fiber was used.

Spectral correction

Each measured photoluminescence spectrum is spectrally corrected for all optical elements and detectors in the setup by using a calibrated halogen light source. To obtain the correction function, a Spectralon-diffusor with a flat reflectance profile and more than 99 % reflection in the desired wavelength range is placed at the sample position. Light from the halogen lamp is guided to the diffusor and reflected inside the measurement setup. With this method, the windows from the cryostat for low temperature measurement are not included in the optical path for the correction function. But the window material Spectrosil-B has a flat transmission profile at all measured wavelengths and only reduces the light collection by a few percentages (see Appendix B) which is not of any concern since low temperature measurements are not calibrated for absolute intensity values. Only a small dip of a few percent in the transmission between 0.9 and 1.0 eV deviates from the flat energy dependence.

The correction function Γ is given by dividing the known halogen (H) lamp spectrum by the measured spectrum:

$$\Gamma = \Phi_{\mathrm{H}}^{\mathrm{cal.}} / \Phi_{\mathrm{H}}^{\mathrm{meas.}} \tag{3.25}$$

For spectral corrections, the actual measured photoluminescence spectrum Φ_{PL} just needs to be multiplied with the correction function:

$$\Phi_{\mathrm{PL}}^{\mathrm{corr.}} = \Gamma \times \Phi_{\mathrm{PL}}^{\mathrm{meas.}} \tag{3.26}$$

The corrected spectrum has the same units as given by the calibrated lamp spectrum and finally is converted into energies by applying the Jacobian conversion [83] for the y-axis and the x-axis:

$$\begin{aligned} y\,[\mathrm{ph/cm^2}/s/\mathrm{nm}] &\mapsto y \times \frac{x^2}{hc}\,[\mathrm{ph/cm^2}/s/\mathrm{eV}] \\ x\,[\mathrm{nm}] &\mapsto \frac{hc}{x}\,[\mathrm{eV}], \end{aligned}$$

with the product of the Planck constant and the speed of light $hc \approx 1240\,\mathrm{eV}\cdot\mathrm{nm}$. If not stated otherwise, all measured spectra in this thesis are given in units of photons/cm^2/s/eV and with an arbitrary amplitude. The calibrated lamp spectrum from the manufacturer is shown in Fig. 3.5 on the left side in units of ph/cm^2/s/nm. On the right side, a typical measured lamp spectrum with a center-wavelength at 1400 nm and the corresponding correction function is depicted and normalized at 1600 nm. Every measured spectrum consists of a well defined sawtooth-shaped line profile which is a systematic characteristic of the pixel read out and which disappears completely after applying the correction function. Two small kinks at ca. 1370 nm are due to known light absorption from water

vapor. Usually these kinks are not visible in the corrected spectra, but it is possible if e.g. the humidity changes between the sample and the lamp measurement. The influence of general water absorption is crucial for the extended setup in the last section of this chapter where much stronger absorption lines occur at ca. 1900 nm and above 2600 nm.

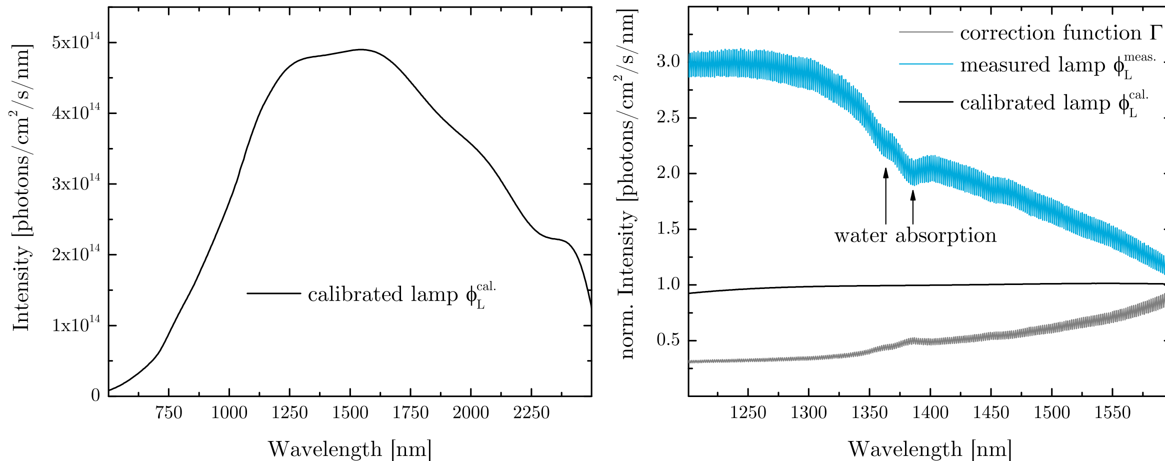

Figure 3.5: Full spectrum of the calibrated halogen lamp (left) and exemplary measured spectrum of the lamp together with the correction function (right).

Excitation density

For quantifying the excitation intensity in a photoluminescence experiment, it is important to know the illuminated area and the laser power used. Often in literature only the laser power is given, which is insufficient, since the generated electron-hole pairs and therefore the excess carrier density in a semiconductor depends on the photon flux per area ϕ. The power density in general can be expressed by Eq. (3.27) with the laser power P [mW] and a circular area A [cm^2].

$$I = \frac{P}{A} = \frac{P}{\pi r^2} \tag{3.27}$$

Because the laser beam has a Gaussian intensity profile, the radius has to be defined by e.g. the position where the maximum intensity I_0 drops by a factor of $1/\mathrm{e}^2$. This definition of the radius r_e is chosen for the reason that the power density in the maximum of the Gaussian beam ($r = 0$) can be simply obtained by:

$$I_0 = \frac{2P}{\pi r_\mathrm{e}^2}, \tag{3.28}$$

The photon flux density in the maximum is directly proportional to the maximum intensity for a fixed laser wavelength λ and can be calculated with:

$$\phi_0 = \frac{2P}{\pi r_\mathrm{e}^2} \frac{\lambda}{hc} \quad \left[\frac{\mathrm{ph}}{\mathrm{cm}^2\,\mathrm{s}}\right] \tag{3.29}$$

While the beam profile of the red laser diode is always fixed, the laser profile of the green argon-ion laser can slightly vary for different intracavity apertures, which set to the same

value for all measurements. In Fig. 3.6, the laser profile cross sections are shown for both lasers in x- and y-direction, measured at the sample position without the focusing lens. The $1/e^2$-radius r_e is about 1.34 mm for the red laser diode with 663 nm and 1.49 mm for the green argon-ion laser with 514 nm, obtained by a Gaussian peak fit and averaging in y- and y-direction.

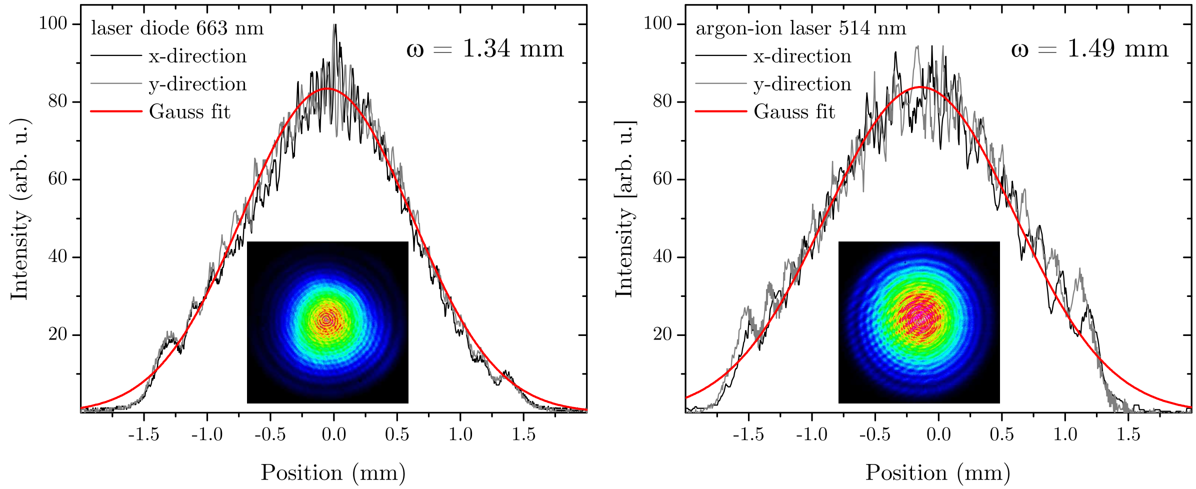

Figure 3.6: Beam profiles of the red laser diode (left) and the argon-ion laser (right).

If not stated otherwise, all spectra in the results of this thesis are measured with the focused laser beam. The beam intensity in the focus is only extended over 8 pixels in the used CCD camera as a beam profiler. But from the fit (not shown here) the radius can be determined to $r_e = 40 \pm 5\,\mu$m and not significantly changes for the red laser diode and the argion-ion laser. Therefore the maximum photon flux of the excitation intensity can be calculated e.g. for the red laser from:

$$\phi_0 = P[\mathrm{mW}] \times 1.3 \cdot 10^{20} \, \left[\frac{\mathrm{ph}}{\mathrm{cm}^2\,\mathrm{s}}\right], \tag{3.30}$$

where P[mW] is the power of the laser beam in units of [mW], measured with a power meter at the sample position.

3.3.2 Extension with InAs-detector

In order to measure even lower energies than 0.77 eV (limit of the InGaAs-array detector at approx. 1600 nm) the setup is extended with an InAs-detector (photovoltaic diode detector). At the beginning of the project an InSb-detector was installed in the system, but later exchanged by an InAs-detector because of a 10 times higher specific detectivity in the desired wavelength range (see Fig. 3.8). Both detector have the same circular area with a diameter of 1 mm. Using the same measurement conditions, this results in an approx. 10 times higher signal-to-noise ratio for the sensitive range of InAs (up to 3100 nm) compared to InSb (up to 5500 nm). Due to the increasing background noise at higher wavelengths from room temperature black body radiation of the surrounding, large unwanted background currents are a general problem for photon detection in the near- or mid-infrared region. These large background currents have to be discriminated from the sample signal by chopping the photoluminescence light together with lock-in amplification. The sketch which is shown in Fig. 3.4 in the previous section contains already the extended setup. A second fiber which is optimized for the mid-infrared region, a chopper for light modulation and a grating monochromator equipped with a nitrogen cooled (77 K) InAs-detector. The signal from the InAs-detector is fed into a preamplifier and from there into a lock-in amplifier. The grating monochromator is also equipped with a conventional InGaAs-detector up to 1600 nm and a photomultiplier tube for measurements up to 900 nm. But since these measurement ranges are already covered with the CDD-cameras in the standard setup, only the InAs-detector is used in the extended configuration.

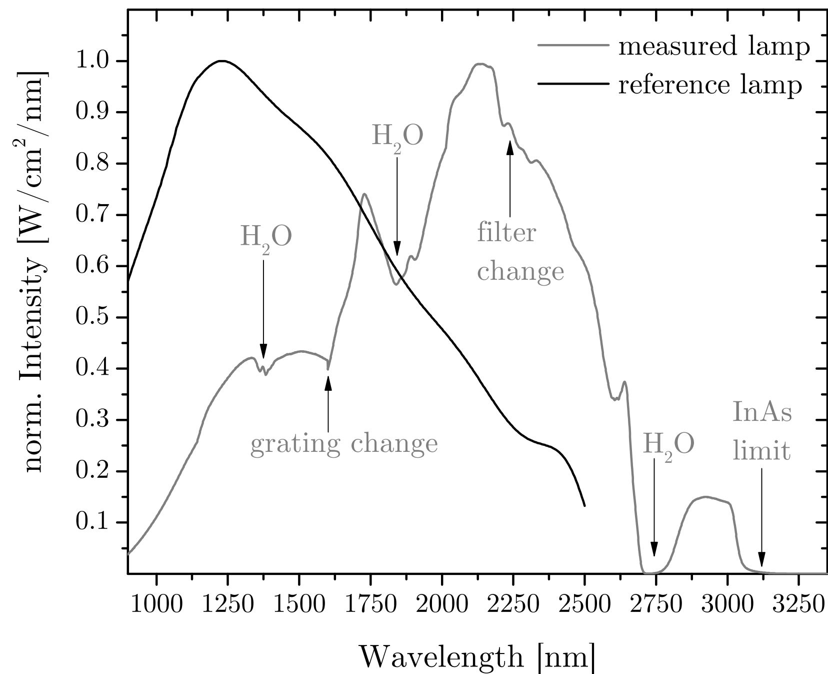

Figure 3.7: Normalized spectrum of the known halogen lamp spectrum in [W/cm^2/nm] in comparison with the raw measured lamp spectrum.

The InAs-detector is cooled down to 77 K by liquid nitrogen. The frequency of the chopper is set to 175 Hz which is far enough from multiples of the power line frequency (150 Hz and 200 Hz). The lock-in integration time constant can be varied between 0.01 and 10 s, depending on the measurement time and is set to 1 s as a standard. It is worth

mentioning that increasing the time constant from 1 s to 10 s increases the signal-to-noise ratio only by a factor of $\sqrt{10}$ due to Poisson distributed shot noise of the photons from background radiation.

Besides the higher background currents, difficulties in the measurements with the extended setup can also arise from strong absorption lines of water vapor. In Fig. 3.7 the known spectrum from the halogen lamp for calibration is compared to the raw, directly measured spectrum. The units are not given in counts or photons since the raw measurements with the extended setup yield values of the photocurrent, which are proportional to the power or energy flux of the detected light. It can be seen, that at 1900 nm and above 2600 nm the absorption from water vapor in the light path strongly affects the signal. The absorption line above 2600 nm cannot be fully corrected since already the signal of the lamp drops nearly to zero and the photoluminescence signal from samples is orders of magnitude lower. But the absorption line at 1900 nm did not appear in spectral corrected sample measurements as it will be seen in Chapter 6. Water absorption lines can occur in standard fiber core material which is avoided with a special infrared-fiber , having ZrF_4 as the core material. Also water absorption can occur due to the Spectrosil-B window material of the cryostat, but already the raw lamp spectrum without using the cryostat shows too strong attenuation of the signal. The most likely origin is the water vapor in the monochromator, which can be purged with nitrogen (no effect) and the water vapor in the laboratory which is unavoidable. Reliable measurement above 2600 nm are not possible at this stage, but because the halogen lamp can only be calibrated until 2500 nm, spectrally corrected measurements with the extended setup are limited until 2500 nm anyway. This wavelength corresponds to approx. 0.5 eV and is equal or below the middle of the band gap in $CuInSe_2$ and especially $CuGaSe_2$.

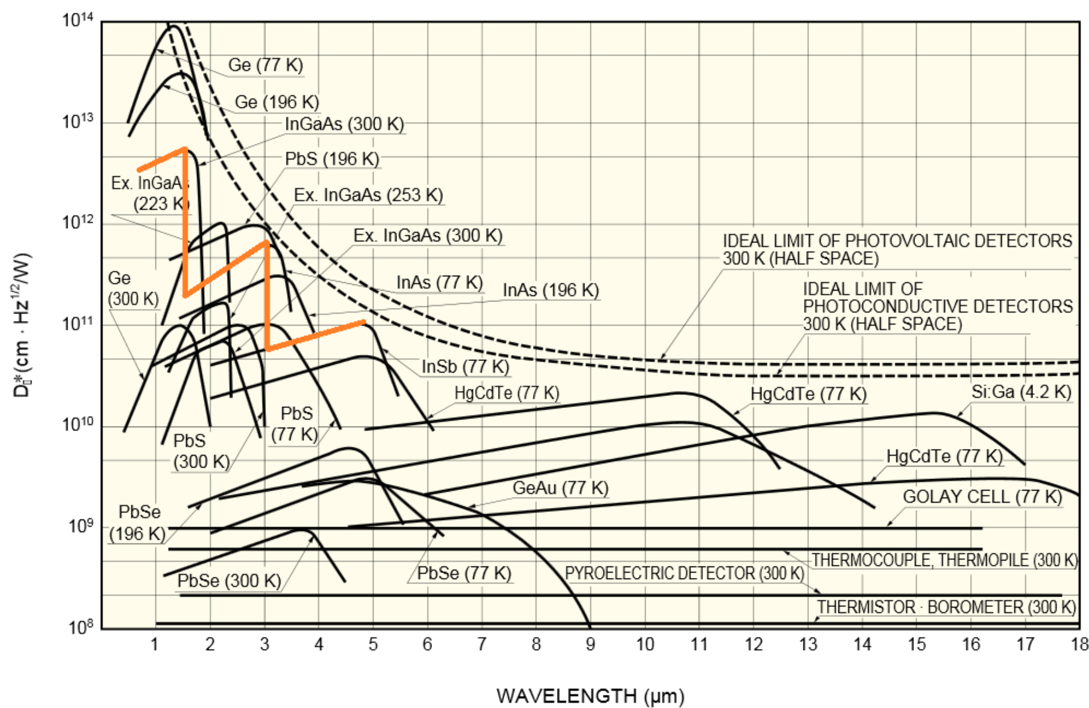

Figure 3.8: Specific detectivity of several photovoltaic and photoconductive detectors in dependence of the band gap, taken from the Hamamatsu Technical Handbook [84]. The possible wavelength range for detectors in the extended setup is highlighted in orange.

Chapter 4

Model for Excitation-dependent Photoluminescence

In the previous chapter, the main characteristics of several photoluminescence transitions are shown. Another important characterization method for the exciton, free-to-bound and donor-acceptor pair transition at low temperatures is the intensity dependence of the corresponding photoluminescence peaks with increasing (laser) excitation.

The results of the following theoretical and experimental parts are submitted for publication. In this chapter, a model for the description of excitation-dependent photoluminescence measurements will be derived. The understanding of the theoretical background for this characterization method will be used in Chapter 5 to discriminate acceptor and donor levels in different donor-acceptor pair transitions which is needed to derive the defect energy of deep donor and finally a conclusive defect model. Furthermore, the motivation for this study was an observed unusual superlinear increase of the photoluminescence intensity with excitation for donor-acceptor pair transitions. This behavior is in contradiction to the common belief in literature.

Excitation dependent photoluminescence measurements are often used as a tool to distinguish exciton, free-to-bound or donor-acceptor-pair transitions in semiconductors [85, 86, 87, 88, 73, 89, 90, 62, 91, 92]. The different transitions are generally identified by measuring the photoluminescence intensity in dependence of the laser power. In Ref. [85], a description of typical transitions with rate equations is given, as well as numerical simulations and experimental measurements on CdTe. It is shown, that the intensity of the photoluminescence transitions follows a power law behavior with $I_{\mathrm{PL}} \propto \phi^k$ in simplified cases, leading to a straight slope in a log-log plot. The excitation power density ϕ is varied over several orders of magnitude. The power law exponent k is between 1 and 2 for free- or bound-exciton transitions and below 1 for free-to-bound or donor-acceptor pair transitions. Whereas the model is valid for a broad range of measurements on semiconductors with shallow acceptors and/or shallow donors [85, 73, 90, 92], it can lead to erroneous results if deep level transitions are observed [89, 87].

Furthermore, for this deep level transitions, curved log-log plots with regions of a well defined linear and square root-like increase of the photoluminescence intensity can be observed (see e.g. Section 5.1.4). This lead to the motivation for a fundamental understanding of the involved processes and to the hypothesis of only discrete power law exponents having values of multiples of 1/2.

In the following it will be shown that the intensity of a shallow donor-acceptor pair transition increases superlinear, if deep recombination center are present. Only few pub-

lications exist for the analytical or numerical description of curved log-log plots and especially for excitation variations over more than two or three orders of magnitude [85, 86, 89, 88]. In Ref. [85, 86] the influence of deep defects is not included, whereas in Ref. [89] just one defect level deep in the gap is assumed. Here, a general model will be derived, which combines limiting cases of low and high excitation regimes and which describes the excitation dependence without numerical approximations. The model is applicable to all cases with and without any number of deep defect levels. The dependence of the power law exponents for the low and high excitation limit provides insights into the energy of discrete defects, the defect saturation and deep defect contributions.

In the first part, a theoretical description of the rate-equations is given for various situations with and without shallow and deep defects. A model function for curved log-log plots is derived in Section 4.2. Finally, the model is compared with numerical data from literature in Section 4.3. The verification of the model by experimental measurements is part of the defect spectroscopy on chalcopyrites in the subsequent chapters of the thesis.

4.1 Theoretical excitation dependence

In the following, a semiconductor with a shallow acceptor, a shallow donor and an additional deep donor-like recombination center will be considered. The schematic overview is given in Fig. 4.1. All considerations can be transferred to any combination of shallow or deep donors and acceptors. Generally, low temperatures will be assumed with negligible thermal activation of carriers into the bands. The steady-state excitation is expected to be low enough such that higher order effects like Auger-recombination, Fermi-levels inside the bands or stimulated emission can be neglected. Also excess carrier generation from defect absorption is not considered here. This process is negligible for excitation energies far above the band gap, which is the typical case in a photoluminescence experiment.

4.1.1 Rate equations and charge balance

In a photoluminescence experiment, electron hole pairs are generated at a rate G. This rate is proportional to the laser power density ϕ. Within 10^{-12} s the excess carriers relax to the band edges [35] and form a thermal distribution with the temperature of the lattice. After this process, transitions between the free carriers and defect levels will occur. An overview of possible transitions for the electrons is shown in Fig. 4.1 as an example. The rate of the transitions is proportional to the electron density in the first state n_i and the hole density (empty states) in the second state n_j with a transition coefficient c_{ij}. The rate equations are derived with the free electron (hole) concentration n (p), the density of neutral donors (occupied by electrons) N_{D}^0, the density of neutral deep defects (occupation by electrons) N_{S}^0 and the density of neutral acceptors (occupied with holes) N_{A}^0. The corresponding constant total defect densities are written without the superscript for the charge state e.g. $N_i = N_i^0 + N_i^{+/-}$ for single charge levels.

Since low temperatures are considered, the band-to-band transition (BB) is dominated by the free exciton transition (FX). Free and bound exciton transitions are labeled by FX and BX, respectively. Bound excitons will be briefly discussed in Section 4.1.6. If not stated otherwise, the exciton transition will be referred to free excitons, which can be treated the same way as band-to-band transitions. Both transitions are proportional to electron and hole concentrations in the band and energetic differences from the binding energy do not need to be considered here. The free carrier concentrations are the sum of

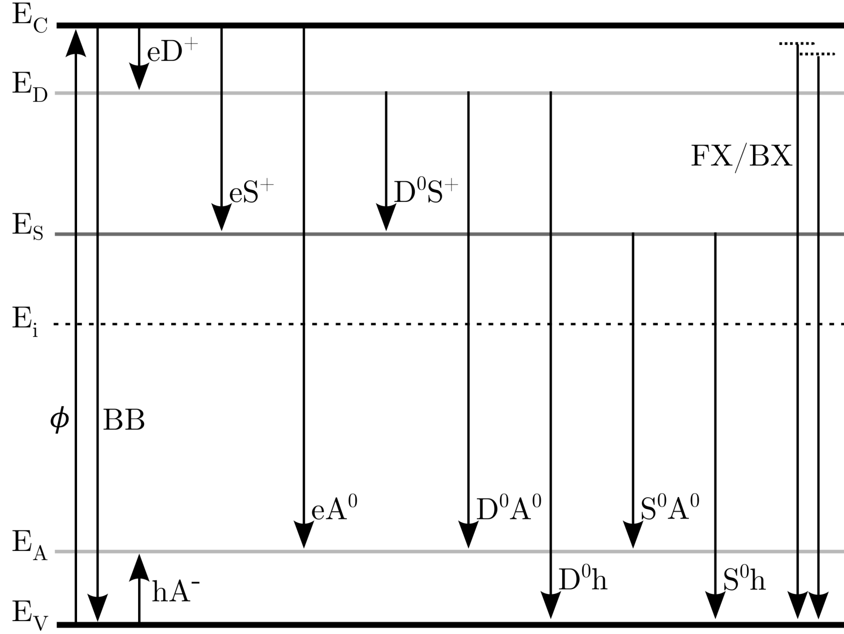

Figure 4.1: Band-diagram of transitions in a semiconductor with a shallow donor level at E_{D}, shallow acceptor level at E_{A} and a deep donor-like level at E_{S}. Free (FX)and bound (BX) exciton transitions are given with reference to the band-to-band (BB) transition. The conduction band minimum is labeled with E_{C}, the valence band maximum with E_{V} and the intrinsic Fermi level with E_{i}.

the equilibrium concentration n_0 and p_0 and the photogenerated excess carriers δn and δp with $n = n_0 + \delta n$ and $p = p_0 + \delta p$. At low enough temperatures, n_0 and p_0 are negligible over the excess carrier concentrations. For each state, the rate equations are given in the following equations (4.1) to (4.4).

$$\frac{\mathrm{d}n}{\mathrm{d}t} = \underbrace{c_\phi\, \phi}_{\text{generation}} - \underbrace{c_{\mathrm{nD}}\, n(N_{\mathrm{D}} - N_{\mathrm{D}}^0)}_{\text{e-capture (eD}^+)} - \underbrace{c_{\mathrm{nS}}\, n(N_{\mathrm{S}} - N_{\mathrm{S}}^0)}_{\text{e-capture (eS}^+)} - \underbrace{c_{\mathrm{nA}}\, nN_{\mathrm{A}}^0}_{\text{FB}_\mathrm{A}\text{ (eA}^0)} - \underbrace{c_{\mathrm{np}}\, np}_{\text{BB/FX}}, \tag{4.1}$$

$$\frac{\mathrm{d}N_{\mathrm{D}}^0}{\mathrm{d}t} = \underbrace{c_{\mathrm{nD}}\, n(N_{\mathrm{D}} - N_{\mathrm{D}}^0)}_{\text{e-capture (eD}^+)} - \underbrace{c_{\mathrm{DS}}\, N_{\mathrm{D}}^0(N_{\mathrm{S}} - N_{\mathrm{S}}^0)}_{\text{e-capture (D}^0\text{S}^+)} - \underbrace{c_{\mathrm{DA}}\, N_{\mathrm{D}}^0 N_{\mathrm{A}}^0}_{\text{DA (D}^0\text{A}^0)} - \underbrace{c_{\mathrm{Dp}}\, N_{\mathrm{D}}^0 p}_{\text{FB}_\mathrm{D}\text{ (D}^0\text{h)}}, \tag{4.2}$$

$$\frac{\mathrm{d}N_{\mathrm{A}}^0}{\mathrm{d}t} = \underbrace{c_{\mathrm{Ap}}\, p(N_{\mathrm{A}} - N_{\mathrm{A}}^0)}_{\text{h-capture (A}^-\text{h)}} - \underbrace{c_{\mathrm{DA}}\, N_{\mathrm{D}}^0 N_{\mathrm{A}}^0}_{\text{DA (D}^0\text{A}^0)} - \underbrace{c_{\mathrm{SA}}\, N_{\mathrm{S}}^0 N_{\mathrm{A}}^0}_{\text{SA (S}^0\text{A}^0)} - \underbrace{c_{\mathrm{nA}}\, nN_{\mathrm{A}}^0}_{\text{FB}_\mathrm{A}\text{ (eA}^0)}, \tag{4.3}$$

$$\frac{\mathrm{d}N_{\mathrm{S}}^0}{\mathrm{d}t} = \underbrace{c_{\mathrm{nS}}\, n(N_{\mathrm{S}} - N_{\mathrm{S}}^0)}_{\text{e-capture (eS}^+)} + \underbrace{c_{\mathrm{DS}}\, N_{\mathrm{D}}^0(N_{\mathrm{S}} - N_{\mathrm{S}}^0)}_{\text{e-capture (D}^0\text{S}^0)} - \underbrace{c_{\mathrm{SA}}\, N_{\mathrm{S}}^0 N_{\mathrm{A}}^0}_{\text{SA (S}^0\text{A}^0)} - \underbrace{c_{\mathrm{Sp}}\, N_{\mathrm{S}}^0 p}_{\text{FB}_\mathrm{S}\text{ (S}^0\text{h)}}\,. \tag{4.4}$$

Charge-neutrality is given by Eq. (4.5), assuming single charge levels for all defects:

$$n + N_{\mathrm{A}}^- = p + N_{\mathrm{D}}^+ + N_{\mathrm{S}}^+\,. \tag{4.5}$$

The different terms are labeled according to transitions from donor-to-acceptor (DA), deep donor-to-acceptor (SA) and free-to-bound (FB) with the subscript of the involved defect level. In steady-state the time derivative of the concentrations are zero and the

generation of carriers equals their recombination. Compared to the rate equations in Ref. [85] the terms for resonant formation of excitons are not included, because the focus will be just on the condition of above band gap excitation. Also explicit rate-equations for free excitons, given in Ref. [85], are not considered here. In steady state conditions they just contain the proportionality to the free electron and hole concentration ($\propto np$) and no additional information. This is already included in the transition labeled with BB/FX. Also the rate equation for free holes in the valence band is not needed since it does not contain additional terms.

Transitions with small energy differences like the electron-capture into the shallow donor and the hole-capture into the shallow acceptor are often non-radiative or usually not measured in standard photoluminescence experiments. The electron-capture by the deep defect level can be radiative but is in many cases outside the energy range of conventional experiments. Therefore, the focus is just on the analysis of transitions commonly detected in photoluminescence, such as exciton, free-to-bound and donor-acceptor pair transitions.

$$I_{\mathrm{FX}} \propto np \quad \Rightarrow \quad k_{\mathrm{FX}} = k_{\mathrm{n}} + k_{\mathrm{p}}, \tag{4.6}$$
$$I_{\mathrm{FB_D}} \propto N_{\mathrm{D}}^0 p \quad \Rightarrow \quad k_{\mathrm{FB_D}} = k_{\mathrm{D}} + k_{\mathrm{p}}, \tag{4.7}$$
$$I_{\mathrm{FB_S}} \propto N_{\mathrm{S}}^0 p \quad \Rightarrow \quad k_{\mathrm{FB_S}} = k_{\mathrm{S}} + k_{\mathrm{p}}, \tag{4.8}$$
$$I_{\mathrm{FB_A}} \propto n N_{\mathrm{A}}^0 \quad \Rightarrow \quad k_{\mathrm{FB_A}} = k_{\mathrm{n}} + k_{\mathrm{A}}, \tag{4.9}$$
$$I_{\mathrm{DA}} \propto N_{\mathrm{D}}^0 N_{\mathrm{A}}^0 \quad \Rightarrow \quad k_{\mathrm{DA}} = k_{\mathrm{D}} + k_{\mathrm{A}}, \tag{4.10}$$
$$I_{\mathrm{SA}} \propto N_{\mathrm{S}}^0 N_{\mathrm{A}}^0 \quad \Rightarrow \quad k_{\mathrm{SA}} = k_{\mathrm{S}} + k_{\mathrm{A}}\,. \tag{4.11}$$

For each transition the power law exponents are defined by $k_i = \mathrm{d}\log(I_i)/\mathrm{d}\log(\phi)$. As the rate of a transition depends linearly on the product of the charge densities of the two levels involved, the k-value of a transition is the sum of the k-values of the two charge densities. The k-value of a charge density N_i is defined as $k_i = \mathrm{d}\log(N_i)/\mathrm{d}\log(\phi)$. The recombination of a donor-acceptor pair, as an example, is proportional to the density of neutral donors and acceptors. In this case, the power law exponent k_{DA} is the sum of the k-values for each density with $k_{\mathrm{D}} = \mathrm{d}\log(N_{\mathrm{D}}^0)/\mathrm{d}\log(\phi)$ and $k_{\mathrm{A}} = \mathrm{d}\log(N_{\mathrm{A}}^0)/\mathrm{d}\log(\phi)$. The equations (4.6)–(4.11) give an overview of the link between these intensities with the carrier densities and the power law exponents.

The steady state excitation will be always considered. The labeling is in accordance with Ref. [85] but without the general condition of $n = p$. In certain cases e.g. when there is only one defect, the free hole concentration in the valence band will not equal the free electron concentration in the conduction band as will be shown in detail in the following. The carrier densities n and p will be treated separately, as well as the corresponding power law exponents k_{n} and k_{p}. The power law exponents will be discussed in low and high excitation conditions for different cases: the hypothetical defect free case, a semiconductor with one shallow defect, a semiconductor with one shallow donor and acceptor as well as the last case with a shallow donor/acceptor and one deep donor (recombination center).

4.1.2 Defect-free case

Assuming that there are no states in the band gap of the material, with $N_{\mathrm{D}} = N_{\mathrm{D}}^{0} = N_{\mathrm{A}} = N_{\mathrm{A}}^{0} = N_{\mathrm{S}} = N_{\mathrm{S}}^{0} = 0$, only Eq. (4.1) remains relevant and reduces to:

$$c_{\phi}\,\phi = c_{\mathrm{np}} np\,. \tag{4.12}$$

The product of the free electron concentration n and free hole concentration p is proportional to the excitation power density ϕ. From the charge balance in Eq. (4.5), the electron concentration equals the hole concentration, leading to $n^2 \propto \phi$ and $p^2 \propto \phi$. Thus, both concentrations increase proportional to $\phi^{1/2}$. The observed free exciton (or band-to-band transition equivalent) increases with a power law exponent of 1. This is summarized in Table 4.1.

Table 4.1: Power law exponents: defect-free

		(a)	(b)
Densities	Exponents		
n, p	k_{n}, k_{p}	1/2	1/2
Transitions		low ϕ	high ϕ
FX	k_{FX}	1	1

The excitation dependence can be fitted with a single power law. The same case is also valid if all defects in the material are saturated at high intensities (i.e. completely neutralized by excess carriers), so that $N_{\mathrm{D}} = N_{\mathrm{D}}^{0}$, $N_{\mathrm{A}} = N_{\mathrm{A}}^{0}$ and $N_{\mathrm{S}} = N_{\mathrm{S}}^{0}$. In this case also other transitions besides the exciton transition can be observed but their intensities would be constant with increasing excitation. It can be concluded that free exciton transitions as well as band-band transitions have k-values equal to 1 in the case where no electron or hole capture takes place. This value cannot be lower in general, since the band states cannot be saturated.

4.1.3 One shallow acceptor (donor)

In this case, the example of a semiconductor having just one shallow acceptor defect with the dopant density N_{A} will be given. Assuming one shallow donor in the material leads to equivalent results. The densities in the dark are given by $N_D = N_{\mathrm{D}}^{0} = N_{\mathrm{S}} = N_{\mathrm{S}}^{0} = 0$. At low excitation, nearly all excess electrons will be captured by the acceptor level, if its defect density is large compared to the photoinduced holes with $p \ll N_{\mathrm{A}}^{0}$. It is $N_{\mathrm{A}}^{0} \approx N_{\mathrm{A}}$, since low temperatures are considered. The intensity of the free exciton transition is very low in this case. Eq. (4.1) reduces to:

$$c_{\phi}\phi \approx c_{\mathrm{nA}} n N_{\mathrm{A}}^{0} \approx c_{\mathrm{nA}} n N_{\mathrm{A}}\,. \tag{4.13}$$

It follows that the concentration of free electrons n is proportional to the excitation power density ϕ at low excitation. The concentration in the band increases linearly with the excitation, unlike the previous case 4.1.2. The ionization of the defect level by excess electrons is balanced by the capture of free holes. This is given in Eq. (4.3) with:

$$c_{\mathrm{Ap}}(N_{\mathrm{A}} - N_{\mathrm{A}}^{0})p = c_{\mathrm{nA}} n N_{\mathrm{A}}^{0}\,. \tag{4.14}$$

And together with Eq. (4.13) reduces to:

$$c_{\mathrm{Ap}}(N_{\mathrm{A}} - N_{\mathrm{A}}^{0})p = c_{\mathrm{Ap}}N_{\mathrm{A}}^{-}p = c_{\phi}\phi\,. \tag{4.15}$$

If the excitation is low enough such that $n \ll N_{\mathrm{A}}^{-}$ is still valid, the charge balance in Eq. (4.5) leads to the condition $N_{\mathrm{A}}^{-} \approx p$. Inserting in Eq. (4.15) gives $p^2 \propto \phi$. Therefore, the hole concentration p is proportional to the square root of the excitation $\phi^{1/2}$.

The corresponding k-values are summarized in Table 4.2. The free exciton transition increases with $k_{\mathrm{FX}} = 3/2$ and the free-to-bound transition from the conduction band into the acceptor increases linearly with excitation[1].

Table 4.2: Power law exponents: One shallow acceptor

		(a)	(b)
Densities	Exponents	$N_{\mathrm{A}}^{0} \approx N_{\mathrm{A}}$	$N_{A}^{0} \approx 0$
n	k_{n}	1	1/2
p	k_{p}	1/2	1/2
N_{A}^{0}	k_{A}	0	0
Transitions		low ϕ	high ϕ
FX	k_{FX}	3/2	1
$\mathrm{FB_A}$	$k_{\mathrm{FB_A}}$	1	1/2

For highest excitation the acceptor level becomes completely filled with excess electrons and one obtains the same results as in the former defect-free case, since it is $N_{\mathrm{A}}^{0} \approx 0$ and $n = p \propto \phi^{1/2}$. However, now the free-to-bound transition can also be observed but will be increased only by excess electrons in the conduction band. From this it can be already concluded that the free-to-bound transitions have k-values larger or equal to 1/2. This is again due to the fact that the electron concentration in the conduction band increases at least with the square root of the excitation intensity. For an excitation between the two limiting cases of the low and high excitation regime a curved power law behavior is expected. This will be further described by the model presented in Section 4.2.

4.1.4 Donor and acceptor: compensated

In the compensated case nearly all donors and acceptors are ionized at low temperatures with $N_{\mathrm{D}} \approx N_{\mathrm{D}}^{+} \approx N_{\mathrm{A}} \approx N_{\mathrm{A}}^{-}$. There are no deep recombination center in this example with $N_{\mathrm{S}} = N_{\mathrm{S}}^{0} = 0$. In the dark, electrons from the donor sites compensate the holes from the acceptor sites.

For lowest excitation, the free carrier concentration is negligible compared to the concentration of ionized defects. The neutral defect densities are negligible compared to ionized ones and capture of electrons by the shallow donor level and capture of holes by the shallow acceptor level dominate. It is $p \ll N_{\mathrm{A}}^{0}$ and Eq. (4.1) can be simplified to:

$$c_{\phi}\,\phi \approx c_{\mathrm{nD}}nN_{\mathrm{D}}\,. \tag{4.16}$$

[1] Even at low temperatures there will be some thermally activated holes in the valence band. If the condition of $p_0 \gg \delta p$ would be valid for very low excitation intensities, the hole concentration would be constant and the free exciton transition would increase only linear. With increasing excitation, a changeover from $k = 1$ to $k = 3/2$ is the result. But this case is unlikely to be observed in experiment at e.g. $T = 10\,\mathrm{K}$.

Because the donor density N_D is independent of ϕ, it follows that the electron concentration n is proportional to ϕ. The charge balance provides $n = p$ and therefore the hole concentration p is also proportional to ϕ. The corresponding k-value for the free exciton or band-to-band transition is 2 with $k_{FX} = k_n + k_p$. Generally k-values above 2 are not observed[2]. This is due to the fact that the free carrier concentrations in the bands cannot increase superlinear with the excitation. They can only increase with a power law exponent of 1/2 or 1. Electrons e.g. can recombine most likely with free holes ($k_n = 1/2$) or they get most likely captured by defects ($k_n = 1$). Additional deep defects would simply also capture the electrons and it would still be $n \ll N_S^0$. Besides, Eq. (4.2) reduces to:

$$c_{nD} n N_D \approx c_{DA} N_D^0 N_A^0 \,. \tag{4.17}$$

The donor-acceptor pair transition increases proportionally to ϕ at low excitation, since it is $n \propto \phi$ from Eq. (4.16). The occupation of the donor with electrons N_D^0 as well as the occupation of the acceptor with holes N_A^0 increases with $\phi^{1/2}$. This is summarized in Table 4.3.

Table 4.3: Power law exponents: Donor and acceptor

Densities	Exponents	(a) $N_D^0 \approx 0$, $N_A^0 \approx 0$	(b) e.g. $N_A^0 = N_A$	(c) $N_D^0 \approx N_D$, $N_A^0 \approx N_A$
n	k_n	1	1	1/2
p	k_p	1	1/2	1/2
N_D^0	k_D	1/2	1/2	0
N_A^0	k_A	1/2	0	0
Transitions		low ϕ	mid ϕ	high ϕ
FX	k_{FX}	2	3/2	1
FB_D, FB_A	k_{FB_D}, k_{FB_A}	3/2	1	1/2
DA	k_{DA}	1	1/2	0

For highest excitation all donors and acceptors get completely neutralized by photogenerated carriers and the high excitation limit of the former examples is reached. The above transition of power law exponents from low to high excitation is observed, if the donor and acceptor levels saturate at the same excitation threshold. It is also likely that e.g. one of the two defect levels in the DA-transition saturates before the other, because the capture coefficients have a large difference or more shallow defect levels are present, while maintaining the compensation condition with $\sum N_A \approx \sum N_D$. Thus, an intermediate region will be observed. If e.g. the acceptor saturates before the donor (see Table 4.3), electrons still get captured by the donor and it is $k_D = 1/2$ and $k_n = 1$. But the hole capture by the acceptor can no longer increase, leading to $k_A = 0$ and $k_p = 1/2$. In comparison to the low excitation case, the k-values for the free exciton I_{FX} and the donor-acceptor pair transition I_{DA} get just reduced by 1/2 in the intermediate region and not by 1 like in the high excitation case.

[2] An exception are bound excitons, where the photoluminescence intensity is proportional to n, p and $N_{D/A}^0$.

4.1.5 Donor and acceptor with deep level: compensated

In the last example with an additional deep defect, the focus will be again on the condition of lowest excitation intensities first, so that $N_D^0 \ll N_D$, $N_A^0 \ll N_A$, $N_S^0 \ll N_S$ and $n, p \ll N_D, N_A, N_S$ is valid. If the defects are compensated with $N_A \approx N_D + N_S$, Eq. (4.1) reduces to:

$$c_\phi \phi = n(c_{nD}N_D + c_{nS}N_S)\,. \tag{4.18}$$

It follows that the free electron concentration is proportional to the excitation intensity and increases with $k_n = 1$. The same argument holds for the free hole concentration and it is $k_p = 1$. The rate equation for the donor in Eq. (4.2) simplifies to:

$$c_{nD}nN_D = N_D^0(c_{DS}N_S + c_{DA}N_A^0 + c_{Dp}p)\,. \tag{4.19}$$

If the defect density of the deep defect level is high enough, so that the condition $c_{DS}N_S \gg c_{DA}N_A^0 + c_{Dp}p$ is valid, most of the electrons fall into the deep defect before recombining with holes in the valence band or at the acceptor site. In this case, the density of occupied shallow donors N_D^0 increases also proportionally to the excitation intensity with $k_D = 1$, since it is $n \propto \phi$ from Eq. (4.18). The deep defect level captures most of the electrons which were first captured by the shallow donor site. Because most of the holes get captured by the shallow acceptor at the same time, the deep SA transition will dominate the photoluminescence spectrum at lowest excitation. Under these conditions, Eq. (4.4) reduces to:

$$c_{nS}nN_S = c_{SA}N_S^0N_A^0\,. \tag{4.20}$$

The left side is proportional to the electron concentration n which is proportional to ϕ from Eq. (4.18). Both densities N_S^0 and N_A^0 are proportional to $\phi^{1/2}$. There is no further capture level between E_S and E_A and the pair transition SA from the deep donor like level into the shallow acceptor increases linear with $k_{SA} = k_S + k_A = 1$.

Apart from this, the shallow DA-transition increases superlinearly, since it is $k_D = 1$ and $k_A = 1/2$ and therefore $k_{DA} = 3/2$. If one assumes a deep acceptor like level instead of a deep donor like level, the values of the power law exponents for k_n and k_p as well as for k_D and k_A would just be exchanged. It is important to mention that in the literature it is generally assumed that the donor-acceptor pair transition has power law exponents below or equal to 1[85]. But this is just valid if no effective capture state like a nearly empty deep defect exists between the two levels.

The value of k_D would reduce to 1/2, if the deep donor like defect does not exist or if it cannot capture more carriers (completely filled or too low capture coefficient). In this case the shallow donor-acceptor pair transition would dominate the spectrum and it is $k_D = 1/2$ like in Section 4.1.4. Therefore, the DA transition intensity increases with $k_{DA} = 1$ as a result. An overview of the power law exponents k is given in Table 4.4.

In this table, five different cases are considered for the defect saturation. From the lowest excitation case (a) with nearly empty defect levels ($N_i^0 \ll N_i$) to the highest excitation case (f) with full occupation of all defects ($N_i^0 \approx N_i$). The table is valid for a broad range of semiconductors since the absence of one of the defects can be treated in the same way as the fully occupied case. But then, obviously no transition would be observed in the spectrum, which involves the missing defect. Also adding another deep recombination center, which is assumed to be highly localized, does not change the results of Table 4.4. The transition between two highly localized levels (S_1 to S_2) is negligible. In

Table 4.4: Power law exponents: Donor, acceptor and deep level

	(a)	(b)	(c)	(d)	(e)	(f)
	$N_D^0 \ll N_D$ $N_S^0 \ll N_S$ $N_A^0 \ll N_A$	$N_D^0 \ll N_D$ $N_S^0 \approx N_S$ $N_A^0 \ll N_A$	$N_D^0 \ll N_D$ $N_S^0 \ll N_S$ $N_A^0 \approx N_A$	$N_D^0 \ll N_D$ $N_S^0 \approx N_S$ $N_A^0 \approx N_A$	$N_D^0 \approx N_D$ $N_S^0 \approx N_S$ $N_A^0 \ll N_A$	$N_D^0 \approx N_D$ $N_S^0 \approx N_S$ $N_A^0 \approx N_A$
k_n	1	1	1	1	1/2	1/2
k_p	1	1	1/2	1/2	1	1/2
k_D	1	1/2	1	1/2	0	0
k_A	1/2	1/2	0	0	1/2	0
k_S	1/2	1/2	1/2	0	0	0
	low ϕ	...	...	...	...	high ϕ
k_{FX}	2	2	3/2	3/2	3/2	1
k_{FB_D}	2	3/2	3/2	1	1	1/2
k_{FB_A}	3/2	3/2	1	1	1	1/2
k_{FB_S}	3/2	1	1	1/2	1	1/2
k_{DA}	3/2	1	1	1/2	1/2	0
k_{SA}	1	1/2	1/2	0	0	0

this situation one would obtain the same k-values for FB_{S_1} and FB_{S_2}, as well as for S_1A and S_2A. An example for this is given in Section 5.1.4 in Fig. 5.11. Furthermore, Table 4.4 can also be used if the deep defect would be acceptor like ($N_S^{0/-1}$), but the values of k_n and k_p as well as k_D and k_A would exchange.

In order to observe different cases of Table 4.4, it is necessary to vary the excitation power over more than 3 orders of magnitude in experiment. Superlinear power law exponents generally result from empty capture levels between the two states involved in the transition. If one level get saturated by excess carriers, the power law exponent observed at low excitation k_{low} gets reduced by 1/2 at high excitation with $k_{high} = k_{low} - 1/2$. Power law exponents of 1/2 or smaller can just be observed if one state is completely saturated.

4.1.6 Bound excitons

Bound excitons are not considered before in order to have a more compact overview of the power law exponents. In Ref. [85] it is assumed that bound excitons leave neutral donors (or acceptors) when recombining. Bound excitons not just depend on the free carrier concentration of free electrons and holes like in the case for free excitons. Their concentration is also proportional to the occupation of the defect to which the exciton is bound to:

$$I_{DX} \propto N_D^0 np \quad \Rightarrow \quad k_{DX} = k_D + k_n + k_p \tag{4.21}$$

$$I_{AX} \propto N_A^0 np \quad \Rightarrow \quad k_{AX} = k_A + k_n + k_p\,. \tag{4.22}$$

In the case of highest excitation, where the defect level of the bound exciton is nearly completely neutralized by excess carriers with $N_D^0 \approx N_D$ or $N_A^0 \approx N_A$ the excitation dependence of bound and free excitons is the same. But when the occupation of the

defect level is nearly empty and can increase with excitation, the power law exponent of the corresponding bound exciton can be higher than for the free exciton.

Besides an increase of the free carriers (increasing free exciton transition), the neutral defect sites increase at the same time. In most cases, when there is no dominant deeper defect present as in Ref. [85, 86], the shallow donor or acceptor occupation increases with a power law exponent of $k_{D/A} = 1/2$ in maximum. Thus, the bound exciton increases with $k_{\mathrm{DX/AX}} = 5/2$, whereas the free exciton increases just with $k_{\mathrm{FX}} = 4/2$ (see Eq. (4.21) and Eq. (4.22) and Table 4.3). It is important to know, that when one of the defects get saturated and the free exciton transition decreases from $k_{\mathrm{FX}} = 4/2$ to $k_{\mathrm{FX}} = 3/2$, the bound exciton transition decreases from $k_{\mathrm{DX/AX}} = 5/2$ to $k_{\mathrm{DX/AX}} = 3/2$ in the same excitation range. Therefore, the excitation dependent curvature of the bound exciton transition in the log-log plot is stronger compared to the free exciton (the slope decreases by 1 rather than 1/2). Both dependencies can be covered by the model in Section 4.2 and they are shown in Fig. 4.2.

4.2 Fitting curved log-log plots

From the discussion above, it is clear that in most cases a simple power law will not be observed over a wide range of excitation intensities. In general the dependence in the log-log plot will have a curvature, resulting from the transition between two limiting power law exponents. In this section a fitting function for these curved log-log plots will be given. If defect saturation occurs from an increasing excitation intensity, the effect is visible in experiment by a curvature of the photoluminescence intensity in a typical log-log plot. The case for two levels and with the saturation of only one level has been published in the scope of this thesis in Ref. [87]. The fitting function is derived by the multiplication of two Fermi functions, which describe the defect occupations. In a second step, the exponential terms are replaced by a power law.

$$I_{\mathrm{PL}} \propto f_1(\phi) f_2(\phi) \tag{4.23}$$

$$I_{\mathrm{PL}} \propto \frac{1}{\exp\left(\frac{E_1 - E_{\mathrm{F1}}(\phi)}{k_{\mathrm{B}}T}\right) + 1} \frac{1}{\exp\left(\frac{E_2 - E_{\mathrm{F2}}(\phi)}{k_{\mathrm{B}}T}\right) + 1} \tag{4.24}$$

$$I_{\mathrm{PL}} \propto \frac{1}{\left(\frac{\phi_1}{\phi}\right)^{k_1} + 1} \frac{1}{\left(\frac{\phi_2}{\phi}\right)^{k_2} + 1} \tag{4.25}$$

$$I_{\mathrm{PL}} \propto \frac{\phi^{k_1+k_2}}{1 + \left(\frac{\phi}{\phi_1}\right)^{k_1} + \left(\frac{\phi}{\phi_2}\right)^{k_2} + \left(\frac{\phi}{\phi_1}\right)^{k_1}\left(\frac{\phi}{\phi_2}\right)^{k_2}} . \tag{4.26}$$

A more general expression is given in Eq. (4.23) to (4.26) without the Boltzmann approximation for one of the involved levels. The photoluminescence intensity is proportional to the occupation function of the defects that influence the intensity by possible saturation, given in Eq. (4.23) (i.e. either the initial and/or final state or a state in between). A more detailed discussion is given in the appendix. The occupation is described by the Fermi function in Eq. (4.24). The step from Eq. (4.24) to Eq. (4.25) is done with the condition of $\frac{E_{\mathrm{F}}(\phi)}{k_{\mathrm{B}}T} = k \cdot \ln \phi + const.$, with the Fermi level E_{F}, the thermal energy $k_{\mathrm{B}}T$ and the power law exponent k. The constants ϕ_1 and ϕ_2 in Eq. (4.25) mark the excitation threshold at which the Fermi level of the defect crosses the defect level so that $E_{\mathrm{F}i} = E_i$.

For a donor-acceptor pair transition with no defect level in between, the Fermi functions f_1 and f_2 would describe the occupation of the donor and the occupation of the acceptor. But generally the photoluminescence can be determined by any two levels involved in the transition or interacting with those levels as it is obvious from the discussions in Section 4.1.

If e.g. the second state is far away from being saturated (e.g. the free carrier concentrations in a free-to-bound transition), the Boltzmann approximation is valid with $\phi_2 \gg \phi$.

The two last terms in the denominator in Eq. (4.26) vanish and it is:

$$I_{\mathrm{PL}} \propto \frac{\phi^{k_1+k_2}}{1+(\frac{\phi}{\phi_1})^{k_1}} = \frac{\phi^{k_{\mathrm{low}}}}{1+(\frac{\phi}{\phi_0})^{k_{\mathrm{low}}-k_{\mathrm{high}}}} \,. \tag{4.27}$$

This equation can be used to fit a single curvature with the turning point at ϕ_0. For low excitation ($\phi \ll \phi_0$) the power law exponent converges to $k = k_{\mathrm{low}}$. For high excitation with $\phi \gg \phi_0$ the 1 in the denominator can be neglected and the power law exponent converges to $k = k_{\mathrm{low}} - (k_{\mathrm{low}} - k_{\mathrm{high}}) = k_{\mathrm{high}}$. Eq. (4.27) describes most experimental situations, where a curved log-log plot is observed. Eq. (4.26), however, describes also situations where two kinks in the log-log plot are observed. An example will be discussed in the next section.

It is also possible that no saturation of the involved states in the photoluminscence transition occurs and that no additional capture state in between gets saturated in the observed measurement range. Under these conditions no discrimination between low and high excitation regimes exist with $\phi_1, \phi_2 \gg \phi$ in Eq. (4.26). One obtains directly a single power law:

$$I_{\mathrm{PL}} \propto \phi^{k_1+k_2} = \phi^k \,. \tag{4.28}$$

In order to give an example, one acceptor level at low temperatures is assumed. For the free exciton transition I_{FX}, the following values for the power law exponents k_{FX} have to be inserted into Eq. (4.27): $k_{\mathrm{low}} = 3/2$ and $k_{\mathrm{high}} = 1$. This corresponds to the last two columns in Table 4.4 or to the low and high excitation case in Table 4.2. The photoluminescence intensity can be described by:

$$\text{example:} \quad I_{\mathrm{FX}} \propto \frac{\phi^{3/2}}{1+(\frac{\phi}{\phi_0})^{1/2}} \,. \tag{4.29}$$

For an arbitrary amplitude, the threshold ϕ_0 is the only free fitting parameter in Eq. (4.29), which marks the turning point in the curved log-log plot. This turning point is in between the low and high excitation regimes and corresponds to the excitation density which is needed to have the same density of occupied and unoccupied states (occupation is 1/2). But if the excitation intensity is just varied in a narrow range (less than 3 orders of magnitude) and around the transition point, any forced fit of a single power law would lead to k-values between 1 and 3/2. This approach can be often found in literature. In this case the value of k is strongly depended on the chosen range of excitation. Often observed single power laws could be a result of narrow excitation variations where the curvature is not clearly visible. Several examples will be given in the following section, where the fitting functions of Eq. (4.26) and Eq. (4.27) are applied to data from literature. Furthermore, the model function is applied to the experimental data in the next chapters of this thesis.

Extended fitting function

In the previous part, the simple case of a donor-acceptor pair recombination is given, where the Fermi-functions f_1 and f_2 correspond to the occupation of the donor and the occupation of the acceptor. Eq. (4.26) can be used generally for two levels, but changes slightly if more levels (e.g. one defect in between the two levels, which can capture carriers) are involved. The unlikely case where 3 different saturation processes are observed will not be shown (e.g. first the deep level saturates, than the acceptor and then the donor). But if only the saturation of two defects is observed, the occupation of the third one can be described with the Boltzmann distribution and Eq. (4.26) changes to:

$$I_{\mathrm{PL}} \propto \frac{\phi^{k_1+k_2}\phi^{k_{\mathrm{const.}}}}{1+(\frac{\phi}{\phi_1})^{k_1}+(\frac{\phi}{\phi_2})^{k_2}+(\frac{\phi}{\phi_1})^{k_1}(\frac{\phi}{\phi_2})^{k_2}}\,. \tag{4.30}$$

In this case all observed slopes in the log-log plot are just increased by a constant value $k_{\mathrm{const.}}$ (which is a multiple of 1/2). Furthermore, for the highest excitation ($\phi \gg \phi_1, \phi_2$) the photoluminescence intensity does not saturate ($k = 0$) but increases proportional to $\phi^{k_{\mathrm{const.}}}$. An example is the donor-acceptor pair transition mentioned before, where a deep level in between saturates (ϕ_1), than the acceptor (ϕ_2) saturates, but not the donor level ($\phi_3 \gg \phi$). This corresponds to the changeover from case (a) to case (b) to case (d) in Table 4.4. The fitting function can be extended for all cases discussed in Section 4.1. If e.g. the free exciton transition is observed together with empty donor and acceptor levels which can become saturated, one can use the following function:

$$I_{\mathrm{FX}} \propto \frac{\phi^{k_1+k_2}\phi^{1/2}\phi^{1/2}}{1+(\frac{\phi}{\phi_1})^{k_1}+(\frac{\phi}{\phi_2})^{k_2}+(\frac{\phi}{\phi_1})^{k_1}(\frac{\phi}{\phi_2})^{k_2}}\,. \tag{4.31}$$

Again, Eq. (4.26) describes the occupation of the donor and the acceptor, but the equation gets extended by some additional power laws $\phi^{1/2}\phi^{1/2} = \phi^1$, which correspond to the not saturating concentration of free carriers in the conduction band and in the valence band. In the resulting Eq. (4.31), all observed k-values are increased by 1 and the high excitation limit is a linear increase with ϕ^1. For a free-to-bound transition, one of the $\phi^{1/2}$ terms just needs to be removed in Eq. (4.31) (just one band involved).

4.3 Testing of the model

In this section it will be shown that the model can be applied to simulations and data from the literature. The model will be tested in comparison to a priori known power law exponents from numerical solutions. The application for experimental data of chalcopyrite thin films will be part of the following results Chapter 5.

First example with data from literature

In Fig. 4.2 the data points are taken from Ref. [86], which were obtained by numerically solving the rate equations. Without the need for numerical solutions, several conclusions can be drawn directly from the model.

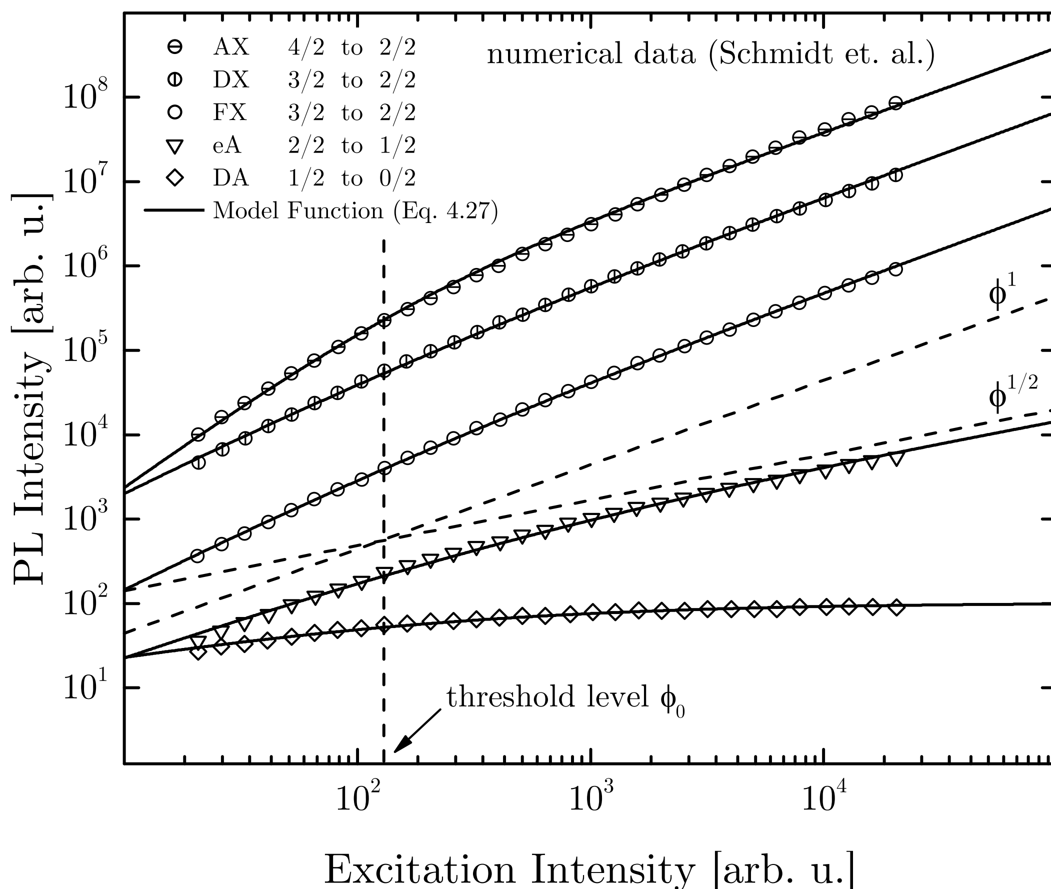

Figure 4.2: Data from numerical solutions of the rate-equations given in Ref. [86]. The data from Ref. [86] describes the experimental measurements on expitaxial CdTe in Ref. [85]. All excitation-intensity dependencies are fitted with Eq. (4.27) and the used fitting parameters are given in the 4.3. Single power laws are shown for comparison with dotted lines.

For low, as well as for high excitation, straight lines with power law exponents of multiples of 1/2 describe the data reasonably. For the lowest curve (diamonds), which is according to Ref. [86] the donor-acceptor pair transition, the power law exponent changes from $k_{\mathrm{DA}} = 1/2$ to constant. This already indicates that the acceptor and the donor are completely saturated at the highest intensities. Just one of the two is already saturated at the lowest intensities, which results in an exponent of $k_{\mathrm{DA}} = 1/2$ rather than $k_{\mathrm{DA}} = 1$

(see Table 4.4). If just the donor-acceptor pair transition would be known, one cannot distinguish if the donor or the acceptor is the saturating defect at the threshold level.

The triangles show the excitation dependence of the free-to-bound transition into the acceptor. At low excitation the single power law corresponds to $k_{\mathrm{FB_A}} = 1$ and becomes $k_{\mathrm{FB_A}} = 1/2$ at high excitation.

The observed excitation dependencies can be already attributed, using Table 4.4, to case (d) or (e) at low excitation and case (f) at high excitation. From this table, it can be directly concluded that the free exciton transition has to change from $k = 3/2$ to $k = 1$ since it plays no role if the acceptor or the donor gets saturated. The curvature of the free exciton transition in Fig. 4.2 confirms the predictions.

But it is still not clear which defect saturates. If the donor level rather than the acceptor level is fully occupied in the whole excitation range, the slope and the curvature of the corresponding bound exciton (DX) will be the same as for the free exciton. The reason for this is given in Eq. (4.21) with the condition $N_{\mathrm{D}}^{0} \approx N_{\mathrm{D}}$ (const.). This behavior is valid for the DX transition in Fig. 4.2. It can be concluded that case (e) from Table 4.4 is observed at low excitation and case (f) at high excitation. The acceptor and not the donor becomes saturated at the transition point.

The last missing intensity dependence, which is the AX transition, is already known by the behavior of the other ones. Compared to the free and donor-bound exciton, the k-value of the acceptor-bound exciton has to be higher by a factor of 1/2 for low excitation (see Section 4.1.6), since the acceptor level is not fully occupied. For high excitation it also approaches the linear dependence like the FX and DX transition. This example from literature shows that the excitation dependence of all transitions can be divided into several single power law exponents of multiples of 1/2. Furthermore it is possible to obtain a full understanding of the defect model and the defect saturation from the low and high excitation limit of the power law exponents. All data points in Fig. 4.2 can be well fitted with Eq. (4.27) and the used fitting parameters are given in the Appendix 4.3. Since the inserted k-values (restricted to multiples of 1/2) for the low and high excitation limit are known from the plot, the only free fitting parameters are an arbitrary amplitude and the threshold level ϕ_0. For all transition, the obtained values for ϕ_0 are between 60 and 330 and the average value is shown in Fig. 4.2.

Second example with data from literature

In the second example with literature data, the excitation dependence of yellow luminescence from undoped GaN at room temperature in Fig. 4.3 will be discussed, taken from Ref. [88]. From the reference, the experimental data points are shown together with the numerical solution of the rate equations by the authors. But instead of using 8 different parameters, the curve can be fitted with Eq. (4.26), by using fixed k-values of 1/2 and just two free parameters ϕ_1 and ϕ_2 for the turning points. The derived fit function (solid line) is in good agreement with the numerical solution in Ref. [88] (dashed line).

Single power laws correspond to $k = 1$ in the low excitation region ($\phi \ll \phi_1$, $k_{\mathrm{low}} = k_1 + k_2$), $k = 1/2$ in the intermediate region ($\phi_1 \ll \phi \ll \phi_2$, $k_{\mathrm{mid}} = k_2$) and $k = 0$ in the high excitation region ($\phi \gg \phi_2$). From the two threshold points one can assume that one defect gets completely filled by the excitation threshold ϕ_1 and a second one by ϕ_2. But since this measurement is done at room temperature, threshold levels with changing power law exponents can also occur when increasing excitation leads to a higher excess carrier concentration than the free carrier concentration (e.g. for n-type $\delta n \gg n_0$). This is usually referred to low and high injection conditions at room temperature.

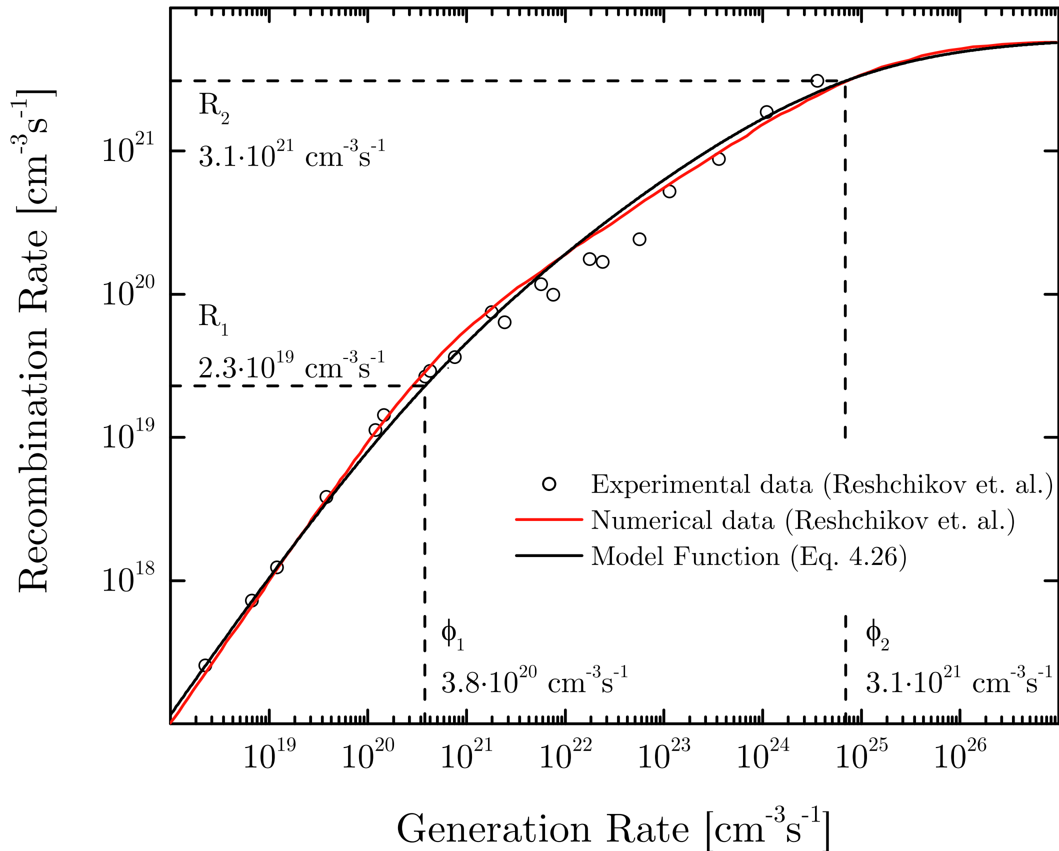

Figure 4.3: The photoluminescence intensity of the deep yellow luminescence from undoped GaN in dependence of the excitation intensity at 295 K (red line, taken from Ref. [88]). The authors fitted the experimental data (circles) numerically by inserting 8 different parameters into the rate equations. The analytical solution by fitting Eq. (4.26) is shown in black. Apart from an amplitude, the only fitting parameters used are the threshold levels ϕ_1 and ϕ_2, while the power law exponents are fixed with $k_1 = k_2 = 1/2$. The x-axis is given in absolute units of the generation rate of excess carriers and the y-axis is given in absolute units of the recombination rate of the photoluminescence transition.

The recombination rates at the fitted threshold levels in Fig. 4.3 are $R_1(\phi_1) = 2.3 \times 10^{19}\,\mathrm{cm^{-3}\,s^{-1}}$ and $R_2(\phi_2) = 3.1 \times 10^{21}\,\mathrm{cm^{-3}\,s^{-1}}$. From Ref. [88], the lifetime of the shown yellow luminescence from undoped GaN is known with $\tau_{\mathrm{YL}} = 52\,\mu$s. One can assume that the shown transition is just radiative, because its photoluminescence intensity in Ref. [88] remains almost constant from 10 K to 400 K. A simple relation for the recombination rate and a defect or carrier density is given by $R_i = \frac{N_i}{\tau}$. Inserting the values for R_1 and R_2 yields $N_1 = 1.1 \times 10^{15}\,\mathrm{cm^{-3}}$ and $N_2 = 1.6 \times 10^{17}\,\mathrm{cm^{-3}}$. Since the threshold levels ϕ_1 and ϕ_2 determine the generation rate at which the Fermi level equals the defect level, the corresponding occupation is 1/2. The values N_1 and N_2 have to be doubled in order to obtain the corresponding defect concentrations. The first value $N_1 = 2.2 \times 10^{15}\,\mathrm{cm^{-3}}$ is close to the acceptor concentration $N_{\mathrm{A}} = 5 \times 10^{15}\,\mathrm{cm^{-3}}$ and the second value $N_2 = 3.2 \times 10^{17}\,\mathrm{cm^{-3}}$ is close to the free carrier concentration $n_0 = 1.7 \times 10^{17}\,\mathrm{cm^{-3}}$, which both were used in Ref. [88] for the numerical fit in Fig. 4.3. The authors argue that the first change of slope appears due to the saturation of the acceptor N_{A} . Furthermore they argue that the excess electrons δn exceed the free carrier concentration n_0 when the photoluminescence intensity saturates (second change of slope). The second turning point is not observed in experiment but in theory.

This conclusions show that it is possible to determine defect or free carrier concentrations from the fitted threshold levels if the experiments are done with calibrated fluxes and if the photoluminescence lifetimes are known by time-resolved measurements. Curved log-log plots can be well described by the power law exponents from theoretical predictions of Section 4.1. Taking into account the power law exponents at low and high excitation from all observed photoluminescence transitions can be used to get further insights of the involved defect model as well as the involved defect saturation. Curvatures can be fitted according to the model functions of Section 4.2. Whereas Eq. (4.26) is more general, Eq. (4.27) can be used in most cases were just one change in slope is observed. Furthermore, the resulting threshold levels can be used to quantify involved defect or carrier concentrations.

Fitting parameters

In Table 4.5 the used fitting parameters for the model function Eq. (4.27) in Fig. 4.2 are given. The used k-values in the low and high excitation regime are fixed. Their value, consisting of multiples of $n/2$, is known by fitting a single power law to the lowest (k_{low}) and the highest (k_{high}) data points. The arbitrary amplitude and the threshold level ϕ_0 are free fitting parameters.

Table 4.5: Parameter used for the fitting of the numerical data in Fig. 4.2 (Schmidt et. al.[86]) with Eq. (4.27)

	ϕ_0(variable)	k_{low}	k_{high}
AX	154 ± 7	2	1
DX	60 ± 7	3/2	1
FX	64 ± 4	3/2	1
$\mathrm{FB_A}$	331 ± 43	1	1/2
DA	119 ± 9	1/2	0
avg.	130		

Table 4.6: Parameter used for the fitting of the numerical data in Fig. 4.2 (Schmidt et. al.[86]) with Eq. (4.30)

	ϕ_1 (variable)	ϕ_2	k_1	k_2	$k_{\mathrm{const.}}$
AX	154 ± 7	≈ 0	1	0	1
DX	60 ± 7	≈ 0	1/2	0	1
FX	64 ± 4	≈ 0	1/2	0	1
$\mathrm{FB_A}$	331 ± 43	≈ 0	1/2	0	1/2
DA	119 ± 9	≈ 0	1/2	0	0
avg.	130 ± 102				

The same fits and threshold levels can be obtained by using Eq. (4.30) together with the fitting parameters in Table 4.6. In this form it is visualized that the k_2-value corresponds to the completely filled donor level (no increase with $k_2 = k_{\mathrm{D}} = 0$ and no threshold level $C_2 \approx 0$), the k_1-value corresponds to the saturating acceptor level and the $k_{\mathrm{const.}}$-value is determined from the bands involved in the transition (0 – no band involved, 1/2 – conduction band involved which cannot saturate, 1 – conduction and valence band involved which cannot saturate).

Just for the AX transition (acceptor-bound exciton) the k_1-value is higher, because the concentration of free holes and the concentration of neutral acceptors are contributing to the intensity (see Section 4.1.6). From the low- to the high-excitation regime, the k_{A}-value of the acceptor decreases from 1/2 to 0 and at the same time the k_{p}-value for the free holes decreases from 1 to 1/2. This process causes the k-value of the AX transition to decrease by 1 ($= k_1$) instead of 1/2 as for the other transitions.

Chapter 5

Defect Band at 1.1 eV

In this chapter, the first part of the experimental results of photoluminescence spectroscopy on the epitaxially grown chalcopyrite thin films will be shown and discussed. The focus of this chapter is on the findings of deep photoluminescence bands around 1.1–1.2 eV in $CuGaSe_2$ and $Cu(In,Ga)Se_2$ with high gallium contents. In the first Section 5.1, a detailed study of these transitions will be given for indium-free $CuGaSe_2$. The crystal quality of the Cu-rich composition is characterized by XRD, Hall and PL measurements. By applying the derived model from the former chapter, intensity dependent measurements confirm that two deep defect bands originate from the recombination of electrons from two deep donor-like defects S1 and S2 into the same shallow acceptor A2 at 100 meV. This is supported by temperature dependent measurements.

Based on these results, the deep defects will be studied for different $Cu(In,Ga)Se_2$ compositions in the second Section 5.2. Starting with small additions of Indium, the energy level of the dominating deep defect S2 will be determined at 1.33 eV by using models for electron-phonon coupling. Furthermore, the Ga/(Ga+In) ratio in the samples will be lowered until the ternary $CuInSe_2$ is reached. It turns out that the deep level S2 remains almost constant with respect to the valence band. This characteristic leads to the appearance of a deep recombination center in wide-gap $Cu(In,Ga)Se_2$ and a less harmful shallow defect for compositions with low gallium content (GGI < 0.45). The influence of the deep recombination center on the electronic properties of solar cells will be supported by SCAPS simulations and compared to literature data of the open circuit voltage. A complete defect model is discussed in depth in Chapter 7.

5.1 Defect spectroscopy on $CuGaSe_2$

In this section, Cu-rich $CuGaSe_2$ thin films with high crystal quality are investigated in detail. First of all, a motivation for the choice of Cu-rich compositions is given by means of XRD measurements, as well as a comparison of the shallow defect luminescence with already known literature. Samples with highest crystal quality are chosen for a full study of excitation-dependent and temperature-dependent photoluminescence measurements. The model derived for excitation-dependent photoluminescence intensities in Chapter 4 will be applied to distinguish the defect levels in the deep transitions. In combination with the excitation-dependent energy position of the peaks, the involved shallow levels for all observed transitions are determined. Two deep donor-like levels and one common shallow acceptor are responsible for the observed deep bands. At the end of this section, temperature dependent measurements will at least support these findings, including

brief discussions of difficulties and erroneous activation energies, which are obtained by conventional characterization of the thermal quenching.

5.1.1 Crystal quality of Cu-rich $CuGaSe_2$

In general, it is necessary that several conditions are fulfilled in order to allow for undisturbed studies of discrete defect levels in a semiconductor by photoluminescence. For example, polycrystalline thin films of Cu(In,Ga)Se_2 with a deficit of copper may give the highest efficiencies in completed solar cell devices, but they are not well suited for defect spectroscopy by photoluminescence. An examplary list of necessary conditions is given in the following:

1. High monocrystalline quality:
   High crystal quality is often linked to the observation of exciton transitions and narrow peak width of the near band edge luminescence [93, 94]. This leads to further information from e.g. characterization of the intensity dependence of the exciton (see chapter 4) and better resolved lines. Polycrystalline thin films can lead to compositional fluctuations of different grains and additional defect states could be induced by grain boundaries [95]. Therefore monocrystalline thin films from epitaxial growth are preferred in the first place.

2. Absence of electrostatic fluctuations:
   A high degree of compensating donor and acceptor defects can lead to local accumulation of charges and therefore to local fluctuations of the potential. This results in an unwanted shift of defect transitions to lower energies and a strong broadening, which makes precise characterizations more difficult and generally even impossible [44, 96].

3. Absence of alloy disorder:
   One would expect the high monocrystalline quality to ensure the absence of compositional fluctuations. In the case of e.g. the solid solution Cu(In,Ga)Se_2, crystals with high quality and homogenous composition can be grown. But nevertheless, possible local interchanges of gallium and indium atoms usually lead to a broadening of the observed peaks compared to the ternary counterparts of $CuInSe_2$ and $CuGaSe_2$ [97, 98]. Furthermore, the ternary structures alone have less possible intrinsic defects than the solid solutions which simplifies the fundamental defect studies.

4. Absence of interference effects:
   Just recently more attention was put on the interference effects in photoluminescence measurements of chalcopyrite thin films [99]. If the film thickness is in the same range as the measured wavelength of the emitted photoluminescence light, it can be difficult to distinguish interference fringes from defect transitions [82]. Furthermore it is not straight forward to correct the disturbed spectra, especially at low temperatures.

In order to ensure the absence of potential and compositional fluctuations of the second and the third point, epitaxial thin films were grown under Cu-rich conditions. This results in stoichiometric compositions with a Cu_2Se phase on the top of the layer (see section 1.1.2). From literature it is known, that no potential fluctuations occur in Cu-rich grown

material [10]. It was already shown in Fig. 1.8 that it is possible to observe distinct shallow defect and excitonic transitions in $CuInSe_2$ and $CuGaSe_2$ in that case. If the Cu-content is approximately above approx. 1.1, the DA2 transition will dominate and the spectra of the near-band-edge luminescence remains almost constant with further increase of the Cu/III ratio. This behavior will be used in the following. Samples of Cu-rich (Cu/III ratio above 1.1) $CuGaSe_2$ are studied in detail and will be used as a starting reference throughout the thesis.

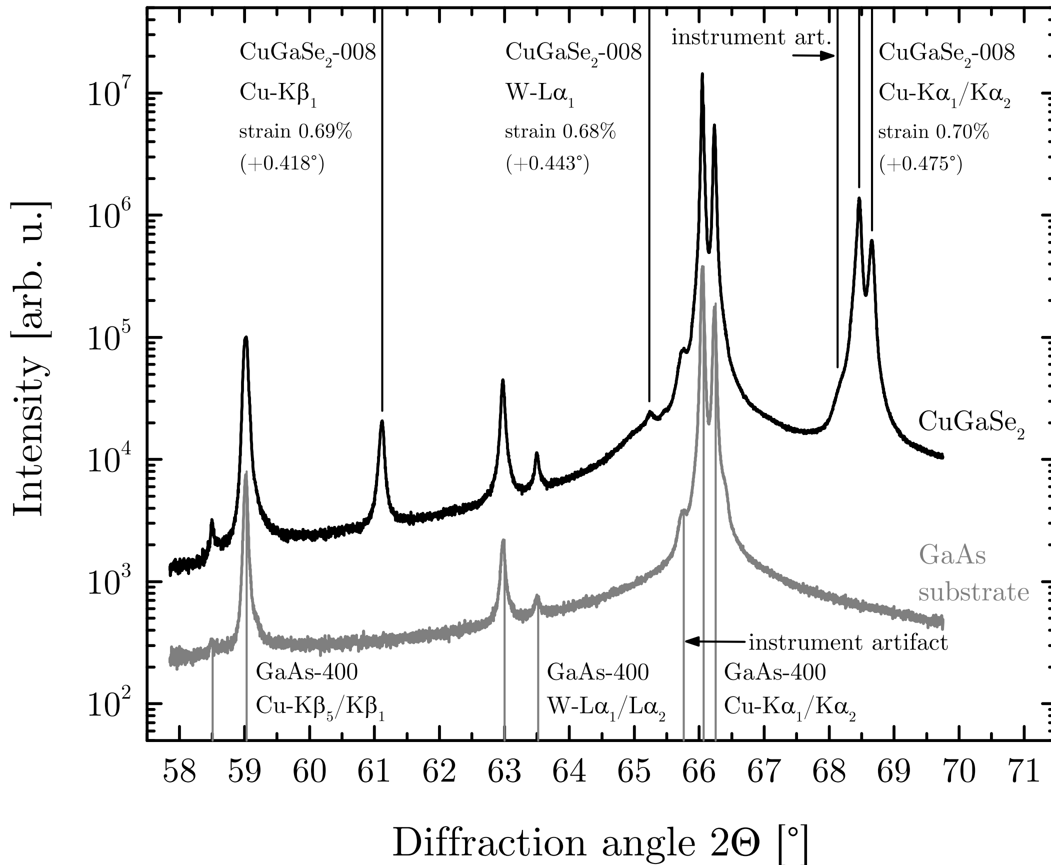

Figure 5.1: XRD diffractogram of sample CGSe-226 and the GaAs-substrate shifted in intensity for better comparison. Diffraction lines are labeled by the (hkl)-planes as well as the involved X-ray lines from the source. Strain is exemplary expressed by the relative peak shift compared to the powder reference. (powder-reference: $CuGaSe_2$ 01-076-1735, GaAs 00-014-0450 from PDF-4+ 2016 database of ICCD, source-reference: NIST X-ray Transition Energies Database Version 1.2 [100])

The high crystal quality and the epitaxial growth without secondary phases is verified by XRD measurements. In Fig. 5.1, the XRD diffractograms of sample CGSe-226 and the bare GaAs-substrate are shown. Measurements by EDX (10 kV, with no signal from the substrate) yield a Cu-content of Cu/III = 1.22 for this sample and the near-band-edge luminescence at low temperatures is in accordance with the literature. In the XRD diffractograms, clearly the GaAs-(400) and $CuGaSe_2$-(008) reflections dominate. Due to the X-ray copper source and its contamination with tungsten (aging effect), lines from Cu-$K_{\alpha1,\alpha2}$, Cu-$K_{\beta1,\beta5}$ and W-$L_{\alpha1,\alpha2}$ can be detected. A small shoulder just before the reflections from the Cu-$K_{\alpha1}$ line is of unknown origin. Because this shoulder is visible close to the GaAs-(400), as well as the $CuGaSe_2$-(008) reflection, it will be referred to

an instrument artifact which was also observed in measurements in the past [52, 43]. No other phases are detected in the measured range.

Due to a lattice mismatch, the reflections of $CuGaSe_2$ are shifted to higher angles when compared to the power references. The strain in Fig. 5.1 is simply expressed by the relative change of the diffraction angle compared to the powder reference. The angular shift increases with higher angles, whereas the relative value remains almost constant around $0.7 \pm 0.02\,\%$. The strain mostly originates from tensile thermal stress during the postgrowth cooling, since the thermal expansion coefficient in $CuGaSe_2$ is higher than in GaAs [101, 102, 103]. But this will not significantly affect the shape of the studied photoluminescence spectra. Former results in literature have shown that the band gap energy, the exciton emission and the near-band-edge luminescence shift equally in energy [104]. But one has to keep in mind that due to the strain, the apparent band gap can be lowered by a few meV [30].

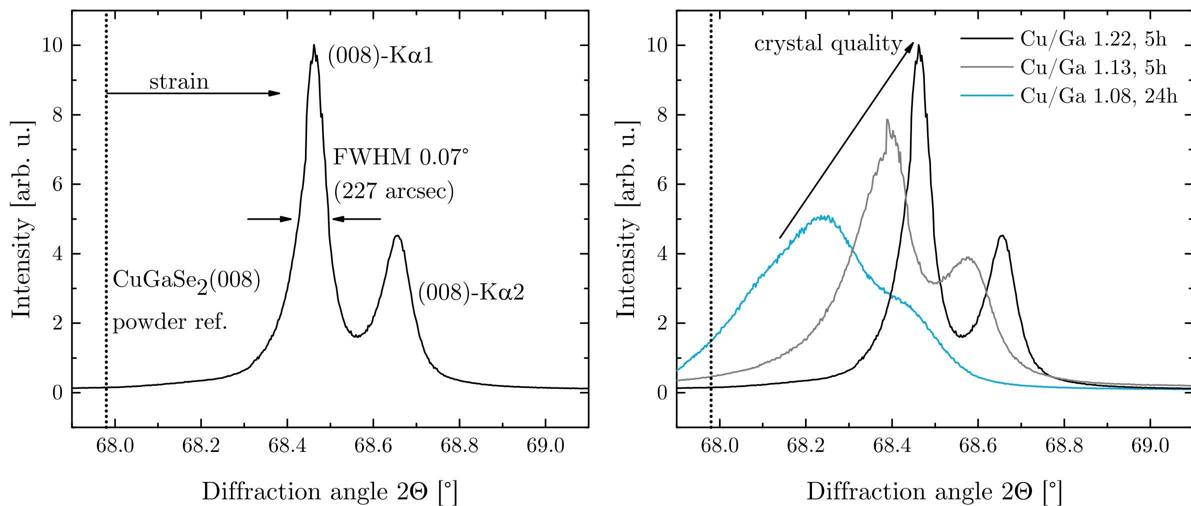

Figure 5.2: XRD diffractograms of (left) the $CuGaSe_2$-(008) reflection of sample CGSe-226 and (right) in comparison with lower Cu-content and longer process duration. (grey line, powder-reference: 01-076-1735 from PDF-4+ 2016 database of ICCD)

On the left side in Fig. 5.2, the $CuGaSe_2$-(008) reflection is shown in detail. The FWHM (full width at half maximum) of the strongest Cu-$K_{\alpha 1}$ line is at 227 arcsec, which suggests a high crystal quality. The GaAs-(004) reflection has a peak width of 108 arcsec, which indicates that the instrument resolution is equal or lower than this value. Thus the FWHM of the $CuGaSe_2$ reflection can be determined without the need for deconvolution.

On the right side of Fig. 5.2, two more $CuGaSe_2$ thin films with lower Cu-content and equal or longer growth duration are shown for comparison. The crystal quality seems to decrease if the film thickness is much higher for a long growth processes (approx. 120 nm per hour). On the other hand, the higher film thickness results in less strain which is indicated by a shift of the Bragg reflections towards the literature value of the powder reference. Nevertheless, higher crystal qualities are preferred over negligible small influences of the strain on the following spectroscopic measurements. Reasons for the lowered crystal quality with a lower measured copper content remain unknown, but the recipe yielding the highest crystal quality was used for growth of the $CuGaSe_2$-228 reference sample in the following part 5.1.2.

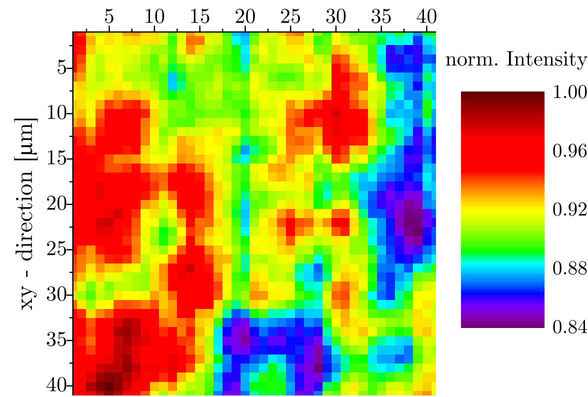

Figure 5.3: Spatially resolved integrated photoluminescence intensity of sample CGSe-226 at 10 K with a resolution of 1 μm.

In order to verify the high lateral homogeneity of the growth process, spatially resolved integrated photoluminescence is shown in Fig. 5.3 for sample CGSe-226 (measured by Max Wolter) with a spatial resolution of approx. 1 μm. The maximum intensity is only reduced by a factor of 0.84 at the lowest points. This factor is negligible and implies a very high homogeneity of the epitaxial film [43]. Based on all the former results, the $CuGaSe_2$ reference sample for extensive studies by photoluminescence spectroscopy is introduced and characterized in the following part.

5.1.2 $CuGaSe_2$ reference sample

The same recipe as the one of sample CGSe-226 was used for sample CGSe-228 in order to guarantee the highest crystal quality. The growth duration of 5 hours resulted in 620 nm film thickness. The photoluminescence spectrum down to 0.85 eV and measured at 10 K, is given in Fig. 5.4. The peak at 1.709 eV is attributed to an exciton-transition. No intensity dependent peak shift can be observed and the intensity increases nearly quadratic with the laser power (see Section 5.1.3 and 5.1.4). By adding the exciton binding energy of 13 meV [71], the low temperature band gap is estimated to be $E_g = 1.722$ eV. The band gap is slightly lower than expected for a single crystal due to the strain mentioned earlier [30]. The shallow donor-acceptor pair transition DA2 at 1.62 eV is in accordance with the literature using the same label [73]. This transition dominates the near band edge luminescence due to the high Cu-content of Cu/Ga $\approx$ 1.16 measured by EDX. Several phonon replica with a phonon-energy of around 33 meV are observed. Furthermore, two deep broad transitions close to 1.24 eV (S1A2) and 1.10 eV (S2A2) can be fitted well with Gaussian distributions and FWHM-values of 110 meV and 190 meV respectively. The labeling is done on the basis of the following results in this chapter. Deep defects involved will be generally labeled with S in order to discriminate them from shallow donors (D) or acceptors (A).

The room temperature spectrum of CGSe-228 is given in Fig. 5.5. In this case only one broad deep band around 1.1 eV with a high intensity occurs. The magnified region shows the band-to-band transition. Two peaks can be resolved which occur from the valence band splitting [30]. The FWHM-value of the fundamental band gap E_{g1} is close to the theoretical expected value at room temperature, which is $W_{BB} \approx 1.8\, k_B T \approx 46$ meV [105]. The small peak width verifies that no potential fluctuations or strong band tailing can be

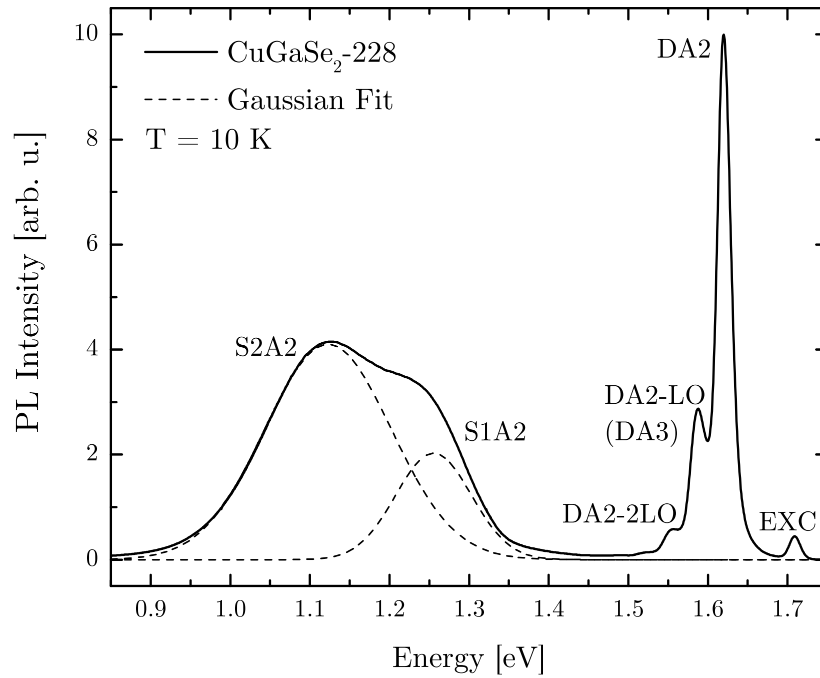

Figure 5.4: Photoluminescence spectrum at 10 K of sample CGSe-228. The peaks are labeled according to exciton (EXC), donor acceptor pair (DA), phonon replica (LO) and deep transitions (SA). The labeling is already based on the following results of this chapter. Gaussian fits of the deep transitions are shown with dashed lines.

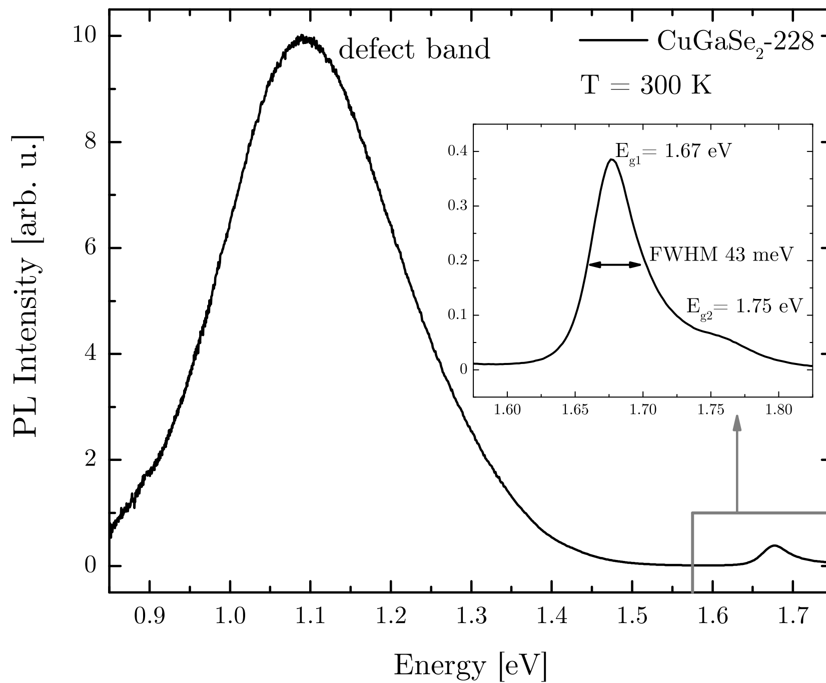

Figure 5.5: Room temperature photoluminescence spectrum of sample CGSe-228. The inset shows the magnified region of the band-to-band transition.

involved. In this case, the room temperature band gap results from $E_g = \hbar\omega_{max} - 1/2k_BT$ (see Section 3.1.1). The first band gap is at approx. $E_{g1} = 1.67$ eV and the second one at approx. $E_{g2} = 1.75$ eV.

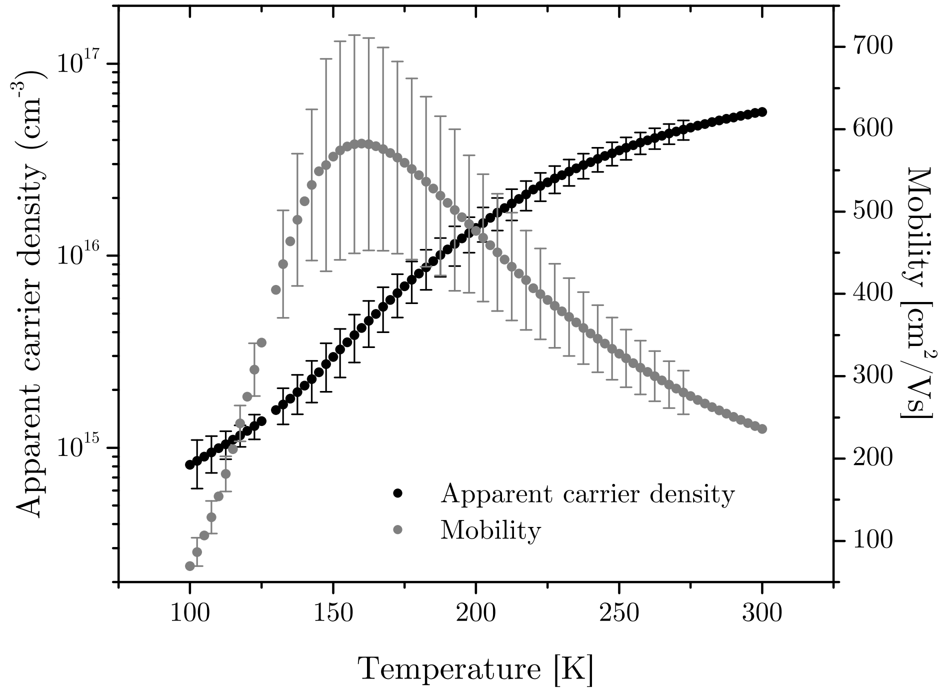

Figure 5.6: Hall measurements of the majority carrier density (black) and carrier mobility (grey) of sample CGSe-228 in dependence of the temperature, measured with the Van-der-Pauw-method.

In order to verify that the reference sample is a non-degenerate p-type semiconductor with reasonable values of the free carrier concentration and the carrier mobility (compared to often observed literature values), Hall-measurements are carried out by Florian Werner and the results are given in Fig. 5.6. At 300 K, the free carrier density is $p_0 = 5 \times 10^{16}$ cm^{-3} and the majority carrier mobility is $\mu = 240$ cm^2/Vs. These values are comparable to the ones in Ref. [40] from a large set of epitaxial samples. By knowing the effective density of states of the valence band in $CuGaSe_2$ ($\approx 1.5 \times 10^{19}$ cm^{-3} [38]), the Fermi level in the dark can be calculated at approx. 150 meV above the valence band maximum.

Furthermore, the quasi Fermi level splitting at room temperature is a parameter for the material quality (see Ref. [74, 106]) and was measured by Finn Babbe from absolute calibrated photoluminescence. The results are shown in Fig. 5.7. The laser excitation density is varied and given in units of equivalent fluxes from the illumination with one sun (AM1.5g). One sun corresponds to the same photon density of the AM1.5g spectrum, integrated from E_g to infinity. Since the photoluminescence intensity of the band-to-band transition for the excitation of one equivalent sun is too low, the quasi Fermi level splitting is measured at higher intensities. By fitting a power law dependence to the data points (linear fit in the lin-log plot of Fig. 5.7), the quasi Fermi level splitting at one sun can be extracted to 0.92 eV. This value seems not very high when compared to the band gap (quasi Fermi level splitting deficit of 0.76 eV), but it is in the same range as the open circuit voltage of state-of-the-art $CuGaSe_2$ solar cells with a record V_{oc} of 1 eV [37]. In general, the quasi Fermi level splitting in the absorber sets the upper limit for the open circuit voltage in the corresponding solar cell. With the shown measurement it is

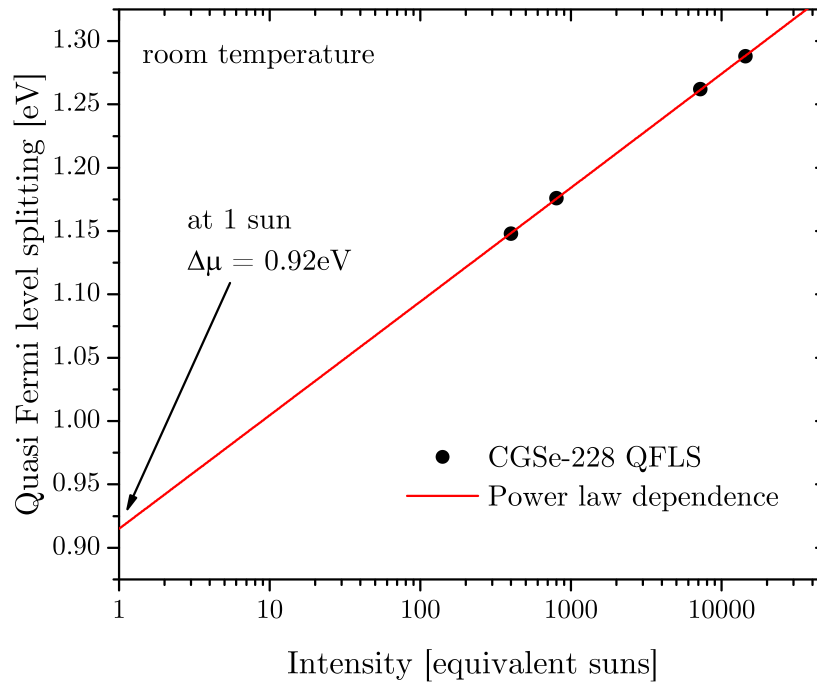

Figure 5.7: Fermi level splitting of sample CGSe-228 for different laser fluxes, equivalent to the illumination of the sun AM1.5g spectrum. The fit with a power law dependence (red curve) allows extrapolation to the value of the quasi Fermi level splitting at 1 sun.

guaranteed that the sample CGSe-228 does not contain extraordinarily higher amounts of recombination centers (deep defects) when compared to the literature, which would lead to even stronger non-radiative recombination and even lower values for the splitting $\Delta\mu$. The measurement was done with a CdS covered sample in order to avoid lowering of the quasi Fermi level splitting by degradation [26].

5.1.3 Excitation-dependent photoluminescence energy

In this part, the first characterization method of excitation-dependent measurements of the peak positions in the spectrum of the reference sample CGSe-228 (see Fig. 5.4) is applied. In section 3.1.4, it was already shown that the peak position of a donor-acceptor pair transition depends on the fixed energy levels of the involved donor and acceptor defects, as well as an additional term for the Coulomb interaction between the two, given in Eq. (3.14). If the laser excitation is varied over several orders of magnitude and plotted against the peak position, usually an s-shape behavior can be observed. For lowest excitation the peak position approaches the transition energy E_∞ of infinite distant donor acceptor pairs. This value is needs to be determined for the energies of the involved defect levels E_D and E_A with:

$$\text{low limit: } \hbar\omega_\mathrm{DA}(r_\mathrm{DA} \to \infty) = E_\mathrm{g} - E_\mathrm{D} - E_\mathrm{A} = E_\infty. \tag{5.1}$$

For highest excitation, the peak position approaches the sum of the infinite transition energy E_∞ and the Coulomb energy which results from a pair separation of twice the Bohr radius. The Bohr radius R_B is determined by the shallower impurity and it is:

$$\text{high limit: } \hbar\omega_\mathrm{DA}(r_\mathrm{DA} \to 2R_\mathrm{B}) = E_\infty + E_\mathrm{Coul.}(2R_\mathrm{B}) = E_\infty + \frac{1}{2}E_\mathrm{B}. \tag{5.2}$$

The Bohr radius and the corresponding binding energy E_B are related to each other by Eq. (3.16) in Section 3.1.4. With the same equation it is further possible to approximate the effective mass of electrons (the donor is shallower than the acceptor) or holes (the acceptor is shallower than the donor), if the shallow defect is correctly described by the hydrogen model. The value of E_B can be determined from the fit with Eq. (3.14). It is also possible to directly calculate the defect level of the shallower impurity E_d with respect to the corresponding band. But these values should not be considered for a quantitative analysis, since they rely on a simple description by the hydrogen model. Nevertheless, the results can be used for a reasonable distinction if either the donor or the acceptor is the the shallower defect level in the donor-acceptor pair.

Before studying the results of the deep defect band with the transitions S1A2 and S2A2, a validation of the model for the excitation-dependent photoluminescence energy in Eq. (3.14) will be given using the shallow DA2 transition. In Fig. 5.8, the dependence of the peak position against the laser power is depicted. It is common to plot the peak position on the abscissa. For comparison, the position of the exciton transitions is also shown. As expected for EXC, no significant peak shift with increasing laser power can be observed and the average energy position of the exciton is at $E_\mathrm{exc} = 1.709\,\mathrm{eV}$. The fitted energy dependence of the DA2 transition according to Eq. (3.15) is shown on the left part in Fig. 5.8. The binding energy as a free parameter is $E_\mathrm{B} = 35\,\mathrm{meV}$. Inserting the dielectric constant of $\varepsilon_\mathrm{r} = \varepsilon_\mathrm{r}(0) = 11.0$ [31] in Eq. (3.16) yields a Bohr radius of 37 Å, an effective mass of $m^*/m_0 = 0.15$ and a defect level at $E_\mathrm{d} = 17\,\mathrm{meV}$. These results are close to the literature values of $m_\mathrm{e}^*/m_0 = 0.14$ and $E_\mathrm{D} = 10...12\,\mathrm{meV}$. Since the effective mass of holes is much higher ($m^*/m_0 = 0.32...1.0$ [107, 69, 10]), the results confirm the characteristic of this transition from a shallow donor into a shallow, but deeper acceptor around $E_\mathrm{A} = 100\,\mathrm{meV}$ [73]. Together with the fitting value of $E_\infty = 1.608\,\mathrm{eV}$, the band gap $E_\mathrm{g} = 1.722\,\mathrm{eV}$ and Eq. (5.1), the shallow acceptor level is calculated at $E_\mathrm{A} = 97\,\mathrm{meV}$.

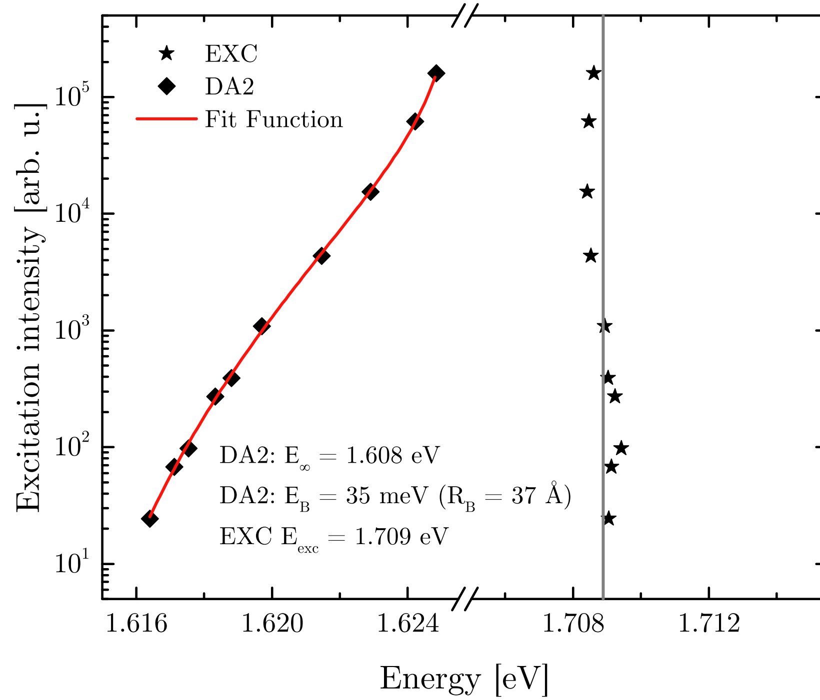

Figure 5.8: Excitation intensity in dependence of the peak positions of the shallow DA2 transition in a semi-log plot at 10 K. The fitted curve according to Eq. 3.15 is shown in red together with the fitting parameters.

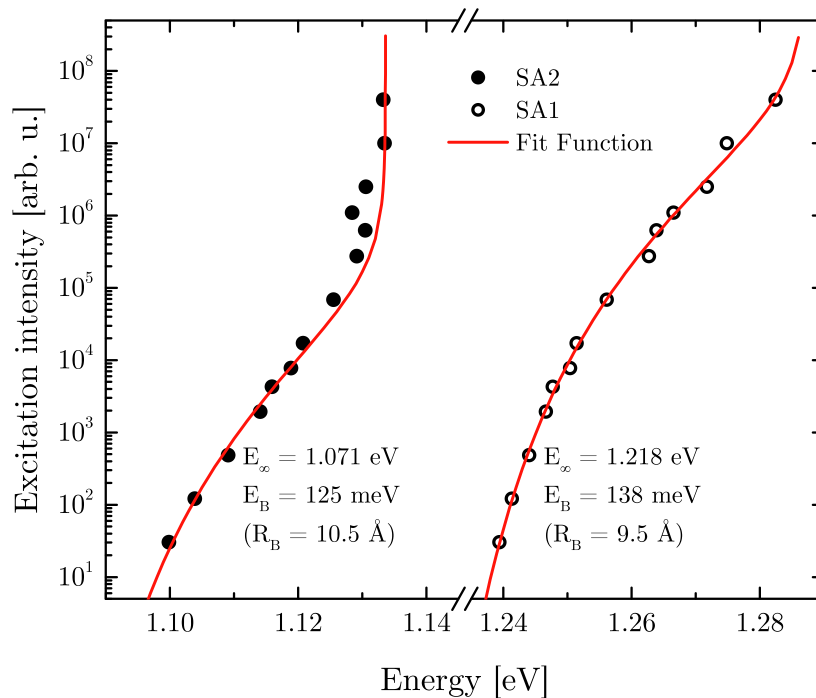

Figure 5.9: Excitation intensity in dependence of the peak positions of the deep transitions S1A2 and S2A2 in a semi-log plot at 10 K. The fitted curves according to Eq. (3.15) are shown in red together with the fitting parameters.

The same approach will be used for the deep transition S1A2 and S2A2, which is shown in Fig. 5.9. Both peaks shift by more than 30 meV when the excitation intensity of the laser is varied by more than 4 orders of magnitude. This relatively high peak shift $\beta = 5 - -8$ meV/dec for changing the laser power by one order of magnitude cannot be explained by e.g. potential fluctuation [10]. Potential fluctuations are absent which is also confirmed by the near-band-edge luminescence. Both deep transitions are therefore occuring from donor-acceptor pairs. Fitting of the experimental data yields much smaller binding energies and Bohr radii and similar values for S1A2 and S2A2. The effective mass can be calculated to $m^*/m_0 = 0.54...0.60$ and leads to the conclusion that the shallower involved defect has to be an acceptor in both transitions rather than a donor.

Unfortunately, there is no direct measurement of the effective hole mass in $CuGaSe_2$ available. Values in the literature vary between 0.32 and 1.2 [107, 108, 69]. In one of the most recent publications by Luckert et. al. [69], the effective hole mass was determined from the diamagnetic shift of an exciton and to $m^*_\mathrm{h}/m_0 = 0.64$. This value is close to the present findings, but it should only be seen as a confirmation for the shallower acceptor. The fitting of the broad deep transitions S1A2 and S2A2 is more inaccurate for high excitation than for DA2, since other signals (most likely free-to-bound transitions) start to contribute (see the next part 5.1.4). The involved acceptor can be described in the hydrogen model and therefore has to be close to the valence band. As a result, the involved donor level in S1A2 and S2A2 has to be relatively deep below the conduction band, since the transition energy of infinite distant pairs E_∞ is more than 500 meV below the band gap (see Eq. (5.1) and the fitting values in Fig. 5.9). The deep donor levels (labeled with S1 and S2) can be calculated from Eq. (5.1), if the involved shallow acceptor levels are known and if no Franck-Condon shift from strong electron-phonon coupling is considered. To do so, the excitation- and temperature-dependent peak intensities are studied in the following two parts and the characterization of involved electron-phonon coupling will be given in the following section 5.2.

5.1.4 Excitation-dependent photoluminescence intensity

Further information on the involved deep donors and shallower acceptors in S1A2 and S2A2 can be obtained from excitation-dependent measurements of the photoluminescence peak intensities. Parts of the following results are already published in Ref. [87].

As it is shown by the derived model in Chapter 7, different values of the power law exponents k for each transition at low and high excitation can discriminate involved defect levels. The photoluminescence intensity of the deep S1A2 and S2A2 transition in dependence of the laser excitation is shown in Fig. 5.10. The abscissa is given in values of the laser power density, which can be easily transferred into a photon flux density. The laser power was varied over 6 orders of magnitude. Using lower laser powers is limited by too long integration times for the photoluminescence signal, whereas the usage of higher laser powers is limited by the heating of the sample. Thermal effects should be avoided, since they can lead to a reduction of the peak intensity due to thermal activation rather than defect saturation. Observing the width of an exciton transition is a sensitive parameter for thermal effects, since the free exciton luminescence shape is determined by the Maxwell-Boltzmann distributed kinetic energy with a linewidth proportional to $k_{\mathrm{B}}T$ [109]. A slight broadening of the exciton transition was just observed at the highest laser power densities above $20\,\mathrm{W/cm^2}$. But on the other hand, the intensity of the S1A2 and S2A2 peaks remains almost constant up to 150 K (see Fig. 5.10 in the following section). For this temperature no exciton transition would be visible anymore, which was not the case in the excitation dependent measurement in Fig. 5.4. Therefore it is save to conclude that this unrealistic high lattice temperature of e.g. 150 K is not reached with the maximum laser power used and 10 K crystat temperature. The peak intensities of S1A2 and S2A2 are not influenced by thermal heating from excitation.

Both transitions S1A2 and S2A2 show exactly the same intensity dependence. The deviation from a straight line of a single power law is clearly visible in Fig. 5.10. For the lowest excitation a linear dependence with a k-value of 1 can be approximated, whereas at the highest excitation a square root like dependence with a k-value of 1/2 is observed. Defect saturation of one of the involved levels (deep donor or shallow acceptor) can explain these findings (see Chapter 4). Fitting with Eq. (4.27) and fixed values of $k_{1,2} = 1/2$ yields very good agreement with the experimental data. Even if the power law exponents are not fixed, the resulting free parameters $k_{1,2}$ of 0.49/0.47 and 0.48/0.56 for S1A2 and S2A2 are close to the expected value of 1/2.

Apart from an arbitrary amplitude the only free fitting parameter is the threshold level ϕ_0, since the k-values are already known from the low and high excitation limit in the curves. Therefore, the fitting of the whole curvature can be reduced to one parameter for the laser power density at which one of the involved defects levels gets saturated. This value corresponds to $1190\,\mathrm{mW/cm^2}$ and $870\,\mathrm{mW/cm^2}$ for the S1A2 and S2A2 transitions respectively and is indicated by the two arrows in Fig. 5.10. Taking into account the large excitation range of 6 orders of magnitude, but just a marginal deviation of the two threshold levels of around 25 %, it can be concluded that the same saturation process occurs in both transitions. Because a shallow acceptor was already attributed to both transitions in the previous parts, there are just two possibilities to explain the experimental data with the model in Chapter 4:

1. The transition from the same saturating deep donor into two different shallow acceptors (column $(a) \rightarrow (b)$ in table 4.4).

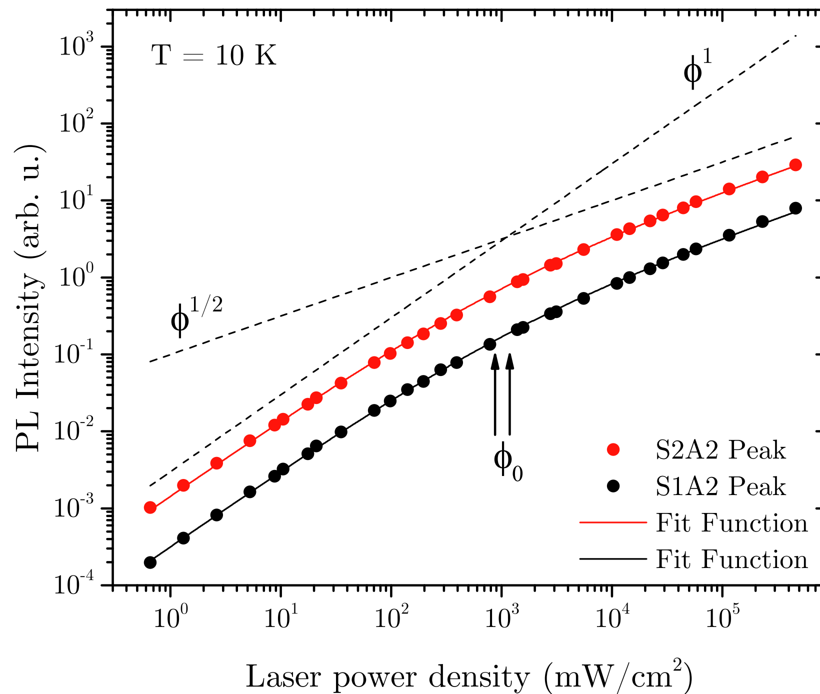

Figure 5.10: Peak intensities of S1A2 and S2A2 in dependence of the laser excitation intensity. Fit functions according to Eq. (4.27) are shown with lines and limiting power laws of square root and linear behavior are shown by dashed lines.

2. The transition from two different deep donors into the same saturating shallow acceptor (column $(a) \rightarrow (c)$ in table 4.4).

In both cases, the power laws from the shallow DA and the deep SA transition are the same. For this reason, the power law of e.g. the exciton transition is needed. In case 1, the exciton transition would not change with excitation. In case 2, the power law exponent would change from 2 to 3/2 if the common acceptor gets saturated (see table 4.4). In Fig. 5.11 the excitation dependence of all observed transitions is given in the same graph. All intensities are fitted with Eq. 4.27 and multiples of 1/2 for the k-values. The average of the fitted threshold level ϕ_0 of all curves is calculated and all curves are normalized to the intensity value at this laser power density for better visibility. The spread of ϕ_0 ranges from approx. 400 mW/cm^2 for the DA2 transition to 2600 mW/cm^2 for the EXC transition. The reason for this is a stronger scattering of the peak values for DA2 and EXC because only a few data points are taken below the threshold and the peak intensities in that range are much lower than for S1A2 and S2A2, resulting in more contribution from noise. Nevertheless, the fitted threshold levels are close when compared to the large measurement range and it is reasonable to assume that the same defect saturation is responsible for the changing power law behavior in the EXC, DA2, S1A2 and S2A2 transition.

As it is already expected from table 4.4 and the possible cases 1 and 2 mentioned earlier, the shallow donor acceptor pair transition DA2 changes from $k_{\mathrm{DA}} = 3/2$ at low excitation to $k_{\mathrm{DA}} = 1$ for highest excitation. The curvature can be fitted with Eq. (4.27) and $k_{low} = 3/2$, $k_{high} = 1$ or $k_1 = 1/2$ and $k_2 = 1$ respectively. In the literature it is often assumed that a donor acceptor pair transition only can follow a power law with an exponent k smaller or equal to 1 and that a superlinear slope can just be observed for

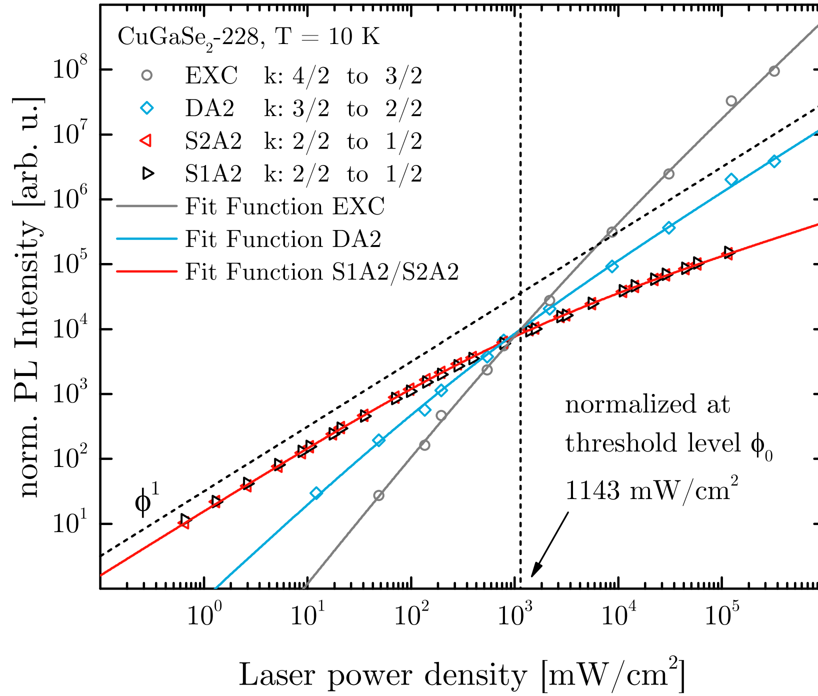

Figure 5.11: Peak intensities of the exciton (EXC), shallow donor acceptor pair (DA2) and deep donor acceptor pair transitions (S1A2 and S2A2) in dependence of the used laser excitation. Fit functions according to Eq. (4.27) are shown in red and the used limiting k-values for the low and high excitation are given with the transition labels.

excitons [85]. This is in contradiction to the present findings in Fig. 5.11 and is explained by the influence of deeper defect states in chapter 4.

The exciton transition changes from a quadratic dependence of $k_{\mathrm{EXC}} = 2$ to $k_{\mathrm{EXC}} = 3/2$. This behavior would be observed if the shallow acceptor level saturates (column $a) \rightarrow c)$ in table 4.4). The transition to column (d) or (e) can be ruled out, since in this case the deep SA luminescence would saturate with $k_{\mathrm{SA}} = 0$. Thus, it is concluded that the origin of S1A2 and S2A2 is a transition from two deep donor levels S1 and S2 into the same common shallow acceptor A2. It has to be the same shallow acceptor which is involved in the DA2 transition because the threshold levels are in the same range. As a result, the DA2, S1A2 and S2A2 transitions all occur into the acceptor A2, located 100 meV above the valence band maximum. Another argument for this assumption is given in the following by studying the peak shapes of S1A2 and S2A2 at highest excitation.

In Fig. 5.12 a), the spectrum of a measurement at low excitation with 66 µW and at high excitation with 23 mW laser power is shown. The peaks at low excitation can be well fitted with two Gaussian distributions. Increasing the intensity over several orders of magnitude only leads to a peak shift of the two transitions to higher energies without changes in the shape. At sufficiently high excitation (e.g. here 26 mW), the spectrum is not only a result of increased intensities plus a peak shift (normalized in Fig. 5.12). The low energy side remains unaffected and is shifted by 28 meV. But the high energy side slightly increases relative to the maximum in the region of S2A2 and at higher energies around 1.35 eV. A possible explanation could the occurrence of the corresponding free-to-bound transitions because the common acceptor gets saturated at this high laser powers. If the shallow acceptor becomes fully occupied with excess carriers and the laser intensity is further increased, an immediate increase of the free hole concentration is expected which

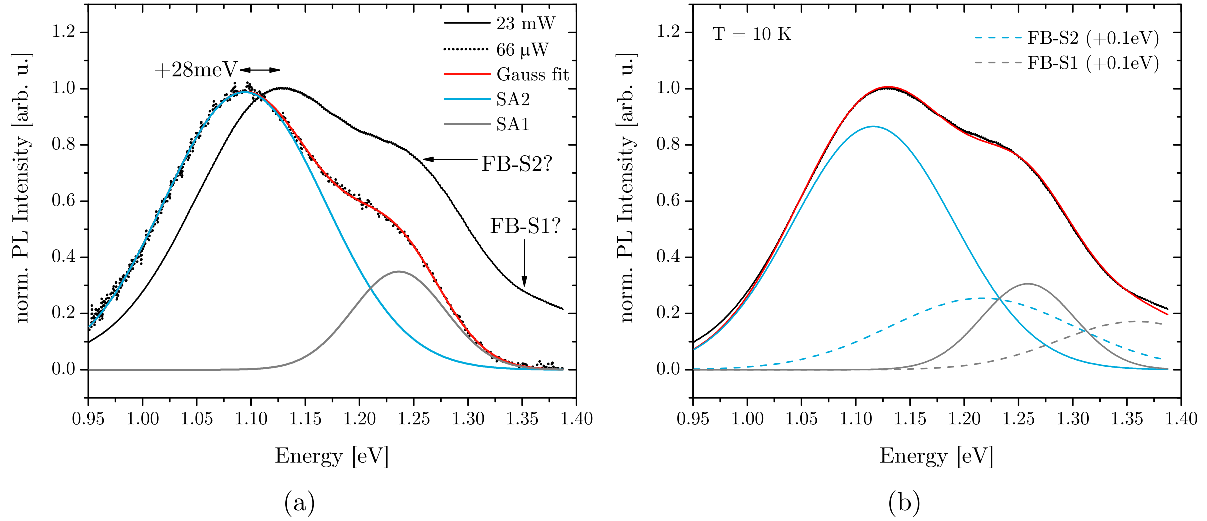

Figure 5.12: a) Deep transitions S1A2 and S2A2 fitted with two Gaussian distributions at low excitation (66 µW) and the normalized high excitation spectrum (23 mW) for comparison. The possible occurrence of free-to-bound transitions is labeled with FB. b) High excitation spectrum normalized and fitted with the same peaks of the low excitation case together with two additional Gaussian peaks shifted by 100 meV to higher energies.

can trigger the free-to-bound transitions of the two.

In Fig 5.12 b) the same spectrum of high laser power of 26 mW is given. For the fit of the spectrum, the same Gaussian peaks of the low excitation spectrum are used. The width and the ratio of their two maxima is kept constant and they are shifted equally by 28 meV to higher energies. Two additional Gaussian peaks are included for fitting of the high energy side. Expecting the corresponding free-to-bound transition of S1A2 and S2A2 to occur at approx. 100 meV higher energies (shallow acceptor A2 at 100 meV not anymore involved), the spectrum can be well fitted. This fitting routine should only be seen as a further support for the finding that the shallow acceptor A2 at 100 meV above the valence band is involved in the deep transitions S1A2 and S2A2. It can explain why at the highest laser powers used, the spectral shape of both transitions slightly deviates from the shape at low laser excitation. In the last part of this section, temperature dependent measurements on the deep transitions S1A2 and S2A2 are analyzed for additional insights on the involved defect levels.

5.1.5 Temperature dependent measurements

The activation energy of the thermal quenching of a photoluminescence transition corresponds in the simplest case to the energetic distance of the involved defect to the closest band. If the thermal quenching of a free-to-bound transition is observed, the activation energy could be directly linked to the defect level. In the case of a donor acceptor pair transition, two linear slopes in the Arrhenius with the activation energies E_D and E_A for the donor and the acceptor level are expected (see Section 3.1.4).

In Fig. 5.13 the photoluminescence intensity for the S1A2 and S2A2 transition is shown in the Arrhenius plot for two different excitation intensities. The corresponding laser power density was set one order of magnitude below (low excitation) and one order of magnitude above (high excitation) ϕ_0 in the excitation dependent measurements in Fig. 5.10. The thermal quenching is fitted with Eq. (3.17) and the obtained activation energies are given in Table 5.1. It cannot be distinguished between donor and acceptor levels and the activation energies are simply labeled with E_{A1}, E_{A2}. The value for $E_{lin.}$ is obtained by a linear fit of the high temperature slope in the Arrhenius plot (corresponding to a single exponential fit). This value $E_{lin.}$ should be equal to the larger activation energy of the two, if the intensity drop is measured over a sufficient range, so that the slope for the larger activation energy is not influenced by the smaller one. Except for the highest intensities (S2A2 with high excitation), where the thermal quenching is too low for appropriate fittings of the slope in the possible measurement range (the intensity does not drop far enough), the linear fitting is in good agreement with the higher activation energy E_{A2}. The comparison supports the usage of the model in Eq. (3.17).

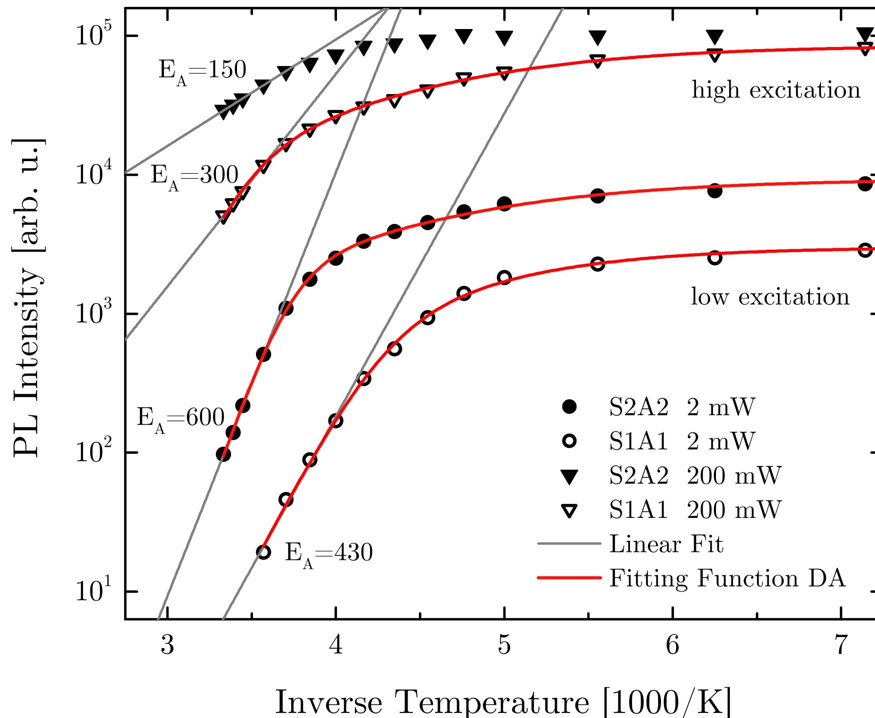

Figure 5.13: Arrhenius plot for the thermal quenching of the deep S1A2 and S2A2 transition. The fitted model of Eq. (3.17) is shown in red and the linear fit of the high temperature slope is shown in grey. The corresponding fitting parameter are given in Table 5.1

.

Table 5.1: Fitting parameter for the thermal activation

Peak	E_{A1} [eV]	E_{A2} [eV]	$E_{lin.}$ [eV]	$\hbar\omega_{DA} + E_{A1} + E_{A2}$ [eV]
S1A2 (lowest)	0.19	0.54	0.59	1.83
S2A2 (lowest)	0.16	0.76	0.80	2.16
S1A2 (low)	0.10	0.43	0.43	1.77
S2A2 (low)	0.08	0.65	0.60	1.83
S1A2 (high)	0.08	0.50	0.30	1.82

From Table 5.1, it can be seen that the obtained activation energies are excitation dependent. Higher excitation tends to result in lower activation energies. The table also contains the fitting parameter for the lowest laser excitation used which are not shown in Fig. 5.13, but where the second activation energy reaches values close to 0.8 eV. From the results of E_{A1} and E_{A2}, it can be already concluded that a rather shallow defect E_{A1} and a deep defect E_{A2} are involved in both transitions, which supports the findings from the former sections. Furthermore the first activation energy could possibly reflect the known involved shallow acceptor at 100 meV apart from the lowest excitation conditions.

But unfortunately, the thermal quenching of the deep bands S1A2 and S2A2 is not suited to characterize the defect energies for the following reasons. In the simplest case, the activation energies correspond to the thermal ionization energies of the donor and the acceptor. Apart from a small energy contribution of the Coulomb-attraction, the sum of the photoluminescence maximum of the donor-acceptor pair transition $\hbar\omega_{DA}$ and the activation energies of the donor E_D and the acceptor E_A should be equal to the band gap (see Eq. (3.14) in Section 4.1.4). The sum is given in the last column in Table 5.1. For both transitions S1A2 and S2A2 and for all excitation intensities used, the sum is above the band gap. Also if strong phonon coupling is involved, so that the optical and thermal transition energies are different (see Section 3.2 or Ref. [17]), the calculated sum would be unreasonable high above the band gap. If a Franck-Condon shift occurs from phonon coupling, the zero-phonon line has to be inserted into the sum instead of the photoluminescence maximum. But the zero-phonon line can only be at higher energies than the photoluminescence maximum. This would result in even higher energy values for the summation, even further above the band gap energy.

The observed thermal quenching with excitation dependent and untypically high activation energies of up to 760 meV could be the result of correlated and not independent thermal quenching processes of a shallow and a deep defect. In the conventionally used model in Eq. 3.17, it is assumed that the thermal quenching of the donor and the acceptor occurs without the influence of other defect levels. A model was proposed by Reshchikov et. al. [110] in order to describe the excitation dependent and abrupt thermal quenching in GaN with very high and unreasonable activation energies. Similar to the present case with a p-type semiconductor and a shallow donor, a deeper but shallow acceptor and a deep defect temperature dependent concentrations of all charged and neutral defects are shown. For high enough temperatures the shallow donor is completely ionized and the deep defect completely filled with electrons. As soon as the temperature increases and the rather shallow acceptor becomes ionized, the so-called "bottleneck" breaks and an interaction between the acceptor, the free holes in the valence band and the deep defect leads to an abrupt decrease of the neutral deep defect density. Therefore also an observed donor-acceptor pair transitions from the neutral deep defect would show an abrupt drop

in intensity, which does not reflect the thermal activation of carriers into the band.

Without further measurements at higher temperatures than room temperature, it is not possible to directly confirm this so-called tunable (excitation dependent) and abrupt (high activation energies) thermal quenching like in GaN. But the model proposed by Reshchikov et. al. [110] is a possible explanation for the present observation of too high activation energies. It further supports the results of deep defects involved in S1A2 and S2A2, which cannot be characterized by conventional models for thermal quenching. In the case for Cu-rich $CuGaSe_2$, the thermal activation of the acceptor at 100 meV could be responsible for breaking the "bottleneck" which leads to abrupt emptying of the levels S1 and S2.

5.2 Defect spectroscopy on Cu(In,Ga)Se_2

Based on the results on the $CuGaSe_2$ reference sample in the previous section, the observed deep defect bands will be studied when indium is added into the process in order to grow solid solutions of Cu(In,Ga)Se_2. In the first part it will be shown that already a small addition of Indium yields just one broad defect band which corresponds to the S2A2 band. Its asymmetric peak shape can be fitted with models for strong phonon coupling which is given in the second part. The fitting model leads to the extraction of the zero-phonon line and thereby to the energetic position of the dominant deep recombination center S2 at around 1.30 – 1.33 eV above the valence band maximum. If more gallium is replaced by indium in the solid solution, the band gap gets mainly reduced by a reduction of the conduction band minimum. It is therefore essential to know how the deep defect position changes with respect to bands, since it will have a direct influence on carrier recombination and solar cell efficiencies as a result. In the third part it will be shown that the deep defect position remains almost constant with respect to the valence band if the amount of indium increases (the Ga/(Ga+In) ratio decreases). Therefore, the deep recombination center becomes shallow in compositions with low gallium content and less harmful. In the last part, from comparison to literature data and from SCAPS simulations, the large open circuit voltage deficit of wide-gap Cu(In,Ga)Se_2 solar cells will be attributed to the found recombination center at 1.30 – 1.33 eV above the valence band maximum. In solar cells with high gallium content, the deep defect S2 is assumed to be one of the major reason for the inferior device efficiency due to increased non-radiative recombination, which lowers the V_{oc}. For gallium contents equal or lower to approx. 50 %, the defect becomes very close or even resonant with the conduction band and cannot act as detrimental recombination center.

5.2.1 Addition of Indium to $CuGaSe_2$

For studying the influence of small additions of indium, the growth recipe for the reference sample CGSe-228 from the previous Section 5.1.2 is just slightly adjusted. The temperature, the growth duration and the partial pressures of copper and selenium are kept constant. Some of the gallium flux is replaced by indium, while keeping the sum of both partial pressures (partial pressure of group-III elements) equal to the recipe of CGSe-228. Details on the growth process in general are described in Chapter 2. The measured composition by EDX is given in Table 5.2 for comparison of the two samples. The copper content of sample CIGSe-130 is nearly unaffected and still in the desired Cu-rich range, whereas the Ga/(Ga+In) ratio is approx. 0.8. From this gallium content, the low temperature band gap is expected at 1.55 eV (see Fig. 1.4 in Section 1.1.3).

Table 5.2: EDX results from sample CGSe-228 and CIGSe-130

	Cu/(Ga+In)	Ga/(Ga+In)
$CuGaSe_2$ (228)	1.16	1.00
$CuIn_{0.2}Ga_{0.8}Se_2$ (130)	1.14	0.79

Before studying the deep defect band, a comparison of the near band edge luminescence at 10 K for both samples is given in Fig. 5.14. It is obvious that the shallow defect transitions are broadened and shifted to lower energies in the solid solution. The peak at

1.55 eV is attributed to an exciton transition. From this, the band gap at 10 K is assumed to be reduced by 0.16 eV compared to $CuGaSe_2$ with an exciton transition at approx. 1.71 eV. This difference is in good agreement with the expected value of approx. 0.17 eV from Fig. 1.4 and a change of the Ga/(Ga+In) ratio from 1.0 to 0.79.

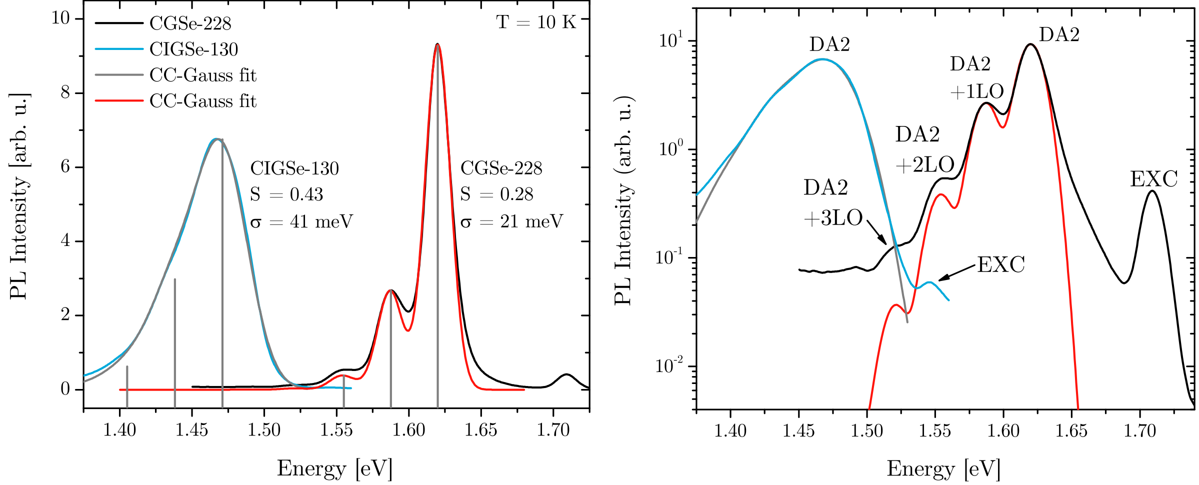

Figure 5.14: Near-band-edge luminescence of $CuGaSe_2$ (CGSe-228) and $CuIn_{0.2}Ga_{0.8}Se_2$ (CIGSe-130) in linear (left) and logarithmic (right) scale. The fits of Eq. (3.22) are shown in red together with the fitting parameter. The involved phonon lines are shown in grey without broadening and a phonon energy of 33 meV.

The near-band-edge luminescence of CGSe-228 in Fig. 5.14 is known from the previous section and in accordance with the literature of Cu-rich compositions (see Section 1.3). The DA2 transition dominates the spectrum and originates from a shallow donor at approx. 10 meV and a shallow acceptor A2 at approx. 100 eV. Furthermore, three phonon replica of this transition with a phonon energy of 33 meV are well resolved. This value is in good agreement with the one from raman spectroscopy in literature (see Section 1.1.3) and corresponds to the longitudinal optical (LO) phonon. Fitting the spectrum of CGSe-228 with Gaussian peaks in the 1-dimensional configuration coordinate model by Eq. (3.22) (see Section 3.2) yields good results. It is worth mentioning that this simplified model is usually insufficient for small phonon interactions with $S < 1$ [17]. In the logarithmic scale in Fig. 5.14 one can see that the amplitude of the first phonon line agrees very well. It is reasonable to assume that the amplitudes of the other phonon lines are too high in the experimental data because of a contribution from unknown broad luminescence (see the apparent luminescent background between 1.45 eV and 1.5 eV). The high energy side above 1.65 eV with a known contribution of the DA1 transition is not taken into account for the fitting. The model yields a Gaussian FWHM of $w = 21$ meV for each line and a Huang-Rhys factor of $S = 0.28$.

Sample CIGSe-130 shows an expected shift of the near-band-edge luminescence together with the band gap by approx. 0.16 eV. This shift is the same for the exciton transition as well as the dominating DA2 transition. Fitting within the 1D-CC model yields very good results with an increase of the line-broadening to $w = 41$ meV and a slight increase of the Huang-Rhys factor to $S = 0.43$. The phonon energy cannot be directly measured from the distance of the phonon replicas in sample CIGSe-130. But

taking the same phonon energy of 33 meV as before or reducing the phonon energy by about 2 meV for 80 % gallium content (see Fig. 1.4 in Section 1.1.3) leads to almost the same results since the difference is too small and the line broadening w is higher. The broader luminescence lines most likely result from the expected alloy disorder in the solid solution which is absent in the ternary crystal. The slight increase of the Huang-Rhys factor could be due to a slightly higher shift q of the defect potential from its equilibrium position (see Fig. 3.2 in Section 3.2) because the surrounding changes by replacing gallium with 20 % of indium. But the phonon coupling remains very weak and the zero-phonon line is nearly equal to the photoluminescence maximum.

Deep defect band

A deep defect band with its maximum around 1.1 eV can also be observed in the sample with the addition of indium. But as seen in Fig. 5.15, no double structure is visible anymore. The reason for this is not understood so far, but possible explanations will be given in the summary of the complete defect picture in Chapter 7. The focus in the current chapter is set on the dominating transition around 1.1 eV. In Fig. 5.15, the full spectrum of CIGSe-130 is shown together with the deep defect band in detail. Again, the donor-acceptor pair characteristic is verified by a blue-shift of several meV per decade of excitation.

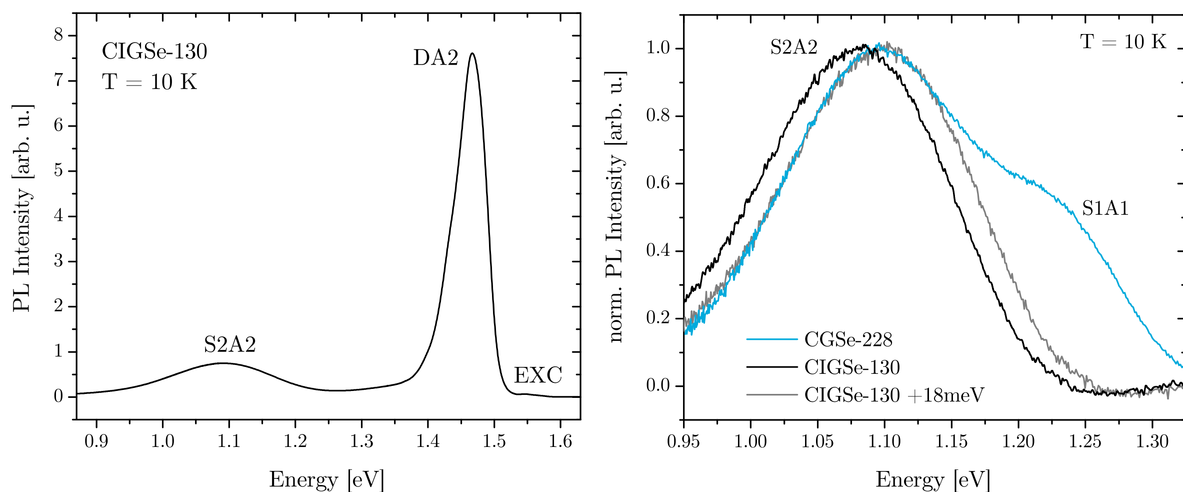

Figure 5.15: The full spectrum of CIGSe-130 at 10 K (left) and the spectrum of the deep defect band alone (rig). The deep band is shown for the lowest used excitation together with the same spectrum shifted by +18 meV. The deep defect band in CGSe-228 with the S1A2 and S2A2 transitions is shown for comparison.

Taking into account a small redshift of the defect band of sample CIGSe-130 by 18 meV, it is obvious that this dominant deep photoluminescence transition is the same in $CuIn_{0.2}Ga_{0.8}Se_2$ and $CuGaSe_2$. A comparison of the two samples on the right side in Fig. 5.15 is shown at lowest excitation intensities in order to keep the Coulomb-interaction of the donor-acceptor pairs as small as possible. A shift of the deep transition from sample CIGSe-130 by 18 meV is shown in grey and perfectly matches the S2A2 transition in CGSe-228. The difference of 18 meV is small compared to the change of the band gap by 0.16 eV. Furthermore, this small change does not necessarily indicate a change of the

energetic level of the involved deep defect. Since the recombination of a deep donor-like level into the shallow acceptor A2 is still assumed, possible explanations for the redshift of 18 meV are given in the following:

- Usually the energy level of a defect is defined with respect to the valence band as the reference level. This is not of concern in Cu(In,Ga)Se_2, since with changing the band gap (here mostly due to a change of the conduction band), deep localized defects can stay constant with respect to the vacuum level. Shallow defects on the other hand stay constant with respect to the corresponding band edges [111]. The difference of the valence band levels in the ternaries is just around $\Delta E_V(CuInSe_2\text{-}CuGaSe_2) = 0.04$ eV [112]. Taking into account that the studied deep transition S2A2 originates from a deep donor and a shallow acceptor, it is possible that the acceptor level stays constant with respect to the valence band and the deep localized level stays constant with respect to the vacuum level. Therefore a change in band gap would just affect the peak position due to a difference of the valence band and the shallow level as a result. If one linearly interpolates the 0.04 eV difference of the valence band between $CuInSe_2$ and $CuGaSe_2$, the valence band of sample CIGSe-130 is 7 meV higher compared to CGSe-228. This could be one possible reason for a redshift of the shown deep band.

- Another source of the observed redshift can be due to a change in the Huang-Rhys factor like it was observed for the shallow DA2 transition. In the DA2 transition, the weak phonon coupling most likely occurs from the acceptor at 100 meV, rather than the very shallow donor at around 10 meV. Generally, the peak maximum differs from the zero-phonon line by approx. $S\hbar\Omega$ (see Section 3.2). Since the phonon energy $\hbar\Omega$ is known with 33 meV, the small change of the Huang-Rhys factor in Fig. 5.14 already induces a redshift of 5 meV in the case of the DA2 transition. This value can be seen as a minimum which is also expected for the deep transition S2A2, since the acceptor A2 at 100 meV is involved in DA2 and S2A2. Such small changes of the Huang-Rhys factor by 0.15 will be hardly visible in the peak shape for strong phonon coupling which is discussed for the S2A2 transition in the following part. Together with the value from the valence band differences, already a redshift of 12 meV can be possible.

- Different defect concentrations can lead to different quantum efficiencies of the deep defect bands in sample CGSe-228 and CIGSe-130. By using the same excitation conditions, the Coulomb-interaction of the donor-acceptor pairs in the two samples can be different, because the defect sites get occupied by different amount of excess carriers. A redshift would be expected if the quantum efficiency decreases, which would lower the Coulomb-interaction. Because the peak shift between the two samples was measured at the lowest possible intensities, the Coulomb-interaction is assumed to have just a small influence, but can not be ruled out completely.

It is thus possible to explain a small redshift of the photoluminescence peak S2A2 by more than 10 meV. These consideration are done in order to motivate the assumption that the same defects are responsible for the deep defect band in sample CGSe-228 and CIGSe-130. This assumption is further supported from the broad, but equal peak shapes, which indicates the same strong phonon coupling as discussed in the following. The advantage of a single resolved deep band in CIGSe-130 ($CuIn_{0.2}Ga_{0.8}Se_2$) will be used to apply models for strong phonon coupling in the next part. The aim is the extraction of the zero-phonon

line, which can deviate far from the peak maximum and which is needed to derive the energetic position S2 of the deep defect involved.

5.2.2 Zero-phonon line of the deep defect band

As it can be seen in Fig. 5.16, the deep S2A2 band in sample CIGSe-130 has an asymmetric shape, which is hardly visible in a linear scale. Given the fact that deep defects usually show a large Franck-Condon shift (see Ref. [64] and Section 3.2), the large width of the deep defect band together with its asymmetry is likely to originate from strong phonon coupling rather than e.g. a broad defect distribution in energy. Fitting with one Gaussian is insufficient and the models for phonon coupling in Section 3.2 with Eq. (3.22) and Eq. (3.24) will be applied. As seen in Fig. 5.16, the fit of the Gauss-CC model with Eq. (3.22) is in better agreement with the experimental data than the fitting with just a symmetric Gaussian function.

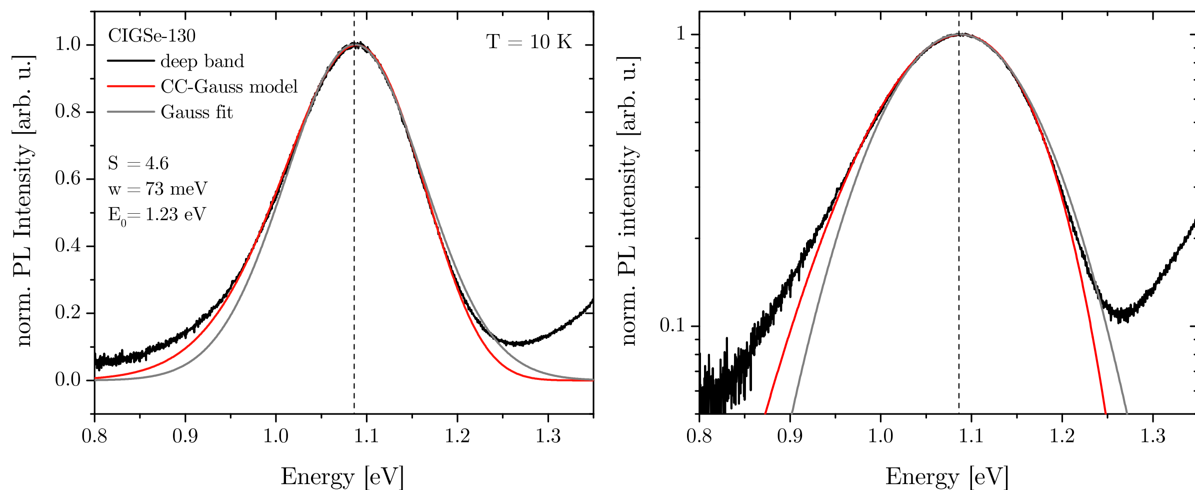

Figure 5.16: Photoluminescence intensity of the deep defect band in $CuIn_{0.2}Ga_{0.8}Se_2$ (CIGSe-130) in linear (left) and logarithmic (right) scale. The fit of Eq. (3.22) is shown in red, together with the fitting parameters

For the CC-Gauss model, all phonon modes are replaced by a Gaussian distribution with the same width and a distance equal to the phonon energy of $\hbar\Omega = 33\,\text{meV}$ as in the case for the near-band-edge luminescence. The free fitting parameters indicate a strong phonon coupling with $S = 4.6$. The phonon linewidth is rather broad with $w = 73\,\text{meV}$ and the zero-phonon line is at $E_0 = 1.23\,\text{eV}$. Nevertheless, better results are obtained if a constant background is taken into account. Even after automated dark count subtraction during the measurement, a small amount of counts can pile up from e.g. scattered light inside the spectrometer or due to "real" unknown signal from the sample or the environment. It is expected due to nearly constant, non-zero count values in the raw spectrum, which are at energies close or even below the sensitive region of the InGaAs-array detector. If just a constant value is added to the fit, very good agreement of the model for phonon coupling is obtained and shown in Fig. 5.17 (constant value already subtracted). In this example, the substracted background is below 5 % of the maximum intensity of the deep band.

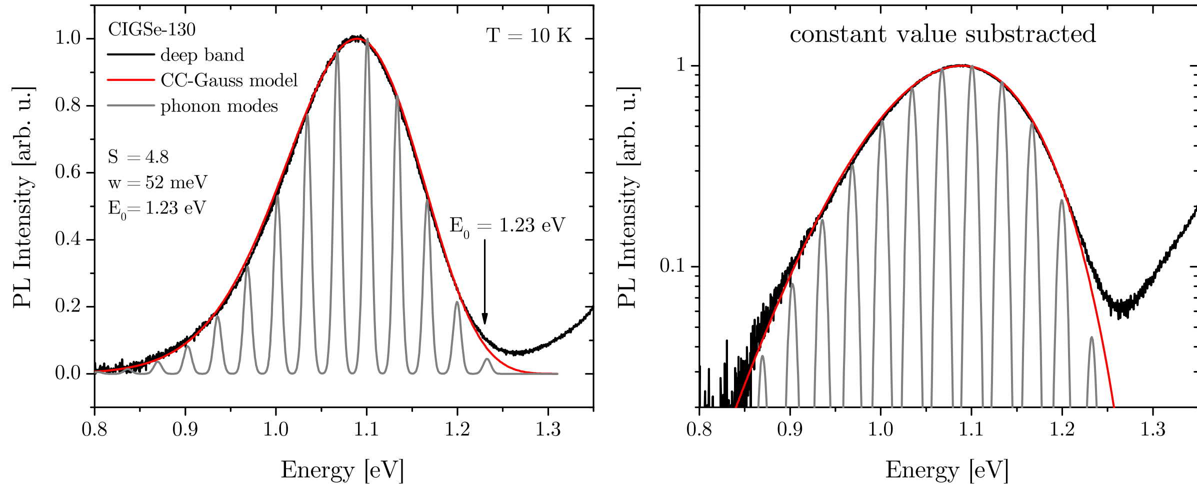

Figure 5.17: Photoluminescence intensity of the deep defect band in $CuIn_{0.2}Ga_{0.8}Se_2$ (CIGSe-130) in linear (left) and logarithmic (right) scale. The experimental data is fitted with Eq. (3.22) plus a constant background (already substracted). To visualize the phonon contribution, the same fit as in red but with narrow Gaussian lines ($w = 10\,\text{meV}$) is shown in grey.

After subtraction of the constant value from the spectrum, the zero-phonon line is unaffected and all the following results for the deep defect position in this section will remain the same. The parameter for the Huang-Rhys factor just increases slightly from 4.6 to 4.8 and the phonon linewidth is decreased from 73 meV to 52 meV. In logarithmic scale it is visible that the fit is now valid over nearly two orders of magnitude of the photoluminescence intensity. In order to visualize the involved phonon modes, in Fig. 5.17, the same fit function as the red curve is shown with a phonon linewidth of just 10 meV in grey. In this case the position and height of the single phonon lines are resolved, since they don't overlap to form a single broad asymmetric peak.

As given in Section 3.2, a fitting model for the strong phonon coupling was also proposed by Reshchikov et. al. and applied to various deep defect transitions in GaN. The difference between the fit function from Reshchikov in Eq. (3.24) and the Gaussian phonon line model in Eq. (3.22) is shown in Fig. 5.18 with the same values for S and E_0. An advantage of the model from Reshchikov is the absence of the fitting parameter w for the FWHM of each phonon line. Instead, the known energy position of the photoluminescence maximum is used in the fit. But at the same time, the absence of the smearing parameter w is the limiting factor of the CC-Reshchikov fitting function. In principle, the model expects an infinitesimal small linewidth of the zero-phonon line. It is true that apart from the phonon sideband, the zero-phonon line can be very narrow, e.g. the ZPL of the NV-center in diamond can reach a width as small as 0.002 meV [113]. But from the near-band-edge luminescence of sample CGSe-130, it is already known from the fit in Fig. 5.14 that a linewidth of 41 meV or even higher is present. Due to the expected broad zero-phonon line, the CC-Reshchikov model can lead to erroneous results which is explained in the following.

In Fig. 5.18, the already used CC-Gauss model is shown again in red with the fitted zero-phonon line at 1.23 eV in grey. The zero-phonon line in this model is simply a

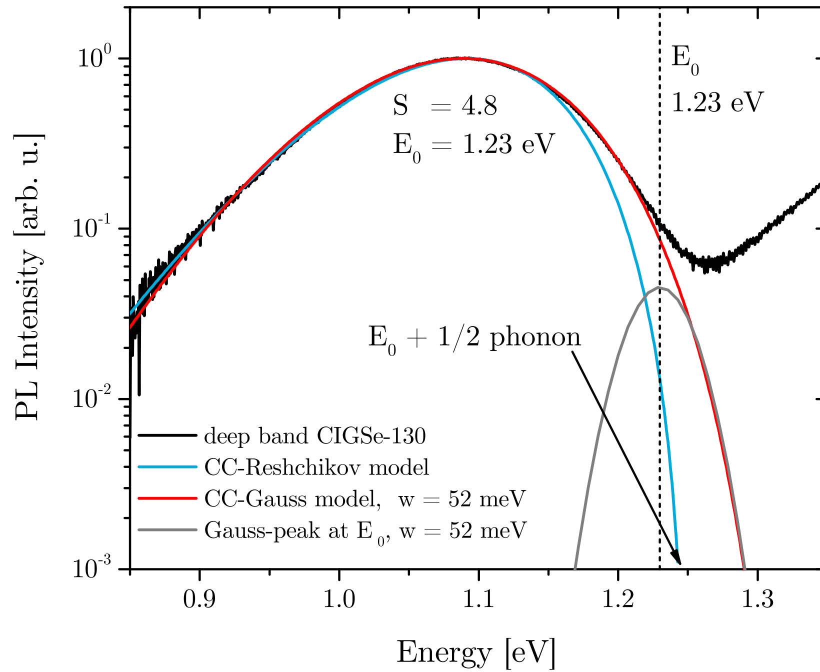

Figure 5.18: Photoluminescence intensity of the deep defect band in $CuIn_{0.2}Ga_{0.8}Se_2$ (CIGSe-130) in logarithmic scale (black) together with a comparison of the fitting models for phonon coupling from Section 3.2. The same fitting values from the formerly used CC-Gauss model (red) are used for the model from Reshchikov (blue, Eq. (3.24)). The zero-phonon line of the CC-Gauss model is shown in grey with a FWHM of $w = 52\,\text{meV}$.

Gaussian peak at E_0 with a full width at half maximum of 52 meV and an amplitude proportional to $\exp(-S)$. If the model from Reshchikov is applied to the experimental data, the free fitting parameters yield a much higher Huang-Rhys factor of $S \approx 14$ and a much higher zero-phonon line at $E_0 \approx 1.35\,\text{eV}$. The fitting curve is not shown since it is essentially the same as for the CC-Gauss fit in red. On the other hand, if one applies the model by Reshchikov with the same parameters for S and E_0 as for the CC-Gauss model (shown in Fig. 5.18), the photoluminescence intensity will drop to zero at exactly $E_0 + 1/2\hbar\Omega = 1.23\,\text{eV} + 16.5\,\text{meV}$. This behavior can be easily seen from the fitting equation (3.24) in Section 3.2. The zero-phonon line is infinitesimal small and determines the beginning of the spectrum. The fit is still valid for energies much lower than E_0, but the high energy side of the photoluminescence band cannot be correctly described due to the absence of the ZPL broadening. But when using the free fitting parameters, the much higher value of the zero-phonon line is proposed to be just an artifact of the CC-Reshchikov model, which is not suited for the present measurements. Since the red curve in Fig. 5.18 drops to zero at 1.3 eV or above, the zero-phonon line of the same resulting fitting curve within the CC-Reshchikov model has to be also at 1.3 eV or above (1.35 eV fitted). The zero-phonon line shifts the whole spectrum to higher energies and is falsely counterbalanced in the fit by a much higher Huang-Rhys factor of nearly 14. But this leads to unreasonable high Franck-Condon shifts between the ZPL and the peak maximum of 460 meV. For the above reasons, only the CC-Gauss model will be used for the results.

The fitting parameters of the CC-Gauss model will be further tested by comparing experimental and theoretical values for the peak width and for the Franck-Condon shift.

From Ref. [65] it is known that different parameter-pairs of the Huang-Rhys factor and the zero-phonon line energy (S,E_0) can lead to the same peak width and the same energy of the maximum of a photoluminescence band with strong phonon coupling. Different parameter-pairs can thus result in nearly the same peak shape and therefore nearly the same fitting curves. It is obvious that e.g. a higher Huang-Rhys factor results in a higher Franck-Condon shift (peak maximum shifts to lower energies), which can be compensated by a higher zero-phonon line energy (peak maximum shifts to higher energies) and vice versa. For this reason, a simple test will be implemented in order to justify the right fitting parameters. The correct evalution of the zero-phonon line energy is hereby the most important value.

Test of the fitting parameters

The FWHM of the full defect band W is known directly from the spectrum. In general if the involved phonon energy is above 4 meV, which is in principle always valid, the peak width at 0 K and 10 K are the same. This results from the temperature dependence of the peak width in Eq. (5.3) [78]. The ratio of $W(10\,\mathrm{K})/W(0\,\mathrm{K})$ is below 1.01 for $\hbar\Omega > 4\,\mathrm{meV}$.

$$W(T) = W(0)\sqrt{\coth\left(\frac{\hbar\Omega}{2k_\mathrm{B}T}\right)}. \tag{5.3}$$

If the Huang-Rhys factor of the ground state and the excited state are assumed to be equal ($S_\mathrm{g} = S_\mathrm{e}$), the peak width at 0 K is given by [78]:

$$W(0) = W_0 = \sqrt{8\ln 2}\frac{S_\mathrm{g}\hbar\Omega}{\sqrt{S_\mathrm{e}}} \overset{S_\mathrm{g}\approx S_\mathrm{e}}{=} \sqrt{8\ln 2}\sqrt{S}\hbar\Omega. \tag{5.4}$$

In this case, the experimentally measured peak width at 10 K can be calculated from W_0 and is just a function of the Huang-Rhys factor S and the phonon energy $\hbar\Omega$. If the phonon energy is not known, it can also be extracted from the temperature dependence of the peak width, but here, only the Huang-Rhys factor is uncertain. As already given in Eq. (3.18) and Eq. (3.21) in Section 3.2, the Franck-Condon shift is defined by the distance of the photoluminescence maximum to the zero-phonon line energy with [65]:

$$d^*_\mathrm{FC} = E_0 - \hbar\omega_\mathrm{max} = (S - \frac{1}{2})\hbar\Omega. \tag{5.5}$$

If the observed peak is close to a Gaussian, which is the case for strong phonon coupling, the Huang-Rhys factor can be approximated from the peak width at low temperatures, if the phonon energy is known. From Eq. (5.4) and Eq. (5.5) it is:

$$E_0 = \hbar\omega_\mathrm{max} + (S - \frac{1}{2})\hbar\Omega = \hbar\omega_\mathrm{max} + \left(\underbrace{\frac{1}{8\ln 2}\frac{W_0^2}{\hbar\Omega^2}}_{\text{Huang-Rhys}} - \frac{1}{2}\right)\hbar\Omega. \tag{5.6}$$

The deep S2A2 band in sample CIGSe-130 has a peak width of 174 meV at 10 K. Inserting this value together with a phonon energy of 33 meV in Eq. (5.4) yields a Huang-Rhys factor of $S = 5.0$. Also the zero phonon line can be estimated by inserting the defect band maximum $\hbar\omega_\mathrm{max} = 1.09\,\mathrm{eV}$ into Eq. (5.6) with $E_0 = 1.24\,\mathrm{eV}$. The fitted values for the Huang-Rhys factor and the zero-phonon line should be close to these values and indeed they are ($S = 4.8$, $E_0 = 1.23\,\mathrm{eV}$). The fitting uncertainty of the Huang-Rhys factor is around ± 0.2 in this example.

In Table 5.3 an overview of possible fitting values for the defect band in sample CIGSe-130 is given. All of this values result in appropriate fitting curves. The phonon energy is fixed and the width of the phonon modes σ is also kept constant in each fit and stepwise varied between 40 meV and 90 meV. Smaller values than 40 meV for w result in ripples on the fitting curves, since the phonon modes get too narrow and therefore the discrete lines become visible. Higher values than 80/90 meV result in inappropriate fitting curves, especially on the high energy side. The Huang-Rhys factor and the zero-phonon line are the free fit parameters. For each fit, the peak width is calculated from Eq. (5.4) and compared to the measured value of 174 meV. Furthermore the Franck-Condon shift is calculated from two different approaches in Eq. (5.5).

From Table 5.3 it is clear that with increasing width of the phonon modes w, the zero-phonon line energy E_0 decreases by 0.03 eV. This corresponds to a decrease of the average amount of involved phonons by approximately 1, which is expresses by a decrease of the Huang-Rhys factor by the same value. But at the same time, it is important to observe that the calculated peak width drifts away from the measured value. Also the Franck-Condon shift in the last column becomes much smaller for increasing w. Thus, small values of w yield the best results. The test shows that it is possible to find parameter-pairs of S and E_0 which give valid fitting curves, but which are also in accordance with the theoretical expected values for the peak width and the Franck-Condon shift. The former fitted zero-phonon line at $E_0 = 1.23$ eV is supported by this comparison.

Table 5.3: Influence of the fitting parameters on the peak width and Franck-Condon shift. (free parameter w yields 52 meV)

Parameter				Peak width		Franck-Condon shift	
$\hbar\Omega$ (fix)	w (fix)	S	E_0	FWHM	$\sqrt{8\ln 2}\sqrt{S}\hbar\Omega$	$E_0 - \hbar\omega_{\max}$	$(S-\frac{1}{2})\hbar\Omega$
33 meV	40 meV	4.85	1.23 eV	174 meV	171 meV	143 meV	143 meV
33 meV	50 meV	4.67	1.23 eV	174 meV	168 meV	143 meV	137 meV
33 meV	60 meV	4.50	1.22 eV	174 meV	165 meV	142 meV	131 meV
33 meV	70 meV	4.29	1.22 eV	174 meV	161 meV	142 meV	125 meV
33 meV	80 meV	4.05	1.21 eV	174 meV	156 meV	141 meV	117 meV
33 meV	90 meV	3.78	1.20 eV	174 meV	152 meV	140 meV	108 meV

Deep defect position

By knowing the zero-phonon line at $E_0 = 1.23\,\mathrm{eV}$ the value of the involved deep donor-like defect can be calculated. The deep S2A2 band stems from a donor-acceptor pair transition into the dominating shallow acceptor at 100 meV. The zero-phonon line was determined at low excitation intensities where the Coulomb-interaction is expected to be small. Thus, adding the 100 meV to the zero-phonon line energy, the deep donor-like level is at $E_\mathrm{S} = 1.33\,\mathrm{eV}$. But considering a possible error in the range of $10 - 20\,\mathrm{meV}$ from the Coulomb-interaction (E_0 could be lower) and 10 meV from the fitting, the deep donor-like defect level will be proposed at $E_{\mathrm{S2}} = 1.30 \ldots 1.33\,\mathrm{eV}$.

Without any fitting of strong phonon coupling and nearly Gaussian peaks, the deep involved defect in a donor-acceptor pair is calculated in general by Eq. (5.7). The concept of the shallow donor-acceptor pair transition in Eq. (3.14) is hereby extended by the Franck-Condon shift, which leads to the estimation of $E_\mathrm{S} = 1.34\,\mathrm{eV}$, if no Coulomb attraction is considered.

$$E_\mathrm{S} = \hbar\omega_\mathrm{max} + \underbrace{\left(\overbrace{\frac{1}{8\ln 2}\frac{W_0^2}{\hbar\Omega^2}}^{\text{Huang-Rhys}} - \frac{1}{2}\right)\hbar\Omega}_{\text{Franck-Condon shift}} + \overbrace{\underbrace{E_\mathrm{A}}_{\text{acceptor}} - \underbrace{(\hbar\omega_\mathrm{max} - E_\infty)}_{\text{Coulomb attraction}}}^{\text{if transition into acceptor}} \tag{5.7}$$

The finding of the deep defect energy at $1.3 \ldots 1.33\,\mathrm{eV}$ is the main result of this chapter. If one simply assumes the same Huang-Rhys factor for the second defect band S1A2 in $\mathrm{CuGaSe_2}$ with lower intensities, the second donor-like defect S1 could be estimated from the difference of the S2A2 and S1A2 peak positions at $E_{\mathrm{S1}} = 1.44 \ldots 1.47\,\mathrm{eV}$.

In the following section, the dominating defect band S2A2 will be studied further on different samples with lower Ga/(Ga+In) ratios to propose the defect position S2 over the whole range of $\mathrm{Cu(In,Ga)Se_2}$. The possible detrimental influence of this deep defect level on the electrical properties of a solar cell will be compared to literature data in the last section of this chapter.

5.2.3 Defect position with varying band gap

In the previous sections it is shown that the defect band at 1.1 eV involves a deep recombination center for electrons at around 1.30 − 1.33 eV. This defect band and thus also the energy level of the deep recombination center remains almost constant in energy when 20 % of gallium is replaced by indium. Therefore, it is interesting to study the defect band in solid solutions with even higher indium contents.

In Table 5.4 the compositions from EDX measurements is given for the series of Cu-rich $Cu(In,Ga)Se_2$. Only the sample with a GGI of about 0.3 is slightly Cu-poor. It will serve as a reference to state-of-the-art absorbers of high efficiency solar cells, which are usually grown under a copper deficiency and with a GGI of 0.3 [114].

Table 5.4: EDX results of the studied $Cu(In,Ga)Se_2$ samples

	Cu/(Ga+In)	Ga/(Ga+In)
$CuGaSe_2$	1.16	1.00
$CuGaSe_2$ (In-residuals)	1.19	0.98
$CuIn_{0.2}Ga_{0.8}Se_2$	1.14	0.79
$CuIn_{0.5}Ga_{0.5}Se_2$	1.29	0.46
$CuIn_{0.7}Ga_{0.3}Se_2$	0.99	0.29
$CuInSe_2$	1.24	0

In Fig. 5.19, an overview of the photoluminescence spectra at 10 K is given for each sample, except the slightly Cu-poor sample. The spectra are normalized to the low energy side of the deep defect band, whereas in the samples with no gallium ($CuInSe_2$) and with a GGI of 0.3, this band cannot be observed (see Fig. 5.20). Sample CGSe-228 (GGI 1.00) is not normalized to the low energy side in order to visualize the small peak shift. It was already shown in Fig. 5.15 that the deep band of this sample has the same shape and width like sample CIGSe-130 (GGI 0.80). Apart from the blue-shift in pure $CuGaSe_2$ (black curve), the deep band at 1.1. eV has nearly the same shape for all samples. Especially the low-energy side of the peaks is unaffected by the addition of indium. For this reason, it can be concluded that the phonon coupling (expressed by the Huang-Rhys factor S) remains also unaffected, if the phonon energy is constant or does not change too much. The phonon energy of the weak coupling in the near-band-edge luminescence is $\hbar\Omega_{\mathrm{CISe}} = 29\,\mathrm{meV}$ in the $CuInSe_2$-sample and $\hbar\Omega_{\mathrm{CGSe}} = 33\,\mathrm{meV}$ in the $CuGaSe_2$-sample. Therefore, the phonon energy will only change by approx. 2 meV when comparing e.g. a GGI of 1.0 and 0.5.

Such small differences in the phonon energy have a negligible influence on the peak shape and a nearly constant Huang-Rhys factor is the only explanation for the similar structure of the deep defect bands. If the Huang-Rhys factor is almost constant, the zero-phonon line will also be almost constant, because the photoluminescence maximum does not significantly change. As a result, the deep donor level around 1.30 − 1.33 eV is proposed to have the same energetic position in all samples with the deep luminescence at 1.1 eV. Due to the fact that precise evaluations of the zero-phonon line can just be done on single resolved peaks (CIGSe-130) it is in general more reasonable to compare the peak maxima and the undisturbed low energy side, than possible fitting models of the phonon coupling which are disturbed by other merging deep or shallow transitions.

Furthermore, it is conclusive that the deep defect band can not be observed at low gallium contents when the conduction band has crossed the defect level. It was already

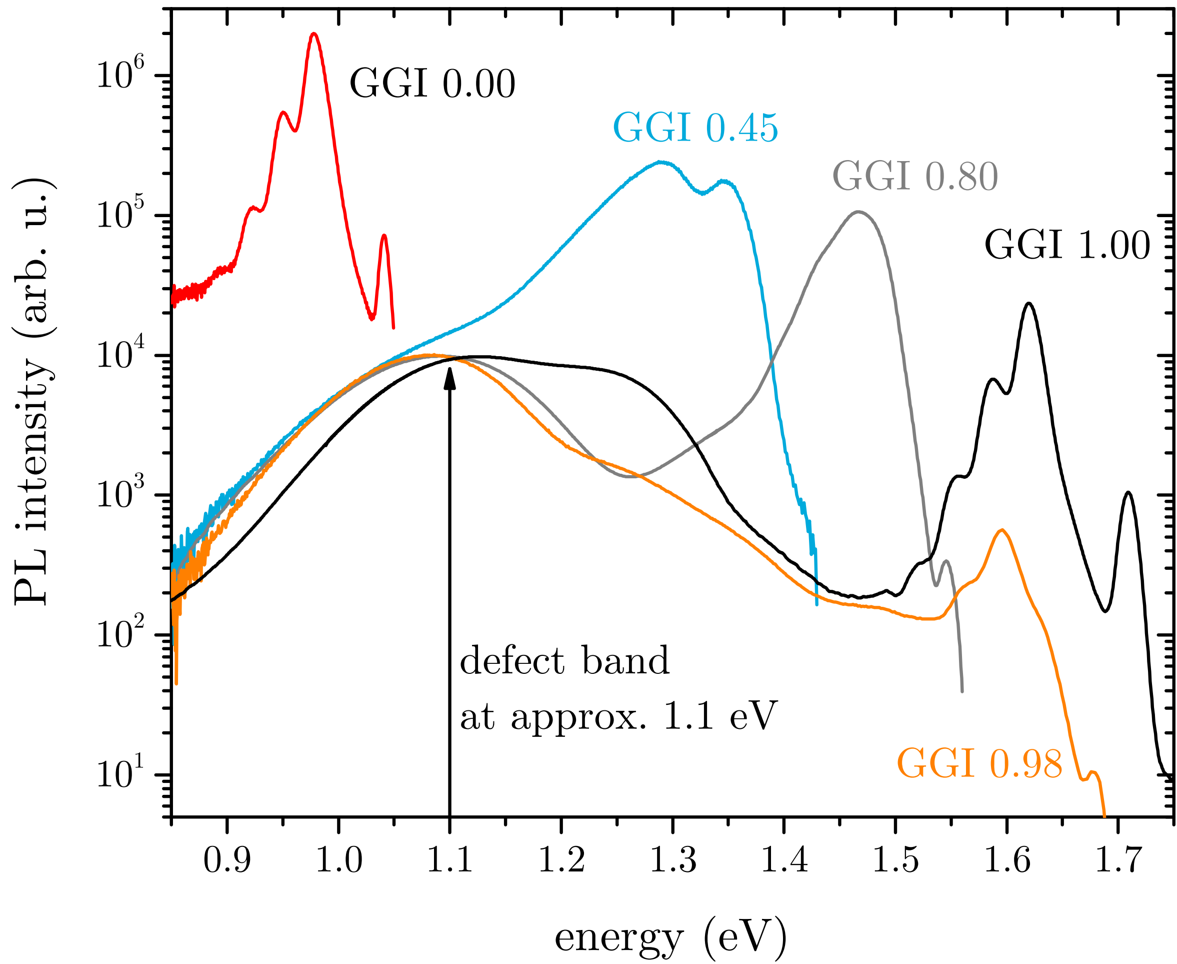

Figure 5.19: Photoluminescence spectra at 10 K from different Cu-rich Cu(In,Ga)Se_2 compositions. The curves are labeled with the Ga/(Ga+In) ratio (GGI) from EDX measurements and normalized to the low energy side of the defect band, except GGI-1.00 to visualize the small peak shift.

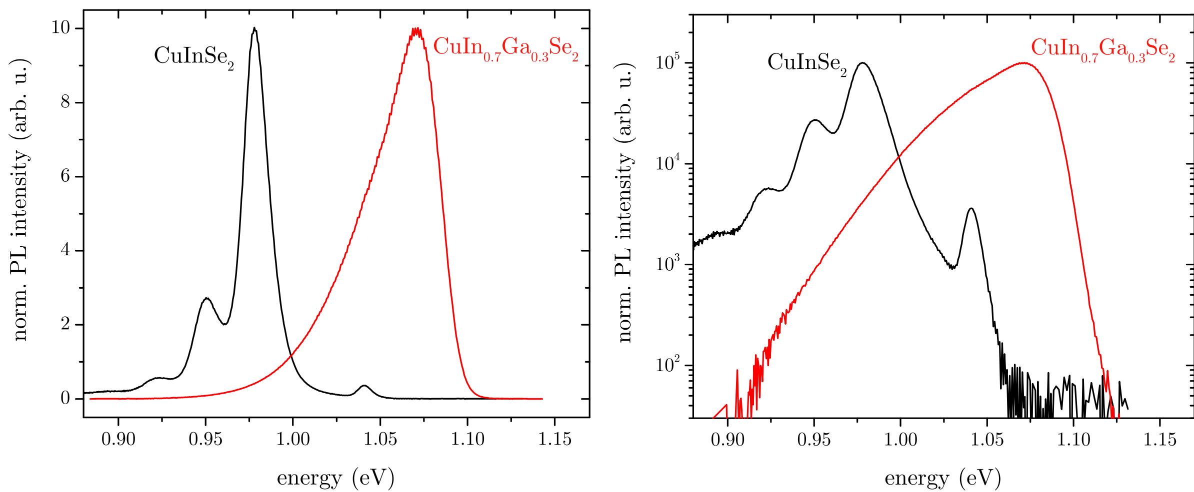

Figure 5.20: Photoluminescence spectra at 10 K of $CuInSe_2$ and Cu(In,Ga)Se_2 with 30 % gallium in linear (left) and logarithmic (right) scale.

mentioned in Section 5.2.1, that the valence band just changes by 0.04 eV with respect to the vacuum level in CuInSe$_2$ and CuGaSe$_2$. For simplicity, the valence band can be treated constant as the reference energy at 0 eV and the conduction band energy equals the band gap energy. If doing so, the conduction band is expected to cross the deep donor level in a single crystal with no strain at a GGI of around 0.42 (low temperature band gap $E_g = 1.3$ eV, see Fig. 1.4 in Chapter 1). This estimation is in good agreement with the photoluminescence results, where the deep defect band already merges with the near-band-edge luminescence in the sample with a GGI of 0.45 and completely disappears in the sample with a GGI of 0.3 (see Fig. 5.19). For the threshold of the GGI, not the maximum of the defect band matters, nor the zero-phonon line of the donor-acceptor pair, but the actual defect level of the deep donor.

Also a Cu-poor sample series was grown and measured at low temperatures which is shown in Fig. 5.21. This sample series was done at 100 mbar reactor pressure for testing the possibility of lowering the decomposition temperature of selenium (see Section 2.2.1). Unfortunately, this growth recipes resulted in very Cu-poor compositions and much thinner films of roughly 200 nm. Due to the small thickness, the composition measurements by EDX are disturbed by the detection of arsenic and gallium from the GaAs substrate. But estimating the amount of copper by reducing the total measured gallium atomic percentage by the measured arsenic atomic percentage yields values for the CGI of around 0.5 − 0.7. But as seen in Fig. 5.21, also for the very Cu-poor compositions a similar appearance of the deep defect band at 1.1 eV as for the Cu-rich thin films is measured. The near-band-edge luminescence shifts proportional to the increasing amount of indium and thus proportional to the band gap, whereas the deep defect band at 1.1. eV seems to be constant in energy. It is proposed that the 1.1 eV defect band and thus the deep donor S2, most likely can occur in measurable quantities in Cu-rich and Cu-poor thin films

As soon as the deep donor at 1.30 − 1.33 eV is resonant with the conduction band, no recombination from this level will occur which could be confirmed by future studies and smaller variations of the GGI. This observation is important for the electronic properties of different gallium compositions, since this defect level can have harmless or detrimental influences on the minority carrier concentration (electrons). For the following discussions, the resonance of the conduction band and the deep defect will be proposed at 1.3 eV. For all compositions below this value, the donor defect can influence the doping density and the defect compensation of the thin film at room temperature, but it cannot be a harmful recombination center.

On the other hand, for compositions above a band gap of 1.3 eV, electrons more likely recombine over the defect, which lowers the quasi Fermi level splitting. According to Shockley-Read-Hall statistics, the recombination rate will depend on the defect depth up to a certain limit where re-emission to the bands get negligible (see Section 1.2.2). Thus, it is expected that with increasing Ga-content, the recombination over the deep donor increases due to an increasing energetic distance of the donor-like defect to the conduction band. A lower electron concentration and lower quasi Fermi level splitting are the consequence. Since the quasi Fermi level splitting is closely connected to the open circuit voltage of a solar cell device as an upper limit, the efficiency of a solar cell can be significantly decreased for high Ga-contents. This hypothesis will be supported in the following section by simulations of solar cell devices with SCAPS.

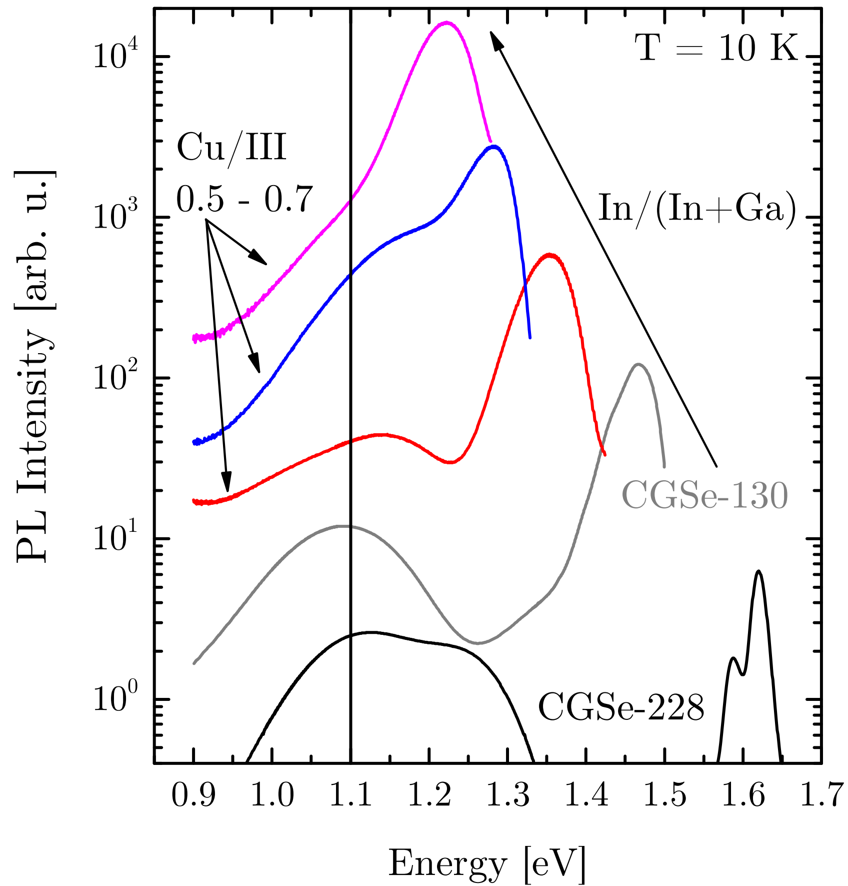

Figure 5.21: Photoluminescence spectra of 10 K measurements for the Cu-rich compositions CGSe-228 and CIGSe-130 in comparison with very Cu-poor compositions (CGI approx. 0.5 − 0.7) from growth processes with 100 mbar reactor pressure. All spectra are arbitrarily shifted in intensity for better visualization of the deep defect band around 1.1 eV.

5.2.4 Simulations for solar cell devices

Based on the findings of a deep recombination center for electrons at $1.30 - 1.33$ eV in Cu(In,Ga)Se_2 with Ga/(Ga+In) ratios above or equal to 0.45, the possible detrimental influence on solar cell devices will be studies in this last part. State of the art thin film solar cells with Cu(In,Ga)Se_2 absorber are made of Cu-poor compositions, where the deep defect band S2A2 is also observed in epitaxial films. The characterization for polycrystalline thin films from growth by physical vapor deposition is currently part of the research at LPV. The deep donor-like level E_{S2} will be attributed to the intrinsic Ga_{Cu} antisites in chapter 7.3. From theory it is expected that this antisite occurs in rather high concentrations in Cu-rich, and even higher concentrations in Cu-poor composition. Therefore it is conclusive to study the influence of this deep recombination center on the electrical parameters of a solar cell device and compare it with available literature data of gallium-variations.

From Shockley-Read-Hall statistics it is known that defects closer to the middle of the band gap are much more efficient non-radiative recombination centers for minority carriers (here electrons) as compared to defects close to the band edge (see section 1.2.2). Increasing recombination of minority carriers by defects reduces the quasi-equilibrium concentration under illumination. Thus the quasi Fermi level is reduced, which limits the maximum possible open circuit voltage in a solar cell device. For visualizing the influence of the deep defect, simulations are performed by simulations with SCAPS [115, 116], version 3.2.0.1. SCAPS is a 1-dimensional numerical simulation tool originally developed for thin film solar cell devices of CdTe or Cu(In,Ga)Se_2. In this thesis, the software will only be used for simulations of current-voltage curves to extract the solar cell parameters for the open circuit voltage V_{oc} [V], short circuit current density j_{sc} [mA/cm^2], fill factor FF [%] and the efficiency η [%] (see Ref. [60] for basic explanations of the parameters).

Table 5.5: Parameters used for the SCAPS-1D simulations

	ZnO	CdS	Cu(In,Ga)Se_2
d (nm)	200	50	3000
E_g (eV)	3.3	2.4	1.0 – 1.68
$\varepsilon/\varepsilon_0$	9	10	13.6
N_C (cm^{-3})	4×10^{18}	4×10^{18}	7×10^{17}
N_V (cm^{-3})	9×10^{18}	9×10^{18}	2×10^{19}
v_{th} (cm/s)	10^7	10^7	10^7
μ_n (cm^2/Vs)	20	20	20
μ_p (cm^2/Vs)	20	20	20
N_D (cm^{-3})	10^{18}	10^{17}	0
N_A (cm^{-3})	0	0	10^{16}
α_0 (1/cm)	0	0	10^4
B_{rad} (1/cm^{3}s)	0	0	10^{-10}
E_d (eV)	–	–	1.3
N_d (cm^{-3})	–	–	5×10^{15} (varied)
σ_n (cm^2)	–	–	10^{-13}
σ_p (cm^2)	–	–	10^{-13}

The used values for the simulation are given in Table 5.5, taken from Ref. [66]. The absorption coefficient is set for all $Cu(In,Ga)Se_2$ compositions to the ideal case with no tail states (no Urbach tailing) by using [66]:

$$\alpha(\hbar\omega) = \alpha_0 \sqrt{\frac{\hbar\omega - E_\mathrm{g}}{k_\mathrm{B}T}} \tag{5.8}$$

The absorption constant α_0 as well as the radiative recombination coefficient B_rad for the ZnO window- and CdS buffer-layer are set to zero, so that an ideal solar cell with only generation and recombination in the absorber is considered. Also the front- and back-contact recombination are negligible small by setting the surface recombination velocities to only 10 cm/s and applying the flat band conditions at the contacts in SCAPS. For simplicity reasons, no intrinsic ZnO layer is added to stack, which does not effect the outcome of this simulation. For the p-type doping of all $Cu(In,Ga)Se_2$ absorber (for all varying band gaps) a reasonable doping density of $10^{16}\,\mathrm{cm}^{-3}$ is chosen. The n-type doping density N_D of the CdS and ZnO layer have no influence on the results as long as the doping density of ZnO is far above the doping density N_A of $Cu(In,Ga)Se_2$. By doing so, it is ensured that the space charge region only extends into the absorber and thus the width of the space charge region is only determined by the doping of the p-type absorber.

For the simulation of the deep donor-like defect, a singly charged donor level at 1.3 eV above the valence band is added to the absorber layer with a homogenous distribution throughout the film. The minimum minority carrier lifetime τ_n0 (only, if the deep defect is active) is given by:

$$\frac{1}{\tau_\mathrm{n0}} = \sigma_\mathrm{n} v_\mathrm{th} N_\mathrm{d}. \tag{5.9}$$

An increase of the unknown capture cross section can be compensated by the same proportional decrease of the defect density N_d, yielding the same minimal lifetime. For this reason, the unknown capture cross sections are set to 10^{-13} for electrons and holes and only the defect density is tuned.

The band gap of the absorber is varied between 1.0 eV and 1.68 eV to match all possible band gaps of $Cu(In,Ga)Se_2$ compositions. The band gap dependent change of the relative permittivity $\varepsilon/\varepsilon_0$ can be neglected and does not change the obtained curves (13.6 in $CuInSe_2$ and 11.0 in $CuGaSe_2$). Furthermore, the band gap dependent electron affinity χ_e is also disregarded. Knowing that usually a "spike" is observed for the band alignment between CdS and low-Ga $Cu(In,Ga)Se_2$ (see Fig. 1.5 in Section 1.2.1) and a "cliff" between CdS and $CuGaSe_2$ or high-Ga $Cu(In,Ga)Se_2$, perfect band alignment is chosen for all simulations. Only the influence of the deep defect to the open circuit voltage will be evaluated and blocking behaviors for the current (high "spike") or high recombination currents at the interface (high "cliff") will be not considered. This approach is also supported by the fact that in recent research, the CdS buffer is replaced with other materials, having a tunable band gap (tunable electron affinity), which ensures a good band alignment. But the solar cell devices of e.g. $CuGaSe_2$ still suffer from too high bulk recombination [37].

In the most recent record cell for $CuGaSe_2$, the CdS buffer layer is replaced by a layer of $Zn_{1\text{-}x}Sn_xO_y$ and the electronic properties yield an efficiency of $\eta = 11.9\,\%$ with $V_\mathrm{oc} = 1017\mathrm{mV}$ [37]. Although this is the first demonstration of a $CuGaSe_2$ device with an open circuit voltage above 1 V, the open circuit voltage deficit is still at 0.66 eV and more than 150 meV higher than in $CuInSe_2$ or $Cu(In,Ga)Se_2$ with low gallium contents. The fact that $CuGaSe_2$ devices with CdS buffer layers can also exhibit values of an open circuit

voltage close to 1 V (946 mV in Ref. [117]) implies that band-misalignment between the buffer and the absorber cannot be the major source for the large deficit alone. Furthermore the authors in Ref. [37] have shown that the temperature dependent open circuit voltage in the record device extrapolates to the band gap at 0 K, which indicates dominating bulk recombination rather than interface recombination.

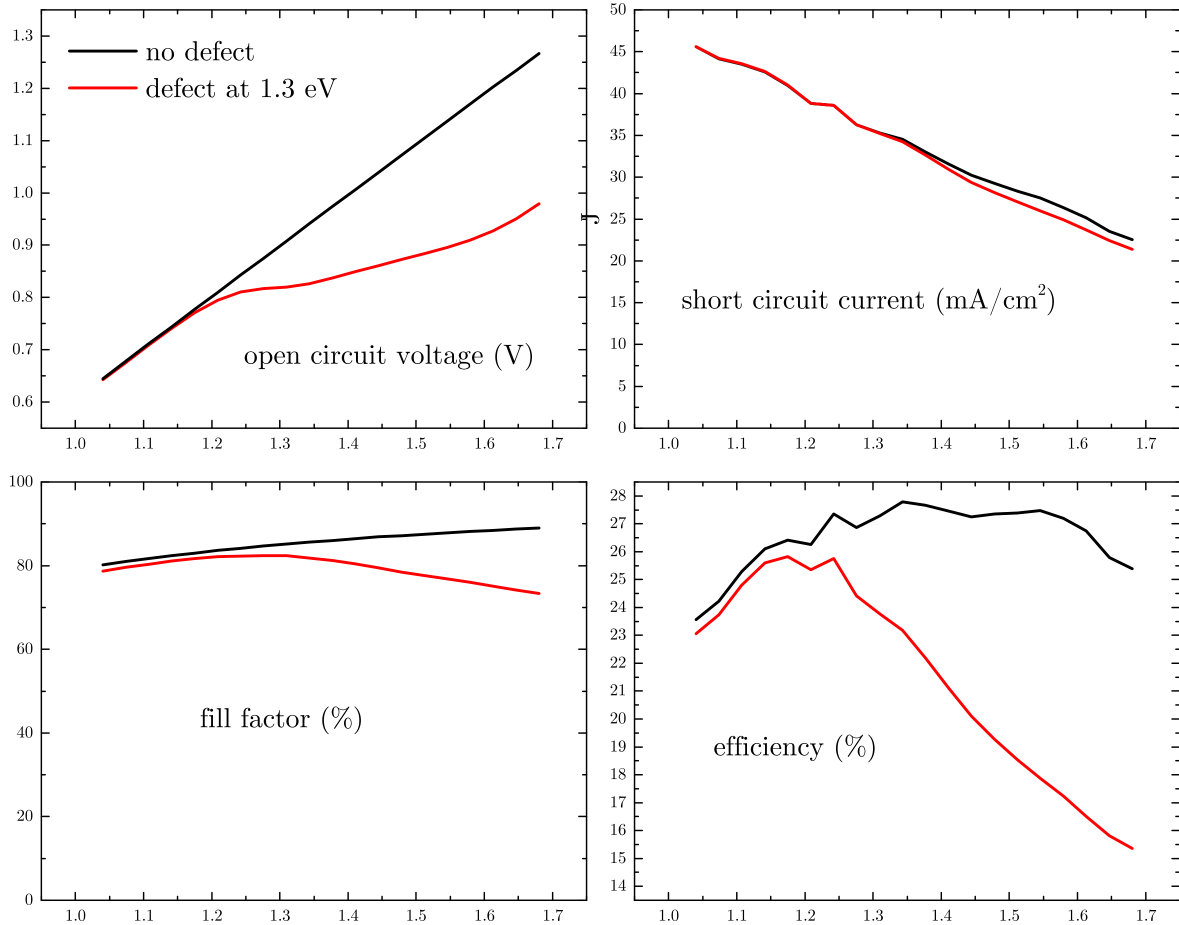

Figure 5.22: Band gap dependence of the open circuit voltage V_{oc}, short current density j_{sc}, fill factor FF and efficiency η from the simulation of the current-voltage characteristic of ZnO/CdS/Cu(In,Ga)Se_2 solar cell devices. The simulation parameters are given in Table 5.5. The defect density of the deep donor set to 1.3 eV above the valence band is 0 (black curve) or 5×10^{15} cm^{-3} (red curve).

After eliminating possible influences of the contacts, band alignment or insufficient absorption, the resulting main solar cell parameters from the simulations are shown in Fig. 5.22. For the black and the red curve, without any deep defect in the absorber, it is obvious that the open circuit voltage is directly proportional to the band gap. The short circuit current density is determined by the full absorption of the sun spectrum for energies above the band gap E_g. If the defect density of the level at 1.3 eV is set to e.g. 5×10^{15} cm^{-3}, the short current density is just slightly affected. But the open circuit voltage deviates strongly for band gaps higher than the defect level compared to the defect-free case, reducing also slightly the fill factor. The defect density N_d was not arbitrarily chosen. It was tuned to $E_d = 5 \times 10^{15}$ cm^{-3}, so that for $CuGaSe_2$ with the highest band gap, the record open circuit voltage around 1 V is matched. It is important

to mention that only the defect density changes the slope of the open circuit voltage in this example (see Appendix C). Other parameters like the radiative recombination coefficient B_{rad}, the front and back-contact recombination velocity $S_{\mathrm{f,b}}$, doping density N_{A}, or absorption α_0 would reduce all values equally and band gap independent.

In principle, the defect energy level (which is fixed and known) determines the turning point at which the open circuit voltage starts to deviate from the ideal defect-free case and its defect density determines the slope of this deviation for large band gaps above the defect level. The higher the defect density, the lower the slope. It is clear that the open circuit voltage deficit ($E_{\mathrm{g}} - V_{\mathrm{oc}}$) increases with higher band gaps if the deep defect is present. This is due to the formerly mentioned increased recombination by Schockley-Read-Hall when the deep defect gets further away from the band edge. In summary, three important conclusions can be drawn:

- Adding the defect results in an efficiency drop, which is mostly induced by the reduced open circuit voltage.
- Adding the defect results in two different band gap regimes. For band gaps below E_{d} the open circuit voltage is not affected and for band gaps above E_{d}, the open circuit voltage deficit is higher.
- For band gaps above E_{d}, the open circuit voltage deficit increases with the band gap, reaching the maximum for $\mathrm{CuGaSe_2}$.

In Fig. 5.23, the obtained open circuit voltages from SCAPS simulations for different band gaps in the defect free-case and with the defect at 1.3 eV are shown in comparison to the experimental data of solar cell devices from literature. From the literature data, the typical observation of a non linear increase for the open circuit voltage with the band gap can be seen. For band gaps below 1.2 – 1.3 eV linear relationships between V_{oc} and E_{g} can be realized [119, 122]. One has to be careful when comparing samples with graded and ungraded Ga/(Ga+In) distributions inside the absorber. Graded absorbers with higher gallium contents at the front and the back outperform ungraded absorbers due to reduced recombination at the interfaces, but not necessarily due to lower amounts of deep recombination centers. As an example, the full curves for the open circuit voltage from simulations are shifted down by 0.1 eV in Fig. 5.23 for possible band gap independent losses. The simulations suggests that it could be possible that the experimentally found deep donor-like defect S2 is responsible for the low open circuit voltages of wide-gap $\mathrm{Cu(In,Ga)Se_2}$ solar cells.

From this chapter it will be assumed that the dominating deep defect S2 remains almost constant at 1.3 eV above the valence band maximum and is resonant with the conduction band for Ga/(Ga+In) ratios lower than approx. 0.45. If the defect level is resonant with the conduction band it can be assumed that a hydrogen-like state close to the conduction band is formed. In this case the defect is a shallow donor which can contribute to doping and compensation of acceptors but not to non-radiative Shockley-Read-Hall recombination. Simulations of the band gap dependent open circuit voltage, where the defect level is set to the conduction band minimum if the defect level energy falls inside the band can be found in the Appendix C. In principle nearly the same shape as in Fig. 5.23 is obtained for the defect level at 1.3 eV but in Fig. 8 the transition from the linear region of V_{oc} to the non-linear region is in this case exactly at the defect position.

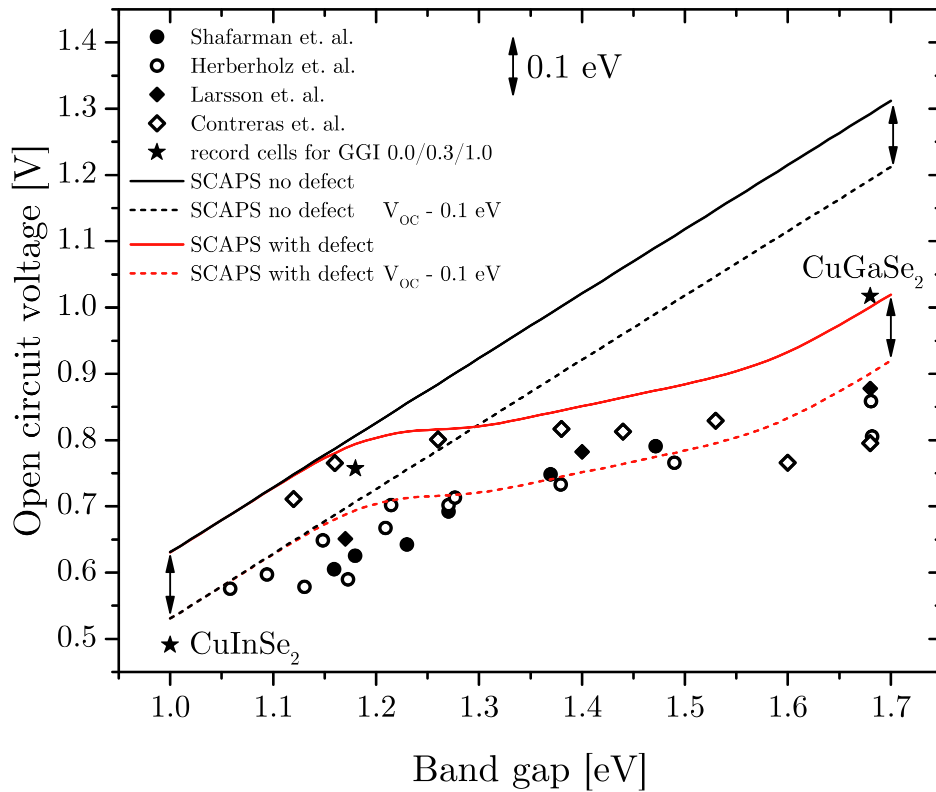

Figure 5.23: Open circuit voltage from SCAPS simulations for the defect-free case (black) and with a defect at 1.3 eV (red) above the valence band in comparison to literature data. The references are Shafarman et. al. [118], Herberholz et. al. [119], Larsson et. al. [37], Contreras et. al. [120] and the record cells with a GGI of 0 [121], approx. 0.3 [114] and 1.0 [37].

Chapter 6

Defect Band at 0.7/0.8 eV

In the present chapter, the observation of two additional defect bands at 0.7 eV and 0.8 eV are studied and described. Starting with measurements on the ternary $CuGaSe_2$ and solid solutions of $Cu(In,Ga)Se_2$ with high Ga-contents in the first section, a deep defect transition is found around 0.7 eV at low temperatures (10 K) with the extended setup. No such transition is observed in a $CuInSe_2$ sample.

At high temperatures (300 K), the signal at 0.7 eV for high Ga-contents is too low for the detection with the InAs-detector of the extended setup. The low energy luminescence is further dominated by the formerly shown defect band around 1.1 eV which is very broad at room temperature. But in the second section it will be shown that with the standard setup and at room temperature, a broad defect band at 0.8 eV can be partly resolved for samples with no or low Ga-contents (low band gap). Whereas this 0.8 eV band seems to appear in all Cu-rich samples, a comparison with a nearly stoichiometric crystal leads to the assumption of a possibly decreasing defect band intensity with decreasing copper content. Furthermore, the deep transition is not detected in Cu-poor compositions. At low temperatures, the 0.8 eV band is measured just in one sample. It is proposed that the observed 0.7 eV and 0.8 eV may have the same structural defect origin and the peak energies may confirm a defect level found exclusively by photocapacitance measurements at 0.8 eV in several publications. This discussion is part of Section 7.2.2 in Chapter 7.

In the last third section, possible influences from the substrate by the EL2 defect transition in GaAs with a comparable photoluminescence peak range of 0.6 – 0.8 eV will be ruled out by measurements of a bare substrate wafer. All results of this chapter are mainly based on the straightforward measurement of photoluminescence peak positions rather than extensive characterization methods like temperature and intensity dependent measurements. The reasons are low signal intensities with the extended setup and the limit of already high laser powers needed to observe the shown peaks. Nevertheless, the present findings reveal novel results for possible defect levels at 0.7 eV or 0.8 eV which are useful and consistent with the proposed defect model in the last Chapter 7.

6.1 Photoluminescence at low temperatures

In this section, the first observation of a very deep defect band close to the middle of the band gap in $CuGaSe_2$ and wide-gap $Cu(In,Ga)Se_2$ will be shown. By using the extended setup with an InAs-detector (see Section 3.3.2), the possible spectrally calibrated measurement range is extended to lower energies from 0.80 to about 0.55 meV, but at the cost of lower sensitivity.

6.1.1 Measurements on $CuGaSe_2$ and high-Ga $Cu(In,Ga)Se_2$

Starting with the reference sample CGSe-228, the low energy spectrum is given in Fig. 6.1. To highlight the importance of a precise spectral correction with the reference lamp, the spectrum is shown with the applied correction function (bottom) and without it (top). If the spectrum is properly corrected, a close to Gaussian shaped peak at 0.69 eV can be clearly resolved. Unfortunately, the extended setup needs much higher laser powers to obtain a reasonable signal-to-noise ratio, which can be verified with the already known deep S2A2 transition. In Fig. 6.1, the maximum excitation density for the red laser diode of 800 W/cm^2 is used at 10 K. In this case heating of the sample cannot be excluded. But comparisons of the already known S1A2 and S2A2 peaks with varying excitation showed only minor influences of the peak width for such high excitation densities. All appearing deep peaks are rather broad and thermal broadening has a negligible contribution. Furthermore, if the broadening is e.g. limited by phonon coupling, Eq. (5.3) together with a phonon energy of 33 meV for $CuGaSe_2$ yields deviations of the full peak width by only 5 % if the temperature would increase due to excitation from 10 K to unreasonable high values of 130 K. It is therefore concluded that a potential temperature increase because of the high laser power used has just a minor influence on the general peak shape. But it can be expected that uncontrolled heating of the sample affects the peak intensities. The signal-to-noise ratio is already low for the highest laser power and intensity dependent measurements of at least one order of magnitude could not be conducted. The same limitation applies for temperature dependent measurements, where the intensity would further decrease with increasing temperature.

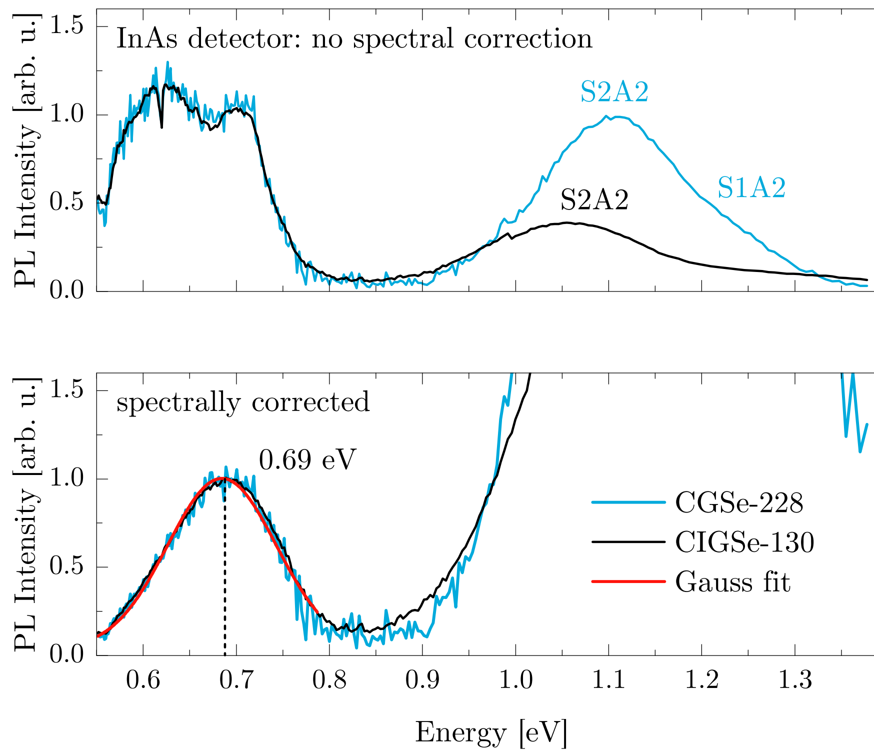

Figure 6.1: Photoluminescence spectrum of sample CGSe-228 and CIGSe-130 at 10 K, measured with the InAs-detector and the extended setup. The spectrum is shown without any spectral correction (top) and with the correction by a calibrated halogen lamp (bottom).

The characterization of the deep defect band at 0.69 eV is limited to the peak width and e.g. the composition dependence. The peak does not change, when comparing the Cu-rich samples CGSe-228 ($CuGaSe_2$) and CIGSe-130 ($CuIn_{0.2}Ga_{0.8}Se_2$) in Fig. 6.1 and it is reasonable to assume that the defect band originates from the same defect level or donor-acceptor pair. As a first conclusion, the free-to-bound transition from the conduction band into a defect level is excluded, since the conduction band gets lowered by 0.16 eV when 20 % of gallium are replaced by indium (see Section 5.2.1). It is unlikely that a deep defect shifts perfectly equal to the conduction band in energy. The other remaining possibilities are the recombination from a deep level into the valence band or into a shallow acceptor level. The shallow level A2 at 100 meV above the valence band is the dominant acceptor in both samples. All the other transitions which were observed at low temperatures before, including DA2, S1A2 and S2A2 occur from a recombination into this level A2. It is possible that also the deep transition at 0.69 eV originates from a recombination into the shallow acceptor A2 if it is a donor-acceptor pair transition. But the recombination into the valence band cannot be ruled out at this stage. In the case of the assumed donor-acceptor pair, the deep defect level would lie at approx. 0.79 eV above the valence band. In the case of the assumed free-to-bound transition, the defect level would lie at approx. 0.69 eV above the valence band, without considering any Franck-Condon shift due to phonon coupling in both cases.

Because the defect band is rather broad, possible influences of phonon coupling have to be considered for the evaluation of the defect level, too. The FWHM peak width W in both samples is 143 meV. By applying the model of phonon coupling as it is done in the previous sections, the zero-phonon line can be estimated from the phonon energy and the peak width alone. Inserting the FWHM-value W and the known phonon energy of $\hbar\Omega = 33$ meV into Eq. (5.4) and Eq. (5.5) yields a Huang-Rhys factor of 3.4, a Franck-Condon shift of 96 meV and a zero-phonon line at $E_0 = 0.79$ eV. With these conditions, the defect level lies at 0.79 meV for the possible free-to-bound transition and at 0.89 eV for the possible donor-acceptor pair transition into the shallow acceptor A2. The values are summarized in Table 6.1.

Table 6.1: Possible energy levels for the deep defect S3, involved in the photoluminescence band at 0.69 eV (10 K) with FB (free-to-bound transition), DA (donor-acceptor pair transition into A2) and PC (phonon coupling).

	FB	DA	FB+PC	DA+PC
E_{S3} [eV]	0.69	0.79	0.79	0.89

From the former considerations, the possible energy range of the involved deep defect is restricted to 0.69 − 0.89 eV. Taking into account that the energy position of the defect band in sample CGSe-228 and CIGSe-130 is exactly the same, the attribution to a free-to-bound transition is more likely than to a donor-acceptor pair transition. The defect densities would need to be the same in both samples in order to have an equal Coulomb-attraction for the same laser power, resulting in the same transition energy for a donor-acceptor pair. Even if the differences in the shift from different terms for the Coulomb attraction are small, the high laser power used and the uncontrolled heating of the sample above the set temperature of 10 K are at least supporting arguments for a free-to-bound transition. Free-to-bound transitions generally can get dominant compared to a donor-acceptor pair transition, if for one of the involved donor or acceptor level, defect saturation

or increased ionization at higher temperatures occurs. The possibility of a donor-acceptor pair transition together with strong phonon coupling cannot be ruled out completely, but in the following, the most reasonable energy range of 0.69 – 0.79 eV is used for discussions of the deep defect S3.

6.1.2 Measurements on $CuInSe_2$

For studying the low energy range and a possible occurrence of the deep band S3 in the gallium-free ternary, also a Cu-rich $CuInSe_2$ sample is measured at low temperatures and with the extended setup. But no distinct peak around 0.7 – 0.9 eV can be observed. The exemplary spectrum of sample CISe-101 is depicted in Fig. 6.2. In the inset the raw and spectrally corrected measurement is shown for energies from 0.65 eV to 0.85 eV in order to highlight the importance of the precise correction for the extended setup. An apparent peak in the same region where the deep S3 level would be expected disappears after the spectral correction is applied.

In accordance to the known results from literature (see Section 1.3), the Cu-rich $CuInSe_2$ sample shows the expected characteristic peaks of the near-band-edge luminescence. The dominating DA2-transition at 0.97 eV from a shallow donor D1 ($\approx$ 10 meV) into a shallow acceptor A2 ($\approx$ 60 meV) together with visible phonon replica DA2-LO1 and DA2-LO2, a small contribution from the DA1-transition as well as an exciton transition can be resolved. For energies lower than 0.9 eV, the photoluminescence signal appears to decrease exponentially. Possible explanations for this dependence could be exponentially distributed tail states [44] and its origin can be a motivation for future studies. Another possible explanation could be the contribution from further phonon replica, where the energy distribution of the phonon lines smears out with increasing phonon number and yields an apparent exponential decrease of the photoluminescence intensity. But from Fig. 6.2 it is clear that a deep defect transition S3 like in the case of $CuGaSe_2$ cannot be observed in this spectrum of $CuInSe_2$. The defect transition is possibly absent or hidden in the exponential decay. But apart from the low temperature measurements, deep luminescence is observed at room temperature, which will be discussed in the following section.

6.2 Photoluminescence at room temperature

In measurements at room temperature, deep luminescence is observed around 0.8 eV in samples with no or low gallium content (GGI$\leq$ 0.5). The partly resolved transition is shown as well as its apparent vanishing with lower copper content.

6.2.1 Measurements on low band gap samples

Any defect level at 0.7 – 0.8 eV is far enough from the band edges, so that it is unlikely to be completely thermally activated at room temperature and radiative recombination over this defect could be possibly observed. Unfortunately, the defect band at 1.1 eV is dominating the sub-band gap spectrum at room temperature in e.g. sample CGSe-228, making it difficult to observe other low intensity transitions (see Fig. 5.5 in Section 5.1.2). Also the fact that the radiative photoluminescence efficiency is much lower at 300 K compared to 10 K hinders the detection of any defect signals with the extended setup and the InAs-detector at room temperature. Nevertheless, with the standard setup and

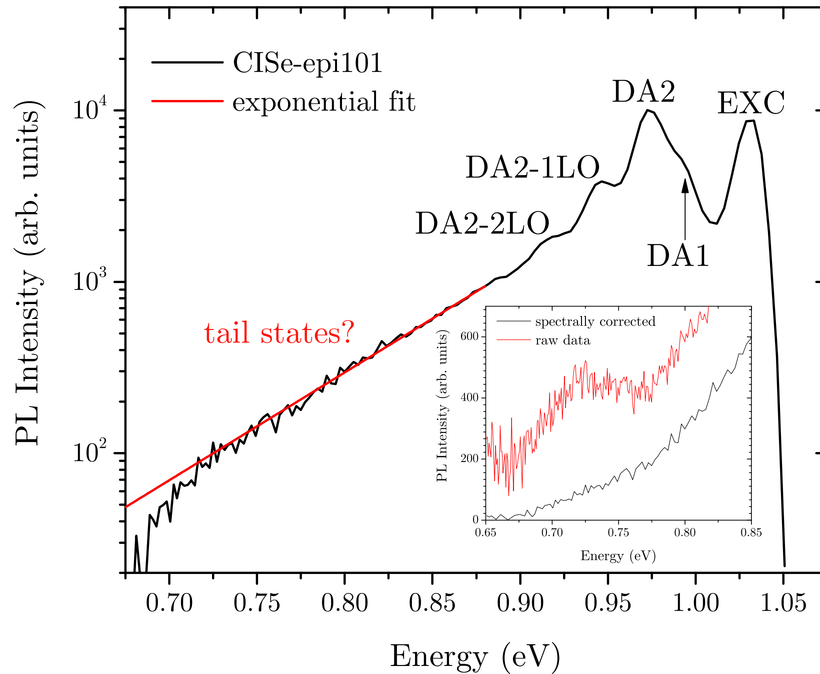

Figure 6.2: Low temperature spectrum (10 K) of a Cu-rich $CuInSe_2$ sample (CISe-101) with the extended setup. Known shallow transitions are labeled according to the literature and a exponential function is fitted to the low energy region (red curve). The inset shows the raw and the spectrally corrected data at 0.65 − 0.85 eV.

the InGaAs-CCD camera with high sensitivity, deep luminescence can be measured for energies down to 0.78 eV.

In gallium free $CuInSe_2$ and in $CuIn_{0.5}Ga_{0.5}Se_2$, a broad defect transition at 0.8 eV can be observed at room temperature. Generally, all Cu-rich samples, independent of the growth process (polycrystalline by PVD or epitaxial by MOVPE) show deep sub-band gap photoluminescence at room temperature. In the case of polycrystalline samples this was studied at LPV by Finn Babbe. At room temperature, the near-band-edge luminescence typically consists of the band-to-band transition with a broadened low energy side due to tail states close to the conduction or valence band. But in Cu-rich compositions, photoluminescence signals are also detected at energies 100 − 200 meV below the band gap which clearly don't belong to the near-band-edge luminescence. The difficulty to resolve these signals arises from the fact that e.g. strong interference effects of photoluminescence light can be present in some samples [82]. Especially for polycrystalline samples it was proven at LPV by Finn Babbe and Max Wolter, that the constructive and destructive interference from photoluminescence light traveling back and forth in a 2 − 3 μm thick thin film, can lead to disturbed measurements. Several interference peaks can appear in the broad photoluminescence signal of only one peak or an usually broad Gaussian defect band can get smeared out and appears more or less like an "apparent background". If furthermore the signal intensity of this "apparent background" is low, it is possible that actual defect transitions can be overseen. The same holds true in epitaxial films by MOVPE and strong interferences are also measured in rather thick samples of more than 1 μm. But standard epitaxial samples with 5 h growth duration have thicknesses of 600 nm or below.

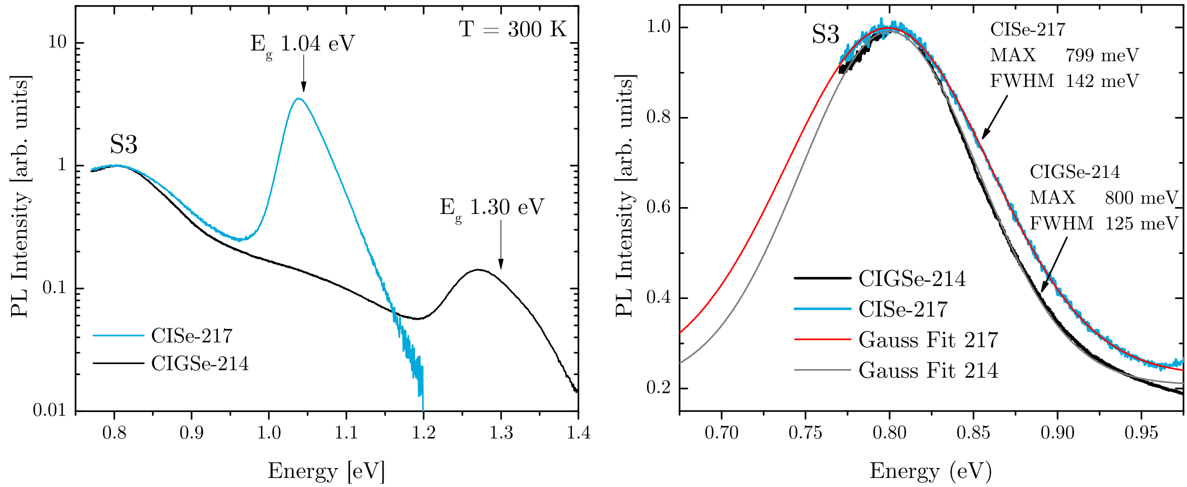

Figure 6.3: Room-temperature photoluminescence of a Cu-rich $CuInSe_2$ sample and Cu-rich $Cu(In,Ga)Se_2$ sample normalized to the deep 0.8 eV transition (left). On the right side, the deep transitions are shown in linear scale together with Gaussian peak fits.

In these thin epitaxial samples, no interferences effects are detected or the wavelength differences of constructive and destructive interference becomes simply too broad. As a result, an undisturbed Gaussian defect transition at 0.8 eV can be partly resolved in room temperature measurements with the standard setup. In Fig. 6.3 the spectra of a Cu-rich $CuInSe_2$ and $CuIn_{0.5}Ga_{0.5}Se_2$ sample are shown in comparison with a normalization to the defect band. As it can be seen, the peak at 0.8 eV is not fully resolved, but the maximum falls inside the available measurement range. The corresponding Gaussian fits are depicted on the right side of Fig. 6.3 for both samples. The peak maxima are identical and the peak width are in a comparable range with 142 meV for CISe and 125 meV for CIGSe. The broad peak width can be result from a broad defect distribution (density of states) or it results again from strong electron-phonon coupling.

In several publications from literature, a so-called 0.8 eV defect is known since more than 15 years [123]. So far this level is exclusively reported in photocapacitance measurements [123, 124, 125]. With only one excepetion, Mansfield et. al. reported a defect transition at 0.79 eV with a maximum temperature of 225 K, but a much smaller peak width of about 30 meV [126]. The observed defect band in Fig. 6.3 matches the energy of 0.8 eV very well. Also in the photocapacitance measurements in literature, rather high temperatures of 150 K were used and Heath et. al. [123] reported a fitted peak width of about 0.13 eV which is again in good agreement with the present findings in Fig. 6.3.

Furthermore, photocapacitance measurements in literature yield the same defect level independent of the Ga/(Ga+In) ratio. Indeed, in the present photoluminescence spectra no peak shift is observed for a sample with 50 % gallium and without, but future studies are needed. Also the previous results of a defect level at 0.69 - 0.79 eV in low temperature measurements of thin films with high gallium contents have possibly the same or similar defect origin as the 0.8 eV defect.

6.2.2 Influence of the copper content

In Cu-rich samples, independent of the Ga/(Ga+In) ratio, deep photoluminescence bands below the well known near-band-edge luminescence are observed in all thin films (see the former parts). In Fig. 6.4, the room temperature spectra of samples with different band gaps and also different copper content are given. The Cu-rich sample CISe-217 is the same as in the previous section with a partly resolved defect band at 0.8 eV. Sample CISe-230 contains also no gallium, but has a Cu/(Cu+In) ratio slightly below 1. This value is measured by EDX and confirmed by the much broader near-band-edge luminescence due to typical potential fluctuations in copper compositions close to or below stoichiometry. The copper deficit also leads to a small reduction of the band gap [127].

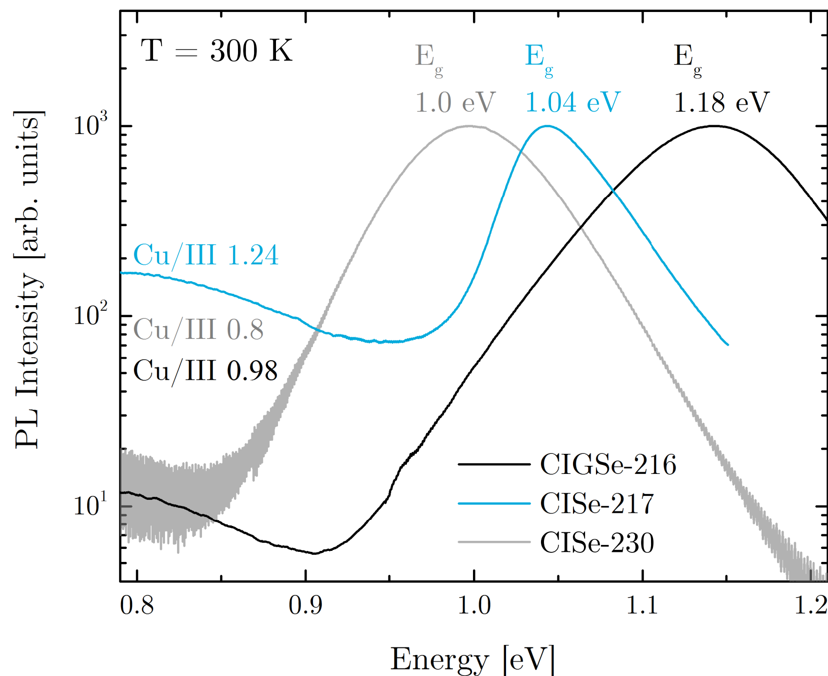

Figure 6.4: Room temperature photoluminescence of Cu-rich $CuInSe_2$ and slightly Cu-poor $Cu(In,Ga)Se_2$ with a Ga/(Ga+In) ratio of 0.3.

When comparing the near-band-edge luminescence relative to the intensity at 0.8 eV, the deep defect signal is at least one order of magnitude higher in the Cu-rich sample. On the other hand, the intensity of sample CISe-230 reaches already the background noise level at 0.8 eV. The measurement of sample CIGSe-216 with the same gallium content as used in state-of-the-art absorber for solar cells (GGI≈ 0.3) supports the copper influence. For this sample, which is close to stoichiometry, the deep defect band can be still detected. The peak ratio to the near-band-edge luminescence apparently shifts downwards by one order of magnitude compared to CISe-217. Furthermore it is worth mentioning that in measurements from Max Wolter on bare absorbers and even lower copper contents (CGI≈ 0.9 no such deep band can be detected.

It can be concluded from a small study that the deep defect intensity at 0.8 eV and room temperature measurements possibly decreases with decreasing copper content in the films. This behavior could be a possible reason for the higher non-radiative recombination in Cu-rich compositions [9]. An attribution to intrinsic defect levels from calculations found in literature will be done in Chapter 7.

6.3 Comparison with substrate luminescence

In GaAs, a well-known intrinsic defect exists, which is labeled as EL2 and attributed to the As_{Ga} antisite [128, 129, 130]. The defect is found to be a deep donor level at $E_V + 0.75$ eV with photoluminescence transition energies spreading from 0.6 eV to 0.8 eV. Considering that this defect is also observed in semi-insulating undoped GaAs wafer, which are used as the substrate for the epitaxial thin films throughout the thesis, the EL2 defect has to be checked as a possible origin for the formerly found deep defect band at 0.69 eV (low temperature) and 0.8 eV (room temperature). The reason for this test arises from the fact that for semi-insulating GaAs, process recipes are developed which increase the density of the known deep defect in GaAs in order to reduce the free carrier density and pin the Fermi level close to the middle of the band gap. No near-band-edge luminescence of the GaAs substrate was detected in the measurements of the epitaxial films, but this does not contradict to possible signals of the deep luminescence from the semi-insulating wafers.

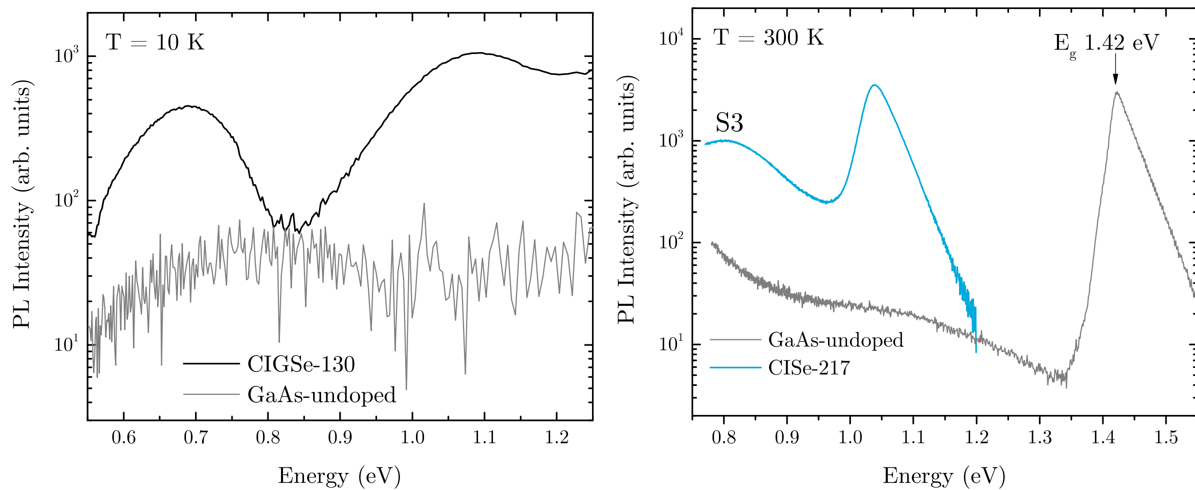

Figure 6.5: Comparison of the spectrum from CGSe-228 and the GaAs substrate at 10 K (left) as well as the spectrum of CISe-217 and the GaAs susbtrate at 300 K (right). At each temperature the same excitation conditions are used for the thin film and the substrate.

Using the same excitation conditions, a bare GaAs-substrate is measured with the extended setup at 10 K and with the standard setup at room temperature. The GaAs wafer was taken directly out of a sealed and packed atmosphere to rule out long-term degradation of the surface which can lower the photoluminescence yield. The comparison between sample CIGSe-130 and the GaAs wafer is depicted on the right side in Fig. 6.5. Indeed a very low signal from the GaAs substrate, peaking at around 0.8 eV, can be observed. But the observed signal on the bare substrate is one order of magnitude lower than the deep luminescence signal from the thin film. The same holds true for a comparison of the GaAs wafer and sample CISe-217 on the right side of Fig. 6.5 at 300 K. Even considering that the epitaxial film can passivate the GaAs wafer, it is unreasonable to assume that a fresh not degraded wafer has a one order of magnitude lower defect signal compared to the case where most of the laser light is already absorbed in the thin film on top. Assuming an absorption coefficient of $8 \times 10^4\,\text{cm}^{-1}$ and a minimal thickness of $d = 500\,\text{nm}$ only 2 % of the laser light reach the substrate. But already with 100 % absorption of the laser light,

the GaAs signal is too low. Furthermore and even more importantly, the shape of the luminescence spectrum of the substrate is in contrast to the deep defect band S3 at low and at room temperature. It is therefore safe to conclude, that the observed deep defect bands at 0.7 eV and 0.8 eV do not originate from the GaAs substrate.

Chapter 7

Defect Model and Summary

In this last chapter a comprehensive defect model for Cu(In,Ga)Se_2 is proposed. It will be shown that the experimental findings of the defect levels throughout this thesis can be attributed to intrinsic defects from theoretical calculations, found in literature. Therefore a defect model will be proposed where every defect level from photoluminescence measurements is linked with a charge transition level from theory. Also a comparison with major experimental findings from literature, which were done with other techniques, is given.

In the first Section 7.1 the large scatter of available literature data for point defect calculations is discussed and summarized for $CuInSe_2$ and $CuGaSe_2$ and defect complex formations are briefly mentioned. In Section 7.2 these results are compared to the experimental findings of this thesis as well as to literature data in three parts: shallow defects, Cu_{III} antisites and III_{Cu} antisites. The observed deep defect band at 1.1 eV most likely originates from the Ga_{Cu} antisites and the 0.8 eV defect band most likely originates from the double charge transitions of Cu_{III} antisites.

In the last section the full overview of the defect model is given, which includes shallow and deep defects in $CuInSe_2$ and $CuGaSe_2$ and its extrapolation for the solid solutions. The inferior device quality for high Ga/(Ga+In) ratios is proposed to stem at least partly from the Ga_{Cu} defect level at around 1.3 eV above the valence band and the inferior device quality for high Cu/(Ga+In) ratios is proposed to stem from the Cu_{III} (-1/-2) double charge transition at around 0.8 eV above the valence band.

7.1 Theoretical predictions from literature

In the literature several publications can be found for the theoretical prediction of intrinsic point defects in $CuInSe_2$ and $CuGaSe_2$ crystals from density functional theory (DFT). In DFT calcuations, the whole system of interacting electrons in a crystal gets reduced to one electron density. Since the exact values of the exchange-correlation energy E_{xc} are not accessible, approximations are needed. One of these approximations is the local density approximation (LDA), where the exchange-correlation is described by a homogeneous electron gas. Metals for example can be well described with this method, since the free electrons behave nearly like an electron gas.

One of the most prominent publications for $CuInSe_2$ is given in Ref. [131], where DFT together with LDA is used. Nevertheless, these calculations underestimate the band gaps of semiconductors and a posteriori corrections are needed. At this time, these corrections were done by adding a constant energy shift to the conduction band states in order to

match the experimental band gap. But these band gap corrections can lead to distorted values of the defect levels (their charge transition levels) with respect to the conduction band or valence band edge [132]. The method of LDA was improved in the past by including a gradient of the electron density (generalized gradient approximation GGA), but the discrepancy of the band gaps was just significantly improved by introducing hybrid functionals [133]. In this case, the conventionally used GGA based functionals are intermixed with a fraction of Hartree-Fock exchange. This fraction α can be tuned. The standard value used is $\alpha = 0.25$, which yields the experimental band gaps over a broad range of materials reasonably well [134].

Furthermore, hybrid-functionals consist of a short-range (includes Hartree-Fock and GGA) and a long-range part (includes only GGA) of the electron-electron interaction. The range seperation is expressed by the variable screening-parameter ω [Å^{-1}], which is $0.2\,\text{Å}^{-1}$ as a standard. By tuning α and/or ω, values for the band gap can be exactly matched with the experimental ones. But this also leads to some problems which can occur when using hybrid functionals. Being more precise in the description of band gaps, charge transition levels and formation enthalpies of defects, hybrid functionals suffer from the problem that the choice of parameter pairs (α, ω) is not defined. In the thesis of Pohl [135] it is shown that by fixing $\alpha = 0.25$, the band gap of $CuInSe_2$ decreases linearly with increasing screening parameter ω from 1.6 eV to 0.9 eV (for $\omega = 0 \ldots 0.2$). On the other hand, if the screening parameter is fixed at $\omega = 0.2$, the band gap increases linearly with increasing fraction of exact exchange α from 0.6 eV to 1.6 eV (for $\alpha = 0.2 \ldots 0.4$). Different parameter pairs can lead to the same band gap of the semiconductor e.g. 1.04 eV of $CuInSe_2$. But different parameter pairs which yield the same band gap can lead to different formation enthalphies and different defect levels [136]. In the case of $CuInSe_2$, differences of the calculated band gap or differences in the calculated charge transition of an intrinsic defect can be as large as 30 % of the band gap energy in the reported literature. But it will be shown in the following that the most recent calculations agree very well on the theoretical calculations, with much lower differences in their results (differences which fall inside the error of the calculations up be up to 100 meV).

In general, the denomination of a defect level from experiments is corresponding to a charge transition level $\epsilon(q, q')$ from theory. The formation enthalpy of a certain defect is usually calculated for each possible charge state and all Fermi energies inside the band gap. If the charge state is fixed, the formation enthalpy depends linear on the Fermi energy (constant for neutral charge states). When two of these linear lines cross, a charge transition level occurs. The formation enthalpy of two charge states is equal in this point. If the Fermi level is below this charge transition ϵ, the defect will be in the charge state q and if the Fermi level is above, the defect level will be in the charge state q'. In photoluminescence experiments these charge transitions become visible since the charge state is changed by thermal activation (e.g. thermal quenching of photoluminescence), capture of carriers (e.g. photoluminescence exitation) or emission of carriers (e.g. photoluminescence recombination).

Besides the two parameter α and ω, also the used charge correction scheme has an influence on the results. Different correction schemes can be responsible for different charge transition levels. In all literature results presented in the following, a certain defect is placed into a supercell with generally 64 and rarely more atoms. This is simply due to the fact that the computational costs get much higher with larger supercells, but the targeted accuracy is often reached already before. These supercells are periodically repeated to have an extended crystal structure, but this approach leads to spurious in-

teractions between e.g. charged defects in each supercell with its periodic images. To solve this problem, different image charge corrections were proposed in the past which are usually named by the first letters of the corresponding authors. It is worth mentioning that some corrections are better for localized (deep) defects and others work better for delocalized (shallow) defects [137]. Malitckaya et. al. [138] showed that just by changing the correction scheme (FNV or LZ) the energetic position of an exemplary deep charge transition can change by about 100 meV. This may not appear too high in order to derive a qualitatively conclusive defect model with shallow and deep defects, but it should be taken into account when comparing different results of published literature.

Some of these issues are discussed in the following, where calculations for $CuInSe_2$ by different authors yield different results despite the fact that the same hybrid functional is used. But the results of some recent publications show a very good convergence. By careful reviewing all available literature data, the most likely results are justified.

7.1.1 Point defects in $CuInSe_2$

The theoretical description of point defects in complex materials like $CuInSe_2$ is still part of the ongoing research which is shown by the fact that five new publications appeared during the project period of this thesis. In Table 7.1 an overview of the computational details of all available literature data with hybrid functional calculations for $CuInSe_2$ is given. Several famous publications which involve the authors Lany and Zunger [131, 42, 139] are based on LDA, but still agree for most of the fundamental findings with the recent calculations. But here, only calculations from hybrid-functionals will be discussed. Another reference by Bakaert et. al. [140] is not included in Table 7.1, because the reference by Saniz et. al. [95] can be seen as an updated version. The authors are the same and it is argued that in the older reference [140], a sign in the calculations was incorrect and no image charge correction was applied as a result. This could probably explain why the old reference [140] had not a single charge transition (defect level respectively) inside the band gap.

Table 7.1: Computational details of hybrid functional calculations for $CuInSe_2$

	Huang [141]	Oikkonen [142]	Pohl [23]	Yee [143]	Malitckaya [138]	Saniz [95]
Hartree-Fock mixing α	0.30	0.25	0.25	0.25	0.25	0.29
Screening parameter ω [Å^{-1}]	0.20	0.20	0.13	0.20	0.20	0.20
Correction scheme	FNV [144]	CHM [145]	LZ [146]	MP [147]	FNV [144]	KO [148]
Band gap calculated E_g [eV]	1.08	0.86	1.07	0.92	0.90	1.00

As can be seen in Table 7.1, there are no two publications with the same correction scheme and the same parameter pair (α, ω). Also the obtained band gaps show a significant variation of up to 20 %. Oikkonen et. al., Yee et. al. and Malitckaya et. al. used the standard parameters for hybrid functionals but different image charge correction schemes. Only Saniz et. al. fixed the sceening parameter ω and tuned α until their targeted band gap of 1.0 eV for $CuInSe_2$ and 1.73 eV for $CuGaSe_2$ was reached. Pohl et. al. tested the tuning of both parameters and decided for the given parameter pair in Table 7.1, because it matches the band gaps of several semiconductors from the same crystal family. In this case, the band gaps of $CuInSe_2$, $CuGaSe_2$, $CuInS_2$, $CuGaS_2$ and $CuIn_3Se_5$ are matched to the experimental values within an error of 50 meV or smaller. Usually, reported errors for the charge transition levels are in the same range at about 50 meV or 100 meV.

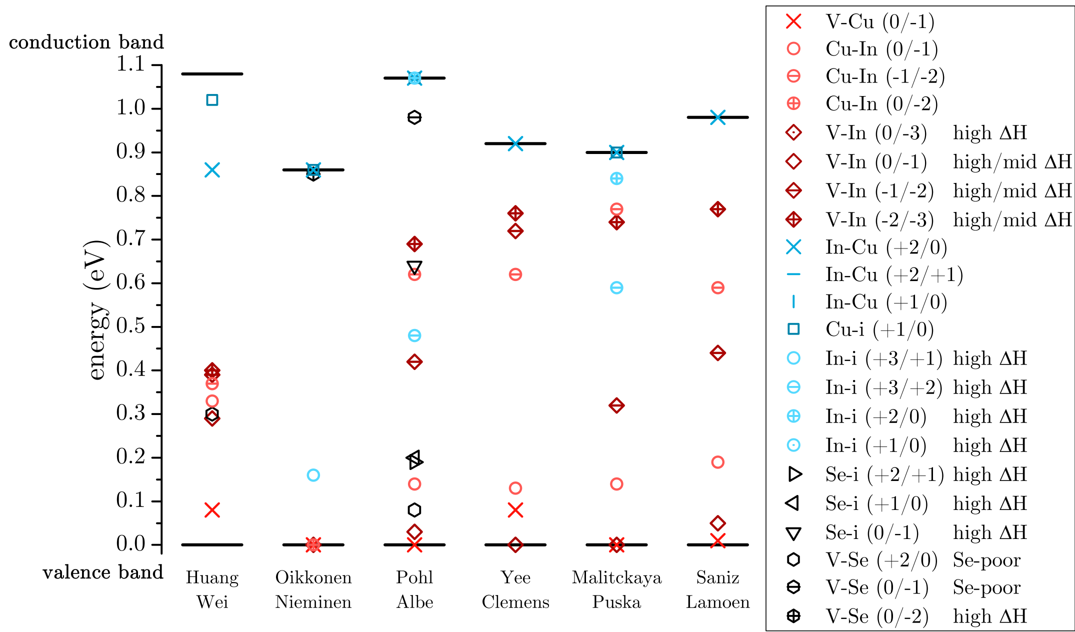

Figure 7.1: Overview of all calculated charge transitions levels for point defects in $CuInSe_2$ by different authors using hybrid functionals. The conduction band minimum and the valence band maximum are shown with black lines and references are listed according to the first and last author, including Huang [141], Oikkonen [142], Pohl [23], Yee [143], Malitckaya [138] and Saniz [95] from the left to the right.

In Fig. 7.1 an overview of all reported charge transition levels from the authors of the publications in Table 7.1 is shown. Defect levels which are resonant with the conduction or valence band form shallow, hydrogen-like states. It is important to mention that not everyone reports all possible charge transition levels and some of the authors focus on the most likely defects with the lowest formation enthalpies under chosen "compositions". Different "compositions" are expressed by the chemical potentials of each constituent copper, indium and selenium. But while the chemical potentials influence the formation enthalpies, the charge transition levels are independent of it. Each reported transition is labeled with the corresponding charges when the Fermi level is below and above the transition state. Additionally, labeling with "high ΔH" labels high formation enthalpies of $\Delta H_f \geq 2\,\text{eV}$ equally found by all authors. The general defect concentration N_d is linked to the formation enthalpy ΔH_f by:

$$N_d = N_0 \exp\left(-\frac{\Delta H_f}{k_B T}\right), \tag{7.1}$$

with the concentration of available defect positions N_0 and the temperature of the thermal equilibrium T (growth temperature). A rough estimation of the defect concentration can be done from the growth temperature $T = 800\,\text{K}$ and the lattice constant $a = 5.8\,\text{Å}$ [19], with $N_0 = a^{-3} = 5 \times 10^{21}\,\text{cm}^2$. Inserting the lower limit for formation enthalpies of $\Delta H_f = 2\,\text{eV}$ yields a defect concentration in the order of $10^8\,\text{cm}^3$ which is far below any detection limit in experiments. The defect levels of the indium and selenium interstitial can be most likely disregarded for further discussions, since all authors agree on their high formation enthalpies, even for different and favorable preparation conditions.

The reported values for the selenium-vacancy by Pohl et. al. are labeled with "Se-poor", since the formation enthalpy is generally too high (also reported by other authors)

and just can get close to 1 eV under very selenium poor growth conditions. But it should be kept in mind that state of the art absorbers are grown under selenium excess [48]. Also the formation enthalpy for the indium vacancy is generally above 2 eV. But due to the fact that under high selenium excess its formation enthalpy can be in the region of 1.5 – 2.0 eV (see Pohl et. al. [23]), small amounts of this defect are not ruled out at this stage and it is labeled with high/mid ΔH. The single charge transition of V_{In} is a shallow acceptor and the formation enthalpy is at least 1 eV higher compared to the remaining and much more abundant intrinsic defects (under all reported preparation conditions). This characteristic sheds doubts for the contribution of the indium vacancy to the doping properties or recombination centers.

When comparing the likely defects, it appears that the defect levels of Huang et. al. are all rather deep inside the band gap or at least further away from the band edges compared to all the other publications. Malitckaya et. al. [138] suggested that this could be an effect of the chosen high value for the Hartree-Fock mixing (see Table 7.1). According to their argumentation, higher values of α result in more localized states. Furthermore, it is unlikely that just the copper vacancy has a rather shallow defect state as seen in the results from Huang. From photoluminescence measurements it is known that at least two shallow acceptors exist in $\mathrm{CuInSe_2}$ (see Section 1.3). Also in $\mathrm{CuGaSe_2}$, Huang et. al. calculated only one shallow charge transition ($\mathrm{V_{Cu}}$) which is in contrast to three shallow acceptors found in experiments (see Section 1.3).

On the other hand, Oikkonen et. al. found just one very unlikely charge transition deeper inside the band gap. This scenario seems to be doubtful due to the fact that in most of the published literature data, the bulk electron lifetimes in Cu(In,Ga)$\mathrm{Se_2}$ samples $(1 - 100\,\mathrm{ns})$ are much lower than the radiative lifetime ($\approx 1\,\mu s$ for $N_{\mathrm{A}} = 10^{16}\,\mathrm{cm^{-3}}$). Therefore, deep defects are already expected from Shockley-Read-Hall statistics. The good agreement between the last four authors will be highlighted in the following, whereas the results from Oikkonen et. al. and Huang et. al. will not be considered in the further discussions. But it should be at least mentioned that the charge transitions of $\mathrm{Cu_i}$, $\mathrm{In_{Cu}}$, $\mathrm{V_{Cu}}$ and $\mathrm{V_{In}}$ also form shallow states in the results from Oikkonen, which is in agreement with the authors to the right (considering no calculation for $\mathrm{Cu_i}$ by Yee et. al. and Saniz et. al.). Only the $\mathrm{Cu_{In}}$ antisite is different in the results from Oikkonen, having no charge transition inside the band gap. But at this point the calculations of Pohl, Yee, Malitckaya and Saniz will be taken for further analysis, since they all independently found the $\mathrm{Cu_{In}}$ antisite to have two charge transitions inside the forbidden band.

In Fig. 7.2, a reduced version of the previous figure 7.1 is shown with the results from Pohl, Yee, Malitckaya and Saniz. Defects with too high formation enthalpies under all preparation conditions are omitted. It is obvious in this depiction that all the four publications show a rather good agreement in their calculations. The copper vacancy $\mathrm{V_{Cu}}$ is the most shallow acceptor in all cases und assumed to be the dominant dopant under Cu-poor growth conditions. The indium on copper antisite $\mathrm{In_{Cu}}$ is a shallow donor and assumed to be the dominant compensating defect under Cu-poor growth conditions. The copper-interstital $\mathrm{Cu_i}$ is just reported by Pohl and Malitckaya, but it is a shallow donor in both cases, which can be abundant under Cu-rich growth.

A second rather shallow (not resonant with valence band) acceptor reported by all authors is the single charge transition of the antisite $\mathrm{Cu_{In}}(0/-1)$. Additionally this defect has a double charge transition which is deep inside the band gap at $0.6 - 0.8\,\mathrm{eV}$ above the valence band. The formation enthalpies are very low under Cu-rich compositions, but can be also present in slightly Cu-poor material. For Cu-poor and Se-rich growth conditions,

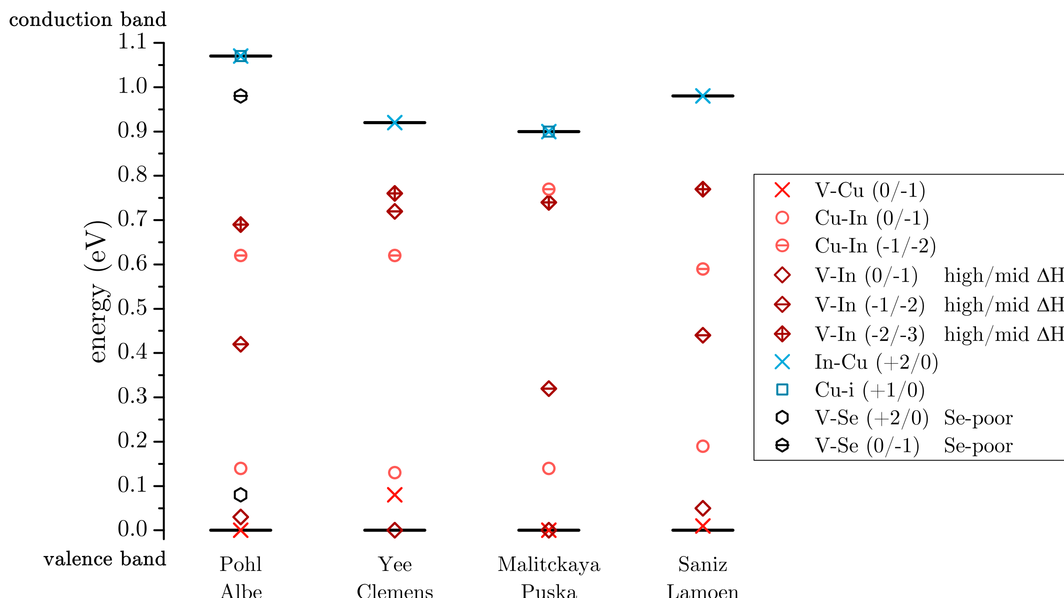

Figure 7.2: Selected publications with convergent results of calculated charge transition levels for point defects in $CuInSe_2$. Charge transition levels with too high formation enthalpies ($\Delta H_\mathrm{f} \geq 2\,\mathrm{eV}$) under all reported preparation conditions are omitted for clarity. The conduction band minimum and the valence band maximum are shown with black lines.

expected for state-of-the-art absorbers, the formation enthalpy of Cu_{In} can still be as low as $H_\mathrm{f}^{CuIn} = 0.7\,\mathrm{eV}$ (Point A in Ref. [23], Point D in Ref. [138]) and in the same range as the abundant copper vacancies V_{Cu}. Even if the chemical potentials from theoretical calculations cannot directly yield the copper content, the occurrence of Cu_{In} even under slightly Cu-poor compositions is also confirmed experimentally [149].

The only significant difference in Fig. 7.2 is the double charge transition (-1/-2) of the indium vacancy V_{In} reported by Yee et. al. Compared to the other authors only this one value is at much higher energies with respect to the valence band. But already the single charge transition level of V_{In} has a rather high formation enthalpy and is expected to be unlikely. The defect concentration of the double charge transition will be even lower for Fermi levels close to the valence band (standard p-type $CuInSe_2$). Since the charge transition V_{In}(-1/-2) is not expected to be very unlikely compared to the other shown defects in Fig. 7.2 the reason for the deviation of the calculation from Yee et. al. remains unknown but will not be further discussed.

In order to better highlight the remaining charge transitions for the further discussion, the band gap values of the four publications are normalized in Fig. 7.3. The bands are shifted up or down to match 1.04 eV. All of the shown shallow donor levels are calculated to be resonant with the conduction band. In this case it can be assumed that these e.g. hydrogen-like states shift together with the conduction band and remain shallow (see Ref. [150]). Similar to the shallow donor states, all of the rather shallow acceptor-like defects can be assumed to remain constant with respect to the valence band edge, indepedent of the band gap. Only the position of the (-1/-2) charge transition of Cu_{In} is not straightforward in the simple normalization.

When the band gaps are normalized in Fig. 7.3 by adjusting the value for the band gap (e.g. by the so-called scissors operator), it is possible that the deep Cu_{In}(-1/-2) state

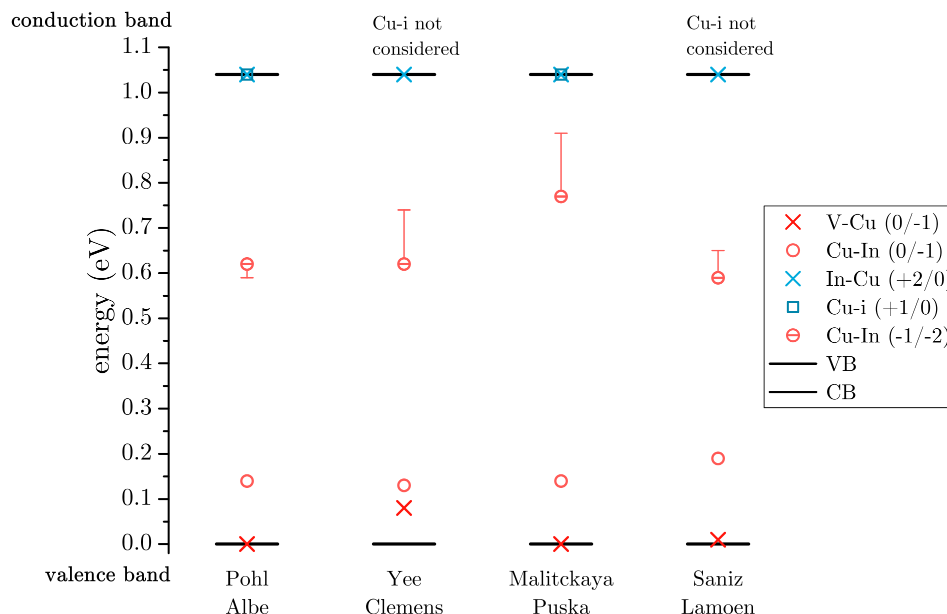

Figure 7.3: Selected publications with convergent results of calculated charge transition levels for point defects in $CuInSe_2$. Charge transition levels with high formation enthalpies ($\Delta H_\mathrm{f} \geq 2\,\mathrm{eV}$) under preparation conditions with selenium excess are omitted for clarity. The conduction band minimum and the valence band maximum are shown with black lines and the conduction band minimum is set to 1.04 eV for all publications, while shifting the shallow resonant donor defects together with the conduction band and letting the acceptor-like defects unaffected with respect to the valence band.

remains constant with respect to the valence band (shown with points in Fig. 7.3). This charge transition is an acceptor-like defect and it could be anchored to the valence band. But on the other hand it is also possible that this defect level remains constant to an unknown average electrostatic potential, independent of the position of the conduction or valence band. The reason is its possibly high localization (see e.g. Ref. [151]). In this case, the widening or shrinking of the band gap in order to fit the experimental value has no influence on the defect level on an absolute scale. The valence and/or the conduction band change with respect to the average potential, but the defect level does not. Even if it is not known how the defect level will change when the band gaps are normalized, the upper limit is assumed by the difference of the calculated band gap to the experimental value of 1.04 eV (shown as error bars), e.g. by keeping the energetic distance between the defect and the conduction band minimum constant.

Finally, it can be seen that all authors in Fig. 7.3 agree very well for the most important defect levels with expected low formation enthalpies. Yee and Saniz have not reported the charge transition values for the copper interstitial Cu_i, but Pohl and Malitckaya both agree that copper interstitials can be the dominant donors under Cu-rich growth. On the other hand the In_{Cu} antisites are the dominant donors under Cu-poor growth. The copper vacancy is expected to be abundant under all preparation conditions and is unequivocally a very shallow acceptor. The copper on indium antisite Cu_{In} has a single and a double charge transition. The single charge transition has a rather shallow acceptor state at 150 meV in average (one should also keep in mind the reported energy errors of 50 or 100 meV) and the second charge transition has a deep level, calculated between 0.6 and 0.8 eV above the valence band.

7.1.2 Point defects in $CuGaSe_2$

Unfortunately much less publications exist for defect calculations with hybrid functionals in $CuGaSe_2$ but it is needed in order to understand the solid solution of $Cu(In,Ga)Se_2$. Huang et. al. [141] reported several charge transition levels for the indium-free ternary, but the strong contradiction to all the other authors in the literature review for $CuInSe_2$ questions these results in $CuGaSe_2$. The same arguments as in the case of $CuInSe_2$ hold true, so that a possible reason could be the high chosen fraction of exact exchange with $\alpha = 0.3$. This leads to more localized states inside the band gap and just one charge transition close to the valence band (copper vacancy) is in contradiction to three experimentally confirmed acceptors. Again as in the case of $CuInSe_2$, the results on $CuGaSe_2$ from Baekert et. al. [140] cannot be considered, since in Ref. [95] the same authors argued that an incorrect sign was used in the previous publication. This resulted in different formation enthalpies and different charge transition levels in $CuInSe_2$ and therefore the results on $CuGaSe_2$ cannot be considered here.

The most recent publication by Han et. al. [152] focuses on the sulfide compound $CuGaS_2$ but reports also calculations for the Cu_{Ga} and Ga_{Cu} antisites in $CuGaSe_2$. In this calculations, the paramter pair ($\alpha = 0.26, \omega = 0.08$) was used to fit the experimental band gap and to fullfill the so-called generalized Koopmans' theorem at the same time. Unfortunately, the calculations where done with a 128-atom supercell only. Pohl et. al. [153] showed that for the Cu_{Ga} antisite, the computationally costly 216-atom supercell needs to be used in order to observe localized defect states without any self-overlap of the defect wavefunctions. Also the single particle energy of Cu^0_{Ga} moves closer to the valence band when the larger and more accurate supercell is used, which could explain the discrepancy between the (0/-1) charge transition of Cu_{Ga} in the calculation of Han et. al. (128-atoms, 0.47 eV) and Pohl et. al. (218-atoms, 0.20 eV). In order to compensate for the smaller supercell used, Han et. al. calculated the charge transition levels with the same parameter pair (α, ω) as Pohl and added the obtained energy differences to their results. This yields a slightly smaller value of 0.35 eV for Cu_{Ga}(0/-1). But this supercell-correction raises some doubt since e.g. even with the same parameter pair, Han calculated a different band gap for the sulfide $CuGaS_2$ (2.32 eV) compared to Pohl (2.44 eV). Pohl used the charge correction scheme from Lany and Zunger and Han used the one from Freysoldt, Neugebauer, and Van de Walle. This difference could be one possibility of the different band gaps. But if already the band gaps differ by 0.12 eV in this example, it is difficult to motivate the charge transition levels as a reference for corrections of smaller supercells. For this reason, the results from Pohl et. al. are preferred for the Cu_{Ga} defect due to the usage of a larger supercell.

In contradiction to this, nearly the the same defect level was calculated for Ga_{Cu}(+1/0) by both authors (Han: $E_C - 0.38$ eV and Pohl: $E_C - 0.35$ eV). Therefore, this defect does not raise further discrepancies and the results from Pohl are sufficient for the literature review of $CuGaSe_2$, since no other charge transitions are reported by Han.

In Fig. 7.4, all results for the charge transitions from Pohl et. al. are shown for $CuInSe_2$ and $CuGaSe_2$ in comparison. Most of the transitions align on the same level with respect to the valence band, except the III_{Cu} antisites. The copper interstitial Cu_i is a shallow donor in both cases, without the need of the exact energy level. Again, a reduced version is depicted in Fig. 7.4 where indium- and selenium-vacancies are omitted for clarity, due to their large formation enthalpies. Only under very selenium poor growth conditions, the selenium vacancy can reach formation enthalpies below 2 eV, but still significantly higher than all the other defects shown.

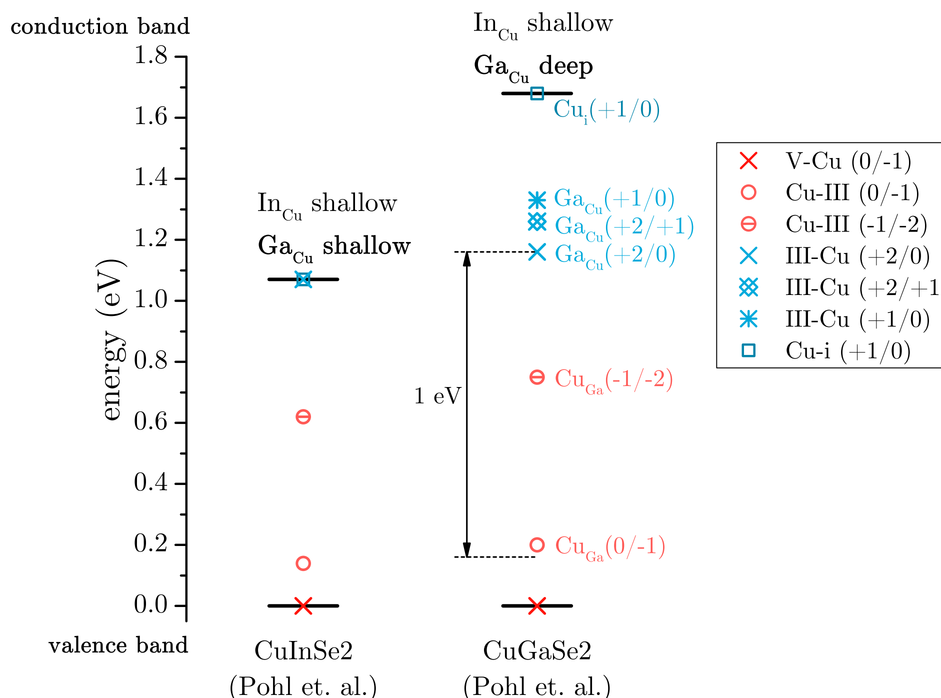

Figure 7.4: Comparison of calculated charge transition levels in $CuInSe_2$ and $CuGaSe_2$ reported by Pohl et. al. [23]. The charge transitions of the indium and selenium vacancies are omitted, which have very high formation enthalpies. The main difference of the shallow (in $CuInSe_2$) and deep (in $CuGaSe_2$) charge transition of the Ga_{Cu} antisite is highlighted.

For both ternaries it can be concluded that V_{Cu}, Cu_i and In_{Cu} are very shallow defects in all $Cu(In,Ga)Se_2$ compounds. Also the charge transitions from the Cu_{In} and the Cu_{Ga} antisites have a comparable distance to the valence band in $CuInSe_2$ and $CuGaSe_2$. The interchange between indium and gallium in these antisites in $Cu(In,Ga)Se_2$ is labeled with Cu_{III}.

In theoretical calculations it is possible to calculate indium-related charge transitions in the ternary $CuGaSe_2$ and gallium-related charge transition in the ternary $CuInSe_2$. By doing so, this allows for conclusions on the charge transition levels in the solid solution $Cu(In,Ga)Se_2$. Pohl et. al. have reported the In_{Cu} antisite to be a shallow donor in both ternaries. On the other hand, the gallium on copper antisite Ga_{Cu} is a shallow donor in $CuInSe_2$, but it has several deep donor-like charge transition in $CuGaSe_2$. For the compound $Cu(In,Ga)Se_2$ it can be expected that the transition from a shallow donor Ga_{Cu} into a deep level has to occur monotonous with increasing Ga/(Ga+In) ratio, whereas the exact behavior is unknown. This assumption is supported by the calculations from Huang et. al. [141] where the absolute values of the charge transitions might not be in agreement with other literature data, but the monotonous trend for the shallow and deep Ga_{Cu} antisites is confirmed with direct calculations for solid solutions of $Cu(In,Ga)Se_2$. Additionally, Pohl et. al. showed that the single particle energy of Ga_{Cu} aligns very well on an absolute scale in $CuInSe_2$ (1.05 eV) and $CuGaSe_2$ (1.15 eV), which leads to the assumption that the highly localized charge transition levels remain nearly constant with respect to a common reference potential, independent of the band gap in $Cu(In,Ga)Se_2$.

The deep Ga_{Cu} levels play another important role in terms of a DX pinning level. First confirmed by Lany and Zunger [42] and also shown by Pohl and Albe, the double charged Ga_{Cu}^{2+} can capture two electrons and may form a metastable DX center which leads to a large lattice relaxation. All four authors also proposed that the $Ga_{Cu}(+2/0)$ charge transition can induce Fermi level pinning. When the electron Fermi level is raised over the so-called DX pinning level (for example by illumination), forming of the DX centers can lead to an increasing capture of free electrons and a pinning of the Fermi level below the conduction band. Pohl et. al. calculated this DX pinning level at 1.16 eV above the valence band. Taking into account that state of the art $CuGaSe_2$ solar cells are still limited to open circuit voltages of 1 eV [37], together with a hole Fermi level around 0.16 eV (doping $N_A \approx 2 \times 10^{16}\,cm^{-3}$), the limitation of the electron Fermi level around 1.16 eV ($E_{Fp} + V_{oc}$) could potentially be induced by this Ga_{DX} pinning level. The example is shown in Fig. 7.4 with dotted lines. Such a Fermi level pinning is calculated by Pohl and Albe to not occur in $CuInSe_2$ due to the very shallow charge transition (+2/0) of both In_{Cu} and Ga_{Cu}.

7.1.3 Defect complexes

Complexes of intrinsic point defects have to be considered, too. In the well known work from Zhang et. al. [131], the complex In_{Cu}–$2V_{Cu}$ is proposed to be responsible for the formation of ordered defect compounds (ODC) and the high tolerance to off-stoichiometry of $CuInSe_2$. But the more recent calculations with hybrid functionals from Pohl and Malickaya doubt its occurrence due to the low binding energies [23, 138]. Additionally, Malitckaya et. al. argue that In_{Cu}–$2V_{Cu}$ is neutral for all Fermi energies and no charge transition occurs, which could still explain the large off-stoichiometries, but it is irrelevant for comparisons with defect spectroscopy. The second complex In_{Cu}–V_{Cu} is singly positive charged for all Fermi energies inside the band and can therefore be just a very shallow donor, but negligible concentrations are expected according to Pohl and Malitckaya.

Furthermore, Malitckaya et. al. reported formation energies and charge transition levels for several other complexes forming with copper interstitials Cu_i. But they again doubt their occurrence, since some of these complexes have too low binding energies and others have too high formation enthalpies of the constituents like V_{Se} or V_{In}. But it is worth mentioning that Pohl et. al. found the binding energy of Ga_{Cu}–V_{Cu} to be higher in $CuGaSe_2$ compared to In_{Cu}–V_{Cu} in $CuInSe_2$ (0.66 eV compared to 0.18 eV). The complex Ga_{Cu}–V_{Cu} has its charge transitions just slightly above the ones of Ga_{Cu}, whereas In_{Cu}–V_{Cu} has no charge transition inside the band gap. This characteristic of e.g. Ga_{Cu}–$V_{Cu}(+1/0)$ should be kept in mind for a less likely (compared to Ga_{Cu}) but possible candidate of a donor-like defect level which is rather deep in wide-gap $Cu(In,Ga)Se_2$ with high Ga/(Ga+In) ratios.

7.2 Summary of experiment and theory

In this section, the defect levels obtained from theoretical calculations in the literature will be attributed to the defect levels from optical measurements in the scope of this thesis. For a conclusive defect model some often observed experimental findings from optical or electrical measurements in the literature will be discussed, too. The section starts with a discussion of the shallow defects, which have a strong influence on the doping, possible detrimental deep defect levels of Cu_{III} and III_{Cu} antisites will be discussed in a separate second and third part.

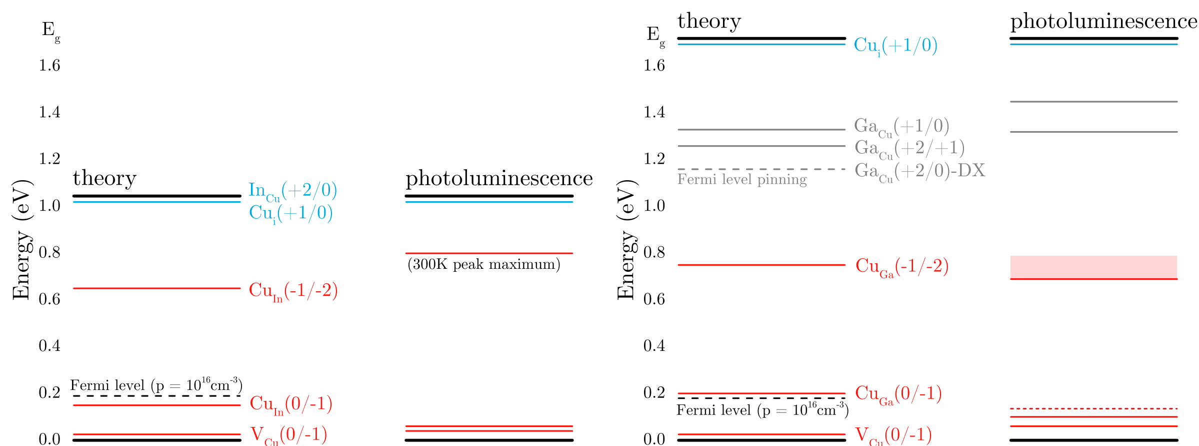

Figure 7.5: Comparison of charge transition levels from theory with the photoluminescence measurements of this thesis and the known near-band-edge luminescence in Ref. [10] for $CuInSe_2$ and $CuGaSe_2$. The theoretical values are averaged values from [23, 138, 95, 143]. Expected low defect concentrations are depicted with dotted levels and the uncertain defect position of the 0.8 eV photoluminescence band is depicted with a shaded area.

A direct comparison of the defect levels from theory and from photoluminescence measurements is given in Fig. 7.5. Calculated defect levels from theory which are resonant with the valence or conduction band are drawn with a minimal offset for better visibility and an assumed hydrogen-like level formed. Details of this comparison will be discussed in the following.

7.2.1 Shallow defects

Shallow donors

It is known that a very shallow donor level D1 around 10 ± 5,meV exists in $CuInSe_2$ and $CuGaSe_2$ and is therefore highly probable in all $Cu(In,Ga)Se_2$ solid solutions [10]. In the hydrogen model with effective mass theory, a shallow donor level is expected around 7 meV for $CuInSe_2$ ($\varepsilon = 13.6$, $m_e^*/m_0 = 0.09$) and 13 meV for $CuGaSe_2$ ($\varepsilon = 11.0$, $m_e^*/m_0 = 0.14$). The values for the calculation can be found in the Appendix of Ref. [10]. The shallow level was observed by photoluminescence when the temperature is slowly raised from 10 K until the free-to-bound transition into the shallow acceptor A1 becomes visible at approx. 10 meV higher energies than the well known shallow donor-acceptor pair transition DA1.

From the previous literature review of defect calculations, this donor level can be attributed to the Cu_i and/or the In_{Cu} antisite. Even if both intrinsic defects are present in measurable quantities, a discrimination of the two by photoluminescence or other techniques will be difficult. Nevertheless, it is assumed that the Cu_i can reach high concentrations in Cu-rich compositions, whereas the In_{Cu} antisite is assumed to be a dominant and abundant donor in Cu-poor ones. This behavior is also qualitatively predicted by composition dependent calculations with a Fermi level fixed at the valence band edge [138]. Furthermore, epitaxial growth of Cu-poor $CuInSe_2$ without extrinsic doping by e.g. sodium from the glass substrate, results in n-type conductivity [154], which can be explained by the high amounts of In_{Cu}.

Shallow acceptors

The most shallow acceptor A1 at around 40 meV in $CuInSe_2$ and around 60 meV in $CuGaSe_2$ in photoluminescence measurements can be attributed to the copper vacancy, which is an abundant acceptor in Cu-poor material. But it can also reach rather high concentrations in Cu-rich material due to its low formation enthalpies. From photoluminescence it is known that the transition into the shallow acceptor A1 is becoming the dominant when the copper content is decreased from Cu-rich compositions towards stoichiometry or even slightly Cu-poor thin films (see Fig. 1.8 in Section 1.3). This behavior would be expected for the copper vacancy but not for the other possible shallow acceptors Cu_{III} or V_{III} and supports the attribution of V_{Cu} to A1.

The second shallow acceptor A2 at around 60 meV in $CuInSe_2$ and around 100 meV in $CuGaSe_2$ is proposed to be the Cu_{In} or Cu_{Ga} antisite (Cu_{III}). From theory, the only different possibility would be the shallow indium- or gallium vacancy V_{III}. But all available defect calculations from the literature in Section 7.1 agree on the high formation enthalpy of V_{III} compared to Cu_{III} with values above 2 eV. Pohl et. al. [23] have shown that the formation enthalpy of Cu_{III} is at least 1.2 eV lower compared to V_{III} for Cu-poor, Cu-rich, Se-poor or Se-rich growth. It is therefore most likely that the second shallow acceptor stems from the Cu_{III} antisites. This acceptor is abundant in Cu-rich films, where the DA2 transition in photoluminescence measurements dominates the near-band-edge luminescence for all Cu-contents above approx. Cu/III = 1.1. For compositions close to stoichiometry, the DA2 transition gets lowered which would be expected from lower concentrations of Cu_{III}. Interestingly, Pohl et. al. and Malitckaya et. al. found that "standard" Cu-poor and Se-rich growth (point M in [138], point A in [23]) yields nearly the same formation enthalpies of V_{Cu} and Cu_{III}, making them both abundant acceptors. Unfortunately, the peak ratios are not accessible by photoluminescence in Cu-poor compositions with high potential fluctuations.

Finally, the V_{III} vacancies might be the origin of a third acceptor, which usually has a much smaller photoluminescence signal and can be just observed under special preparation conditions. In epitaxial $CuGaSe_2$ thin films close to stochiometry a small signal from a third acceptor at 135 meV was observed, which tends to form islands [43]. It cannot be observed in lower Cu-contents due to the occuring potential fluctuations and it cannot be observed in higher Cu-contents since the signal is overlapped by the much stronger DA2 transition and its phonon replicas. A third acceptor level in $CuInSe_2$ could not yet be confirmed in epitaxial samples, but it is found in single crystals [155, 156] and polycrystalline samples from PVD growth at again 130 – 140 meV and is part of the current research at LPV. In any of these cases, the photoluminescence transition of A3 is never the dominating one and the assumption of A1 and A2 as the main acceptors in all

films remains valid.

The fact that the A3 level is rarely observed could be a supporting argument for the usually high formation enthalpies of V_{III} in calculations. But even if the formation enthalpies of V_{III} are always much higher than V_{Cu} and Cu_{III}, at least its quantity alone could be favoured by e.g. higher growth temperatures. This behavior could e.g. explain the absence of A3 in epitaxial $CuInSe_2$ films from the MOVPE-process at LPV with about 100 K lower growth temperatures compared to PVD. Furthermore, under Cu-rich growth conditions the chemical potential of copper just varies in a narrow range, whereas the chemical potential of selenium can in principle vary between 0 and less than -2 eV (see points B, D and F in Fig. 1 in Ref. [23]). From theory, a decrease of the formation enthalpy of V_{III} is observed for an increase in selenium availability (lower chemical potential of selenium [23]) which supports again its absence in $CuInSe_2$ from MOVPE-processes where the selenium incorporation is lower compared to PVD (see Section 2.1). The attribution of A3 to V_{III} is possible but not as clear as for A1 and A2.

7.2.2 Deep Cu_{In} and Cu_{Ga} doubly charged defects

As already mentioned in the previous parts, both the Cu_{In} and the Cu_{Ga} antisite are proposed to be linked with the rather shallow acceptor A2 at 60 and 100 meV respectively (CISe and CGSe). But according to the theoretical calculations there exists also a second charge transition (-1/-2) inside the band gap at 0.6 – 0.8 eV. Taking into account some scattering of the level for different authors, the energy position has similar values for the indium- and gallium-related antisite in a narrow range compared to the band gap (see Fig. 7.4 and Fig. 7.3). The charge transitions will be assumed to be equal in $CuInSe_2$ and $CuGaSe_2$ for simplicity reasons and there is no significant difference in the formation enthalpy of the Cu_{In} antisite in $CuInSe_2$ and the Cu_{Ga} antisite in $CuGaSe_2$.

In Chapter 6 a defect band at 0.7 eV in compositions with high gallium content and 0.8 eV for low gallium was found. The zero-phonon line is not precisely known from experiment, but even if the possible range of calculated charge transitions is extended to 0.8 ± 0.2 eV, the only levels which fall inside this range in $CuInSe_2$ and in $CuGaSe_2$ are the Cu_{III}(-1/-2) and the V_{III}(-2/-3) charge transition (see Fig. 7.2 in Section 7.1.1). Indium and selenium interstitials are not considered since all authors agree on the too high formation enthalpies. But the same arguments for the abundance of Cu_{III} and the unlikely formation of V_{III} from the previous part hold true. In all Cu-rich thin films, A2 is dominating the near-band-edge luminescence, independent of the growth processes. That makes it safe to rule out the unlikely single charge transition of V_{III}. In p-type material the higher charge transitions of V_{III} cannot occur in larger quantities than the single charge transition, since they are further away from the valence band. Thus, the V_{III}(-2/-3) transition is also unlikely to occur and cannot be responsible for the deep luminescence which is observed in all Cu-rich thin films (epitaxial and polycrystalline) of $Cu(In,Ga)Se_2$. Also the observation of the 0.8 eV defect in Cu-poor thin films by photocapcitance (CGI $\approx$ 0.9 [123, 124, 125, 157]) can be explained by the low formation enthalpy of Cu_{III} rather than V_{III}, even for a copper deficiency [138, 23]. But its concentration is expected to at least decrease with the copper content.

The attribution of 0.8 eV defect from photocapacitance to the double charge transition of Cu_{III} was also proposed by Pohl et. al. [23]. The authors argue that this defect transition can just be observed if high amounts of Cu_{III} antisites get charged by excess carriers from e.g. illumination. This behavior is a possible explanation for the absence of the

0.8 eV defect in dark measurements like admittance spectroscopy or deep-level transient spectroscopy (DLTS). Indeed, the only reported experiments in which this defect is observed are photocapacitance methods or photoluminescence. Pohl and Albe also proposed that this deep charge transition is not necessarily a detrimental recombination center. If the Fermi level in equilibrium is below the (0/-1) transition (proposed shallow acceptor A2), most of the Cu_{III} antisites are neutral and the deep (-1/-2) transition will become less probable. But typical equilibrium Fermi level energies for p-type Cu(In,Ga)Se_2 absorbers are in the range of E_F =250 − 120 meV ($p_0 \approx 10^{15} - 10^{17} cm^{-3}$) above the valence band. The single charge transition Cu_{III}(0/-1) is attributed to A2 at 60/100 meV which is below typically values of E_F. Therefore, the antisites would be in the negative charge state and the double charge transitions could be a detrimental recombination center.

In order to give an explanation for the rather large discrepancy between the defect level found in experiments at 0.7 − 0.8 eV and the calculated levels of Cu_{In} at 0.62 eV (Pohl), 0.62 eV (Yee), 0.77 eV (Malitckaya) and 0.59 eV (Saniz), a careful analysis of the literature is needed. The value from Malickaya is closest to the proposed 0.8 eV which will be justified in the follwing. Pohl reported that the density of states of the Cu_{In} antisites gets highly localized when the calculation is done with a 216-atom supercell [153], which was already discussed in part 7.1.2. This is an important observation since Komsa et. al. [137] reported that the FNV image charge correction is more accurate for localized defects than the LZ correction scheme. Malitckaya et. al. showed as an example that just by changing the correction scheme, the double charge transition (-1/-2) changes from around 0.77 eV (FNV) close to the value of 0.62 eV found by Pohl (LZ). Both independent calculations from the authors are in good agreement when using the same correction scheme. But due to the high localization of Cu_{In} antisites, the value for the corresponding charge transition is expected to be more accurate within the FNV correction used by Malitckaya. This puts the double charge transition at around 0.77 eV in $CuInSe_2$ and supports the attribution to the 0.8 eV defect.

In the case of Cu_{Ga}(-1/-2) only the results from Pohl, which contain the LZ correction scheme, can be considered. In comparison to the Cu_{In}(-1/-2) antisite in $CuInSe_2$ at 0.62 eV, the Cu_{Ga}(-1/-2) antisite in $CuGaSe_2$ is calculated closer to the middle of the band gap at 0.75 eV above the valence band. The impact of the FNV correction scheme on Cu_{Ga}(-1/-2) is not reported. If a similar shift of the charge transition like the one for Cu_{In}(-1/-2) is assumed as an upper limit, the possible energy range for Cu_{Ga}(-1/-2) can be estimated between 0.75 − 0.88 eV which is not in contradiction to the 0.8 eV defect. As already done for the single charge transitions, for the double charge transition an exchange of indium and gallium in Cu_{III} antisites is assumed to hardly affect the defect position compared to the change in band gap.

Apart from the results in Chapter 6, the only observation of a defect close to 0.7− 0.8 eV in photoluminescence experiments was found in Ref. [126]. The authors show a free-to-bound transition at 0.79 eV at low temperatures (CIGSe, GGI ≈ 0.3), but further studies are needed.

The last experimental example from literature is a defect level found at 0.72 − 0.80 eV in $CuInSe_2$ and $CuGaSe_2$ by photoinduced current transient spectroscopy. Again, light excitation is used in this method which possibly charges the antisite first. The authors argue that the defect was not observed in highly conductive samples. According to the former discussion, the Fermi level of the used highly conductive samples possibly was below the single charge transition, so that the second charge transition becomes unlikely. Not knowing the carrier concentrations, this literature reference is not in contradiction

with the present defect attribution and the importance of the position of the Fermi level should be always considered for the acceptor A2 or the Cu_{III} antisites respectively.

7.2.3 Shallow In_{Cu} and shallow/deep Ga_{Cu} defects

In the literature results for hybrid-functional calculations in Section 7.1, the In_{Cu} antisite is calculated as a shallow donor, resonant with the conduction band for $CuInSe_2$ and $CuGaSe_2$ and therefore assumed for all compositions of Cu(In,Ga)Se_2. Especially in Cu-poor compositions this defect is expected to be abundant and acting as the main compensating defect for the copper vacancies. It is also reasonable to propose that this defect is the main donor for n-type conductivity in Cu-poor $CuInSe_2$ epitaxial thin films [154]. Whereas this defect can have a strong impact on the doping properties of the material, it is no detrimental recombination center for electrons or holes.

This is not the case for the Ga_{Cu} antisite. Already in the first calculations by DFT 20 years ago [158], this defect was proposed to be a detrimental recombination center for electrons due to its charge transition levels deep inside the band gap. This is also calculated by the recent studies with hybrid functionals and very low formation enthalpies are reported under Cu-poor and even Cu-rich growth [23]. Calculated charge transition levels in $CuGaSe_2$ are at 1.26 eV (+2/+1) and 1.33 eV (+1/0). Since these levels are close to the determined donor-like defect at 1.3 − 1.33 eV above the valence band (the origin of the 1.1 eV band in Chapter 5) it can be most likely attributed to the Ga_{Cu} antisites in general.

All theoretically calculated Ga_{Cu} charge transitions are resonant with the conduction band in $CuInSe_2$. Even more important is the fact that the single particle and charge transition energies of Ga_{Cu} align nearly constant on an absolute scale in both ternaries and Pohl et. al. [23] argue that this is most likely true for Cu(In,Ga)Se_2, too. This assumption is in accordance to the experimental findings, where the 1.1 eV defect band (involving the deep defect at 1.3 − 1.33 eV) remains almost constant with decreasing Ga/(Ga+In) ratio. It nearly disappears for Ga-contents at approx. 45 % since the involved defect level starts to merge with the conduction band states. For standard Cu(In,Ga)Se_2 compositions with a Ga-content of 30 %, this defect could then contribute to compensation and n-type doping in the same way as In_{Cu} antisites, but is not recombination center.

It is not clear, which of the Ga_{Cu} charge transitions is responsible for the deep defect found at 1.32 eV. But in equilibrium, all of the antisites are in the +2 charge state. The more likely charge transition observed would be the one into the singly positive charge state Ga_{Cu}(+2/+1). In Ref. [153], Pohl et. al. attributed a broad photoluminescence band at 1.17 eV in $CuGaSe_2$ to the possible transition of an electron from the Ga_{Cu} antisite into the Cu_{Ga} antisite by radiative tunneling. This process $Ga^{+}_{Cu} + Cu^{0}_{Ga} \rightarrow Ga^{++}_{Cu} + Cu^{-}_{Ga}$ is in good agreement with the present experimental findings of the deep donor acceptor pair transition S2A2 at 1.23 eV (zero-phonon line) and the attribution of the gallium antisite Ga_{Cu} to the deep donor S2 and the copper antisite Cu_{Ga} to the shallow acceptor A2. The rather low formation enthalpies of Ga_{Cu} under all preparation conditions [23] could further explain the difficulty to achieve high open circuit voltages in wide-gap compositions due to large amounts of recombination centers. After more than 30 years of research, the best $CuGaSe_2$ solar cells have an open circuit voltage deficit of about 0.7 eV [37] whereas the best $CuInSe_2$ solar cells reach 0.5 eV [121] and the best Cu(In,Ga)Se_2 solar cells with band gap grading reach even 0.4 eV [114]. Already in Fig. 5.23 in Section 5.2.4 an overview of several results from literature for the band gap dependent open circuit voltage was

given. Straightforward simulations show that a defect level at around 1.3 eV has nearly no influence on the open circuit voltage if it is resonant with the conduction band. If it gets closer to the middle of the band gap for higher Ga-contents, the open circuit voltage deficit is increased.

Other reasons for the gallium dependent deficit can be unfavorable band offsets to the buffer [159], where an increasing cliff is observed for increasing high Ga/(Ga+In) ratios or it is attributed to deep defects [125, 160] and resulting lower diffusion lengths [81]. But in recent studies, the buffer layer was replaced and optimized in order to achieve a good band alignment with $CuGaSe_2$ absorber [37]. Nevertheless, the open circuit voltage deficit is still around 0.7 eV for the best cells, implicating that the band offset at the buffer interface can contribute but is unlikely the main reason for the low open circuit voltages. This assumption is supported by the fact that measurements on bare absorber also show a decrease in the quasi Fermi level splitting [161] as well as the minority carrier lifetime [125] with increasing Ga-content. This is a strong argument that recombination over deep defects is dominating, since shallow defect states cannot act as recombination centers and will therefore not significantly decrease the apparent lifetime (see Fig. 1.6 in Section 1.2.2).

7.3 Defect model conclusion

In the last section of this thesis, the full proposed defect picture from photoluminescence measurements is given in an overview in Fig. 7.6. In this sketch, the band gap values are chosen for stoichiometric crystals at room temperature with 1.04 eV for $CuInSe_2$ and 1.68 eV for $CuGaSe_2$ (see Section 1.1.3). Donor-like levels are colored in blue and acceptor-like levels are shown in red. Interpolated defect levels in the Cu(In,Ga)Se_2 solid solution are depicted with dashed lines, which is confirmed by measurements from literature for the shallow defects [13] and for the deep defects confirmed by several compositions within the measurements of this thesis. The valence band maximum of $CuInSe_2$ is the reference level, whereas a downshift of the valence band maximum in $CuGaSe_2$ by 40 meV [112] is taken into account for the valence band offset [112]. The proven strong phonon coupling (Section 5.2.2) of the deep donor-like defect (Ga_{Cu}) is depicted with grey lines, where the lower limit corresponds to the optical transition energy and the higher limit to the zero phonon line (the actual defect level). The expected low amount of the third acceptor A3 in $CuInSe_2$ and $CuGaSe_2$ in comparison to A2 and A3 is sketched with a light colored line. An arrow at a Ga/(Ga+In) ratio of 0.45 indicates the composition were the deep donor-like defect is shallow enough to be resonant with the conduction band.

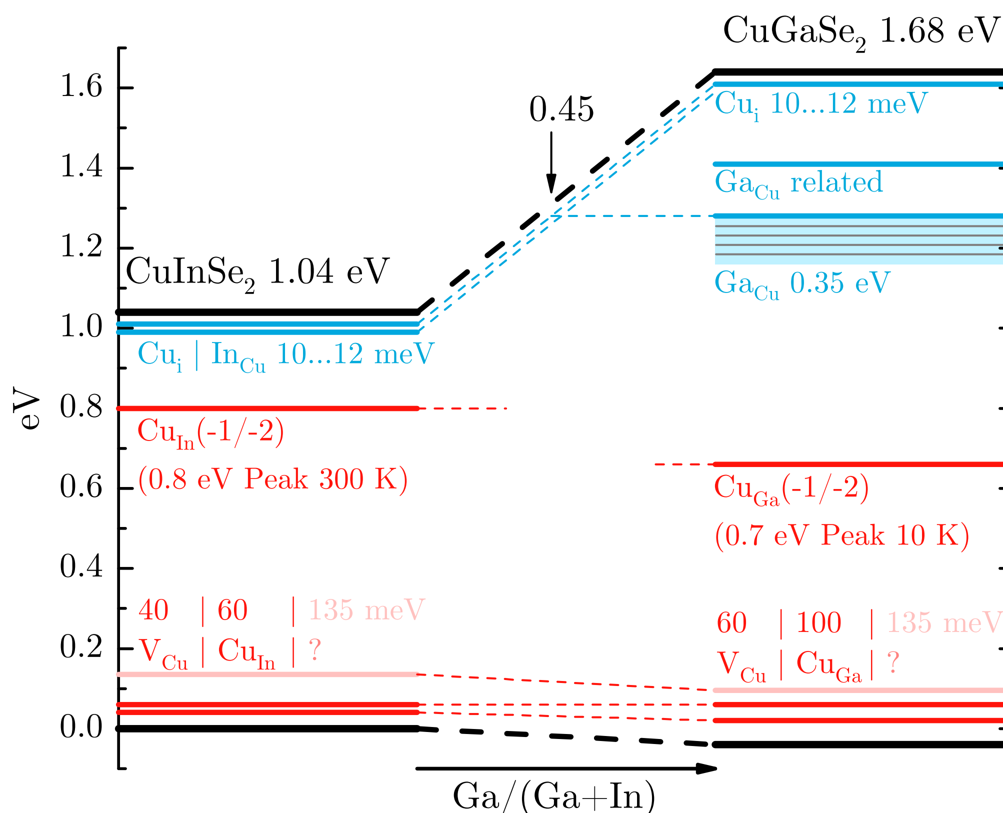

Figure 7.6: Full overview of the proposed defect model in Cu(In,Ga)Se_2 from photoluminescence measurements. Donor-like levels are colored blue and acceptor-like levels are colored red. The Franck-Condon shift of the Ga_{Cu} antisite is highlighted with grey lines for the phonon lines. The reference level at 0 eV corresponds to the valence band minimum of $CuInSe_2$ with a valence band offset in $CuGaSe_2$ of 40 meV [112].

Outlook

The results from the project of the present thesis can be useful for further optimization of the $Cu(In,Ga)Se_2$ growth processes in order to achieve higher solar cell efficiencies for wide-gap or Cu-rich absorber compositions. All industrial applications currently make use of polycrystalline crystals. Therefore, the found new defect levels and the derived defect model should be confirmed on polycrystalline samples from e.g. growth by physical vapor deposition (PVD), too. It can be expected that the same abundant shallow and deep point defects are present in epitaxial and polycrystalline crystals. The studies and characterizations already started in our laboratory at the end of this project and the deep 1.1 eV defect band was confirmed in the ternary $CuGaSe_2$. Having equal defect signatures in epitaxial and polycrystalline samples, for very different growth techniques, can rule out their possible origin from grain boundaries (much lower or no amount in epitaxial samples), stacking faults (much lower amount in polycrystalline samples), hydrogen or carbon (high amounts in MOVPE precursor, but below detection limit in PVD).

Further studies on polycrystalline samples should be done to observe the constant energy level of the deep S2 defect at 1.3 eV above the valence band maximum for a larger set of different Ga/(Ga+In) ratios and for state-of-the-art absorber compositions with Cu/(In+Ga) ratios of approx. 0.9. Difficulties can arise from possible thin film interference of the emitted photoluminescence light in typical 2 - 3 micrometer thick samples for standard polycrystalline solar cell absorber. This problem also appeared in first measurements on $CuGaSe_2$ in the scope of this project. But recent studies of Max Wolter, here at LPV, solved this problem for future measurements by depositing a layer of polystyrene beads on top of the thin film in order to have a rough scattering surface which annihilates the coherence of the emitted photoluminescence light. If the S2 defect can be confirmed in all wide-gap polycrystalline $Cu(In,Ga)Se_2$ samples, processes have to be developed to reduce its density. The detection of the occurring deep defect band can already be done at room temperature by fast and simple photoluminescence measurements. But if this Ga_{Cu} defect, according to theory, occurs in very high amounts in thermal equilibrium, it remains questionable if its density can be significantly reduced with new growth recipes.

The second important deep defect at 0.8 eV should be further characterized in the future by using an extended spectral energy range with higher signal-to-noise ratio. This can be done e.g. by an extended InGaAs-array detector which has superior sensitivity below 0.8 eV compared to the lock-in amplified InAs-diode used in this thesis. Further studies need to confirm that the broad defect band at 0.8 eV stems from a defect level at approx. 0.8 eV above the valence band and is not the result of e.g. a deep donor and deep acceptor pair recombination. This can be proven by temperature and excitation dependent measurements. Additionally, this band should be characterized over the full band gap range of $Cu(In,Ga)Se_2$. If the assignment of this defect level to the second charge transition of Cu_{III} is correct, this defect should be present in all Cu-rich samples, independent of the Ga/(Ga+In) ratio.

With regard to the optimization of Cu-rich solar cell efficiencies, the influence of Cu_{III} as a recombination center needs to be minimized. This could be done e.g. by lowering the Cu-excess to Cu/(In+Ga) ratios close to stoichiometry which most likely lowers the defect density of this antisite. Furthermore it seems plausible to increase the p-type doping density, so that the Fermi level moves closer to the valence band, which increases the amount of neutral Cu_{III} antisites and reduces the amount of recombination centers under illumination.

But even if the solar cell efficiencies of Cu-rich or wide-gap $Cu(In,Ga)Se_2$ cannot be further increased because the abundant defect densities of Cu_{III} or Ga_{Cu} cannot be significantly lowered, already the full characterization of their defect energies can be used in the future to optimize hybrid functional calculations. If additional studies confirm the exact energetic level of the two deep states and if additional calculations by hybrid functionals are then optimized towards the experimental results, large deviations of experiment and theory in the past can be understood and prevented. This not only leads to the possibility of improved calculations for other complex materials like $Cu(In,Ga)Se_2$, but also to the possibility of future reliable predictions of intrinsic defects for new solar cell materials.

For the above reasons it is suggested as an outlook to advance the present experimental results on a large set of polycrystalline samples, to improve the detectivity at low energies for better characterizations of the 0.8 eV band and to maintain a close collaboration between theoreticians and experimentalists for defects in $Cu(In,Ga)Se_2$. Especially the steady ongoing improvement of calculations in the community by e.g. using the Koopmans' theorem, which fixes the choice of the hybrid functional parameters for a certain band gap, can yield even more reliable defect models for the comparison of the present experimental findings.

Appendix

A Optical density filters

Table 2: Transmission of optical density filters for laser attenuation

	OD1	OD2	OD3	OD4
514 nm (argon-ion-laser)	9.6×10^{-2}	6.9×10^{-3}	6.3×10^{-4}	4.6×10^{-5}
663 nm (diode-laser)	9.7×10^{-2}	1.1×10^{-2}	1.4×10^{-3}	2.0×10^{-4}

B Spectrosil-B transmission

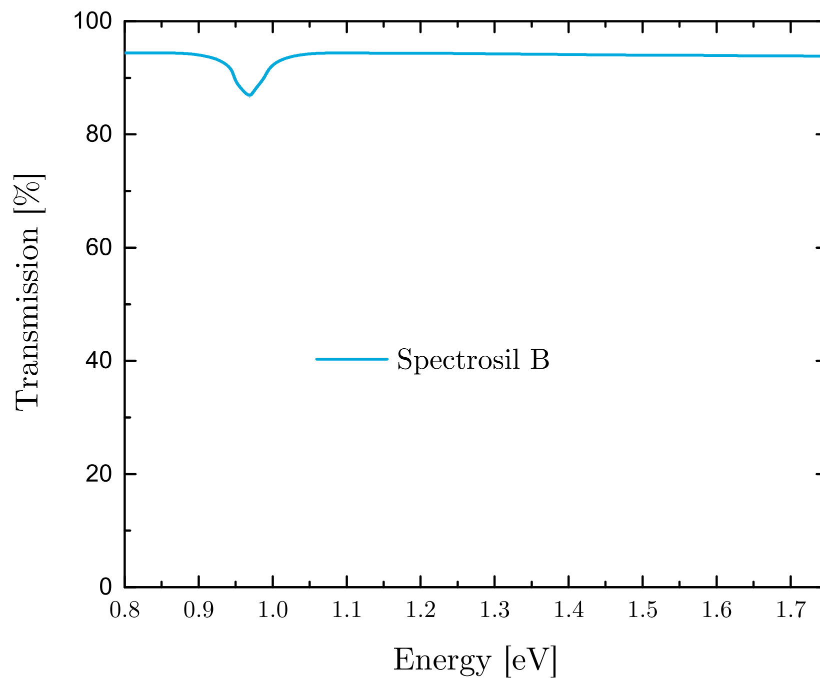

Figure 7: Transmission of Spectrosil-B cryostat windows taken from Oxford Instruments, Technical Note - Windows for cryogenic environments.

C SCAPS simulations

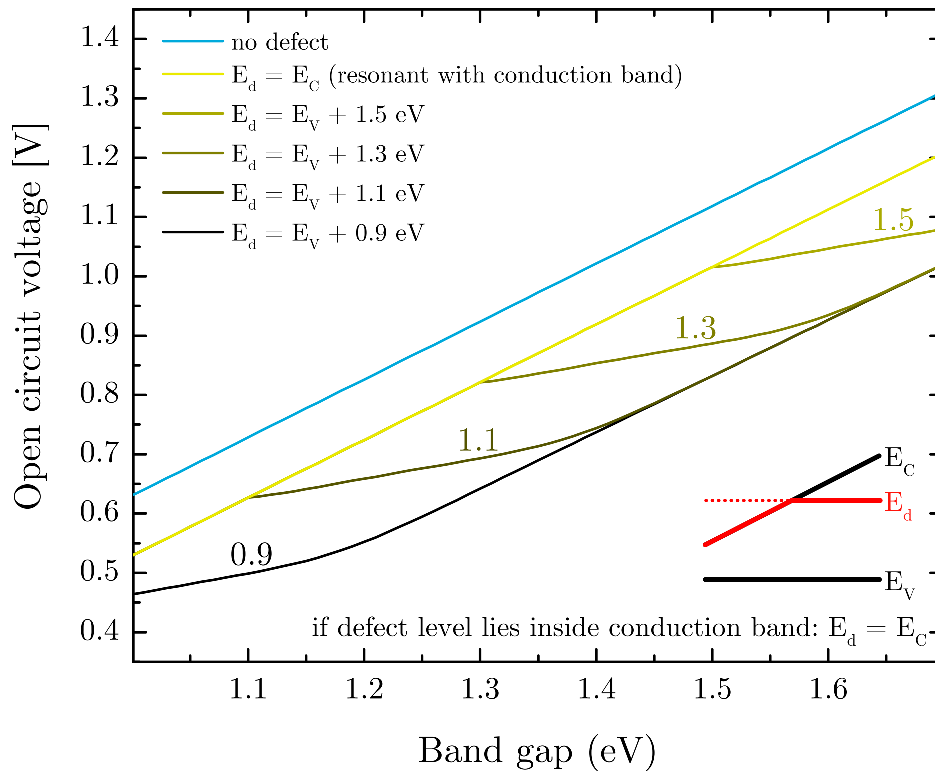

Figure 8: The same parameters as used in Fig. 5.22, but the defect energy E_d is varied and set to the conduction band minimum $\mathrm{E_C}$ if it is below ($E_\mathrm{C} < E_\mathrm{d}$).

Publications and Presentations

List of publications

C. Spindler, D. Regesch, and S. Siebentritt
Revisiting radiative deep-level transition in $CuGaSe_2$,
Applied Physics Letters, 109 (032105), 2016

C. Spindler, G. Rey, and S. Siebentritt
Excitation dependence of shallow and deep-level photoluminescence transitions,
Physical Review B, in review

C. Spindler, F. Babbe, M. H. Wolter, K. Santosha, F. Werner, and S. Siebentritt
Electronic Defects in $Cu(In,Ga)Se_2$ - a comprehensive model,
in preparation

M. Maiberg, C. Spindler, E. Jarzembowski, and R. Scheer
Electrical Characterization of $Cu(In,Ga)Se_2$ solar cells by voltage dependent time-resolved photoluminescence,
Thin Solid Films, 582 (379), 2015

G. Rey, C. Spindler, F. Babbe, W. Rachad, and S. Siebentritt, M. Nuys, and R. Carius, S. Li, and C. Platzer-Björkman
Absorption coefficient of semiconductor thin-films: measurement from photoluminescence,
Physical Review Applied, accepted

G. Rey, T. Weiss, J. Sendler, A. Finger, C. Spindler, F. Werner, M. Melchiorre, M. Hala, M. Guennou, and S. Siebentritt
Ordering kesterite improves solar cells: A low temperature post-deposition annealing study,
Solar Energy Materials & Solar Cells, 151 (131), 2016

F. Werner, D. Colombara, M. Melchiorre, N. Valle, B. El Adib, C. Spindler, and S. Siebentritt
Doping mechanism in pure $CuInSe_2$,
Journal of Applied Physics, 119 (173103), 2016

D. Colombara, F. Werner, T. Schwarz, I. C. Infante, Y. Fleming, N. Valle, C. Spindler, E. Vacchieri, G. Rey, M. Guennou, M. Bouttemy, M. Melchiorre, B. El Adib, B. Gault, D. Raabe, P. J. Dale, and S. Siebentritt
Na enhances In-Ga interdiffusion in Cu(In,Ga)Se_2 photovoltaic absorber,
Nature Communications, 9 (826), 2018

E. V. C Robert, R. Gunder, J. de Wild, C. Spindler, F. Babbe, B. El Adib, R. Treharne, S. Schorr, and P. Dale
Synthesis and characterization of thin film $Cu_2Sn_{1-x}Ge_xS_3$ ternary alloys: homogeneous intermixing of Sn and Ge,
Acta Materialia, 151 (125), 2018

F. Werner, F. Babbe, J. Burkhart, C. Spindler, and S. Siebentritt
Interdiffusion and doping gradients at the buffer/absorber interface in thin-film solar cells,
Advanced Energy Materials, in review

List of presentations

C. Spindler, D. Regesch, and S. Siebentritt
Deep electron traps in $CuGaSe_2$ characterized by photoluminescence
E-MRS Spring Meeting, Lille 2016, oral presentation

C. Spindler
Intrinsic point defects in Cu(In,Ga)Se_2
Sharc25 Defect Seminar, Luxembourg 2017, oral presentation

C. Spindler, G. Rey, and S. Siebentritt
Extraction of absorption coefficients from photoluminescence
GRS Defects in Semiconductors, New London 2016, poster presentation

C. Spindler, and S. Siebentritt
Excitation dependence of photoluminescence transitions
GRC Defects in Semiconductors, New London 2016, poster presentation

C. Spindler, and S. Siebentritt
Luminescence detection of the 0.8 eV defect in Cu(In,Ga)Se_2
MRS Spring Meeting, Phoenix 2017, poster presentation

C. Spindler, G. Rey, and S. Siebentritt
Can deep defects limit the open circuit voltage in Cu(In,Ga)Se_2?
MRS Spring Meeting, Phoenix 2017, poster presentation

Acknowledgments

First of all I will thank Susanne Siebentritt for giving me the opportunity to work in her group, for having a very interesting research topic, learning plenty of new things, participating in international conferences and spending a very good time in Luxembourg. Knowing that in Germany the word Doktorvater exists, I am thankful that I had a very helpful Doktormutter for the guidance of this thesis. We had a lot of good discussions throughout the years, Susanne was always supporting me and it was a really nice working atmosphere at LPV.

I will also thank Roland Scheer and Ludger Wirtz for being part of the thesis committee, as well as Alex Redinger and Jürgen Christen for participating in the defense committee. Fortunately, the Photovoltaics Group of Roland Scheer and my master thesis project arouse my interest in the field, which finally brought me to Luxembourg.

Special thanks go also to all the former and current members of LPV and the LEM group from Phillip Dale. I am happy that I had so many nice colleagues which made the time at work being so good.
I will thank Patricia Ramoa for plenty of administrative work, Thomas Schuler for endless repairs, help with the machines and his accurate scheduling of kitchen meetings, David Regesch for teaching me all the sample preparations and photoluminescence characterizations, Maxime Thevenin and Michele Melchiorre for their support with EDX and SEM measurements, Florian Werner for discussions and help with MOVPE, Finn Babbe, Max Wolter, Jan Sendler and Germain Rey for all their support and best times in our unforgettable PL team, Erika Robert, Alexandre Crossay, Sara Tombolato and Tobias Betram for a lot of good days outside of work and all the other LPV and LEM members, too.

I will further thank Alex Gansen, Mads Weber, Charlotte Cochard, David Spirito, Constance Toulouse and Shankari Nadupalli from LIST for having nice times at the institute or out of work and I will thank the Crazy People United who made Luxembourg City a nice place to live in.

At the end, I will especially thank my parents and my sister for always supporting and helping me during the good and the difficult times during my PhD.

Bibliography

[1] Solar Frontier. Solar Frontier Achieves World Record Thin-Film Solar Cell Efficiency of 22.9%. http://www.solar-frontier.com/eng/news/2017/1220_press.html, 2017. (accessed 06-March-2018).

[2] W. Shockley and H. J. Queisser. Detailed Balance Limit of Efficiency of pn Junction Solar Cells. *Journal of Applied Physics*, 32(3):510–519, 1961.

[3] S. Siebentritt. What limits the efficiency of chalcopyrite solar cells? *Solar Energy Materials and Solar Cells*, 95(6):1471–1476, 2011.

[4] M. Topic, R. M. Geisthardt, and J. R. Sites. Performance Limits and Status of Single-Junction Solar Cells With Emphasis on CIGS. *IEEE Journal of Photovoltaics*, 5(1):360–365, 2015.

[5] J. Zeitouny, E. A. Katz, A. Dollet, and A. Vossier. Band Gap Engineering of Multi-Junction Solar Cells: Effects of Series Resistances and Solar Concentration. *Scientific Reports*, 7(1):1766, 2017.

[6] R. C. Valderrama, P. J. Sebastian, J. Pantoja Enriquez, and S. A. Gamboa. Photoelectrochemical characterization of CIGS thin films for hydrogen production. *Solar Energy Materials and Solar Cells*, 88(2):145–155, 2005.

[7] A. Gerhard, W. Harneit, S. Brehme, A. Bauknecht, U. Fiedeler, M. C. Lux-Steiner, and S. Siebentritt. Acceptor activation energies in epitaxial $CuGaSe_2$ grown by MOVPE. *Thin Solid Films*, 387(1-2):67–70, 2001.

[8] S. Siebentritt, L. Guetay, D. Regesch, Y. Aida, and V. Depredurand. Why do we make $Cu(In,Ga)Se_2$ solar cells non-stoichiometric? *Solar Energy Materials and Solar Cells*, 119:18–25, 2013.

[9] F. Babbe, L. Choubrac, and S. Siebentritt. Quasi Fermi level splitting of Cu-rich and Cu-poor $Cu(In,Ga)Se_2$ absorber layers. *Applied Physics Letters*, 109(8):082105, 2016.

[10] S. Siebentritt. *Wide-Gap Chalcopyrites*, chapter 7 - Shallow Defects in the Wide Gap Chalcopyrite $CuGaSe_2$, pages 113–156. Springer-Verlag Berlin Heidelberg, 2006.

[11] J. Krustok, J. Raudoja, J. H. Schon, M. Yakushev, and H. Collan. The role of deep donor-deep acceptor complexes in CIS-related compounds. *Thin Solid Films*, 361:406–410, 2000.

[12] A. Meeder, D. F. Marron, V. Tezlevan, E. Arushanov, A. Rumberg, T. Schedel-Niedrig, and M. C. Lux-Steiner. Radiative recombination in CVT-grown $CuGaSe_2$ single crystals and thin films. *Thin Solid Films*, 431:214–218, 2003.

[13] S. Siebentritt, M. Igalson, C. Persson, and S. Lany. The electronic structure of chalcopyrites-bands, point defects and grain boundaries. *Progress in Photovoltaics*, 18(6):390–410, 2010.

[14] S. Siebentritt, I. Beckers, T. Riemann, J. Christen, A. Hoffmann, and M. Dworzak. Reconciliation of luminescence and Hall measurements on the ternary semiconductor $CuGaSe_2$. *Applied Physics Letters*, 86(9), 2005.

[15] A. Meeder, D. F. Marron, V. Chu, J. P. Conde, A. Jager-Waldau, A. Rumberg, and M. C. Lux-Steiner. Photoluminescence and sub band gap absorption of $CuGaSe_2$ thin films. *Thin Solid Films*, 403:495–499, 2002.

[16] J. Krustok, J. Raudoja, M. Yakushev, R. Pilkington, A. Hill, and H. Collan. Deep Level Photoluminescence in $CuIn_{1-x}Ga_xSe_2$. *Japanese Journal of Applied Physics*, 39(1):332–333, 2000.

[17] A. Alkauskas, M. D. McCluskey, and C. G. Van de Walle. Tutorial: Defects in semiconductors - Combining experiment and theory. *Journal of Applied Physics*, 119(18):181101, 2016.

[18] H. G. Grimm and A. Sommerfeld. Über den. Zusammenhang des Abschlusses der Elektronengruppen im Atom mit den chemischen Valenzzahlen. *Zeitschrift für Physik*, 36(1):36–59, 1926.

[19] J. L. Shay, J. H. Wernick, and B. R. Pamplin. *Ternary Chalcopyrite Semiconductors: Growth, Electronic Properties, and Applications.* Pergamon Press Oxford, 1975.

[20] T. Bertram. *Doping, Defects And Solar Cell Performance Of Cu-rich Grown $CuInSe_2$*. PhD thesis, University of Luxembourg, 2016.

[21] J. C. Mikkelsen. Ternary phase relations of the chalcopyrite compound $CuGaSe_2$. *Journal of Electronic Materials*, 10(3):541–558, 1981.

[22] S. B. Zhang, S.-H. Wei, and A. Zunger. Stabilization of Ternary Compounds via Ordered Arrays of Defect Pairs. *Physical Review Letters*, 78:4059–4062, 1997.

[23] J. Pohl and K. Albe. Intrinsic point defects in $CuInSe_2$ and $CuGaSe_2$ as seen via screened-exchange hybrid density functional theory. *Physical Review B*, 87(24), 2013.

[24] T. Goedecke, T. Haalboom, and F. Ernst. Phase equilibria of Cu-In-SeIII. The In(2)Se(3)-Se-Cu(2)Se subsystem. *Zeitschrift fr Metallkunde*, 91:651–662, 2000.

[25] Y. Hashimoto, N. Kohara, T. Negami, M. Nishitani, and T. Wada. Surface Characterization of Chemically Treated Cu(In,Ga)Se_2 Thin Films. *Japanese Journal of Applied Physics*, 35(9R):4760, 1996.

[26] D. Regesch, L. Gtay, J. K. Larsen, V. Deprdurand, D. Tanaka, Y. Aida, and S. Siebentritt. Degradation and passivation of $CuInSe_2$. *Applied Physics Letters*, 101(11):112108, 2012.

[27] F. Werner, F. Babbe, J. Burkhart, C. Spindler, and S. Siebentritt. Interdiffusion and doping gradients at the buffer/absorber interface in thin-film solar cells. *Advanced Energy Materials*, under review, 2018.

[28] M. I. Alonso, M. Garriga, C. A. Durante Rincon, E. Hernandez, and M. Leon. Optical functions of chalcopyrite $CuGa_xIn_{1-x}Se_2$ alloys. *Applied Physics A*, 74(5):659–664, 2002.

[29] S. Chichibu, T. Mizutani, K. Murakami, T. Shioda, T. Kurafuji, H. Nakanishi, S. Niki, P. J. Fons, and A. Yamada. Band gap energies of bulk, thin-film, and epitaxial layers of $CuInSe_2$ and $CuGaSe_2$. *Journal of Applied Physics*, 83(7):3678–3689, 1998.

[30] S. Chichibu, Y. Harada, M. Uchida, T. Wakiyama, S. Matsumoto, S. Shirakata, S. Isomura, and H. Higuchi. Heteroepitaxy and characterization of $CuGaSe_2$ layers grown by low-pressure metalorganic chemical-vapor deposition. *Journal of Applied Physics*, 76(5):3009–3015, 1994.

[31] N. N. Syrbu, M. Bogdanash, V. E. Tezlevan, and I. Mushcutariu. Lattice vibrations in $CuIn_{1-x}Ga_xSe_2$ crystals. *Physica B: Condensed Matter*, 229(2):199–212, 1997.

[32] M. A. Green, Y. Hishikawa, E. D. Dunlop, D. H. Levi, J. HohlEbinger, and A. W. Y. HoBaillie. Solar cell efficiency tables (version 51). *Progress in Photovoltaics*, 26(1):3–12, 2017.

[33] D. Hariskos, S. Spiering, and M. Powalla. Buffer layers in Cu(In,Ga)Se2 solar cells and modules. *Thin Solid Films*, 480–481:99–109, 2005.

[34] D. Koenig, K. Casalenuovo, Y. Takeda, G. Conibeer, J. F. Guillemoles, R. Patterson, L. M. Huang, and M. A. Green. Hot carrier solar cells: Principles, materials and design. *Physica E*, 42(10):2862–2866, 2010.

[35] D. Sangalli and A. Marini. Complete collisions approximation to the Kadanoff-Baym equation: a first-principles implementation. *Journal of Physics: Conference Series*, 609(1):012006, 2015.

[36] Y. Aida, V. Depredurand, J. K. Larsen, H. Arai, D. Tanaka, M. Kurihara, and S. Siebentritt. Curich $CuInSe_2$ solar cells with a Cupoor surface. *Progress in Photovoltaics*, 23(6):754–764, 2014.

[37] F. Larsson, N. S. Nilsson, J. Keller, C. Frisk, V. Kosyak, M. Edoff, and T. Toerndahl. Record 1.0 V open-circuit voltage in wide band gap chalcopyrite solar cells. *Progress in Photovoltaics*, 25(9):755–763, 2017.

[38] R. Scheer and H.-W. Schock. *Chalcogenide Photovoltaics*, chapter 4 - Thin Film Material Properties, pages 175–234. WILEY-VCH Verlag, 2011.

[39] W. Shockley and W. T. Read. Statistics of the Recombinations of Holes and Electrons. *Physical Review*, 87(5):835–842, 1952.

[40] S. Schuler, S. Siebentritt, S. Nishiwaki, N. Rega, J. Beckmann, S. Brehme, and M. C. Lux-Steiner. Self-compensation of intrinsic defects in the ternary semiconductor $CuGaSe_2$. *Physical Review B*, 69(4), 2004.

[41] Van Vechten. *Handbook on Semiconductors*, volume 3. Elsevier Science Ltd, 1980.

[42] S. Lany and A. Zunger. Intrinsic DX centers in ternary chalcopyrite semiconductors. *Physical Review Letters*, 100(1), 2008.

[43] J. K. Larsen. *Inhomogeneities in Epitaxial Chalcopyrites Studied by Photoluminescence.* PhD thesis, University of Luxembourg, 2011.

[44] S. Siebentritt, N. Papathanaslou, and M. C. Lux-Steiner. Potential fluctuations in compensated chalcopyrites. *Physica B: Condensed Matter*, 376:831–833, 2006.

[45] J. K. Larsen, L. Guetay, Y. Aida, and S. Siebentritt. Spatial variations of optoelectronic properties in single crystalline $CuGaSe_2$ thin films studied by photoluminescence. *Thin Solid Films*, 519(21):7332–7336, 2011.

[46] A. C. Jones and P. OBrien. *CVD of Compound Semiconductors*, chapter 1 - Basic Concepts, pages 1–42. VCH Verlagsgesellschaft, 1997.

[47] G. Stringfellow. *Organometallic Vapor-Phase Epitaxy.* Academic Press, 1999.

[48] G. Hanna, J. Mattheis, V. Laptev, Y. Yamamoto, U. Rau, and H. W. Schock. Influence of the selenium flux on the growth of $Cu(In,Ga)Se_2$ thin films. *Thin Solid Films*, 431–432:31–36, 2003.

[49] E. Wallin, T. Jarmar, U. Malm, M. Edoff, and L. Stolt. Influence of the average Se-to-metal overpressure during co-evaporation of $Cu(In_xGa_{1x})Se_2$. *Thin Solid Films*, 519(21):7237–7240, 2011.

[50] U. Pohl. *Epitaxy of Semiconductors.* Springer-Verlag Berlin Heidelberg, 2013.

[51] C. Downs and T. E. Vandervelde. Progress in Infrared Photodetectors Since 2000. *Sensors*, 13:5054–5098, 2013.

[52] D. Regesch. *Photoluminescence and Solar Cell Studies of Chalcopyrites: Comparison of Cu-rich vs. Cu-poor and Polycrystalline vs. Epitaxial Material.* PhD thesis, University of Luxembourg, 2014.

[53] E. D. Bourret, F. X. Zach, K. M. Yu, and J. M. Walker. Growth and characterization of ZnSe grown by organometallic vapor phase epitaxy using diisopropyl selenide and diethyl zinc. *Journal of Crystal Growth*, 147(1-2):47–54, 1995.

[54] G. H. Fan, N. Maung, T. L. Ng, P. F. Heelis, J. O. Williams, A. C. Wright, D. F. Foster, and D. J. Cole-Hamilton. Thermal decomposition of di-tertiarybutyl selenide and dimethylzinc in a metalorganic vapour phase epitaxy reactor. *Journal of Crystal Growth*, 170(1):485–490, 1997.

[55] W. Taudt, B. Wachtendorf, R. Beccard, A. Wahid, M. Heuken, A. L. Gurskii, and K. Vakarelska. Low-temperature growth and nitrogen doping of ZnSe using diethylzinc and ditertiarybutylselenide in a plasma-stimulated low-pressure metalorganic vapour phase epitaxy system. *Journal of Crystal Growth*, 145(1):582–588, 1994.

[56] S. Chichibu, S. Shirakata, S. Isomura, and H. Nakanishi. Visible and Ultraviolet Photoluminescence from CuIIIVI$_2$ Chalcopyrite Semiconductors Grown by Metalorganic Vapor Phase Epitaxy. *Japanese Journal of Applied Physics*, 36(3S):1703, 1997.

[57] N. I. Buchan, C. A. Larsen, and G. B. Stringfellow. Mass spectrometric studies of trimethylindium pyrolysis. *Journal of Crystal Growth*, 92(3):591–604, 1988.

[58] P. W. Lee, T. R. Omstead, D. R. McKenna, and K. F. Jensen. In situ mass spectroscopy and thermogravimetric studies of GaAs MOCVD gas phase and surface reactions. *Journal of Crystal Growth*, 85(1):165–174, 1987.

[59] S. Fujita and S. Fujita. Photo-assisted metalorganic vapor phase epitaxial growth of wide-gap IIVI semiconductors. *Journal of Crystal Growth*, 117(1):67–74, 1992.

[60] P. Wuerfel. *Physics of Solar Cells*. WILEY-VCH Verlag, 2005.

[61] D. Abou-Ras, T. Kirchartz, and U. Rau. *Advances Characterization Techniques for Thin Film Solar Cells*. WILEY-VCH Verlag, 2011.

[62] S. Siebentritt and U. Rau. *Wide-Gap Chalcopyrites*. Springer-Verlag Berlin Heidelberg, 2006.

[63] H. B. Bebb and E. W. Williams. *Semiconductors and Semimetals Vol. 8*, volume Volume 8, chapter 4 - Photoluminescence I: Theory, pages 181–320. Elsevier, 1972.

[64] J. I. Pankove. *Optical Processes in Semiconductors*. Dover Publications, 1975.

[65] M. A. Reshchikov, D. O. Demchenko, J. D. McNamara, S. Fernandez-Garrido, and R. Calarco. Green luminescence in Mg-doped GaN. *Physical Review B*, 90(3), 2014.

[66] R. Scheer and H.-W. Schock. *Chalcogenide Photovoltaics*. WILEY-VCH Verlag, 2011.

[67] J. H. Werner, J. Mattheis, and U. Rau. Efficiency limitations of polycrystalline thin film solar cells: case of Cu(In,Ga)Se$_2$. *Thin Solid Films*, 480:399–409, 2005.

[68] J. K. Katahara and H. W. Hillhouse. Quasi-Fermi level splitting and sub-bandgap absorptivity from semiconductor photoluminescence. *Journal of Applied Physics*, 116(17), 2014.

[69] F. Luckert, M. V. Yakushev, C. Faugeras, A. V. Karotki, A. V. Mudryi, and R. W. Martin. Diamagnetic shift of the A free exciton in CuGaSe$_2$ single crystals. *Applied Physics Letters*, 97(16):162101, 2010.

[70] M. V. Yakushev, F. Luckert, C. Faugeras, A. V. Karotki, A. V. Mudryi, and R. W. Martin. Excited states of the free excitons in CuInSe$_2$ single crystals. *Applied Physics Letters*, 97(15):152110, 2010.

[71] A. Bauknecht, S. Siebentritt, J. Albert, Y. Tomm, and M. C. Lux-Steiner. Excitonic Photoluminescence from CuGaSe$_2$ Single Crystals and Epitaxial Layers: Temperature Dependence of the Band Gap Energy. *Japanese Journal of Applied Physics*, 39(Suppl. 39-1):322–325, 2000.

[72] H. Atzmueller and U. Schroeder. Theoretical Investigations of Haynes' Rule. *Physica Status Solidi B*, 89(2):349–356, 1978.

[73] A. Bauknecht, S. Siebentritt, J. Albert, and M. C. Lux-Steiner. Radiative recombination via intrinsic defects in $Cu_xGa_ySe_2$. *Journal of Applied Physics*, 89(8):4391–4400, 2001.

[74] T. Unold and L. Guetay. *Advanced Characterization Techniques for Thin Film Solar Cells*, chapter 7 - Photoluminescence Analysis of Thin-Film Solar Cells, pages 151–175. WILEY-VCH Verlag, 2011.

[75] E. Zacks and A. Halperin. Dependence of the Peak Energy of the Pair-Photoluminescence Band on Excitation Intensity. *Physical Review B*, 6(8):3072–3075, 1972.

[76] J. Krustok, H. Collan, and K. Hjelt. Does the low-temperature Arrhenius plot of the photoluminescence intensity in CdTe point towards an erroneous activation energy? *Journal of Applied Physics*, 81(3):1442–1445, 1997.

[77] M. A. Reshchikov. Temperature dependence of defect-related photoluminescence in III-V and II-VI semiconductors. *Journal of Applied Physics*, 115(1), 2014.

[78] M. A. Reshchikov and H. Morkoc. Luminescence properties of defects in GaN. *Journal of Applied Physics*, 97(6), 2005.

[79] G. Davis. *Identification of Defects in Semiconductors*, chapter 1 - Optical Measurements of Point Defects, pages 1–92. Academic Press, 1998.

[80] M. A. Reshchikov, J. D. McNamara, F. Zhang, M. Monavarian, A. Usikov, H. Helava, Yu. Makarov, and H. Morkoç. Zero-phonon line and fine structure of the yellow luminescence band in GaN. *Physical Review B*, 94:035201, 2016.

[81] R. Kniese, M. Powalla, and U. Rau. Evaluation of electron beam induced current profiles of Cu(In,Ga)Se_2 solar cells with different Ga-contents. *Thin Solid Films*, 517(7):2357–2359, 2009.

[82] M. H. Wolter, B. Bissig, P. Reinhard, S. Buecheler, P. Jackson, and S. Siebentritt. Correcting for interference effects in the photoluminescence of Cu(In,Ga)Se_2 thin films. *Physica Status Solidi C*, 14(6):1600189, 2017.

[83] J. Mooney and P. Kambhampati. Get the Basics Right: Jacobian Conversion of Wavelength and Energy Scales for Quantitative Analysis of Emission Spectra. *The Journal of Physical Chemistry Letters*, 4(19):3316–3318, 2013.

[84] Hamamatsu. Characteristic and use of infrared detectors. Technical report, Technical Information SD-12, 2011.

[85] T. Schmidt, K. Lischka, and W. Zulehner. Excitation-power dependence of the near-band-edge photoluminescence of semiconductors. *Physical Review B*, 45(16):8989–8994, 1992.

[86] T. Schmidt, G. Daniel, and K. Lischka. The excitation power dependence of the near band edge photoluminescence of II-VI semiconductors. *Journal of Crystal Growth*, 117(1-4):748–752, 1992.

[87] C. Spindler, D. Regesch, and S. Siebentritt. Revisiting radiative deep-level transitions in $CuGaSe_2$ by photoluminescence. *Applied Physics Letters*, 109(3):032105, 2016.

[88] M. A. Reshchikov and R. Y. Korotkov. Analysis of the temperature and excitation intensity dependencies of photoluminescence in undoped GaN films. *Physical Review B*, 64(11), 2001.

[89] W. Grieshaber, E. F. Schubert, I. D. Goepfert, R. F. Karlicek, M. J. Schurman, and C. Tran. Competition between band gap and yellow luminescence in GaN and its relevance for optoelectronic devices. *Journal of Applied Physics*, 80(8):4615–4620, 1996.

[90] N. M. Gasanly, A. Serpenguezel, A. Aydinli, O. Guerlue, and I. Yilmaz. Donor-acceptor pair recombination in $AgIn_5S_8$ single crystals. *Journal of Applied Physics*, 85(6):3198–3201, 1999.

[91] H.-H. Fang, R. Raissa, M. Abdu-Aguye, S. Adjokatse, G. R. Blake, J. Even, and M. A. Loi. Photophysics of Organic-Inorganic Hybrid Lead Iodide Perovskite Single Crystals. *Advanced Functional Materials*, 25(16):2378–2385, 2015.

[92] D. P. Halliday, R. Claridge, M. C. J. Goodman, B. G. Mendis, K. Durose, and J. D. Major. Luminescence of Cu_2ZnSnS_2 polycrystals described by the fluctuating potential model. *Journal of Applied Physics*, 113(22):223503, 2013.

[93] Z. C. Feng, M. J. Bevan, S. V. Krishnaswamy, and W. J. Choyke. A photoluminescence comparison of CdTe thin films grown by molecular beam epitaxy, metalorganic chemical vapor deposition, and sputtering in ultrahigh vacuum. *Journal of Applied Physics*, 64(5):2595–2600, 1988.

[94] W. Z. Shen, H. Z. Wu, and P. J. McCann. Excitonic line broadening in PbSrSe thin films grown by molecular beam epitaxy. *Journal of Applied Physics*, 91(6):3621–3625, 2002.

[95] R. Saniz, J. Bekaert, B. Partoens, and D. Lamoen. Structural and electronic properties of defects at grain boundaries in $CuInSe_2$. *Physical Chemistry Chemical Physics*, 19:14770–14780, 2017.

[96] J. Krustok, H. Collan, M. Yakushev, and K. Hjelt. The role of spatial potential fluctuations in the shape of the PL bands of multinary semiconductor compounds. *Physica Scripta*, T79:179–182, 1999.

[97] N. Rega, S. Siebentritt, J. Albert, S. Nishiwaki, A. Zajogin, M. C. Lux-Steiner, R: Kniese, and M. J. Romero. Excitonic luminescence of $Cu(In,Ga)Se_2$. *Thin Solid Films*, 480:286–290, 2005.

[98] E. F. Schubert, E. O. Gobel, Y. Horikoshi, K. Ploog, and H. J. Queisser. Alloy broadening in photoluminescence spectra of $Al_xGa_{1-x}As$. *Physical Review B*, 30(2):813–820, 1984.

[99] J. K. Larsen, S. Y. Li, J. J. S. Scragg, Y. Ren, C. Hagglund, M. D. Heinemann, S. Kretzschmar, T. Unold, and C. Platzer-Bjorkman. Interference effects in photoluminescence spectra of Cu_2ZnSnS_4 and $Cu(In,Ga)Se_2$ thin films. *Journal of Applied Physics*, 118(3), 2015.

[100] R. D. Deslattes, E. G. Kessler, P. Indelicato, L. de Billy, E. Lindroth, and J. Anton. X-ray transition energies: new approach to a comprehensive evaluation. *Reviews of Modern Physics*, 75:35–99, 2003.

[101] H.-G. Bruehl and H. Neumann. Thermal expansion of $CuGaSe_2$. *Solid State Communications*, 34(4):225–227, 1980.

[102] H.-G. Bruehl, H. Neumann, T. Pfeiffer, and G. Kuhn. Anisotropic thermal expansion of Cu-III-VI_2 compounds. *Physica Status Solidi A*, 66(2):597–600, 1981.

[103] T. Soma, J. Satoh, and H. Matsuo. Thermal expansion coefficient of GaAs and InP. *Solid State Communications*, 42(12):889–892, 1982.

[104] W. Shan, W. Walukiewicz, J. Wu, K. M. Yu, J. W. Ager, S. Siebentritt, and N. Rega. Pressure-dependent photoluminescence study of $CuGaSe_2$. *Physica Status Solidi B*, 241(14):3117–3122, 2004.

[105] R. P. Prasankumar and A. J. Taylor. *Optical Techniques for Solid-State Materials Characterization*. CRC Press, 2012.

[106] P. Wuerfel, S. Finkbeiner, and E. Daub. Generalized Planck's radiation law for luminescence via indirect transitions. *Applied Physics A*, 60(1):67–70, 1995.

[107] C. Persson. Anisotropic hole-mass tensor of $CuIn_{1-x}Ga_x(S,Se)_2$: Presence of free carriers narrows the energy gap. *Applied Physics Letters*, 93(7), 2008.

[108] L. Mandel, R. D. Tomlinson, M. J. Hampshire, and H. Neumann. Electrical properties of $CuGaSe_2$ single crystals. *Solid State Communications*, 32(3):201–204, 1979.

[109] I. Pelant and J. Valenta. *Luminescence Spectrsocopy of Semiconductors*. Oxford University Press, 2012.

[110] M. A. Reshchikov, A. A. Kvasov, M. F. Bishop, T. McMullen, A. Usikov, V. Soukhoveev, and V. A. Dmitriev. Tunable and abrupt thermal quenching of photoluminescence in high-resistivity Zn-doped GaN. *Physical Review B*, 84(7), 2011.

[111] A. Alkauskas, P. Broqvist, and A. Pasquarello. Defect levels through hybrid density functionals: Insights and applications. *Physica Status Solidi B*, 248(4):775–789, 2011.

[112] S. H. Wei and A. Zunger. Band offsets and optical bowings of chalcopyrites and Znbased IIVI alloys. *Journal of Applied Physics*, 78(6):3846–3856, 1995.

[113] H. Bernien, L. Childress, L. Robledo, M. Markham, D. Twitchen, and R. Hanson. Two-Photon Quantum Interference from Separate Nitrogen Vacancy Centers in Diamond. *Physical Review Letters*, 108:043604, 2012.

[114] P. Jackson, R. Wuerz, D. Hariskos, E. Lotter, W. Witte, and M. Powalla. Effects of heavy alkali elements in Cu(In,Ga)Se_2 solar cells with efficiencies up to 22.6 %. *Physica Status Solidi RRL*, 10(8):583–586, 2016.

[115] M. Burgelman, P. Nollet, and S. Degrave. Modelling polycrystalline semiconductor solar cells. *Thin Solid Films*, 361:527–532, 2000.

[116] M. Burgelman, K. Decock, S. Khelifi, and A. Abass. Advanced electrical simulation of thin film solar cells. *Thin Solid Films*, 535:296–301, 2013.

[117] M. Saad, H. Riazi, E. Bucher, and M. C. Lux-Steiner. $CuGaSe_2$ solar cells with 9.7 % power conversion efficiency. *Applied Physics A*, 62(2):181–185, 1996.

[118] W. N. Shafarman, R. Klenk, and B. E. McCandless. Device and material characterization of Cu(InGa)Se_2 solar cells with increasing band gap. *Journal of Applied Physics*, 79(9):7324–7328, 1996.

[119] R. Herberholz, V. Nadenau, U. Ruhle, C. Koble, H. W. Schock, and B. Dimmler. Prospects of wide-gap chalcopyrites for thin film photovoltaic modules. *Solar Energy Materials and Solar Cells*, 49(1-4):227–237, 1997.

[120] M. A. Contreras, L. M. Mansfield, B. Egaas, J. Li, M. Romero, R. Noufi, E. Rudiger-Voigt, and W. Mannstadt. Wide bandgap Cu(In,Ga)Se_2 solar cells with improved energy conversion efficiency. *Progress in Photovoltaics*, 20(7):843–850, 2012.

[121] J. AbuShama, R. Noufi, S. Johnston, S. Ward, and X. Wu. Improved performance in $CuInSe_2$ and surface-modified $CuGaSe_2$ solar cells. *Conference Record of the 31st IEEE Photovoltaic Specialists Conference*, pages 299–302, 2005.

[122] M. Edoff, T. Jarmar, N. S. Nilsson, E. Wallin, D. Hoegstroem, O. Stolt, O. Lundberg, W. Shafarman, and L. Stolt. High V_{oc} in (Cu,Ag)(In,Ga)Se_2 Solar Cells. *IEEE Journal of Photovoltaics*, 7(6):1789–1794, 2017.

[123] J. T. Heath, J. D. Cohen, W. N. Shafarman, D. X. Liao, and A. A. Rockett. Effect of Ga content on defect states in $CuIn_{1-x}Ga_xSe_2$ photovoltaic devices. *Applied Physics Letters*, 80(24):4540–4542, 2002.

[124] X. B. Hu, T. Sakurai, A. Yamada, S. Ishizuka, S. Niki, and K. Akimoto. Investigation of the relative density of deep defects in Cu(In,Ga)Se_2 thin films dependent on Ga content by transient photocapacitance method. *Japanese Journal of Applied Physics*, 53(6), 2014.

[125] X. B. Hu, T. Sakurai, A. Yamada, S. Ishizuka, S. Niki, and K. Akimoto. Investigation of the properties of deep-level defect in Cu(In,Ga)Se_2 thin films by steady-state photocapacitance and time-resolved photoluminescence measurements. *Japanese Journal of Applied Physics*, 54(4), 2015.

[126] L. M. Mansfield, D. Kuciauskas, P. Dippo, J. V. Li, K. Bowers, B. To, C. DeHart, and K. Ramanathan. Optoelectronic Investigation of Sb-Doped Cu(In,Ga)Se_2. *IEEE Journal of Photovoltaics*, 5(6):1769–1774, 2015.

[127] L. Guetay, D. Regesch, J. K. Larsen, Y. Aida, V. Depredurand, A. Redinger, S. Caneva, S. Schorr, C. Stephan, J. Vidal, S. Botti, and S. Siebentritt. Feedback mechanism for the stability of the band gap of $CuInSe_2$. *Physical Review B*, 86(4), 2012.

[128] J. C. Bourgoin and T. Neffati. The energy level of the EL2 defect in GaAs. *Solid-State Electronics*, 43(1):153–158, 1999.

[129] J. Windscheif, H. Ennen, U. Kaufmann, J. Schneider, and T. Kimura. Annealing behavior of the 0.8 eV luminescence in undoped semiinsulating GaAs. *Applied Physics A*, 30(1):47–49, 1983.

[130] H. J. Bardeleben, D. Stiévenard, D. Deresmes, A. Huber, and J. C. Bourgoin. Identification of a defect in a semiconductor: EL2 in GaAs. *Physical Review B*, 34:7192–7202, 1986.

[131] S. B. Zhang, S.-H. Wei, A. Zunger, and H. Katayama-Yoshida. Defect physics of the $CuInSe_2$ chalcopyrite semiconductor. *Physical Review B*, 57:9642–9656, 1998.

[132] A. Alkauskas, P. Broqvist, and A. Pasquarello. Defect energy levels in density functional calculations: Alignment and band gap problem. *Physical Review Letters*, 101(4), 2008.

[133] J. Heyd, G. E. Scuseria, and M. Ernzerhof. Hybrid functionals based on a screened Coulomb potential. *The Journal of Chemical Physics*, 118(18):8207–8215, 2003.

[134] J. P. Perdew, M. Ernzerhof, and K. Burke. Rationale for mixing exact exchange with density functional approximations. *The Journal of Chemical Physics*, 105(22):9982–9985, 1996.

[135] J. Pohl. *Structure and Properties of Defects in Photovoltaic Absorber Materials: Atomic Scale Computer Simulations of Si and Cu(In,Ga)Se_2*. PhD thesis, Technical University Darmstadt, 2013.

[136] J. E. Moussa, P. A. Schultz, and J. R. Chelikowsky. Analysis of the Heyd-Scuseria-Ernzerhof density functional parameter space. *The Journal of Chemical Physics*, 136(20):204117, 2012.

[137] H.-P. Komsa, T. T. Rantala, and A. Pasquarello. Finite-size supercell correction schemes for charged defect calculations. *Physical Review B*, 86:045112, 2012.

[138] M. Malitckaya, H.-P. Komsa, V. Havu, and J. M. Puska. First-Principles Modeling of Point Defects and Complexes in Thin-Film Solar-Cell Absorber $CuInSe_2$. *Advanced Electronic Materials*, 3(6):1600353, 2017.

[139] C. Persson, Y. J. Zhao, S. Lany, and A. Zunger. n-type doping of $CuInSe_2$ and $CuGaSe_2$. *Physical Review B*, 72(3), 2005.

[140] J. Bekaert, R. Saniz, B. Partoens, and D. Lamoen. Native point defects in $Culn_{1-x}Ga_xSe_2$: hybrid density functional calculations predict the origin of p- and n-type conductivity. *Physical Chemistry Chemical Physics*, 16(40):22299–22308, 2014.

[141] B. Huang, S. Y. Chen, H. X. Deng, L. W. Wang, M. A. Contreras, R. Noufi, and S. H. Wei. Origin of Reduced Efficiency in Cu(In,Ga)Se_2 Solar Cells With High Ga Concentration: Alloy Solubility Versus Intrinsic Defects. *IEEE Journal of Photovoltaics*, 4(1):477–482, 2014.

[142] L. E. Oikkonen, M. G. Ganchenkova, A. P. Seitsonen, and R. M. Nieminen. Formation, migration, and clustering of point defects in $CuInSe_2$ from first principles. *Journal of Physics: Condensed Matter*, 26(34), 2014.

[143] Y. S. Yee, B. Magyari-Kope, Y. Nishi, S. F. Bent, and B. M. Clemens. Deep recombination centers in $Cu_2ZnSnSe_2$ revealed by screened-exchange hybrid density functional theory. *Physical Review B*, 92(19), 2015.

[144] C. Freysoldt, J. Neugebauer, and C. G. Van de Walle. Electrostatic interactions between charged defects in supercells. *Physica Status Solidi B*, 248(5):1067–1076, 2011.

[145] C. W. M. Castleton, A. Hoeglund, and S. Mirbt. Density functional theory calculations of defect energies using supercells. *Modelling and Simulation in Materials Science and Engineering*, 17(8):084003, 2009.

[146] S. Lany and A. Zunger. Assessment of correction methods for the band-gap problem and for finite-size effects in supercell defect calculations: Case studies for ZnO and GaAs. *Physical Review B*, 78:235104, 2008.

[147] G. Makov and M. C. Payne. Periodic boundary conditions in ab initio calculations. *Physical Review B*, 51:4014–4022, 1995.

[148] Y. Kumagai and F. Oba. Electrostatics-based finite-size corrections for first-principles point defect calculations. *Physical Review B*, 89:195205, 2014.

[149] C. Stephan, S. Schorr, M. Tovar, and H.-W. Schock. Comprehensive insights into point defect and defect cluster formation in $CuInSe_2$. *Applied Physics Letters*, 98(9):091906, 2011.

[150] A. Alkauskas, J. L. Lyons, D. Steiauf, and C. G. Van de Walle. First-Principles Calculations of Luminescence Spectrum Line Shapes for Defects in Semiconductors: The Example of GaN and ZnO. *Physical Review Letters*, 109(26), 2012.

[151] A. Alkauskas, P. Deak, J. Neugebauer, A. Pasquarello, and C. G. Van de Walle. *Advanced Calculations for Defects in Materials: Electronic Structure Methods*. WILEY-VCH Verlag, 2011.

[152] M. Han, Z. Zeng, T. Frauenheim, and P. Deák. Defect physics in intermediate-band materials: Insights from an optimized hybrid functional. *Physical Review B*, 96:165204, 2017.

[153] J. Pohl, T. Unold, and K. Albe. Antisite traps and metastable defects in Cu(In,Ga)Se_2 thin-film solar cells studied by screened-exchange hybrid density functional theory. *ArXiv e-prints*, 1205.2556, 2012.

[154] F. Werner, D. Colombara, M. Melchiorre, N. Valle, B. El Adib, C. Spindler, and S. Siebentritt. Doping mechanism in pure $CuInSe_2$. *Journal of Applied Physics*, 119(17):173103, 2016.

[155] M. V. Yakushev, Y. Feofanov, R. W. Martin, R. D. Tomlinson, and A. V. Mudryi. Magneto-photoluminescence study of radiative recombination in $CuInSe_2$ single crystals. *Journal of Physics and Chemistry of Solids*, 64(9):2011–2016, 2003.

[156] M. V. Yakushev, A. V. Mudryi, V. F. Gremenok, V. B. Zalesski, B. I. Romanov, Y. V. Feofanov, R. W. Martin, and R. D. Tomlinson. Optical properties and band gap energy of $CuInSe_2$ thin films prepared by two-stage selenization process. *Journal of Physics and Chemistry of Solids*, 64(9):2005–2009, 2003.

[157] X. B. Hu, A. Gupta, T. Sakurai, A. Yamada, S. Ishizuka, S. Niki, and K. Akimoto. Investigation of deep-level defects in $Cu(In,Ga)Se_2$ thin films by two-wavelength excitation photo-capacitance spectroscopy. *Applied Physics Letters*, 103(16), 2013.

[158] A. Zunger, S. B. Zhang, and S. H. Wei. Revisiting the defect physics in $CuInSe_2$ and $CuGaSe_2$. *Conference Record of the 26th IEEE Photovoltaic Specialists Conference*, pages 313–318, 1997.

[159] M. Gloeckler and J. R. Sites. Efficiency limitations for wide-band-gap chalcopyrite solar cells. *Thin Solid Films*, 480:241–245, 2005.

[160] G. Hanna, A. Jasenek, U. Rau, and H. W. Schock. Influence of the Ga-content on the bulk defect densities of $Cu(In,Ga)Se_2$. *Thin Solid Films*, 387(1-2):71–73, 2001.

[161] G. H. Bauer, R. Bruggemann, S. Tardon, S. Vignoli, and R. Kniese. Quasi-Fermi level splitting and identification of recombination losses from room temperature luminescence in $Cu(In_{1-x}Ga_x)Se_2$ thin films versus optical band gap. *Thin Solid Films*, 480:410–414, 2005.